SYNTHESIS, ELECTROCHEMISTRY, KINETICS AND DENSITY FUNCTIONAL THEORY CALCULATIONS ON IMINO AND THENOYL-BIDENTATE COMPLEXES OF RHODIUM

A dissertation submitted in accordance with the requirements for the degree

Magister Scientiae

in the

Department of Chemistry
Faculty of Natural and Agricultural Sciences

at the

University of the Free State

by

Hendrik Ferreira

Supervisor

Prof. J. Conradie

Co-supervisor

Dr. M.M. Conradie

2015

Acknowledgements:

- Thanks must go to our Lord God and His son Jesus Christ, my personal Lord and Saviour, for always being with me as well as continuing to give me the strength, stamina and assistance through my studies and my life.

- A large thank you to my promoter, Prof. Jeanet Conradie, for her patience, wisdom, motivation, guidance and help she provided during and after this study.

- Thank you to Dr. Marianne Conradie for her guidance, motivation and help to understand and develop my skills in DFT computational chemistry.

- My late father, Willem Hendrik Ferreira, for his unconditional love, his wacky sense of humour and being the provider and protector of our family.

- My mother, Elizabeth Ann Ferreira, for her unconditional love, acceptance and pushing me to finish and do my best.

- My sister, Alida Ferreira, for her unconditional love, patience and offering to help me wherever she can.

- A very special thank you to Mrs. Tessa Swarts and Mrs. Callie Loubscher, without whom we as students would be completely lost in the maze that is administration and paperwork.

- The entire Physical Chemistry research group and all my friends for all the support, laughs, chats and general distractions from day to day life.

- The Chemistry department and the University of the Free State (UFS) for the facilities.

- The National Research Foundation (NRF) and UFS for the financial support.

TABLE OF CONTENTS

List of ligands and complexes *v*

Chapter 1: Introduction **1**

1.1 Introduction **1**

1.2 Monsanto process **2**

1.3 Aim of this study **3**

Chapter 2: Literature survey and fundamental aspects **5**

2.1 Introduction **5**

2.2 Computational Chemistry **5**

2.2.1 Introduction 5

2.2.2 Quantum mechanics 6

2.2.3 Basis sets 8

2.2.4 DFT 9

2.2.5 GGA 10

2.2.6 ADF 10

2.3 Electrochemistry **11**

2.3.1 Introduction 11

2.3.2 Experimental setup of CV 11

2.3.3 Information obtained from CV 15

2.3.4 Solvents, supporting electrolytes and reference electrodes 17

2.4 Reaction Kinetics **18**

2.4.1 Introduction 18

2.4.2 Reaction order 20

2.4.3 Transition State theory 23

2.4.4 Oxidative addition 24

2.4.5 Methyl migration/Carbonyl insertion 25

2.4.6 Tools for Analysis 27

2.5 L,L'-BID ligands 39

2.5.1 Introduction 39

2.5.2 Synthesis 40

2.5.3 Structural isomers 41

2.5.4 Cyclic voltammetry of L,L'-BID ligands 43

2.6 [Rh(L,L'-BID)$(CO)_2$] complexes 44

2.6.1 Introduction 44

2.6.2 Synthesis 44

2.6.3 Solid state structures 45

2.7 [Rh(L,L'-BID)(CO)(PPh_3)] complexes 46

2.7.1 Introduction 46

2.7.2 Synthesis 46

2.7.3 Structural isomers 47

2.7.4 Solid state structures 48

2.7.5 Cyclic voltammetry of [Rh(L,L'-BID)(CO)(PPh_3)] complexes 49

2.7.6 Kinetic reactions of [Rh(L,L'-BID)(CO)(PPh_3)] complexes 53

Chapter 3: Results and discussion 61

3.1 Bidentate ligands, L,L'-BID 61

3.1.1 Introduction 61

3.1.2 Synthesis 62

3.1.3 Cyclic Voltammetry (CV) 67

3.1.4 DFT computational study 72

3.2 [Rh(L,L'-BID)(CO)$_2$] complexes with (L,L') = (O,N), (O,NPh), (NPh,NPh) **79**

3.2.1 Synthesis 79

3.2.2 DFT computational study 85

3.3 [Rh(L,L'-BID)(CO)(PPh$_3$)] complexes with (L,L') = (O,NH) or (O,NPh) **89**

3.3.1 Synthesis 89

3.3.2 Cyclic Voltammetry (CV) 96

3.3.3 DFT computational study: Rh(L,L'-BID)(CO)(PPh$_3$) with L,L'-BID = $(CH_3CNHCHCOCH_3)^-$, $(CH_3CNPhCHCOCH_3)^-$ 104

3.4 [Rh(L,L'-BID)(CO)(PPh$_3$)] complexes with (L,L') = (O,O) **110**

3.4.1 Cyclic Voltammetry (CV) 110

3.4.2 DFT computational study: [Rh(L,L'-BID)(CO)(PPh$_3$)] with L,L'-BID = $(C_4H_3SCOCHCOCPh)^-$, $(C_4H_3SCOCHCOC_4H_3S)^-$ and $(C_4H_3SCOCHCOCF_3)^-$ 115

3.5 [Rh(L,L'-BID)(CO)(PPh$_3$)] + CH$_3$I kinetics **119**

3.5.1 IR in situ kinetic analysis 119

3.5.2 UV/VIS in situ kinetic analysis 125

3.5.3 NMR in situ analysis 134

3.5.4 Comparison of oxidative addition reaction rates for [Rh(L,L'-BID)(CO)(PPh$_3$)] + CH$_3$I reactions 143

3.5.5 Computational analysis of reaction mechanism 144

3.5.6 Summary of oxidative addition reaction kinetics: CH$_3$I + [Rh(L,L'-BID)(CO)(PPh$_3$)] 157

Chapter 4: Experimental 161

4.1 Experimental: Synthesis **161**

4.1.1 [$CH_3COCH_2CNHCH_3$] 1a 161

4.1.2 [$CH_3COCH_2CNPhCH_3$] 1b 161

4.1.3 [$CH_3CNPhCH_2CNPhCH_3$] 1c 162

4.1.4 [Rh(L,L'-BID)$(CO)_2$] 2 162

4.1.5 [Rh(L,L'-BID)(CO)(PPh_3)] 3 163

4.2 Experimental: Instrumentation and characterization 164

4.2.1 Spectroscopic measurements: NMR 164

4.2.2 Spectroscopic measurements: IR 164

4.2.3 Spectroscopic measurements: UV/VIS 165

4.2.4 Electrochemistry 165

4.3 DFT computational 166

4.3.1 ADF 166

4.3.2 Gaussian 167

Chapter 5: Concluding remarks and future perspectives 169

5.1 Concluding remarks 169

5.2 Future perspectives 170

APPENDIX 173

A NMR spectra 173

B IR spectra 181

C Electrochemistry 186

ABSTRACT 195

OPSOMMING 197

List of ligands and complexes

Ligand Precursors:	**Assigned Label**	
$CH_3COHCHCOCH_3$	(Hacac)	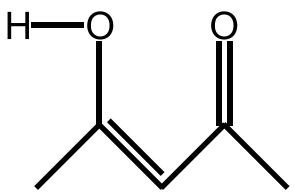
$CH_3COCHCNH_2CH_3$	**1a**	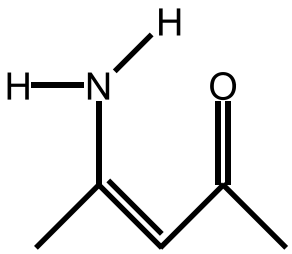
$CH_3COCHCNHPhCH_3$	**1b**	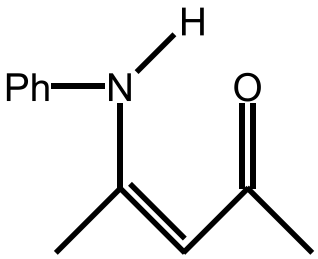
$CH_3CNHPhCHCNPhCH_3$	**1c**	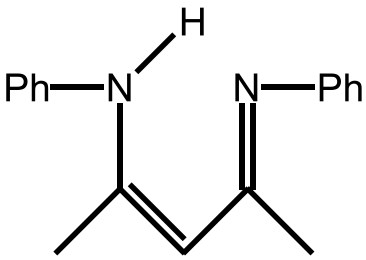

Dicarbonyls: **Assigned Label**

$Rh(CH_3COCHCNHCH_3)(CO)_2$ **2a**

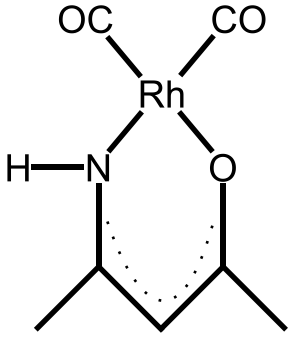

$Rh(CH_3COCHCNPhCH_3)(CO)_2$ **2b**

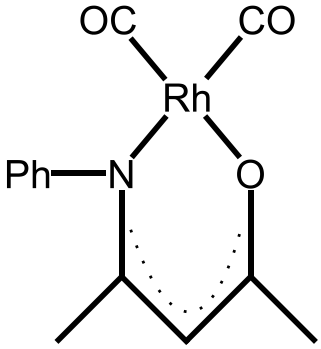

$Rh(CH_3CNPhCHCNPhCH_3)(CO)_2$ **2c**

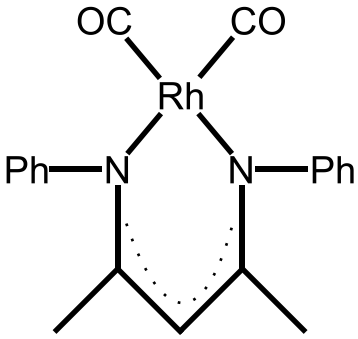

Phosphines: **Assigned Label**

$Rh(CH_3COCHCNHCH_3)(CO)(PPh_3)$ **3a**

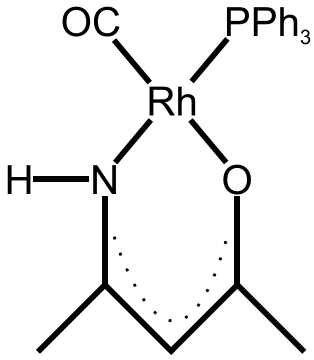

$Rh(CH_3COCHCNPhCH_3)(CO)(PPh_3)$ **3b**

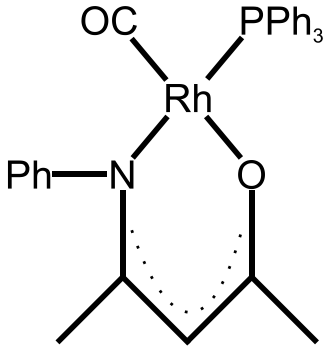

Thenoyls: Assigned Label

$Rh(C_4H_3SCOCHCOCPh)(CO)(PPh_3)$ **M1**

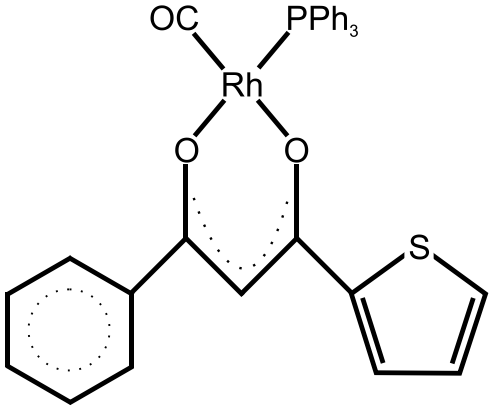

$Rh(C_4H_3SCOCHCOCC_4H_3S)(CO)(PPh_3)$ **M2**

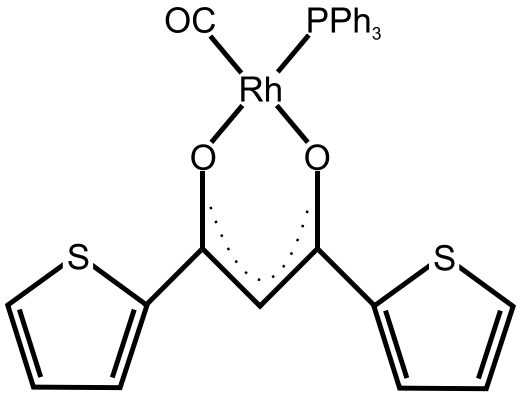

$Rh(C_4H_3SCOCHCOCF_3)(CO)(PPh_3)$ **M3**

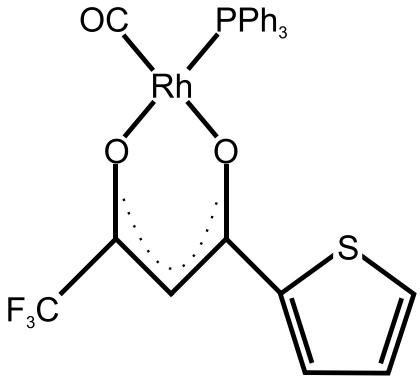

1 Introduction

1.1 Introduction

Rhodium complexes are very useful due to their use in various chemical reactions, mainly as catalysts such as in the reactions for alkene hydroformylation,[1] olefin hydrogenation[1,2] and carbonylation of methanol to acetic acid.[3,4] The most successful application of Rh as a catalyst is in the Monsanto process, which is also probably the most well-known industrial process. Monsanto started the development of a rhodium catalysed process for the production of acetic acid from methanol through carbonylation in 1966.[5] It required milder conditions (lower pressures and temperatures) than previous methods to facilitate the reaction, therefore reducing the production cost as well as exhibiting higher selectivity. However it uses Rh complexes, of which the Rh metal is a rare (natural abundance of 10^{-7}%) and expensive platinum group metal.[6] Therefore the effectiveness and recoverability of the rhodium catalyst is of great importance. The catalytic reactivity of rhodium complexes is found to be dependent on the nature of the ligands attached to the rhodium.[7] Researchers thus continuously do work to get a better understanding of the ways of purposeful alteration of the reactivity of such systems. For example, researchers utilized bidentate ligands in an attempt to determine the effect of either the groups or atoms that coordinate[8,9] to Rh or the groups or atoms that are bonded to the ligand

---

[1] C. Masters, *Homogeneous Transition-Metal Catalysis: A Gentle Art,* Chapman & Hall, London, 1981

[2] M.G. Pedrós, A.M. Maseu-Bultó, J. Bayardon, D. Sinou, *Catal. Lett.,* 2006, **107**, 205

[3] P.M. Maitlis, A. Haynes, G.J. Sunley, M.J. Howard, *J. Chem. Soc., Dalton Trans.,* 1996, 2187-2196

[4] A. Haynes, B.E. Mann, G.E. Morris, P.M. Maitlis, *J. Am. Chem. Soc.,*1993, **115**, 4093-4100

[5] J.F. Roth, J.H. Craddock, A. Hershman, F.E. Paulik, *Chem. Technol.,* 1971, 600; F.E. Paulik, J.E. Roth, *Chem. Commun.,* 1968, 1578; K.K. Robinson, A. Hershman, J.H. Craddock, J.F. Roth, *J. Catal.,* 1972, **27,** 389; F.E. Paulik, A. Hershman, W.R. Knox, J.E. Roth, *Monsanto Company, US Pat. 3 769 329,* 1973

[6] F.A. Cotton, G. Wilkinson, P.L. Gaus, *Basic Inorganic Chemistry,* John Wiley and Sons, 3rd Edition, pp 705-708

[7] E.A. Shor, M.A. Shor, V.A. Nasluzov, A.I. Rubaylo, *J. Struct. Chem.,* 2005, **46,** 220-229

[8] D.E. Graham, G.J. Lamprecht, I.M. Potgieter, A. Roodt, J.G. Leipoldt, *Trans. Met. Chem.,* 1991, **16,** 193-195

[9] A. Roodt, G.J.J. Steyn, *Recent Res. Dev. Inorg. Chem.* 2000, **2,** 1-23

structure,[10,11,12] on the oxidative addition reaction between CH_3I and the Rh complexes as model Monsanto catalysts. This study focuses on the synthesis and characterization of new square planar Rh(I) complexes containing a bidentate ligand. The oxidative addition of methyl iodide to the Rh(I) complex will also be studied to mimic the first step in the methyl iodide oxidative addition to the well known square planar $[Rh(CO)_2(I)_2]^-$ Monsanto catalyst.

1.2 Monsanto process

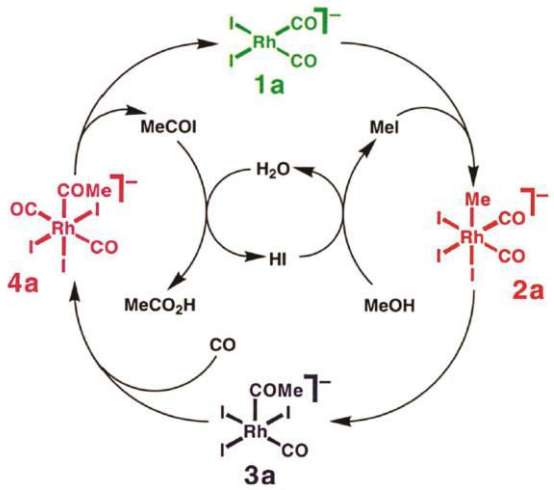

Figure 1.1: Graphical representation of the Monsanto catalytic cycle for the formation of acetic acid from methanol utilizing $[Rh(CO)_2(I)_2]^-$ as a catalyst. Reproduced from {Maitlis MP, Haynes A, Sunley GJ, Howard MJ, *Dalton Trans.,* (1996) p 2187-2196} with permission of The Royal Society of Chemistry.

Figure 1.1 illustrates the catalytic cycle of the Monsanto process in which methanol is converted to acetic acid utilizing the $[Rh(CO)_2(I)_2]^-$ catalyst. In the reaction cycle, the reaction between HI and methanol yields methyl iodide (CH_3I) and the reaction between water and acetyl iodide regenerates the HI. The reaction steps from **1a**-**4a** are S_N2 type organometallic reactions.

---

[10] W. Purcell, J. Conradie, T.T. Chiwehse, J.A. Venter, L. Twigge, M.P. Coetzee, *J. Organomet. Chem.,* 2013, **745-746,** 439-453

[11] D.W. Shaffer, S.A. Ryken, R.A. Zarkesh, A.F. Heyduk, *Inorg. Chem.,* 2012, **51,** 12122-12131

[12] S. Warsink, F.G. Fessha, W. Purcell, J.A. Venter, *J. Organomet. Chem.,* 2013, **726,** 14-20

Through studies utilizing IR spectroscopy it was found that **1a** was the major rhodium species.[3] The overall reaction rate was found to be first order but zero order for the CO and CH_3OH. The oxidative addition of the CH_3I to **1a** was then suggested to be the rate-determining step in order to produce **2a**. Forster *et al*,[13] however, showed that in practice **3a**, formed due to methyl migration in **2a**, was the 'first' detectable product. Compound **3a** is then carbonylated to **4a**, a six coordinate complex, which undergoes reductive elimination to regenerate **1a** and form the CH_3COI product. The cycle then repeats.

1.3 Aim of this study

For this study the focus is placed on the effect of varying L and L' on the rate of the oxidative addition reaction of CH_3I to [(Rh(L,L'-BID)(CO)(PPh_3)] where L,L'-BID is a bidentate ligand with coordinating atoms L and L' varied between O, NH and NPh.

The goals of this study were for the:

1) Synthesis, characterization, electrochemistry and density functional theory (DFT) calculations of the geometries of selected bidentate ligands (L,L'-BID with L,L' varied between O,NH; O,NPh and NPh,NPh).

2) Synthesis, characterization and DFT calculations of the geometries of selected dicarbonyl Rh complexes [Rh(L,L'-BID)$(CO)_2$].

3) Synthesis, characterization, electrochemistry and DFT calculations of the geometries of selected phosphine Rh complexes [(Rh(L,L'-BID)(CO)(PPh_3)].

4) Electrochemistry and DFT calculations of the geometries of selected phosphine Rh complexes [(Rh(O,O'-BID)(CO)(PPh_3)] with O,O'-BID = $C_4H_3SCOCHCOR$ with R = C_4H_3S, Ph, CF_3.

5) Kinetics of the oxidative addition reaction between CH_3I to the synthesized Rh(L,L'-BID)(CO)(PPh_3) complexes through the use of UV/VIS-, IR- and NMR spectroscopy.

6) DFT computational study of the reaction mechanism in (5) as well as the possible reaction products.

---

[13] T.W. Dekleva, D. Forster, *Adv. Catal.,* 1968, **34**, 81

INTRODUCTION

2 Literature survey and fundamental aspects

2.1 Introduction

Before any experiment or study can be started, a grasp of the fundamental aspects of chemical principles and properties is required. In this chapter the principles of synthetic techniques, chemical kinetics, spectroscopic techniques, electrochemistry and computational chemistry are reviewed.

2.2 Computational chemistry

2.2.1 Introduction

The combination of the fundamental laws of physics with mathematical methods forms the basis of theoretical chemistry.[1,2] Molecules are considered to be made up of atoms that consist of charged particles namely negative electrons and positive nuclei. Regarding chemical phenomena, the only physical force of interest of these particles is the Coulombic interactions between them. Theoretical chemistry focuses on the development of suitable theory to determine (1) the geometric arrangements of atoms in stable molecules, (2) their relative energies, (3) their properties, (4) molecular interactions, and other chemical phenomena.[1]

With the advent of powerful computers, computational chemistry was established as a new field where the computer is used as a tool much like a spectrometer would be used in experimental chemistry. Computational chemistry focuses on solving chemical problems *e.g.* predicting the structure of a possible compound, the energy of a system, the chemical properties, etc.[1,2] An important aspect in computational chemistry is the selection of a relevant and suitable theory

---

[1] F. Jensen, *Introduction to Computational Chemistry,* John Wiley and Sons, 2nd Edition, p 1-9, 14-15, 80, 192-196, 232-233, 247-249

[2] C.J. Cramer, *Essentials of Computational Chemistry: Theories and Models,* John Wiley and Sons, 2nd Edition, p 4-10, 105-110, 126, 166, 170-173, 249-253, 257-259, 263

level for a specific problem and the evaluation of the results' quality.[1,3] The equations utilized in theoretical chemistry are solvable for single atom systems, however in reality systems are comprised of multiple atoms therefore computational methods are able to produce approximate solutions to these multiple atom systems.[1]

2.2.2 Quantum mechanics

Matter has properties of both particles and waves, as proposed by De Broglie. Quantum mechanics was developed to account for this duality of particles.[2] Quantum mechanics allows for the calculation of the probability for any particular particle to be at a certain place and time. This probability function (P(r,t)) is described as the square of the wave function (ψ(r,t)) as seen in Equation 1 with r (a spatial position) and t (time). [1,3]

$$(P(r,t)) = (\psi^2(r,t)) \qquad \text{Equation 1}$$

Quantum mechanics states that any chemical system has a wave function, ψ, and that certain functions utilizing ψ will return an observable property of the selected system.[2,4,5,6]

The wave function is calculated by solving either the Dirac equation, a relativistic equation, or the Schrödinger equation, a non-relativistic equation. The difference between these two equations is the Hamiltonian operator (H) for each.[1] The Hamiltonian operator is dependent on the atomic numbers and positions of nuclei and the amount of electrons to determine the system's energy. It takes five contributions to the system's total energy into account namely the nuclei and electron's kinetic energy, nuclei and electron's attraction and internuclear and interelectronic repulsions.[2,6]

---

[3] D.C. Young, *Computational Chemistry: A Practical Guide for applying techniques to real world problems,* Wiley Interscience, New York, 2001, p 3-4, 10-12, 19-22, 42-43, 78

[4] U. Von Barth, *Physica Scripta,* 2004, **T109**, 9-39

[5] W.J. Hehre, *A guide to molecular mechanics and quantum chemical calculations,* Wavefunction, Irvine, 2003, p 22-26, 30-32

[6] W. Koch, M.C. Holthausen, *A chemist's guide to density functional theory,* Wiley-VCH, Weinheim, 2nd Edition, 2001, p 3-5, 8-9, 14-15, 33-39, 41-43, 70-74, 75-78, 97-98

CHAPTER 2

A hydrogen atom is used as a model to describe quantum mechanics. It has one electron and one nucleus, which are held together through Coulombic interaction. It is an interaction dependent on the distance between the two particles, however due to their low mass, the Schrödinger equation, Equation 2, is used in the calculations.[1] The Hamiltonian operator is relatively simple.[1,3,4,5,6]

$$H_{Schrödinger} = T + V \qquad \text{Equation 2}$$

Where T is the potential energy and V is the kinetic energy of the particle. If light particles move at a significant fraction of the speed of light, then the Dirac equation is used (see Equation 3). It has a more complicated Hamiltonian operator.[1,6]

$$H_{Dirac} = (c\alpha.\rho + \beta mc^2) + V \qquad \text{Equation 3}$$

Where α and β are 4 x 4 matrices for the various spins of electrons and positrons, ρ is the momentum of an electron, m is the mass of an electron at rest and c is the speed of light in a vacuum (3×10^6 m s^{-1}). If an approximate variable separation in quantum mechanics is not possible, then the many-body problem could typically be changed into pseudo one-particle systems through the process of taking the average interaction of the particles. This is known as the Hartree-Fock approximation. In this approximation the average repulsion between electrons is taken into account and calculated.[1,2,3,5,6]

In order to improve on the accuracy of the many-body system and account for many various factors of the system, the Born-Oppenheimer approximation is applied. In the Born-Oppenheimer approximation it is postulated that the nuclei move much slower than electrons, where any electronic reactions to external actions are effectively instantaneous. Therefore the two motions are decoupled and the electronic energies for static nuclear positions are then calculated.[2,5,6]

The Born-Oppenheimer approximation is a vital part to solving Schrödinger's equation since it makes the coupling of the electronic and nuclear motions negligible during calculations.[1]

2.2.3 Basis sets

Calculations solving the Schrödinger equation without fitting the parameters and data to experimental data directly is referred to as *ab initio* methods. Experimental data is merely used as a selection guide for the computational model. Approximations inherent to almost all *ab initio* methods, is the use of basis sets.[1,5]

The basis set has the smallest amount of functions which describes the position of all the electrons of a neutral atom.[1,2,3,5,6] Molecular orbitals are thought of as unknown functions in an infinite coordinate system. The basis set attempts to solve the unknown for a selected level of accuracy by expanding the molecular orbitals. The size of the basis set as well as the type determine the accuracy of the molecular orbital representations.[1,5,6,7]

To illustrate the electron occupation of molecular orbitals, a simple orbital model is used to assign the electrons to orbitals of increasing energy while ensuring Pauli's exclusion principle is followed. It can be quantized by the self-consistent field (SCF) approximation where it is assumed that each electron moves in all the other electrons' average potential. Hartree-Fock approximations account for most electronic interactions except the details of the electronic motion.[5,6,7]

In determining the electronic structure, two types of basis functions are available. They are Gaussian Type orbitals (GTO) and Slater Type orbitals (STO).[1] STO's are used for systems of atoms or diatomic molecules requiring high accuracy. GTO's are used when the accuracy is not required to be as high as with STO's however GTO basis functions are easier to use in calculations.[1]

When the basis function type and nuclei positions are selected, then the amount of basis functions to be used must be specified.[1,6] There are multiple types of basis sets that can be used. Some examples are the Single Zeta (SZ), which contains the same amount of functions as the basis set, Double Zeta (DZ), which contains two times the amount of basis functions and Triple Zeta (TZ), which contains three times the amount of functions as a basis set.[1,2,3,5,6]

---

[7] A. Ghosh, P.R. Taylor, *Curr. Opi. Biol.,* 2003, **7**, 113-114

Functions of high angular momentum are referred to as polarization functions (P).[1,2] Polarization allows for a better description of electron distribution in bonds *e.g.* the H-C bond, which is mainly described by the carbon's *s* and p_z orbitals and the hydrogen's *s* orbitals. The electronic distribution along the bond will be different from those perpendicular to the bond. If a p_z orbital is added to the hydrogen, the bond description can be improved. Thus in polarization a preceding orbital's description can be improved upon by adding the next orbital to the equation. Thus *p* orbitals polarize *s* orbitals, *d* orbitals polarize *p* orbitals, etc. Therefore a TZP basis set as and example, combines the TZ functions with the P functions, accounting for all orbital types as well as the polarization effect that each orbital has on the preceding, lower levelled orbitals.[1,2]

2.2.4 DFT

Density functional theory (DFT) is based on the Hohenberg and Kohn theory that the electron density in a molecular system determines the ground state electronic energy of the molecule. The electrons are theorized to interact with an external potential as well as with one another. This means that the energy of a system and the electron density have a one to one correspondence. DFT utilizes various functionals to determine energy values from the variables in a system. [1,2,3,4,6,7]

Utilizing the wavefunction approach in DFT, the only unknown in a system is the exchange-correlation energy (XC), which is only a small fraction of a system's total energy.[1,2] The correlational energy is typically defined in quantum chemical calculations as the difference between the calculated Hartree-Fock energy of a system and the exact energy value. The exchange energy is the energy that arises from taking the repulsion between electrons as well as the spin = ½ of electrons into account, which is largely neglected or assumed zero in the assumptions made in Coulombic calculations. Combined, these two energies make up the total exchange-correlation energy, which improves on the accuracy of system energy calculations done without them.[1,2,3,4,6] The simplest model used, the local density approximation (LDA), assumes that the electron density varies slowly therefore it derives formulae from an essentially uniform electron density.[1,2,4,6,7] Although it is considered an improvement on the previous Hartree-Fock method, it overestimates the molecular binding.[7]

HF is very good for calculating exchanges that favour higher spin states, however not as good for calculating the correlations. It has also been found that DFT generally favours the calculations of lower-spin state systems.[7]

2.2.5 GGA

In generalized gradient approximations (GGA) there are attempts made to improve over LDA by taking into account a non-uniform electron gas. It attempts to improve on the correlational energy by taking into account not only a specific local density value, but also the extent to which the local density is changing.[1,2,6] JP Perdew and his coworkers have formulated a few functionals that remove some undesired oscillations to the Taylor-like expansion, which is a mathematical method of representing various electronic actions and interactions, and which assists in meeting the accuracy requirements for the calculations. In this study, the refinements made in 1991 to the underlying model described by Perdew and Wang is utilized (PW91).[1,4,6] The PW91 functional[8] contains both the exchange and correlation energy functions whereas other functionals may only possess one of the functions, for example Becke[9] containing only the exchange part and Perdew[10] containing only the correlation part.[11]

2.2.6 ADF

The Amsterdam density functional (ADF) is a computational chemistry program that has been in development since the 1970's. There are constant improvements being made, which has made ADF a state of the art program for quantum-chemistry. This program contains a large variety of functionals which also incorporates relativistic effects. ADF utilizes Slater-type orbital (STO) functions and is a user-friendly program that is easy to use and flexible. [11] The use of STO's over GTO's best displays the required behaviour for molecular

---

[8] J.P. Perdew, J.A. Chevary, S.H Vosko, K.A. Jackson, M.R. Pederson, D.J. Singh, C. Fiolhais, *Phys. Rev. B,* 1992 **46**, 6671-6687; J.P. Perdew, J.A. Chevary, S.H. Vosko, K.A. Jackson, M.R. Pederson, D.J. Singh, C. Fiolhais, *Phys. Rev. B,* 1993, **48**, 4978

[9] A.D. Becke, *Phys. Rev. ,* 1988, **A38**, 3098-3100

[10] J.P. Perdew, *Phys. Rev.,* 1986, **B33**, 8822-8824; J.P. Perdew, *Phys. Rev.,* 1986, **B34**, 7406

[11] G. Te Velde, F.M. Bicklehaupt, E.J. Baerends, C.F. Guerra, S.J.A. Van Gisbergen, J.G. Snijders, T. Ziegler, *J. Comp. Chem.,* 2001, **22**, 931-967

orbitals, therefore fewer functionals are used in the construction of basis sets for the elements on the periodic table.[11]

2.3 Electrochemistry

2.3.1 Introduction

Cyclic Voltammetry (CV) is possibly one of the most versatile techniques in electroanalytics for qualitatively studying electrochemically active species' oxidation and reduction nature, reaction intermediates as well as subsequent follow-up product reactions that occur at an electrode surface.[12,13] A new oxidation state is rapidly generated in cyclic voltammetry during a forward scan and the resultant behaviour is then probed during a reverse scan.[14] It can also be used by electrochemists to determine the concentrations of the species in the solution quantitatively.[12]

The technique's versatility, in combination with the ease of use, has resulted in the extensive use of cyclic voltammetry in various fields. It is quite often the first experiment that is performed in an electrochemical study of a complex. A triangular waveform and rapid redox behaviour determination makes CV very effective for chemical analysis of simple or complicated reactions. Measurements are able to be done over a wide potential range and at various scan rates utilizing simple equipment.[14,15,16]

2.3.2 Experimental setup of CV

Modern instrumentation uses a three electrode setup as seen in Figure 2.1. There is a controlled potential that is applied to the working electrode contrasted with the potential at the reference electrode. The auxiliary electrode supplies the current required to sustain the species'

---

[12] J. Osteryoung, *J Chem Ed,* 1983, **60**, 296

[13] D.A. Skoog, D.M. West, F.J. Holler, S.R. Crouch, *Fundamentals of Analytical Chemistry,* Thomson Brooks Cole, 8th Edition, p 694-697

[14] P.T. Kissinger, W.R. Heineman, *J Chem Ed,* 1983, **60**, 702-706

[15] A.J. Bard, L.R. Faulkner, *Electrochemical Methods: Fundamentals and Applications,* John Wiley and Sons Inc, New York, 2nd Edition, p 257-261

[16] H.J. Gericke, N.I. Barnard, E. Erasmus, J.C. Swarts, M.J. Cook, M.A.S. Aquino, *Inorg. Chim. Acta,* 2010, **363**, 2222-2232

electrolysis. The reference electrode can be protected from large currents that could alter the potential of the electrode, by using this bridged reference electrode setup.[14,17]

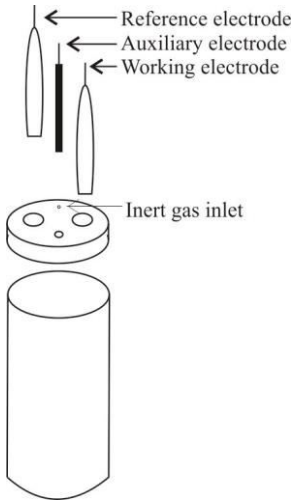

Figure 2.1: Electrochemical cell with the three electrodes used in cyclic voltammetry.

The potential is applied to a stationary, working electrode during a cyclic voltammetry experiment, which is changed linearly with respect to time. During a CV experiment, the potential is started where there is no electrode reaction and is then swept just beyond a potential where oxidation or reduction of a dissolved species occurs, at which point the sweep direction is then reversed all whilst the solution remains unstirred.[17] The current that is generated is measured throughout the cyclic voltammetry experiment. Variations in the time scale of the scan can be obtained by alteration of the scan rate (sweep rate). To suppress fast migration of charged product and reactant radicals, a supporting electrolyte is used in the solvent.[18] The three electrode system employed in a CV experiment minimizes the voltage errors that could occur due to ohmic loss via the solution by placing the working electrode and reference electrode close to each other.[17]

Another error source could arise from the differences in ion diffusion rates across the separating bridge of the reference electrode. The resultant difference between the anion and cation movements causes a charge separation and thus a difference in electrochemical potentials, known as a junction potential. This junction potential is minimized by selecting a supporting electrolyte that has similar coefficients of diffusion for its ions.[17]

---

[17] G.A. Mabbott, *J. Chem. Ed.,* 1983, **60**, 697

[18] D.H. Evans, K.M. O'Connell, R.A. Peterson, M.J. Kelly, *J. Chem. Ed.,* 1983, **60**, 290-293

The signal used for excitation in cyclic voltammetry has a triangular waveform, where the potential is linearly changed between two predetermined values (switching potentials) as seen in Figure 2.2.

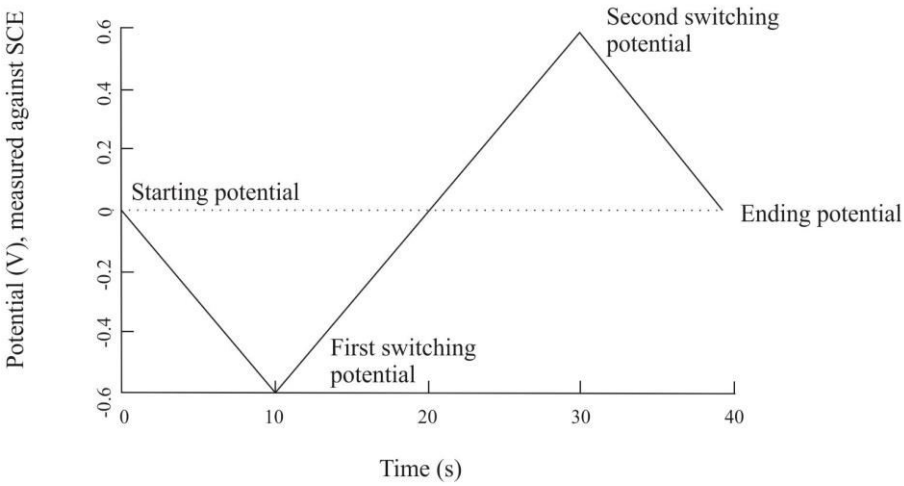

Figure 2.2: Triangular waveform of a typical excitation signal for cyclic voltammetry with switching potentials at -0.6 V and 0.6 V versus a standard calomel electrode (SCE) as reference electrode.[18]

Measuring the current generated at the working electrode during the scan is how a cyclic voltammogram (CV) is obtained. An example of a cyclic voltammogram is given in Figure 2.3. The voltammogram displays the current against the linear potential change. The European convention is to have the positive potential and current values on the right hand side (top part of CV) and the negative potential and current values on the left hand side (bottom part of CV). The American convention is the reverse of the European convention namely positive potential and current values on the left hand side (bottom part of CV) and the negative potential and current values on the right hand side (top of CV). The convention utilized in this study is the European convention.

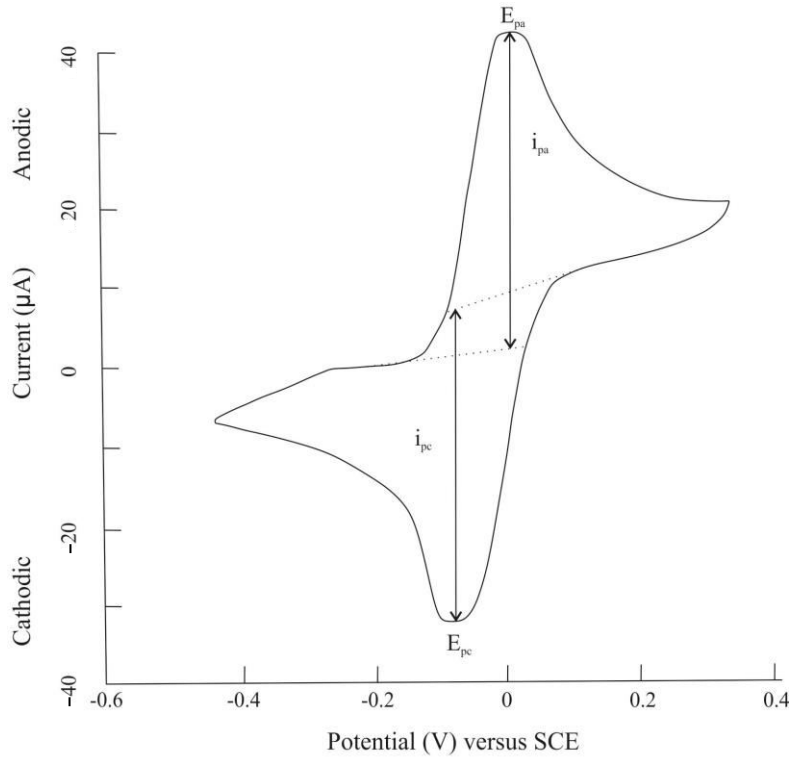

Figure 2.3: An example of a typical CV illustrating the basic shape, showing the anodic peak current (i_{pa}), the cathodic peak current (i_{pc}), the anodic peak potential (E_{pa}) and the cathodic peak potential (E_{pc})

The size and position (potential) of the cathodic peak, E_{pc}, which appears due to the reduction of a species when scanning into the negative direction, is a result of the competition between two different factors during reduction. The first is the increase in the reduction rate as the potential is swept to a more negative value and secondly is the thickening of the depletion layer at the working electrode across which the reactant has to diffuse, illustrated in Figure 2.4.[18]

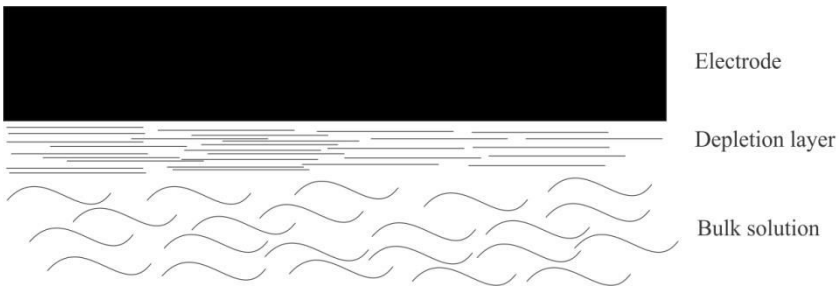

Figure 2.4: A graphical representation of the depletion layer at the electrode surface.

The anodic peak, E_{pa}, in a cyclic voltammogram occurs for similar reasons to the cathodic peak, though due to the oxidation of a species and the sweeping towards a more positive potential, and is affected by similar conditions and restrictions.[18]

The current that is generated in the oxidation or reduction experiment is thus dependant on two steps in the process, the electron transfer rate between the electrode and the species in solution and the migration of electrochemically active material towards the electrode surface (diffusion rate).[17]

2.3.3 Information obtained from CV

Important parameters that can be obtained from a cyclic voltammogram are the anodic and cathodic peak potentials, E_{pa} and E_{pc}, the anodic and cathodic peak currents, i_{pa} and i_{pc} and the current ratios.[13,14,15,18] The number of electrons that flow for each molecule during the redox process for an electrochemical reversible process can be obtained from Equation 4: $\Delta E_p = E_{pa} - E_{pc} = 0.059$ V/n, with n = number of electrons. The formal reduction potential $E^{0'}$ for an electrochemical reversible process can easily be obtained by the use of Equation 6.[14,16]

$$\Delta E_p = E_{pa} - E_{pc} \qquad \text{Equation 4}$$

$$i_{pa}/i_{pc} \text{ (reduction process) or } i_{pc}/i_{pa} \text{ (oxidation process)} \qquad \text{Equation 5}$$

$$E^{0'} = (E_{pa} + E_{pc})/2 \qquad \text{Equation 6}$$

A redox reaction at the electrode surface with a specific scan rate is electrochemically reversible if the electron transfer rate between the species analysed (analyte) and the electrode is fast enough to keep the concentrations of the reduced and the oxidized species at equilibrium.[16] The electrochemical reversibility of a process or reaction is characterized by the difference between the peak potentials (ΔE_p) being 0.059 V for a one electron process (see Equation 4).[13,14,15] This peak separation should be independent of the analyte concentration and scan rate.[16,17,18] This diagnostic value is an ideal value. However due to overpotentials and cell resistance, values up to 0.090 V per electron process is accepted to be electrochemically reversible.[16,19]

The Randles-Sevcik equation in Equation 7 describes the peak current of a chemically reversible system. In a reversible couple, the measured current is directly proportional, or linearly related, to the square root of the scan rate as well as the concentration.[14] When the species obeys the Randles-Sevcik equation, it indicates that the electrochemical process is diffusion controlled.[16]

$$i_p = (2.69 \times 10^5) n^{3/2} A D^{1/2} \nu^{1/2} C \qquad \text{Equation 7}$$

Where i_p is the peak current, A is the electrode area, D is the diffusion coefficient, C is the bulk concentration, n is the amount of electrons flowing per reactant molecule and ν is the scan rate.[13]

Chemical reversibility (as opposed to the electrochemical reversible process described above) is where a species can both be oxidized or reduced and the resultant radical returned to its initial state quantitatively without limitations to the rate at which these changes occur.[16] This requires that the electrochemically generated product or radical is stable on the timescale of the CV experiment. If this is the case then the ratio of the cathodic and anodic currents will be close or equal to unity: Equation 5 = 1.[13,17,18] This unity will be present and independent of the scan rate. The peak current, i_p, is measured relative to the baseline as seen in Figure 2.3.[15]

Irreversibility is defined as large deviations from the characteristics of reversible processes. Electrochemical irreversibility is where the peak separation, ΔE_p, is greater than 0.090 V. This deviation is due to the electron transfer kinetics between the electrode and the species studied being too slow.[13,14] Chemical irreversibility is where the ratio of the cathodic and anodic currents is not equal to or close to unity.[14,18] This deviation of the ratio is usually indicative of

[19] M. Landman, R. Liu, P.H. Van Rooyen, J. Conradie, *Electrochim. Acta,* 2013, **114**, 205-214

the instability of the oxidised or reduced species, or that follow-up reactions after the oxidation or reduction occur.[18]

During electrolysis, the concentration of reactant at the surface of the electrode becomes small in comparison with the bulk of the solution. The current evoked during the experiment is controlled by the diffusion rate of the reactant across the depletion layer, see Figure 2.4.[18] Since the experiment is being performed in an unstirred solution at a stationary electrode, the primary means of species movement towards the electrode surface is diffusion. This is a slow method of transport and is unable to maintain a steady concentration in the region that is close to the electrode surface. Thus the zone of depletion increases and the subsequent distance that the species must travel also increases. This causes the decrease in the mass transport rate and a decrease of the current after the peak oxidation or reduction potential, leading to the typical form of the current seen in Figure 2.3.[17]

Another use for the current that is measured is that it could be used in determining the species concentration in the bulk solution using Equation 7.[17] Qualitatively analysing and diagnosing the homogeneous chemical reactions that occur at or near the working electrode surface is one of the most useful aspects of cyclic voltammetry, along with the variable time scale of the experiment *via* scan rate adjustments. This variation in time scales allows for some assessment of the various reaction rates.[14]

2.3.4 Solvents, supporting electrolytes and reference electrodes

In an electrochemical cell the solvent system plays a very important role. It consists of a solvent and a supporting electrolyte. These two components determine the experimental potential window where the background current is at a minimum. The electrolyte ensures charged particle movement without obstructions. The system must thus be chemically and electrochemically inert within the potential window. The solvent system must not undergo any reaction with the intermediate radicals formed during electrolysis of the species studied, nor undergo electrolysis itself. The dielectric constant of the solvent system must be as high as possible to ensure low electrical resistance, to which the contributions stem from the solvent type used as well as the electrolyte. In organic solvents such as acetonitrile or dichloromethane, tetrabutylammonium hexafluorophosphate (TBAHFP) is used as electrolyte.[13,14,18]

During the experiment the reference electrode's potential remains constant. In an aqueous medium, the saturated calomel electrode (SCE), the silver/silver chloride electrode (Ag/AgCl) or standard hydrogen electrode (SHE/NHE) is typically used as reference electrode (RE). A salt bridge is used to isolate the electrode from the solution in order to prevent possible contamination through leakage. Some examples of a reference electrode in non-aqueous media are an Ag-wire directly placed in the solution or an Ag/Ag^+ (0.01 M $AgNO_3$ in CH_3CN) electrode. To compare electrochemistry data reported against different reference electrodes, conversion is necessary using for example Equations 8 – 12. IUPAC recommended that all potentials should be referenced against the FcH/FcH^+ couple.[20]

$$(FcH/FcH^+)\ E^{0'} = 0.66(5)\ \text{V } vs \text{ SHE in } [^n(Bu_4)N][PF_6]/CH_3CN \quad \text{Equation 8}$$

Decamethylferrocene (Fc*) $E^{0'}$ = -0.508 V *vs* FcH/FcH^+ in $[^n(Bu_4)N][PF_6]/CH_3CN$[22] Equation 9

$$E_{SHE} = 0.2414 - E_{SCE} \quad \text{Equation 10}$$

$$\text{SCE} = 0.2414\ \text{V } vs \text{ NHE} \quad \text{Equation 11}$$

$$\text{Ag/AgCl (KCl sat)} = 0.197\ \text{V } vs \text{ NHE} \quad \text{Equation 12}$$

2.4 Reaction Kinetics

2.4.1 Introduction

Kinetics is fundamentally concerned with the details of how a system transits between states and the time that has elapsed. Chemical kinetics allow for the determination of the reaction rate but also provides a general method for determining the reaction mechanism. The reaction mechanism encompasses all the collisions and other processes involving the molecules during

---

20 G. Gritzner, J. Kuta, 1984, **56**, 461-466.

21 A.J.L. Pombeiro, *J. Organomet. Chem.,* 2005, **690**, 6021-6040

22 M. Landman, B.E. Buitendach, M.M. Conradie, R. Fraser, P.H. Van Rooyen, J. Conradie, *Journal of Electroanalytical Chemistry*, 2015, **739**, 202-210

the transition from starting material to products. All mechanisms are merely theories, which receive support from experimental kinetic measurements. The justification for a mechanism's acceptance as fact is in its ability to predict the types of products or the ideal operating conditions for chemical reactions. Kinetic measurements may give information regarding a reaction's individual steps however it is relatively limited in providing stereochemical details.[23] Reaction rates are an indication of the speed at which a specific reaction, or process, is taking place. It is defined as the concentration change rate of a species in a reaction, dependant on whether the species is a product or reactant.[23] Reaction rates are affected by the state of the participating reactants (solid, gas, liquid), their concentrations, catalyst presence and the temperature.[24] Reaction rates are represented by rate laws denoting the reaction order. The order describes the rate in terms of its dependence on reactant concentrations.[24,25]

Consider the general reaction:[24,25]

$$aA + bB \longrightarrow gG + hH \qquad \text{Equation 13}$$

It can be seen that there are four different representations of the reaction rate possible.[25,26]

$$\text{Rate} = -d[A]/dt \text{ or } -d[B]/dt \text{ or } d[G]/dt \text{ or } d[H]/dt \qquad \text{Equation 14}$$

Reactions may cause different amounts of moles of the products and reactants to be used or produced, therefore the rate law is better expressed as:[23]

$$\text{Rate} = 1/a\,(-d[A]/dt) = 1/b\,(-d[B]/dt) = \text{etc}\ldots \qquad \text{Equation 15}$$

The signs are placed to ensure the positive numerical value of the rate.

---

[23] A.A. Frost, R.G. Pearson, *Kinetics and mechanism,* John Wiley and Sons, p 1, 2, 9-10

[24] T.L. Brown, H.E. LeMay Jr, B.E. Bursten, C.J. Murphy, *Chemistry the central science,* Pearson Prentice Hall, 10th Edition, p 574-610

[25] J.F. Van Staden, W.D. Basson, *Basiese beginsels in fisiese, analitiese en anorganiese chemie,* Sigma-Pers Bpk, p 221-252

[26] S.W. Benson, *The foundation of chemical kinetics,* McGraw-Hill, p 10-20, 55, 81-82

Since the rate of a reaction decreases with time as well as with the decrease in the concentrations of the reactants, the rate constant (k) is used to describe the speed of a reaction.[25] The rate expression for the general reaction is:[25]

$$\text{Rate} = 1/a\ (d[A]/dt) = 1/b\ (d[B]/dt) = k[A]^m[B]^n \qquad \text{Equation 16}$$

Where k = rate constant; m = order of reaction with respect to A and n = order of reaction with respect to B.[25] The reaction rate is not typically obtained from an experiment directly but rather from the concentration changes measured over time, under various conditions. Determining the change in concentration is most often done through *in situ* analysis like UV/VIS spectroscopy, IR spectroscopy or NMR spectroscopy.[27]

2.4.2 Reaction order

The order of a reaction shows the correlation between the concentration of a species with time.[25] Zero order reactions have no dependence on the concentration of the reactants, first order reactions are dependent on only one reactant's concentration and second order reactions are dependent on either the square of one reactant's concentration or dependant on two reactants concentrations.[26]

With zero order reactions the rate expression is:[26,25]

$$\text{Rate} = d[A]/dt = k \qquad \text{Equation 17}$$

Where the values for m and n, in Equation 16, are 0. This implies that the reaction has no dependence on the concentration of any of the species in a reaction or of the time. The integrated form of Equation 17 gives Equation 18, that can be applied to experimental data to determine if the reaction is of zero order. For a graph of [A] against t, a straight line will be the result with a gradient of k thus the equation for the line, with $A = A_0$ at $t = 0$.[26,25]

$$kt = [A] - [A]_0 \qquad \text{Equation 18}$$

[27] G.M. Barrow, *Physical Chemistry,* McGraw-Hill, 5th Edition, p 751-756

For first order reactions of the general reaction in Equation 13, the rate expression is:[24,26,25]

$$\text{Rate} = k[A] \qquad \text{Equation 19}$$

The integrated form, Equation 20, is used for testing if the reaction is first order. Plotting [A] against t would yield a curve, not a straight line, however plotting ln[A] against t would yield a straight line.

$$\ln[A]_t = -kt + \ln[A]_0 \qquad \text{Equation 20}$$

Where $[A]_0$ is the concentration of A at time t = 0 and k is the first order rate constant.[23,24,25]

Pseudo first order reactions are where an isolation of the species in a reaction is possible through adjustments of the concentrations to have one of the species present in a large excess. This excess species concentration will remain practically constant as the reaction progresses and therefore the order is experimentally reduced.[26] From the assumed general reaction, Equation 13, the true second order rate is for eample expressed as:

$$-dA/dt = k[A][B] \qquad \text{Equation 21}$$

However under pseudo first order conditions, one of the concentrations is selected to be in large excess *e.g.* A, therefore the rate is expressed as:

$$\text{Rate} = -dA/dt = k[A][B] = k'_{obs}[B] \qquad \text{Equation 22}$$

Where $k'_{obs} = k[A]$. This is in the form of a first order reaction and k'_{obs} is called the observed pseudo first order rate constant.[26]

Second order reactions have two types of reaction rate laws. The first is where the rate is proportional to the square of a reacting species concentration:[26,25]

$$d[A]/dt = -k[A]^2 \qquad \text{Equation 23}$$

The second is where the rate is proportional to the product of two different species concentrations:[26]

$$d[A]/dt = -k\,[A][B] \qquad \text{Equation 24}$$

For the first type, integration yields the equation:[23,26,25]

$$1/[A] - 1/[A]_0 = kt \qquad \text{Equation 25}$$

Where $[A]_0$ is the concentration of A at the starting time.[26]

With the second type the general reaction rate law for a balanced reaction is:[26]

$$d[A]/dt = -k_A[A][B] \text{ or } d[B]/dt = -k_B[A][B] \qquad \text{Equation 26}$$

After integration and simplification:[24,26]

$$\ln([A]/[B]) = ((b[A]_0 - a[B]_0)/a)kA_t + \ln([A]_0/[B]_0) \qquad \text{Equation 27}$$

is obtained which is a straight line equation.[26]

In chemical reactions that follow more than one step, it is possible for one of the steps to be slower than the rest. The reaction rate would then depend largely on this slower step, rather than any other since they would be fast relative to the slow step.[26] This slow step is referred to as the rate determining step.[25]

The rate of a reaction increases with temperature. This is due to the higher movement speed of the molecules ensuring a larger amount of collisions. These collisions lead to reactions if (1) the molecules have enough energy, (2) the molecules are oriented correctly to react and (3) if the collisions are effective. The energy needed for a molecule to react is called the Arrhenius activation energy (E_a) and it is the energy barrier required to be overcome for a reaction to occur.[25] Figure 2.5 illustrates the energy profile with the formed transition state, at the peak of the curve, from the starting reactants to form the product.[24]

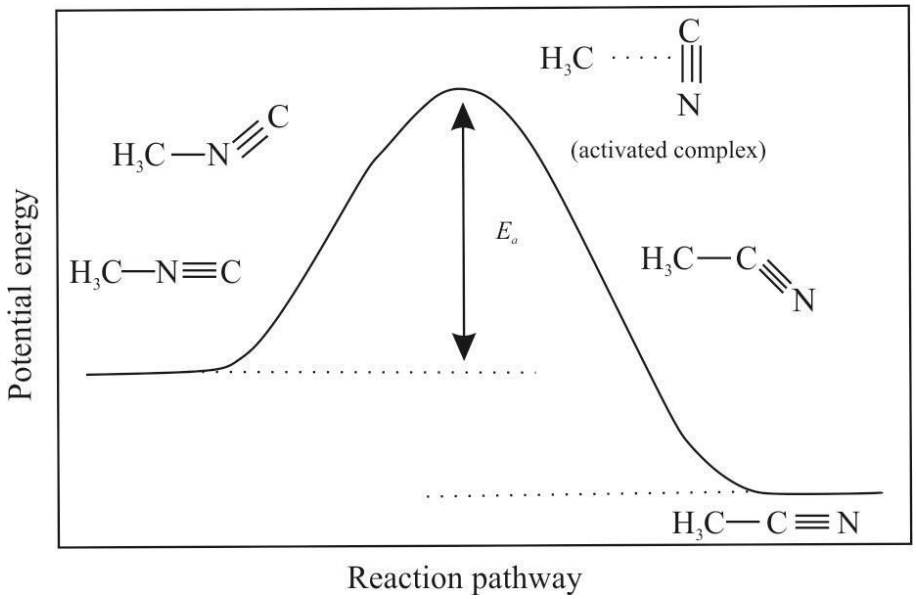

Figure 2.5: Using the methyl isonitrile → acetonitrile reaction as an example it can be seen from the potential energy curve that an energy barrier, the activation energy (E_a) must be overcome in order to form the product acetonitrile.[24]

2.4.3 Transition State theory

Transition state theory, developed by Eyring,[28] has a focus on the species in the chemical reaction that relates to the highest energy stage of the reaction namely the activated complex also referred to as the transition state. This activated complex is treated as a formal, distinct molecule,[27,28,29] leading to products or towards the reactants.[29]

Assuming that two complexes react to form products, the transition state theory states that as the reaction progresses there is always a small amount of the reactants that have enough energy in order to form products. If the reaction is not too violent then an equilibrium exists between the reactants and the activated complex:[27,29]

$$A + B \underset{}{\overset{K^{\#}}{\rightleftharpoons}} (AB)^{\#} \xrightarrow{k^2} \text{products} \qquad \text{Equation 28}$$

[28] A.W. Adamson, *A textbook of physical chemistry,* Academic Press, 2nd Edition, p 574-577

[29] D. Katakis, G. Gordon, *Mechanisms of Inorganic reactions,* John Wiley and Sons, p 57-58

The reaction rate is then dependent on two factors ,1) transition state molecule concentration and 2) rate of transition towards the final product.[27] The rate is then related to a vibrational frequency that facilitates the transition from activated complex to products along the reaction coordinate:[27,28]

$$\text{Rate} = -d[A]/dt = -d[B]/dt = \nu_{RC}K^{\#}[A][B] \qquad \text{Equation 29}$$

Where ν_{RC} = vibration frequency and $K^{\#}$ = equilibrium constant with respect to the activated complex and reactants in Equation 28. $K^{\#}$ is related to enthalpy of activation ($\Delta H^{\#}$), entropy of activation ($\Delta S^{\#}$) and free energy of activation ($\Delta G^{\#}$):[27,28]

$$\Delta G^{\#} = -RT\ln K^{\#} \qquad \text{Equation 30}$$

$$\Delta G^{\#} = \Delta H^{\#} - T\Delta S^{\#} \qquad \text{Equation 31}$$

The rate constant in Equation 28, after mathematical manipulations is given by:[27,28,29]

$$k_2 = (kT/h)(e^{(\Delta S\#/R)})(e^{(\Delta H\#/RT)}) \qquad \text{Equation 32}$$

Chemical reactions are generally divided into the following types: oxidative addition, insertion, substitution and radical reactions. The first two are important for this study.

2.4.4 Oxidative addition

When both the oxidation state and coordination number of a metal in a molecule is increased by two through the addition of a ligand to the molecule, the reaction is termed as an oxidative addition reaction.[30,31,32] Transition metal complexes with d^8 or d^{10} electron configurations are the most common complexes involved in oxidative addition reactions.[30,31,33] However oxidative

---

[30] F.A. Cotton, G. Wilkinson, P.L. Gaus, *Basic Inorganic Chemistry,* John Wiley and Sons, 3rd Edition, p 705-708

[31] B.E. Douglas, D.H. McDaniel, J.J. Alexander, *Concepts and Models of Inorganic Chemistry,* John Wiley and Sons, 2nd Edition, p 465-468

[32] I.S. Butler, J.F. Harrod, *Inorganic Chemistry: Principles and Applications,* Benjamin/Cummings Publishing, p 604-605

addition is not limited to metals only and can also occur in complexes made of main group elements.[32]

There are three parameters that must be fulfilled in order for an oxidative addition reaction to occur. The first is that the metal must have stable oxidation states that are separated by two units, secondly the molecule's metal must have two coordination sites that are vacant and lastly there should be nonbonding electron density on the molecular metal.[30,32,33]

There have been four mechanisms found for oxidative addition.[30,31]

1) In a polar medium, an ionic mechanism is favoured.[30,31]

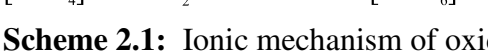

Scheme 2.1: Ionic mechanism of oxidative addition.

2) In organic chemistry the S_N2 type attack is quite common. The transition metal complex is the molecule to attack an alkyl halide *e.g.*[30,31]

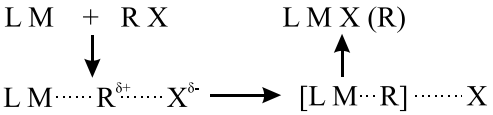

Scheme 2.2: S_N2 mechanism of oxidative addition.

3) The oxidative addition reaction could be free radical in nature.[30,31]
4) A one step, concerted process for molecules with little to no polarity have been observed.[30,31]

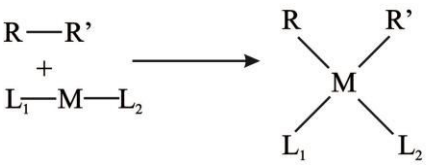

Scheme 2.3: One step concerted process of oxidative addition.

2.4.5 Methyl migration/Carbonyl insertion

The chemical definition for insertion describes any reaction where an atom or group gets inserted between two other atoms of a molecule that are bound together.[33,34] Small molecules getting

---

[33] F.A. Cotton, G. Wilkinson, P.L. Gaus, *Basic Inorganic Chemistry,* John Wiley and Sons, 3rd Edition, p 708-710

[34] F.A. Cotton, G. Wilkinson, C.A. Murillo, M. Bochmann, *Advanced Inorganic Chemistry,* John Wiley and Sons, 6th Edition, p 1207-1212

inserted between metal-ligand bonds are part of this large class of reactions.[35] The term only describes the end result of this type of reaction, it does not have any mechanistic significance.[35]

There are various terms for insertion reactions depending on which atom the migrating group gets transferred to. One of interest in this study is the 1,1-insertion of CO into a metal-carbon bond (M-CR):[34]

Scheme 2.4: 1,1-insertion process.

When looking at the mechanistically studied CO insertion through the use of labelled reagents, it has been found that (1) a CO that is already coordinated to the metal atom migrates and not an external CO gets inserted, (2) The external CO is bonded to the metal *cis* to the newly formed acyl group (inserted newly formed group) and (3) the external atom does not have to be CO, it can be any other ligand.[33,34,35] The mechanism of insertion can be seen in Scheme 2.5.

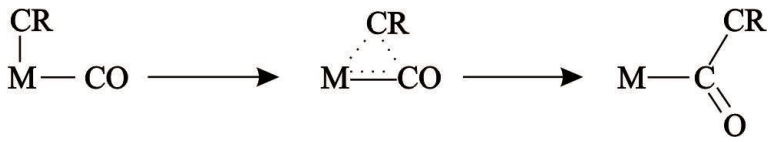

Scheme 2.5: 1,1-insertion mechanism of insertion. [33]

More than one isomer may be formed since five- coordinated species could undergo rearrangements intramolecularly.[33] During insertion reactions, especially regarding olefins, the oxidation state of the transition metal remains unchanged.[35]

---

[35] B.E. Douglas, D.H. McDaniel, J.J. Alexander, *Concepts and Models of Inorganic Chemistry,* John Wiley and Sons, 2nd Edition, p 461

2.4.6 Tools for Analysis

Knowledge and understanding of the fundamentals of chemical kinetics may answer the theoretical questions that arise regarding reactions, however the question arises of how they are determined experimentally. The answer is to follow the reaction progress spectroscopically. The methods that can be used for *in situ* analysis of a reaction, utilized in this study, are Ultraviolet and Visible (UV/VIS) spectroscopy, Infrared (IR) spectroscopy and Nuclear Magnetic Resonance (NMR) spectroscopy.

2.4.6.1 Ultraviolet and Visible spectrophotometry (UV/VIS)

Spectrophotometry is a science that measures the ability of a chemical system's absorption of incident radiant energy of certain wavelengths.[36,37,38] Electromagnetic radiation from the UV region is used to stimulate the sample, where the sample gets converted from a low energy ground state to a higher energy excited state.[36] For absorption to occur the energy of the radiation must be exactly equal to the energy difference between the two states. During this process an electron in a low-energy molecular orbital of the sample moves to a higher energy molecular orbital also known as electronic transitions.[36,39,40] Bonding electrons of the outer shell of the molecule are involved during the excitation during UV absorption.[41]

The nature of the absorption provides useful information regarding the substance and the extent of the occurring absorption is an indicator of the amount of substance.[38,41] The information obtained is in graphic form as a curve and is commonly known as an absorption spectrum or a transmittance spectrum.[38]

---

[36] D.A. Skoog, D.M. West, F.J. Holler, S.R. Crouch, *Fundamentals of Analytical Chemistry,*, Thomson Brooks Cole, 8th Edition, p 715-716, 720-727,728, 784-802

[37] J.H. Richardson, R.V. Peterson, *Systematic materials analysis,* Academic Press Inc, Vol 2, p 199-227

[38] G.L. Clark, *The Encyclopedia of Spectroscopy,* Theinhold publ. Co., p 1-3, 7-12

[39] D.L. Pavia, G.M. Lampman, G.S. Kriz, *Introduction to spectroscopy,* Brooks and Cole, 3rd Edition, p 353-389

[40] J.W. Moore, W.G. Davies, R.W. Collins, *Chemistry,* McGraw-Hill, p 727-728

[41] D.A. Skoog, F.J. Holler, S.R. Crouch, *Principles of Instrumental Analysis,* Thomson Brooks Cole, 6th Edition, p 336-348, 367-378

(i) *Beer's Law*

During absorption there are two fundamental laws that govern the absorption of radiation by substances. The first is Bouguer's law (most often attributed to Lambert) and the second is Beer's law, which quantitatively illustrates the relationship between the concentration of a substance and its capacity to absorb radiation.[36,38] Combining the two laws gives the well-known Beer-Lambert law

$$A = \varepsilon C l \qquad \text{Equation 33}$$

Where A is the absorbance, C is the concentration of the sample, l is the path length travelled and ε is the molar extinction coefficient of the sample.

(ii) *UV/VIS spectra:*

Sharp peaks or lines are expected in a pure absorption spectrum. This is only possible in a gaseous form where there is sufficient separation between molecules that allow free rotation and vibration. In a liquid form the freedom of rotation and vibration is restricted leading to the rotation and vibration levels being modified in a non-uniform manner.[36,39] These various states are quite closely packed and discrete due to their small energy differences between the vibrational and rotational levels relative to the electronic transitions. These small energy differences are superimposed on the electronic spectrum, which results in broad peaks observed due to the instrument used not being able to resolve the various transitions.[39,40,41]

Factors affecting the spectrum are the solvent, which should be transparent or non absorbing in the region studied, the slit width as well as the scattering of the radiation as can be seen in Figure 2.6.[36]

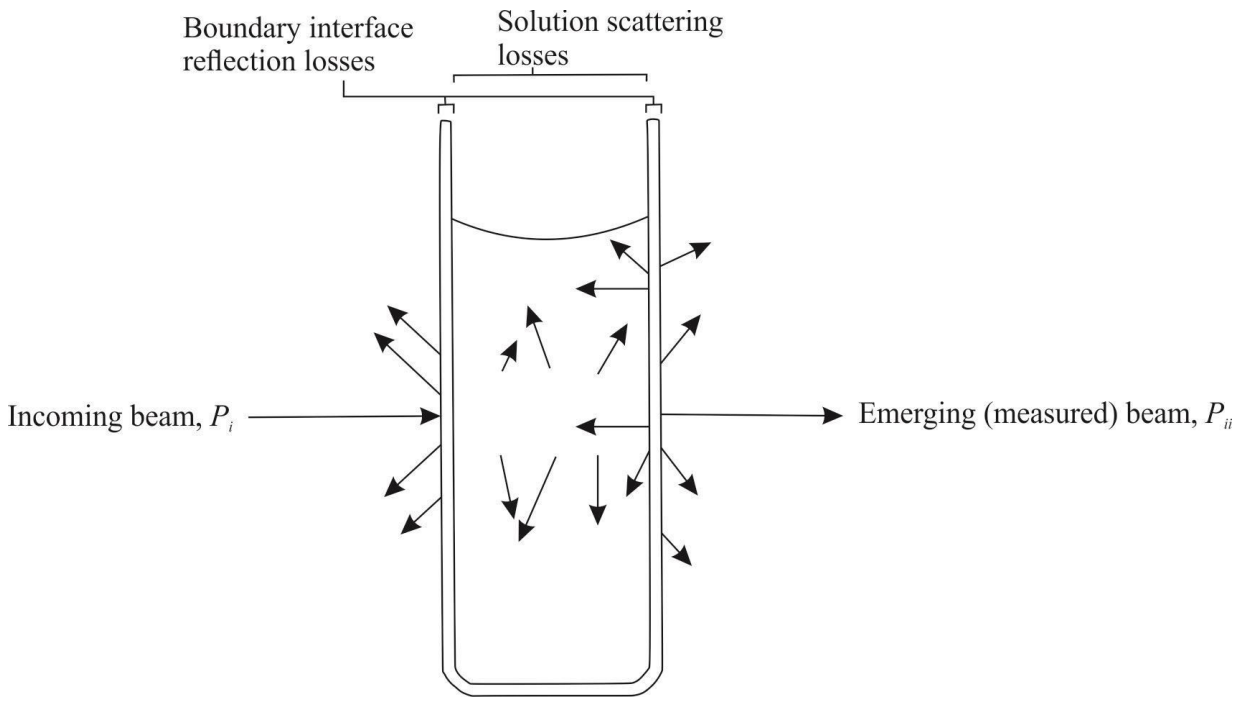

Figure 2.6: Scattering and reflection losses with a glass cell contained solution. Reflection losses could occur at all separation boundaries of the differing materials.

(iii) *Applications of UV/VIS*

Qualitative:

Spectrophotometry is a non-discriminatory method of analysis, particularly UV/VIS. It shows the overall effect of all the absorbers when a mixture of substances is analysed. Therefore the curves of pure compounds may be significantly changed through interactions with a substance that absorbs in the same region as the pure compound such as the solvent molecules.[38] Measurements utilizing ultraviolet radiation are used in the detection of chromophoric groups or groups acting like chromophores however UV/VIS spectra do not have the fine structure to always permit unambiguous identification of analytes and must therefore be supplemented with additional chemical or physical evidence like NMR spectra, infrared spectra, etc.[41]

Quantitative:

UV/VIS absorption spectroscopy is a useful tool available for quantitative analysis due to its wide applicability to various systems, low detection limits, high selectivity and accuracy and the ease and convenience of acquiring data.[41] These principles as well as Beer's law must be adhered to for the information to be relevant and accurate.[38] One example of the uses of UV/VIS spectroscopy in chemistry is to determine the catalytic activity of transition metal complexes.

For example the oxidative addition reaction of different Rh(I) complexes reacting with methyl iodide utilizing UV/VIS spectroscopy was done by various researchers[42,43,44,45,46,47,48] by following the change in absorption of the reactant, as is illustrated in Figure 2.7. In Figure 2.7 it can be seen that as the reaction proceeds, the absorbance for the Rh(I) complex decreases, which allows for the determination of the rate constant of the oxidative addition reaction.

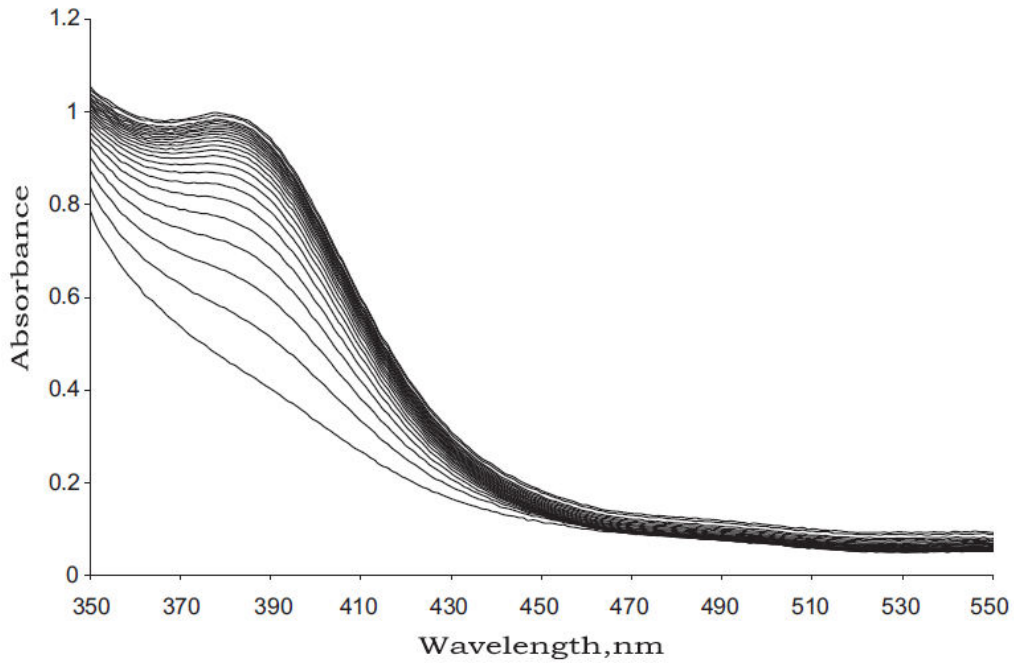

Figure 2.7: UV spectra of the reaction between CH_3I and Rh(Me-Cupf)(CO)(PPh_3) at 25°C. The Rh complex concentration was 1.7 x 10^{-4} M and the concentration of CH_3I was 0.2 mol dm^{-3}. [42] Reprinted from J. Organomet. Chem., 726, S. Warsink, F.G. Fessha, W. Purcell, J.A. Venter, Synthesis and characterization of rhodium (I) 2-methylcupferrate complexes and their kinetic behaviour in iodomethane oxidative addition, pp 14-20, Copyright (2012), with permission from Elsevier.

---

[42] S. Warsink, F.G. Fessha, W. Purcell, J.A. Venter, *J. Organomet. Chem.,* 2012, **726**, 14-20

[43] F.P. Pruchnik, R. Starosta, M.W. Kowalska, E. Galdecka, Z. Galdecki, A. Kowalski, *J. Organomet. Chem.,* 2000, **597**, 20-28

[44] W. Purcell, J. Conradie, T.T. Chiweshe, J.A. Venter, L. Twigge, M.P. Coetzee, *J. Organomet. Chem.,* 2013, **746**, 439-453

[45] M.M. Conradie, J. Conradie, *Inorg. Chim. Acta,* 2008, **361**, 2285-2295

[46] M.M. Conradie, J.J.C. Erasmus, J. Conradie, *Polyhedron,* 2011, **30**, 2345-2353

[47] J.J.C. Erasmus, J. Conradie, *Inorg. Chim. Acta,* 2011, **375**, 128-134

[48] J. Conradie, J.C. Swarts, *Organometallics,* 2009, **28**, 1018-1026

2.4.6.2 Infrared Spectroscopy (IR)

Chemists have been using IR spectroscopy since the late 1950's to identify organic compounds even though IR radiation is only a small portion of the whole electromagnetic spectrum.[49] Almost all species absorb infrared radiation to some extent. It is therefore a powerful instrument or technique in the identification of pure inorganic and organic compounds.[50] IR radiation is insufficient in energy to break bonds, however it does make molecules vibrate more strongly.[51] For interactions between the radiation and a molecule to occur there has to be a change in the dipole moment of the molecule.[49] The dipole moment is determined by the difference in charge or size between at least two atoms that make up a molecule as well as the distances between the centres of the charges.[51,52] As a molecule vibrates, the position of the different atoms changes with respect to each other, which causes the fluctuation in the dipole moment, which in turn creates a field that can interact with the radiation.[53] Certain frequencies of the radiation have an energy that exactly matches the frequency of the dipole moment change and gets absorbed by the molecule.[51,52,53] When the radiation is absorbed, a change in the vibrational amplitude occurs.[51,53] The greater the dipole moment change, the larger the absorption.[51] In this same manner all asymmetric molecules rotating around a centre of mass or that vibrates, also result in dipole moment fluctuations.

The scales used in the IR spectrum is typically wavenumber ($\bar{\nu} = \frac{1}{\lambda}$ in cm^{-1}), frequency (ν) or wavelength (λ).[52]

$$E = h\nu = hc/\lambda \qquad \text{Equation 34}$$

---

[49] D.A. Skoog, F.J. Holler, S.R. Crouch, *Principles of Instrumental Analysis,* Thomson Brooks Cole, 6th Edition, p 430-438, 455-469

[50] D.A. Skoog, D.M. West, F.J. Holler, S.R. Crouch, *Fundamentals of Analytical Chemistry,* Thomson Brooks Cole, 8th Edition, p 811-818

[51] J.W. Moore, W.G. Davies, R.W. Collings, *Chemistry,* McGraw-Hill, p 724-727

[52] N.L. Alpert, W.E. Keiser, H.A. Szymanski, *IR: Theory and Practice of Infrared Spectroscopy,* Plenum publ. Co., Plenum/Rosetta Edition, p 1-6, 78-79, 99, 184-186, 303-305

[53] G.L. Clark, *The Encyclopedia of Spectroscopy,* Rheinhold publ. Co., p 389-390, 450-453

Where E is the energy of a system, h is Planck's constant and c is the speed of light. The most commonly used is wavenumber since the number of digits used is more manageable than the true frequency values as well as the direct proportionality with both frequency and energy. This frequency is the molecular vibrational or rotational frequency responsible for absorption during the analysis.[49,52]

(i) *Applications of IR*

Qualitative:

The IR spectrum of any molecule is an extremely unique trait of that specific molecule. It is often referred to as a fingerprint of a molecule. It can be used to identify an unknown spectrum with a known spectrum by comparison with a library of compounds.[52] Organic compounds containing various functional groups can be characterized or identified. Various functional groups have characteristic absorption peaks in specific regions of the infrared spectrum. There are also variations in the exact peak positions, giving additional information of the group's relationship to the remainder of the molecule.[52] In the region of 600 cm^{-1} to 1200 cm^{-1} small variations in the species constitution and structure cause significant changes in peak positions. This area is known as a fingerprint region.[49]

Quantitative:

Though it does not possess the accuracy of other quantitative analytical methods like UV/VIS spectroscopy, IR spectroscopy can function just as well as the typically utilized quantitative technique that is typically applied.[53] Since the absorption or transmittance spectrum of a mixture of compounds is merely a superposition of each individual component molecule's spectrum, which displays the different concentrations present, the frequencies characteristic to individual components can be selected and analysed to relate the concentrations to the measurements.[52]

(ii) *The disadvantages of quantitative IR spectroscopy:*

There are large deviations from Beer's Law in IR spectra. This is due to the richness of the features on an IR spectrum. There is thus an increase in the likelihood of having overlapping absorption bands. The narrow path length cells used in analysis as well as the scattering within the sample increase the uncertainties during measurements. Therefore IR is not typically applied in quantification methods.[49,53]

An example of the use of IR spectroscopy in chemistry is the identification of reaction products and determining the reaction rate constants. As can be seen in Figure 2.8, Warsink *et al.* utilized this technique in the reaction between methyl iodide and Rh(cupf)(CO)(PR_3) complexes to determine the rate constants and identify the products that are formed. They could identify, through the observation of the various CO stretching frequencies, the disappearance of the Rh(I) starting material at 1978 cm^{-1}, the formation of an alkyl product at 2056 cm^{-1} and of an acyl product at 1722 cm^{-1}.[42,82]

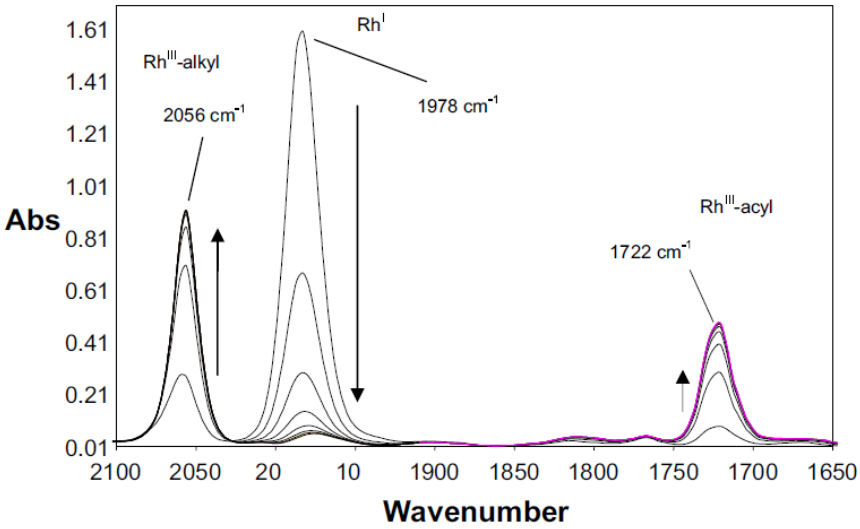

Figure 2.8: IR spectra of the consecutive scans at 25°C of the reaction between CH_3I and Rh(Me-Cupf)(CO)(PPh_3) in chloroform. The reactant concentrations were [Rh] = 0.02 M, [CH_3I] = 0.2 M.[42] Reprinted from J. Organomet. Chem., 726, S. Warsink, F.G. Fessha, W. Purcell, J.A. Venter, Synthesis and characterization of rhodium (I) 2-methylcupferrate complexes and their kinetic behaviour in iodomethane oxidative addition, p 14-20, Copyright (2012), with permission from Elsevier.

2.4.6.3 Nuclear Magnetic Resonance spectroscopy (NMR)

In 1924 Pauli proposed the theoretical basis for nuclear magnetic spectroscopy. His suggestion was that exposing certain atomic nuclei to magnetic fields would cause a splitting of the nucleus' energy levels due to them possessing properties of a magnetic moment and spin. Nucleii without a spin property such as those with even atomic and even mass numbers cannot be analysed with NMR techniques. The most commonly studied is carbon and hydrogen. Using different NMR techniques an unknown molecule's complete structure can often be elucidated, for example with

hydrogen atom studies, the amount of distinct nuclei and information about the surrounding chemical environment can be determined.[54,55,56,57,58]

(i) *Basic principles*

The nucleus is made of protons and neutrons with the protons providing a positive charge. It is assumed that the nuclei rotate on an axis creating a small magnetic field along the spin axis due to its charge. This magnetic field has its own moment, μ, which is proportional to the nucleus' angular momentum, ρ. γ is known as the gyromagnetic ratio and has a different value for each type of nucleus.[54,55,57,58]

$$\mu = \gamma\rho \qquad \text{Equation 35}$$

When a spinning nucleus is placed in an external magnetic field, the nucleus' magnetic moment orients itself in one of two possible directions in terms of the external field direction. This orientation depends on the nucleus' magnetic quantum state (m), which in turn is dependent on the spin states of the nucleus. The spin states of the nucleus are always a fractional amount dependent on the quantum spin nr (I) *e.g.* for ^{1}H nuclei with quantum spin number of I = ½, the spin states will be ½ and – ½.[54,55,57,58] The spinning charged nucleus will have 2I+1 non-degenerate energy levels in the external magnetic field.[57]

$$m = I, I-1, \ldots, -I \qquad \text{Equation 36}$$

The emission or absorption of electromagnetic radiation in the radio frequency region brings about energy state transitions in the energy levels of the nuclear spin states, with the absorption of a frequency equal in energy to the energy difference between the energy states. The difference between the states being dependent on the strength of the external magnetic field. In

---

[54] D.A. Skoog, F.J. Holler, S.R. Crouch, *Principles of Instrumental Analysis,* Thomson Brooks Cole, 6th Edition, p 499-542

[55] D.L. Pavia, G.M. Lampman, G.S. Kriz, *Introduction to spectroscopy,* Brooks and Cole, 3rd Edition, p 102-154

[56] J.H. Richardson, R.V. Peterson, *Systematic materials analysis,* Academic Press Inc, Vol 2, p 73-117

[57] R.K. Harris, *Nuclear Magnetic Resonance Spectroscopy,* Longman Scientific and Technical, p 1-14, 17, 18

[58] E.D. Becker, *High Resolution NMR: Theory and Chemical Applications,* Academic Press, 2nd Edition, p 9-20, 55-85

NMR, radio frequencies (RF) are utilized to excite the nuclei and the responding radio frequency intensity is measured.[54,55,57]

Nuclear absorption of electromagnetic radiation can be illustrated by its behaviour in an applied magnetic field. The spinning nucleus' axis of rotation rotates in an orbit around the direction of the externally applied magnetic field referred to as the Larmor precession as seen in Figure 2.9. Where θ is the angle between the spin axis and the magnetic field vector (direction of the applied magnetic field). If radio frequencies (RF) get absorbed, the angle will change. This angle change is described as the flip from one direction to the opposite direction as seen in Figure 2.10.[54,55,58]

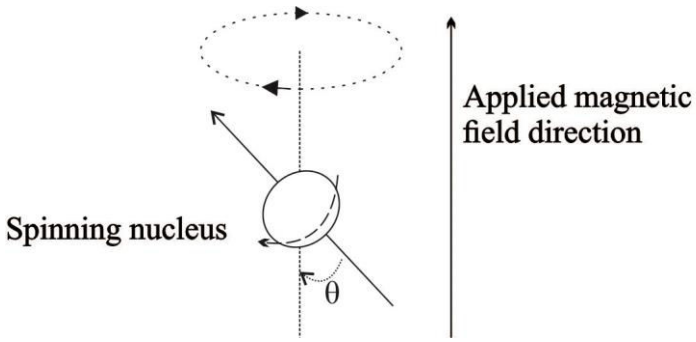

Figure 2.9: An illustration of the larmor frequency from the spinning nucleus rotating about an axis around the external magnetic field.

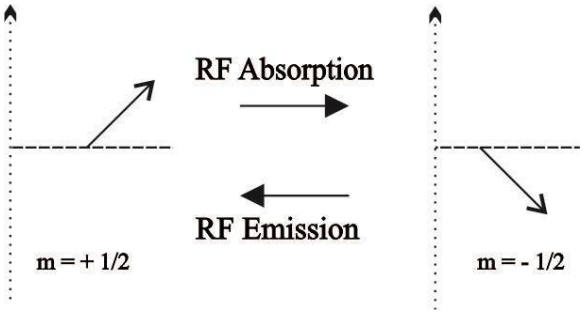

Figure 2.10: An illustration of the flip in direction that occurs during the absorption of RF radiation.

(ii) *Relaxation:*

Relaxation of the excited particles or nuclei to the ground state must be as fast as possible to prevent saturation. Saturation is where the amount of unexcited particles is too small and the excited particles cannot relax in time with respect to the excitation intervals.[54]

(iii) *Chemical Shift*

The RF that gets absorbed is affected strongly by the chemical environment. A factor affecting the frequency of radiation that gets absorbed is the atom or group bonded to the studied nucleus. This is an effect called the chemical shift and arises from smaller magnetic fields that are produced through the circulation of electrons. These small fields interact with the external field by increasing or decreasing the overall strength a nucleus experiences.[54,55,57,58] Chemical shifts are presented in parts per million (ppm), since the frequency increases proportionally with the external field increase.[58] Multiple nuclei of the same type may be equivalent to each other *i.e.* have identical environments and therefore they will then have the same chemical shift.[57]

(iv) *Peak Multiplicity*

The splitting of a single peak into multiple peaks is called spin-spin splitting or coupling. The splitting arises from the detection and influence of neighbouring nuclear spin states on each other. This is termed coupling. The coupling is characteristic to a molecule and independent of the external magnetic field. Coupling can occur between similar nuclei, homonuclear coupling, or between different nuclei, heteronuclear coupling. This interaction between the nuclei is mainly affected by the magnetic environments. Different magnetic environments for the nuclei cause a slight shielding and deshielding effect. The shielding and deshielding effect is caused by the addition or removal of electron density in the vicinity of the studied nucleus. The flow of the electrons along a structure causes a small local magnetic field, which influences the magnetic field experienced by the studied nucleus as a whole. The nuclei absorb slightly different radiation energies. The strength of the couplings is measured by the coupling constant (J), which is the distance between the peaks on a spectrum.[54,55,57,58]

In spin-spin splitting, the number of peaks that a single peak is split into is called the multiplicity calculated as:[54]

$$\text{multiplicity} = n+1 \qquad \text{Equation 37}$$

Where n is the number of equivalent nuclei.

Two dimensional NMR is a technique that allows the unravelling of very complex spectra. It identifies resonances that are connected by through-space interactions, through bond coupling or through chemical exchanges.[54]

(v) *Proton NMR(^{1}H):*

The most vital applications, in a chemical sense, of proton NMR studies have been for the elucidation and identification of structures.[54] There is direct proportionality between the amount of nuclei that emit a response to the peak area of the response. Therefore quantification is easy if there is no peak overlap.[54,55] A very useful application for NMR is determining the functional groups present *e.g.* hydroxyl group.[54]

(vi) *^{13}C NMR:*

The NMR active carbon isotope, ^{13}C, is significantly weaker than those for proton NMR. These weaker resonances are more difficult to analyse. It is weaker due to the very low natural abundance (1%) of the ^{13}C isotope.^{13}C has a spin quantum number (I) of ½, which gives a ^{13}C NMR spectrum sharp peaks. The magnetogyric ratio of ^{13}C is also much lower than for ^{1}H, therefore the resonances for ^{13}C are at lower frequencies and the chemical shifts over a much larger range (20 to 30 fold of ^{1}H). The shift is primarily affected by either being bonded directly to or through one bond, unlike protons which couple through multiple bonds. There is very rarely peak overlap.[54,55,58] These spectra provide information regarding the molecular backbone of an organic or organometallic complex.[54,58,57] There is generally no homonuclear spin-spin coupling observed since the natural abundance of ^{13}C is very low.[54,58,57] Proton decoupling can be done by irradiating a sample with a broad spectrum of RF signals, which encompasses the full proton spectral range, while the ^{13}C spectrum is recorded as per usual. The decoupling simplifies spectra by removing all C-H coupling, which splits the ^{13}C peaks into multiplets.[54,55,58]

(vii) *^{31}P NMR:*

^{31}P spectra also have sharp peaks since I = ½ and since there is a 100% abundance of the atom, small species concentrations are required. The values for chemical shift are extended over a very large range (400ppm) with substituent effects the major contributor to the shift values.[54] The sharp peaks do undergo homonuclear spin-spin coupling.[54]

One use of NMR, specifically ^{1}H NMR, in chemical characterization and investigations is to determine the effect that different metal atoms have on the resonances of protons in CpM(μ^4-C_5H_6) with M, = Co, Rh, Ir in solution. Szajek *et al.,* determined the effect of the metal type on the resonances of 23 protons in exo and endo positions with respect to the cyclopentadienyl ring.[59]

Another example of the use of NMR in kinetic studies was done by Stuurman *et al.*[82] Due to different chemical environments of the phosphorous in Rh(I)-P, Rh(III)(CO)-P and Rh(III)($COCH_3$)-P, they were able to clearly distinguish all the various products of the reaction between their Rh((C_6H_5)COCHCO((CH_2)nCH_3))(CO)(PPh_3) complexes (n = 1-3) and CH_3I as seen in Figure 2.11 for n = 2. The coupling constants of the alkyl and acyl isomers differ significantly between them and can thus be easily identified.[82]

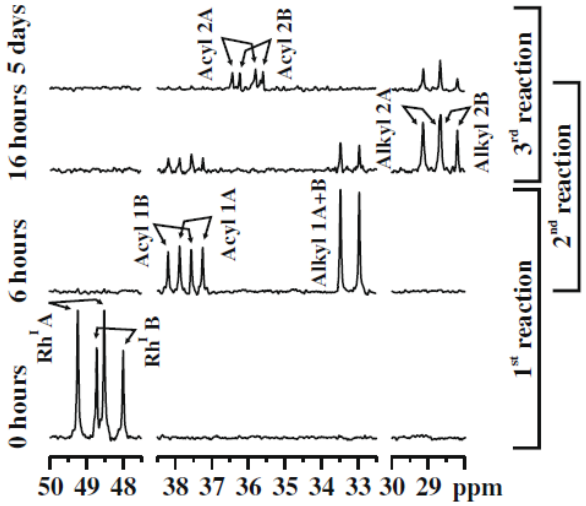

Figure 2.11: Products and reactants illustrated *via* ^{31}P NMR spectra of the three reaction steps at 25°C of the reaction between CH_3I and $[Rh((C_6H_5)COCHCO(CH_2CH_2CH_3)]$. Doublets appear due to the coupling between the Rh and P atoms. [82] Reprinted from J. Organomet. Chem., 694, N.F. Stuurman, J. Conradie, Iodomethane oxidative addition and CO migratory insertion in monocarbonylphosphine complexes of the type $[Rh((C_6H_5)COCHCO((CH_2)nCH_3))(CO)(PPh_3)]$: Steric and electronic effects, p 259-268, Copyright (2009), with permission from Elsevier.

2.5 L,L'-BID ligands

2.5.1 Introduction

L,L'-BID is used as a notation to indicate a bidentate ligand that contains two atoms, L and L', on the molecular structure that are able to coordinate to a metal atom. L,L'-BID ligands important for this study, are β-diketones, imino-β-diketones and diimino-β-diketones, as illustrated in Figure 2.12.

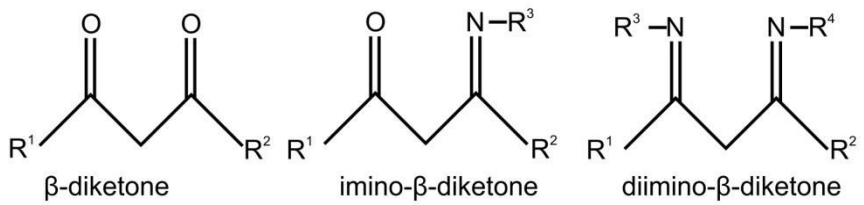

Figure 2.12: A graphic representation of the L,L'-BID ligands of this study. R^1-R^4 are groups such as CH_3, CF_3, Ph or C_5H_3S.

2.5.2 Synthesis

One method of synthesizing the β-diketone class of bidentate ligands is *via* Claissen-condensation. It can be done with a basic initiator as was done by Du Plessis *et al.*[59] They utilized sodium amide as the inititator in the Hauser method of synthesis to manufacture various ferrocene containing diketones.[59,60] A method of synthesis through use of an alkoxide is slower but gives better yields.[61,62]

A method for the synthesis of the imino-β-diketone bidentate ligands is *via* condensation reactions, which substitute the oxygen atoms of Hacac (acetylacetone). Fischer and Bulow were possibly the first researchers to react a β-diketone with an amino compound in the year 1885. They showed that a benzoylacetonediketone reacted with ammonium hydroxide to give the imino-β-diketone product upon heating.[63,64]

The synthesis of the diimino-β-diketone, where both the oxygens of a diketone are substituted by N atoms, was achieved by the acid catalysed route for the condensation of an aniline derivative with a diketone to form a β-ketoamine ligand as done by various researchers.[65,66,67] The ketoamine ligand was then further reacted with another, different aniline derivative to form the β-diketimine, also known as diimino-β-diketones, ligand.[65,66,67] A ligand-salt method is also possible by using a fluoroborate salt with a ketoamine, which can then be reacted with a methoxide salt to yield the free base or ligand. This pathway was followed by McGeachin for the synthesis of β-diketimines with a general structure as seen in Figure 2.12.[68] The acid is not necessarily required for the substitution reaction as was shown by Lacey.[69] Lacey synthesized a β-ketoamine from the substitution of the oxygen atoms of acac with an amine by the slow

---

[59] W.C. Du Plessis, T.G. Vosloo, J.C. Swarts, *J. Chem. Soc. Dalton Trans.*, 1998, 2507-2514

[60] C.R. Hauser, C.E. Cain, *J. Org. Chem.*, 1958, **23**, 1142-1146

[61] V. Weinmayr, *Naturwissenschaften*, 1958, **45**, 311

[62] P.K. Dhondi, P. Carberr, J.D. Chisholm, *Tetrahedron Letters*, 2007, **48**, 8743-8746

[63] E. Fischer, C. Bulow, *Berichte*, 1885, **18**, 2131

[64] L.M. Tang, Y.Q. Duan, X.F. Li, Y.S. Li, *J. Organomet. Chem.,* 2006, **691**, 2023-2030

[65] A.F. Dove, V.C. Gibson, E.L. Marshall, A.J.P. White, D.J. Williams, *J. Chem. Soc. Dalton Trans.*, 2004, 570-578

[66] J.E. Parks, R.H. Holm, *Inorg. Chem.*, 1968, **7**, 1408-1416

[67] P.H.M. Budzelaar, N.N.P. Moonen, R. De Gelder, J.M.M. Smits, A.W. Gal, *Eur. J. Inorg. Chem.*, 2000, 753-769

[68] S.G. McGeachin, *Can. J. Chem.*, 1968, **46**, 1904-1912

addition of concentrated ammonia. One method was where the solution was left overnight and another is where the solution was heated whereby the product was obtained at a quicker pace.[69]

2.5.3 Structural isomers

β-diketones, in solution, can exist in three possible tautomeric forms namely a keto form and two enol forms. The main form observed is the enol form when stabilized by the delocalization of the π-electrons. The interconversion between the keto and enol forms is generally fast, quantifiable, and the ratio between the tautomers is dependent on the type of solvent used for dissolution.[70,71,72,73] Tautomerism in bidentate ligands like acetylacetone (Hacac) and its derivatives, involves the intramolecular hydrogen transfer, with a change in the distribution of electrons in the molecule.[70] The two enol forms are in a dynamic and rapid equilibrium as seen in Scheme 2.6.[70]

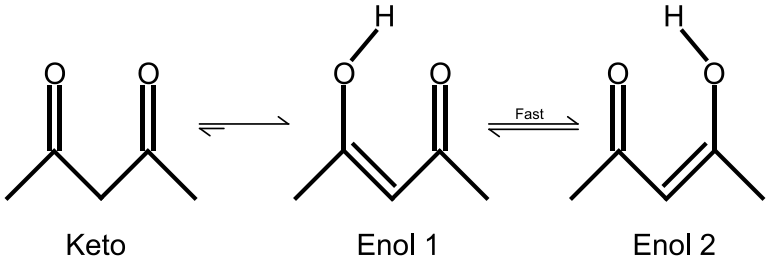

Scheme 2.6: Keto-Enol tautomerization of L,L'-BID ligands.

It was found by various researchers[59,66,70,74,77] that the enolisation occurs away from electron-donating side groups *e.g.* the enolisation was found to be away from the ferrocenyl side group[59] in the complexes synthesized by Bell *et al.*[75] There was conjugation found between the β-diketone skeleton and ferrocene, with the conjugation being far more pronounced between the ferrocene and the β-diketone core.[72,74]

---

[69] M.J. Lacey, *Aust. J. Chem.*, 1970, **23**, 841-842

[70] A. Kuhn, K.G. Von Eschwege, J. Conradie, *Electrochim. Acta*, 2011, **56**, 6211-6218

[71] T.E. Neal, R.W. Murray, *Anal. Chem.*, 1970, **42**, 1654-1656

[72] E. Iglesias, *Langmuir*, 2000, **16**, 8436-8446

[73] E. Iglesias, *J. Phys. Chem.*, 1996, **100**, 12592-12599

[74] M.M. Conradie, A.J. Muller, J. Conradie, *S. Afr. J. Chem.,* 2008, **61**, 13-21

[75] W. Bell, J.A. Crayston, C. Glidewell, M.A. Mazid, M.B. Hursthouse, *J. Organomet. Chem.*, 1992, **434**, 115

In the complexes of Du Plessis *et al.* the tautomerism was strongly affected by the concentration of the compound where high concentrations drove the equilibrium to favour the enol formation.[59] They found a preference for enol formation over ketone formation, which could be driven by two possible forces, an electronic and a resonance driving force as illustrated in Figure 2.13.

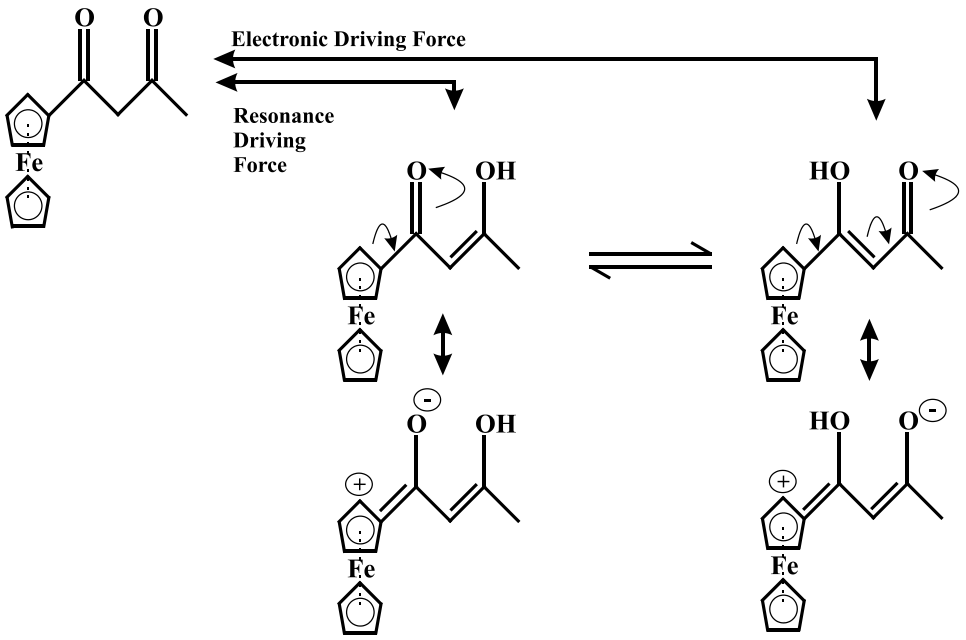

Figure 2.13: Illustration of the electronic and resonance driving forces in Ferrocenylacetylacetone.

The first type of driving force is an electronic force where the formation is determined by the electronegativity of the side groups in the β-diketone. The greater electronegativity of one of the groups leads to a larger partial positive character of the adjacent carbon atom (carbonyl group). This greater positive character results in a partial electron deficit, which the compound attempts to correct for through the formation of the carbonyl group, forcing the 2nd carbonyl group to be converted to an enol group through the bonding of the hydrogen atom.[59,73] A resonance force is the second type of force driving the enolisation of β-diketones containing an aromatic side group. It implies that the formation of different forms of an isomer may lower the isomer's energy allowing for the dominant formation of the isomer.[59] Du Plessis *et al.* found that the resonance stabilisation was a good explanation when there are aromatic side groups bonded to the ligand.[59]

2.5.4 Cyclic voltammetry of L,L'-BID ligands

The β-diketones exhibit a one electron reduction process with the reduced ligand being an unstable anionic radical that generally decomposed on the timescale of the CV. [70, 76]

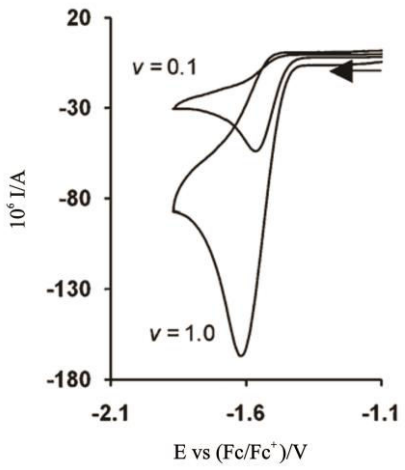

Figure 2.14: CV of $CF_3COCHC(OH)Ph$ at scan rates of 0.1 and 1.0 $V.s^{-1}$ with scans initiated in the direction indicated by the arrow. The measurements were done in a 0.1 M $[NBu_4][PF_6]$ in acetonitrile solution with a glassy carbon working electrode at room temperature 25°C. The analyte concentration was 0.003 mol dm^{-3}.[70] Reprinted from J. Electrochim. Acta, 56, A. Kuhn, K.G. Von Eschwege, J. Conradie, Electrochemical and density functional theory modeled reduction of enolized 1,3-diketones, p 6211-6218, Copyright (2011), with permission from Elsevier.

Kuhn *et al.* utilized cyclic voltammetry to determine the electrochemical reduction of enolized 1,3-substituted β-diketones, see for example Figure 2.14.[70] They found that the radical nature for ligands containing two aromatic side groups was stabilized enough to allow for a semi reversible reduction at high scan rates. The aliphatic containing β-diketone radicals did not exhibit a similar stability.[70]

An increase in the electron withdrawing ability of a side group increases the reduction potential. The electron density removed from the β-diketone's backbone makes it slightly more positive, therefore easier to reduce. This suggests that there is excellent electronic communication between the side groups and the diketone-centre *via* conjugation.[70] Chelated β-diketonato ligands displayed similar electrochemical activity but only at a more negative potential. This is

---

[76] R.C. Buchta, D.H. Evans, *J. Org. Chem.*, 1970, **35**, 2844

due to greater electron density on the β-diketone that arises from the delocalized aromatic system between the metal centre and the diketone. [70]

2.6 [Rh(L,L'-BID)(CO)$_2$] complexes

2.6.1 Introduction

[Rh(L,L'-BID)(CO)$_2$] is a notation used in this study that represents a Rh metal atom coordinated to a L,L'-BID ligand of the type shown in Figure 2.12, and to carbonyl (CO) ligands. The general structure is seen in Figure 2.15.

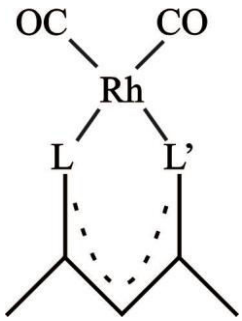

Figure 2.15: Schematic representation of the general structure of [Rh(L,L'-BID)(CO)$_2$] complexes.

2.6.2 Synthesis

The synthesis of [Rh(L,L'-BID)(CO)$_2$] dicarbonyl complexes is relatively easy and illustrated in Scheme 2.7. It can be done by reacting the bidentate ligands directly with the μ-dichloro-tetracarbonyl-dirhodium(I) [Rh(CO)$_2$Cl]$_2$ intermediate along with a $BaCO_3$ buffer, to neutralize the evolved acidic side-product.[77,78] The μ-dichloro-tetracarbonyl-dirhodium(I) intermediate can be synthesized directly by reacting rhodium trichloride hydrate ($RhCl_3.3H_2O$) with carbon monoxide.[78] The dicarbonyl complexes can also be synthesized *in situ* by refluxing $RhCl_3.3H_2O$ in DMF solution for 30 min and then adding in the ligand after the solution has cooled, as was done by Bonati *et al.* and Pretorius *et al.*.[78,79]

---

[77] J. Han, L.F. Zhang, W. Wan, *J. Organomet. Chem.*, 2003, **672**, 86-93

[78] F. Bonati, G. Wilkinson, *J. Chem. Soc.*, 1963, 3156-3160

[79] C. Pretorius, A. Roodt, *Acta. Cryst.*, 2012, **E68**, m1451-m1452

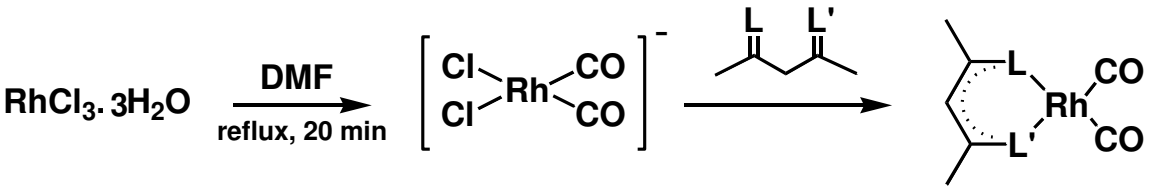

Scheme 2.7: Schematic representation of the synthesis of [Rh(L,L'-BID)$(CO)_2$].

2.6.3 Solid state structures

The [Rh(L,L'-BID)$(CO)_2$] dicarbonyl complex has a square planar geometry, which could be distorted[79] or near perfect.[80] The square planar geometry is formed by L and L' atoms on the ligand and the 2 C atoms of the carbonyl groups with the Rh centre being slightly displaced above or below the plane formed, see Figure 2.16 as an example.[79]

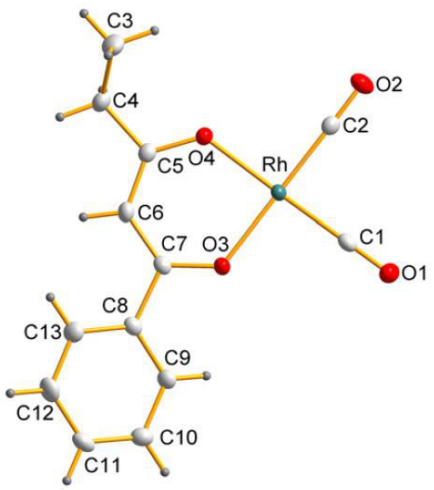

Figure 2.16: Crystal structure [Rh(PhCOCHCOCH_2CH_3)$(CO)_2$] showing 50% displacement ellipsoids and the atom labellings.[81] Reprinted from Polyhedron, 30, N.F. Stuurman, R. Meijboom, J. Conradie, Characterization of [Rh(PhCOCHCO$CH_2CH_2CH_3$)$(CO)_2$] by Xray crystallography, a computational and a statistical study, p 660-665, Copyright (2011), with permission from Elsevier.

[80] K.H. Hopmann, N.F. Stuurman, A. Muller, J. Conradie, *Organometallics*, 2010, **29**, 2446-2458

[81] N.F. Stuurman, R. Meijboom, J. Conradie, *Polyhedron,* 2011, **30**, 660-665

2.7 [Rh(L,L'-BID)(CO)(PPh_3)] complexes

2.7.1 Introduction

[Rh(L,L'-BID)(CO)(PPh_3)] is a notation used in this study to indicate that a Rh metal atom is bonded to a L,L'-BID ligand of interest, a CO group and a PPh_3 group. The structure of the molecule shows a tendency towards a square planar geometry with the plane formed between the two chelating atoms of the ligand and the C and P atoms of the two other groups as seen in Figure 2.17.

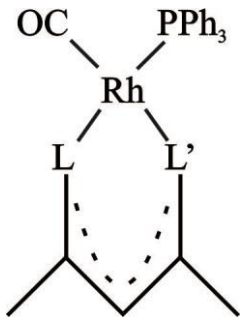

Figure 2.17: Schematic representation of the general structure of [Rh(L,L'-BID)(CO)(PPh_3)] complexes.

2.7.2 Synthesis

The synthesis of the phosphine complexes is quite straightforward as seen in the general reaction scheme in Scheme 2.8. Dissolving the dicarbonyl complex in hot n-hexane and adding in PPh_3 allows for the evolution of CO gas bubbles. The mixture is continuously stirred until there is no more bubbles evolving and the product filtered out.[80,82,83,84,85] To purify the complex, silica gel column chromatography may be utilized.[80] The formation of CO gas arises from the nucleophilic attack of the PPh_3 on the complex, which substitutes a CO group.[80,83,84]

---

[82] N.F. Stuurman, J. Conradie, *J. Organomet. Chem.*, 2009, **694**, 259-268

[83] M.M. Conradie, J. Conradie, *Inorg. Chim. Acta*, 2008, **361**, 208-218

[84] J. Conradie, G.J. Lamprecht, S. Otto, J.C. Swarts, *Inorg. Chim. Acta*, 2002, **328**, 191-203

[85] G.J. Lamprecht, J.C. Swarts, J. Conradie, J.G. Leipoldt, *Acta Cryst.*, 1993, **C49**, 82-84

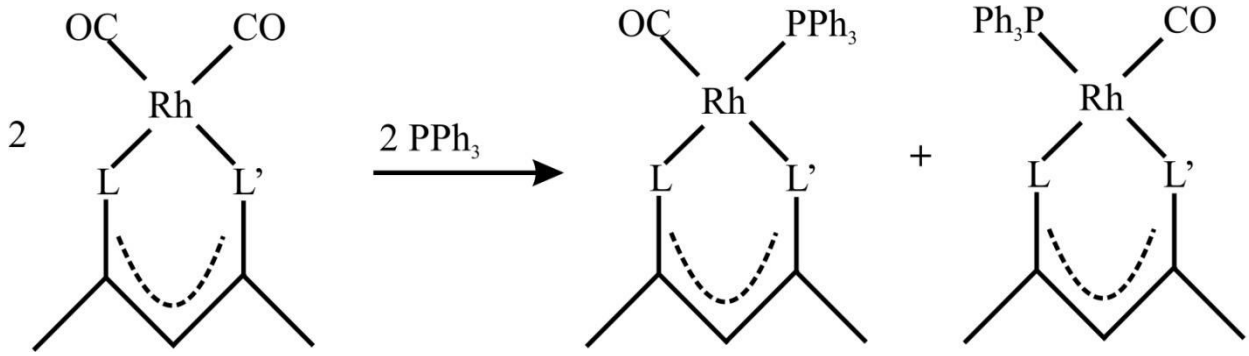

Scheme 2.8: Schematic representation of the synthesis of [Rh(L,L'-BID)(CO)(PPh_3)].

2.7.3 Structural isomers

When [Rh(L,L'-BID)(CO)(PPh_3)] complexes are synthesized using asymmetric L,L'-BID-ligands, two isomers of the products are possible as seen in Figure 2.18.[80,83,86] Several researchers were able to characterize both isomers by NMR and selected solid state X-ray structures.[83] The isomers exist in equilibrium with each other in solution, which was determined by the ratio of the integration of the non-overlapping peaks. This isomer ratio is more dependent on solvent and temperature, rather than concentration.[83,86]

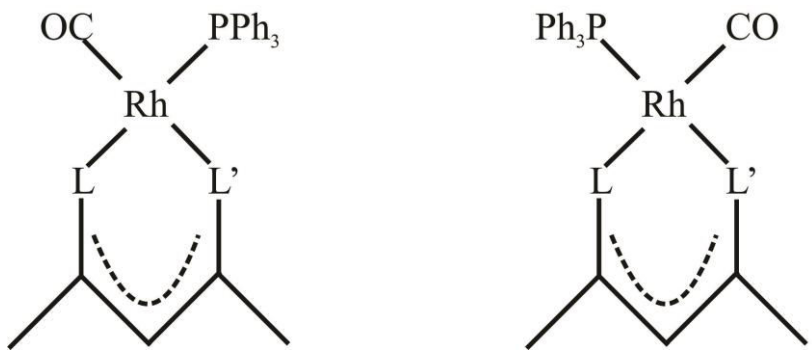

Figure 2.18: Two possible structural isomers that are possible of [Rh(L,L'-BID)(CO)(PPh_3)] complexes.

[86] M.M. Conradie, J. Conradie, *Inorg. Chim. Acta*, 2009, **362**, 519-530

2.7.4 Solid state structures

A list of selected known crystal structures of the type [Rh(L,L'-BID)(CO)(PPh_3)] is given in Table 2.1.[83, 87, 88]

Table 2.1: List of known [Rh(L,L'-BID)(CO)(PPh_3)] crystal structures as found on the crystallographic database.

CSD Reference	L,L'	R^1*	R^2*
ZAWQAP	O,O	Ph	CH_3
OJEWOQ	O,O	CH_2CH_3	Ph
SUPROK	HN,O	CH_3	CH_3
ACRHCP	O,O	CH_3	CH_3
TFAPRH	O,O	CF_3	C_4H_3S
FODJEN	O,O	CH_2CH_3	CF_3
CASPER	O,O	$CH(CH_3)_2$	CF_3
DUWHIM	O,O	$C(CH_3)_3$	CF_3
KUNBIE	O,O	Fc	CF_3

*R^1 and R^2 are the side groups attached to the L,L'-BID ligand.

Typically only one of the possible isomers is observed in solid state analysis.[80,85,88] The selection of the type of isomer that crystallizes in the solution is dependent on the size of the side group substituents on the β-diketone[85], the solvent polarity and temperature.[80,83] All these factors contribute to the crystallization energy of the complex, which determines the isomer that will be present in the crystal lattice. This is due to the very fine balance of the entropy and enthalpy, which causes a minimum in the energy for crystallization.[88]

However, finding a single isomer in the solid state is not always the case. Both Purcell *et al.* and Conradie *et al.* found both isomers in the solid state.[80,83,88]

In the crystallization of [Rh(β-diketonato)(CO)(PPh_3)] complexes there are electronic influences (*trans* influences) that were often used to explain the preferential appearance of a specific isomer. The *trans* influence is defined as a ground state thermodynamic property where a ligand

[87] D. Lamprecht, G.J. Lamprecht, J.M. Botha, K. Umakoshi, Y. Sasaki, *Acta Cryst.*, 1997, **C53**, 1403-1405

[88] W. Purcell, S.S. Basson, J.C. Leipoldt, A. Roodt, H. Preston, *Inorg. Chim. Acta.*, 1995, **234**, 153-156

can weaken the ligand-metal bond that is *trans* to it, thereby increasing the length.[88] In a [Rh(β-diketonato)$(CO)_2$] complex, the CO *trans* to the oxygen atom nearest to the more electron donating β-diketonato side group has the largest *trans* influence, and will thus be substituted by PPh_3.

2.7.5 Cyclic voltammetry of [Rh(L,L'-BID)(CO)(PPh_3)] complexes

The electronic oxidation of various rhodium complexes gives clues as to what the electronic influence of various substituents, on the backbone of the chelating monoanionic β-diketone ligands attached to the metal centre, are on oxidative addition reactions.[89]

A proposed mechanism for the electrochemical oxidation of [Rh(L,L'-BID)(CO)(PPh_3)] complexes, with L,L'-BID = β-diketone, is given in Figure 2.19.

[89] E.A. Shor, M.A. Shor, V.A. Nasluzov, A.I. Rubaylo, *J. Struct. Chem.,* 2005, **46**, 220-229

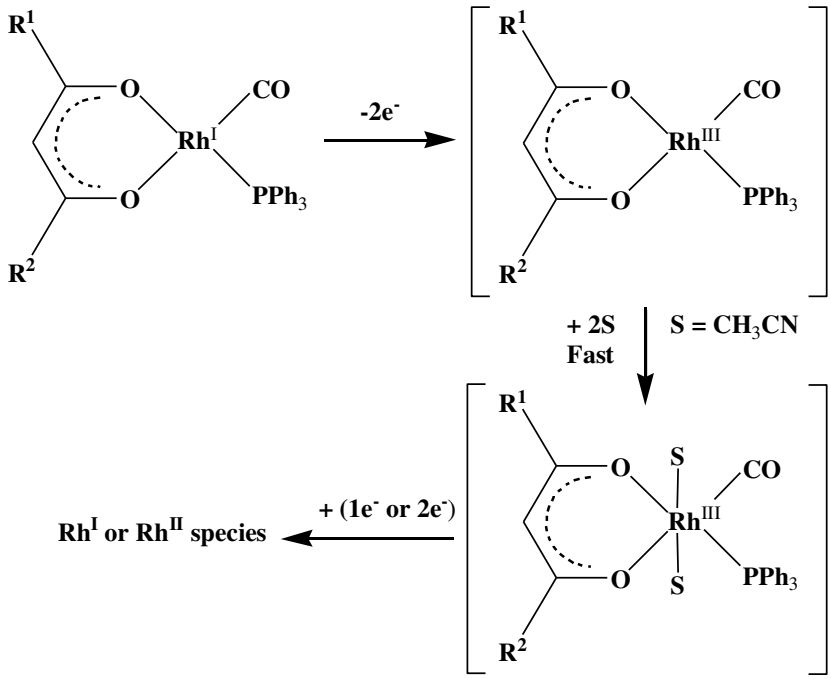

Figure 2.19: A mechanism proposed for the electrochemical oxidation of the Rh(I) species to Rh(III) with S = solvent molecule. The two isomers of the unsymmetric species exist and are in a fast equilibrium with each other, however only one is shown.[90] Reprinted from Electrochim. Acta, 726, H. Ferreira, M.M. Conradie, J. Conradie, Electrochemical study of carbonyl phosphine β-diketonato rhodium(I) complexes, p 519-526, Copyright (2013), with permission from Elsevier.

In Figure 2.20 the CV of [Rh(PhCOCHCOPh)(CO)(PPh_3)] complex is shown and it can be seen that there is only one oxidation peak at all applied scan rates, which is assigned to the oxidation of the Rh(I) species to the Rh(III) species. A single reduction peak can be seen at relatively high scan rates and is assigned to the reduction of the Rh(III) species to an as yet unidentified Rh(II) or Rh(I) species (see Figure 2.19), with the current of the peak cathodic peak significantly smaller than that of the peak anodic potential. The ΔE_p of the two peaks exceed the 0.059 V limit for electrochemically reversible processes and the large difference between the peak currents shows that the oxidation of the rhodium complex is also chemically irreversible.[91,92]

---

[90] H. Ferreira, M.M. Conradie, J. Conradie, *Electrochim. Acta*, 2013, **113**, 519-526

[91] J.J.C. Erasmus, J. Conradie, *Dalton Trans.*, 2013, **42**, 8655-8666.

[92] D. Lamprecht, G.J. Lamprecht, *Inorg. Chim. Acta*, 2000, **309**, 72-76.

The lack of, or presence of a very small, reduction peak at slow scan rates is an indication of the mobility and instability of the electrochemically generated Rh(III) complexes. The mobility presents itself as the Rh(III) complex molecules that diffuse away from the electrode surface into the bulk solution, therefore decreasing the amount of oxidized molecules available to be reduced back to the Rh(I) or Rh(II) species (see Figure 2.19). As the scan rate increases, the speed of diffusion is slowly overcome and thus the peak cathodic current increases as well. The instability presents itself in that the Rh(III) is a d^2sp^3 hybrid molecule that can only exist as an octahedral complex. Therefore the square planar conformation of the complex becomes unstable and there is stabilization of the complex through the coordination with two solvent molecules into the octahedral form.[92]

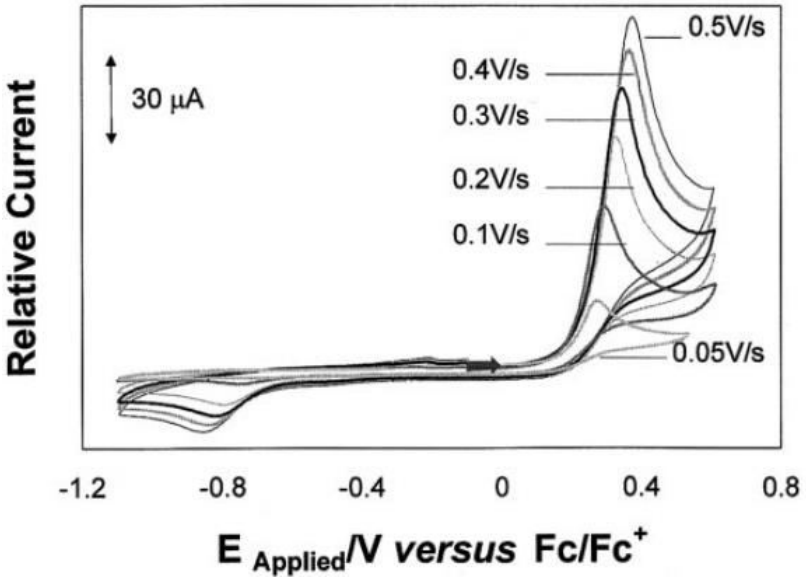

Figure 2.20: Cyclic Voltammograms of the [Rh(dibenzoylmethanato)(CO)(PPh_3)] complex utilizing a glassy carbon working electrode in a 0.1 mol dm^{-3} TBAHFP/CH_3CN solvent and supporting electrolyte system. The sweep rates were varied between 0.05 $V.s^{-1}$ and 0.5 $V.s^{-1}$. [92] Reprinted from Inorg. Chim. Acta, 309, D. Lamprecht, G.J. Lamprecht, Electrochemical oxidation of Rh(I) to Rh(III) in rhodium(I) β-diketonato carbonyl phosphine complexes, p 72-76, Copyright (2000), with permission from Elsevier.

To illustrate the relationship between the anodic and cathodic peaks, [Rh(PhCOCHCOPh)(CO)(PPh_3)] is used as an example (see Figure 2.21). The coupling of the two peaks observed was characterized by initiating the scans in different directions in terms of the positive or negative axis. Scans initiated in the positive direction, Figure 2.21 (b), show the typical one oxidation and one reduction peaks with no ability to distinguish what the relationship between the peaks is. Scans initiated in the negative direction, Figure 2.21 (a), show no peak presence at first then an oxidation peak after the scan direction is reversed. This is explained in

that with the initial, negative oriented scan there is no Rh(III) present to be reduced to a Rh(I) or Rh(II) complex, however there is Rh(I) present that can be oxidized when the scan direction is changed to the positive direction.[92]

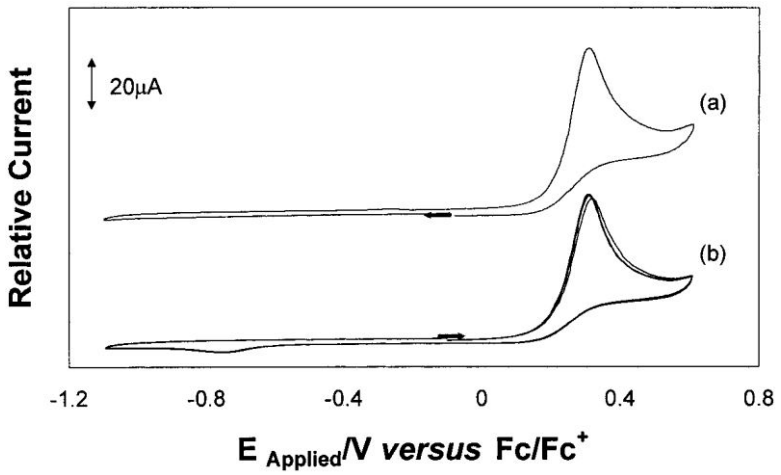

Figure 2.21: Cyclic voltammograms of a [Rh(PhCOCHCOPh)(CO)(PPh_3)], initiated in a (a) negative direction and (b) a positive direction as indicated by the arrows at a scan rate of 0.1 $V.s^{-1}$. The cell comprised of a glassy carbon working electrode with a solution concentration of 0.1 mM of the complex and 0.1 $mol.dm^{-3}$ TBAHFP/CH_3CN. Reprinted from Inorg. Chim. Acta, 309, D. Lamprecht, G.J. Lamprecht, Electrochemical oxidation of Rh(I) to Rh(III) in rhodium(I) β-diketonato carbonyl phosphine complexes, p 72-76, Copyright (2000), with permission from Elsevier.[92]

When one of the substituents on the backbone of the β-diketone is also electrochemically active in the potential energy window of the solvent, there are additional peaks observed on the cyclic voltammogram. For example, the CV's of the ferrocene-containing [Rh(FcCOCHCOR)(CO)(PPh_3)] complexes (R = CF_3, CH_3 or Ph) exhibit two oxidation peaks. The first irreversible oxidation peak observed is assigned to the rhodium metal. Following directly after the first peak is a second reversible oxidation peak that is assigned to the ferrocene attached to the ligand.[93,94] In the case of two ferrocene substituents on the ligand, *e.g.* [Rh(FcCOCHCOFc)(CO)(PPh_3)], there will be a third peak observed for the second ferrocene at

---

[93] J. Conradie, J.C. Swarts, *Dalton Trans.*, 2011, **40**, 5844-5851.

[94] J. Conradie, T.S. Cameron, M.A.S. Aquino, G.J. Lamprecht, J.C. Swarts, *Inorg. Chim. Acta*, 2005, **358**, 2530-2542.

a slightly higher potential (see Figure 2.22). The two seperate redox peaks observed for the two ferrocenyl groups, is due to good communication between the unoxidised ferrocene group and the oxidised ferrocenium group. This communication allows for the delocalization of electron density from the unoxidised ferrocene across the ligand backbone to help stabilize the radical formed. The delocalization makes the oxidation of the remaining ferrocene group more difficult, shifting the peak to a slightly higer potential.[95]

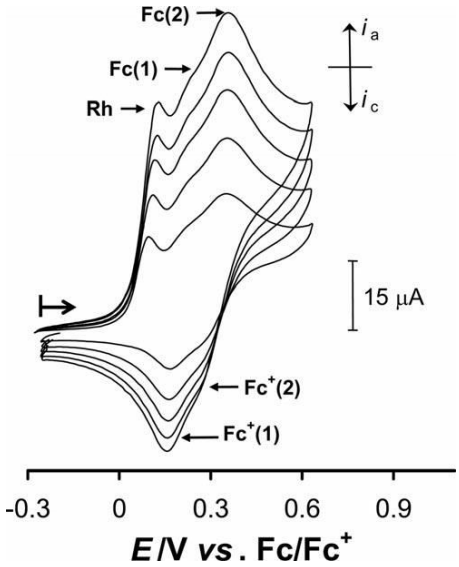

Figure 2.22: Cyclic voltammograms of a [Rh(FcCOCHCOFc)(CO)(PPh_3)] complex at scan rates of 0.05 $V.s^{-1}$ (smallest currents) to 0.25 $V.s^{-1}$ in 0.1 $mol.dm^{-3}$ [N(*n*Bu_4)][PF_6]/CH_3CN] with the complex concentration as 1 mM on a working electrode of glassy carbon with scans initiated in the direction of the arrow.[95] Copyright (2011) Wiley. Used with permission from J. Conradie, J.C. Swarts, The Relationship between the Electrochemical and Chemical Oxidation of Ferrocene-Containing Carbonyl-Phosphine-β-Diketonato-Rhodium(I) Complexes – Cytotoxicity of [Rh(FcCOCHCOPh)(CO)(PPh_3)], Eur. J. Inorg. Chem.).

2.7.6 Kinetic reactions of [Rh(L,L'-BID)(CO)(PPh_3)] complexes

The oxidative addition of CH_3I to Rh(I) complexes generally shows a series of products when studied *in situ* by UV/VIS-, IR- and NMR spectroscopy.

In the study utilizing UV, IR and NMR spectroscopy by Conradie *et al.*[83] of the oxidative addition of CH_3I to Rh(FcCOCHCOCF_3)(CO)(PPh_3), they could show by comparing their results

[95] J. Conradie, J.C. Swarts, *Eur. J. Inorg. Chem.*, 2011, 2439-2449.

to all previouly published results on related [Rh(β-diketonato)(CO)(PPh_3)] + CH_3I reactions, that all the [Rh(β-diketonato)(CO)(PPh_3)] and CH_3I reactions occur according to the general scheme, comprising of four reaction steps, as given in Scheme 2.9.[82,83,96,97]

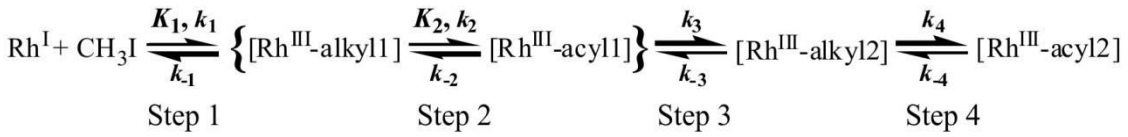

Scheme 2.9: General reaction scheme for the oxidative addition reaction between a [Rh(β-diketonato)(CO)(PPh_3)] complex and CH_3I. The end scripts 1 and 2 in Rh^{III}-alkyl1, Rh^{III}-acyl1, Rh^{III}-alkyl2 and Rh^{III}-acyl2 denote the first- or second-formed alkyl or acyl species during the course of the reaction.

The first step, the formation of the [Rh(β-diketonato)(CO)(PPh_3)(CH_3)(I)] complex, was found to follow an associative mechanism to form the transition state since the $\Delta S^{\#}$ values for the second order reaction step were largely negative. This is where the coordination number of the complex changes from 4 to 6. In the consecutive steps the coordination number varies between 5 and 6, depending on the type of product formed.[82,83,96,97] UV/VIS spectroscopy was used to determine the kinetic rates of the different reaction steps. IR spectroscopy was used to gain a more in depth view of the reaction to determine the product formations.[82,83,96,97] Four steps, combined into three raction steps as shown in Scheme 2.9, were identified from the IR spectra. The different Rh^{III}-alkyl1, Rh^{III}-acyl1, Rh^{III}-alkyl2 and Rh^{III}-acyl2 reaction products could be identified during the course of the reaction. However, only one isomer of each species was observed on IR.[82,83,96, 97]

In order to determine whether there is more than one isomer of each species observed during the reaction on IR, Conradie *et al.*[83] did a ^{1}H NMR study on the reaction. They found that there were different geometrical isomers for each of the products, an A and B isomer of which the assignment is arbitrary. The first isomer, *e.g.* isomer A, is where the ferrocene group in their complexes is attached to a carbon on the β-diketone backbone closest to the oxygen that is *cis* with respect to the CO ligand and the second isomer is *trans* with respect to the CO ligand.

[96] J. Conradie, G.J. Lamprecht, A. Roodt, J.C. Swarts, *Polyhedron*, 2007, **26**, 5075-5087

[97] M.M. Conradie, J. Conradie, *Dalton Trans.*, 2011, **40**, 8226-8237

These isomers were in a fast equilibrium with one another. The equilibrium was also found to exist after the Rh^{III}-alkyl2B isomer, which was crystallized, was dissolved in $CDCl_3$. Isomerization to Rh^{III}-alkyl2A took place until an equilibrium was reached. After some time, the Rh^{III}-alkyl1 and Rh^{III}-acyl1 isomers were observed in trace amounts. [82,83,96,97]

Comparison with DFT calculations:

The [Rh(β-diketonato)(CO)(PPh_3)] + CH_3I reactions were also investigated utilizing DFT calculations. The DFT calculated results shed light on the transition states and reaction mechanism, and were in agreement with the experimental observation.[97]

Some studies focuced on the geometry and relative energy of the reaction products. When the formed products are compared to all the DFT calculated geometries that are possible, it is found that there are certain theorized geometries that correspond with the observations of the NMR study and that those that show good correlation, are lowest in relative energy. These geometries are the thermodynamically favoured geometrical products. These deductions turned true when, during calculations, solvent effects were taken into account. Since there was found to be a relatively small energy difference between the calculated alkyl and acyl energies, the equilibrium between the two products is possible. The calculated stereochemistry of the products that correlate with the NMR results also correlated with the crystal structures.[86] The most stable acyl product geometry was where the $COCH_3$, the acyl group, was above or below the square planar plane (see Scheme 2.10, Rh^{III}-acyl2).

However, information regarding the transition states formed during the reaction sequence is not obtainable through the NMR studies. Therefore Conradie *et al.* utilized DFT calculations on the model reaction [Rh(acac)(CO)(PPh_3)] + CH_3I to answer these questions.[97]

For the first oxidative addition step, of the three types of transition state structures possible, as seen in Figure 2.23, it was found that a linear arrangement of RH-CH_3-I, during oxidative addition, was energetically favourable due to the lower energy of this transition state geometry than the two other possible geometries of oxidative addition as a result of *cis* addition.[97]

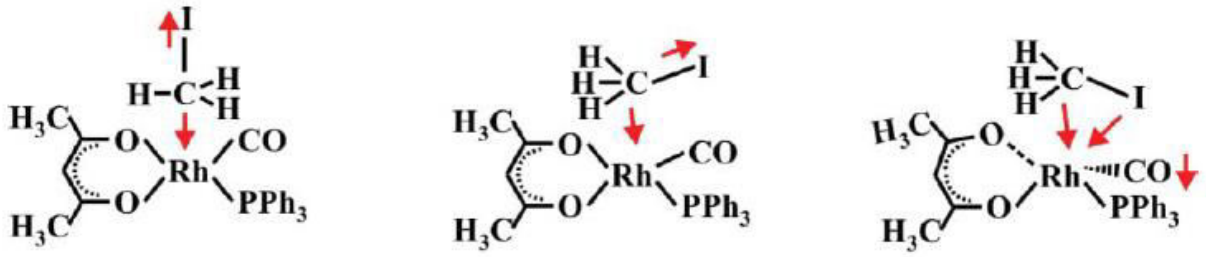

Figure 2.23: 3 possible ways of oxidative addition of the CH_3I to the Rh(I) centre. Left is a linear method of attack, centre is a bent method of attack leading to the breaking away of I to the bulk solution and right is a frontal attack leading to both the CH_3 and I bonding directly to the Rh(I) center.[97] Reproduced from M.M. Conradie, J. Conradie, *Dalton Trans.,* 40 (2011) p 8226-8237 with permission of The Royal Society of Chemistry.

Thus the DFT results corroborate a *trans* addition mechanism. The free I drifts away and reacts with any 5-coordinated intermediate through a barrierless energy reaction to form the Rh^{III}-alkyl1 product as seen in Scheme 2.10 (a).[86,97]

Scheme 2.10 (b) shows that during the second reaction step, the intramolecular CH_3 migration to the CO causes an increase of the Rh-CH_3 bond length and the CO group shifts out of the plane formed by the beta-diketonato ligand to bond with the CH_3. After the migration, the C_{co}-O angle increases and the Rh^{III}-acyl1 product is then formed. The PPh_3 and $COCH_3$ are in the plane and I is apical, as suggested by the NMR.[97]

In the third reaction step, the slow conversion of the Rh^{III}-acyl1 to Rh^{III}-alkyl2, there are 4 steps as seen in Scheme 2.10 (c). The PPh_3 moves to the apical position while the oxygen moves as well to relieve the steric stress from the changing angles. The $COCH_3$ rotates to lie flat in the plane and then the CH_3 group breaks away and bonds with the metal centre.[97]

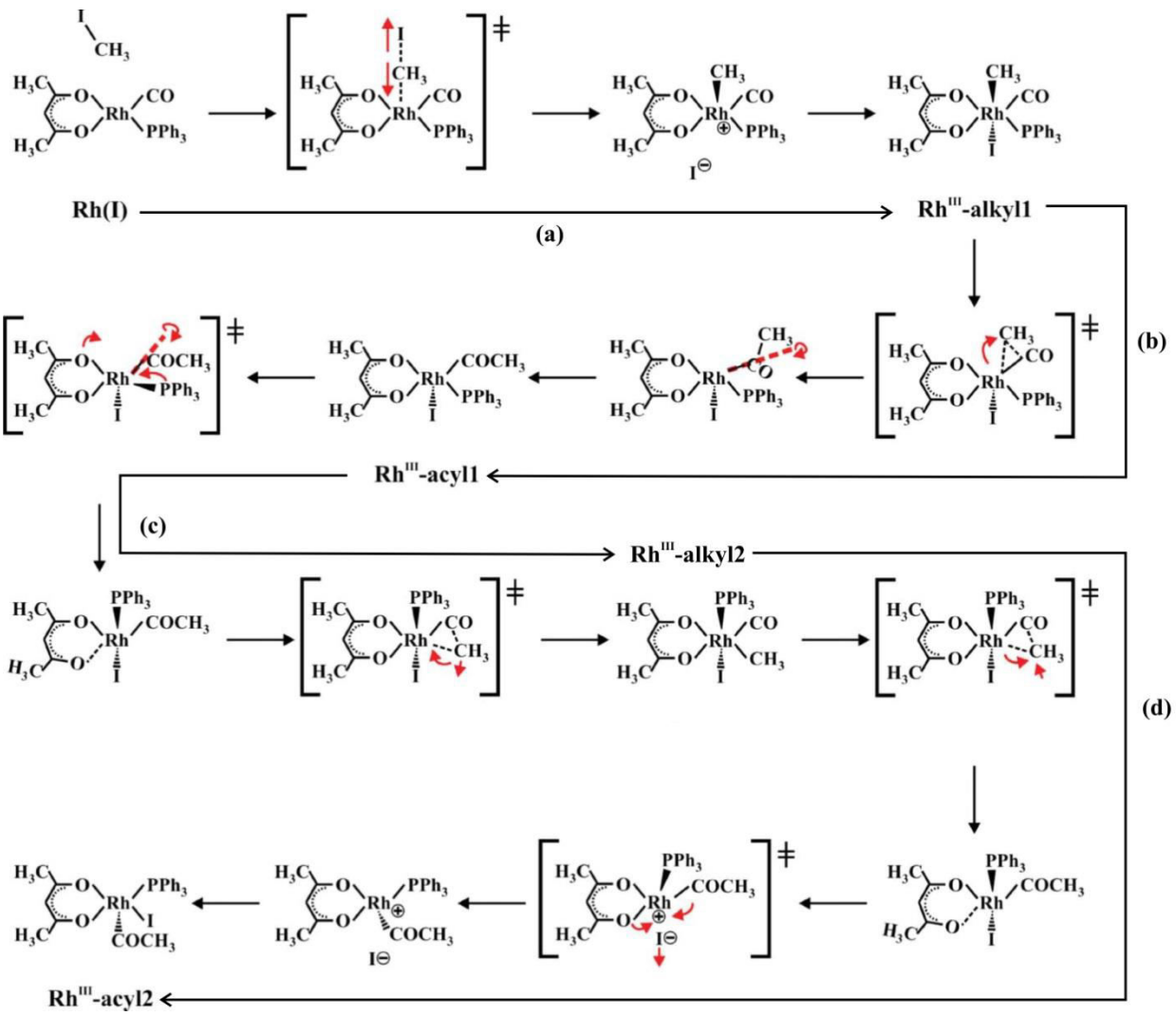

Scheme 2.10: A representation of the first reaction step in the oxidative addition reaction between CH_3I and Rh(acac)(CO)(PPh_3). [97] Reproduced from M.M. Conradie, J. Conradie, *Dalton Trans.,* 40 (2011) p 8226-8237 with permission of The Royal Society of Chemistry.

The fourth reaction step, the very slow formation of the Rh^{III}-acyl2 product proceeds via 5 steps as seen in Scheme 2.10 (d). The CH_3 moves away from the metal centre and back to the CO group. The reformed $COCH_3$ moves to the apical position and the iodine breaks away, which then rebonds to the metal centre of any of the 4-coordinated complexes in solution and stabilizes within the plane.[97]

The DFT calculated Gibbs energy profile of the mechanism of the oxidative addition and methyl migration steps of the reaction [Rh(acac)(CO)(PPh_3)] + CH_3I, is given in Figure 2.24. The DFT calculated thermodynamic data compared well with experimentally determined data.[97]

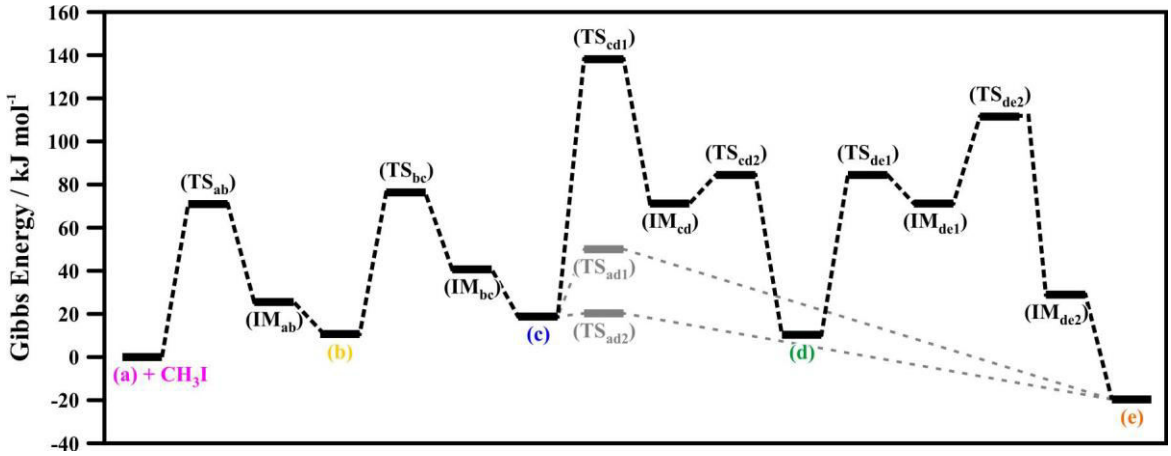

Figure 2.24: The DFT calculated Gibbs energy of the reactants, transition states, intermediate products and reaction products during the multistep reaction [Rh(acac)(CO)(PPh_3)] + CH_3I.[97] Reproduced from M.M. Conradie, J. Conradie, *Dalton Trans.,* 40 (2011) p 8226-8237 with permission of The Royal Society of Chemistry.

CHAPTER 2

3 Results and Discussion

In this chapter, the synthesis, electrochemistry, chemical kinetics and computational chemistry studies of selected bidentate ligands and their rhodium complexes, will be presented.

3.1 Bidentate ligands, L,L'-BID

3.1.1 Introduction

Coordination chemistry involves a central metal atom surrounded by a group or groups, which are referred to as ligands. One type of ligand is a bidentate ligand,L,L'-BID, where L and L' are indicative of atoms on the ligand that could coordinate to a metal centre.[1] These donor atoms have an electron pair that it donates to the metal centre, which explains the classification of these bidentate ligands as Lewis bases, due to the nucleophilic nature they possess.[2]

One type of L,L'-BID ligand that is used to bond with metal atoms is the β-diketonato ligand (Figure 3.1 a), generally referred to as $(RCOCHCOR')^-$ with the donor atoms L,L' = O,O and R and R' alkyl or aryl groups such as CF_3, CH_3, Ph, C_4H_3O, C_4H_3S *etc*. Some examples of β-diketonato ligands that are bonded to metal atoms are $(FcCOCHCOR)^-$ with R = Fc (ferrocenyl), C_6H_5 (Ph or phenyl),[3] CH_3, CF_3; $(C_6H_5COCHCO(CH_2)_nCH_3)^-$ with n = 1, 2, 3[4] and $(CF_3COCHCOR')^-$ with R' = C_4H_3S, C_4H_3O.[5] In this study an electrochemical study of 2-thienyl containing [Rh(β-diketonato)(CO)(PPh_3)] complexes with β-diketonato = $(C_4H_3SCOCHCOR')^-$ with R' = C_4H_3S (2-thienyl), CF_3 or Ph, will be presented in Section 3.4. The rest of this study focuses on bidentate ligands where the donor atoms, L and L',

---

[1]F.A. Cotton, G. Wilkinson, P.L. Gaus, *Basic Inorganic Chemsitry*, John Wiley and Sons Inc, 3rd edition, p 165-166

[2]F.A. Cotton, G. Wilkinson, C.A. Murillo, *Advanced Inorganic Chemistry*, Wiley-Interscience, 4th edition, p 62

[3]J. Conradie, G.J. Lamprecht, S. Otto, J.C. Swarts, *Inorg. Chim.Acta,* 2002, **328**, 191-203

[4]N.F. Stuurman, J. Conradie, *J. Organomet. Chem.*, 2009, **694**, 259-268

[5]M.M. Conradie, P.H. Van Rooyen, J. Conradie, *J. Mol. Struct.,* 2013, **1053**, 134-140

are varied between O, H-N and Ph-N, as illustrated in Figure 3.1 b-d, as well as the Rh-complexes containing these ligands.

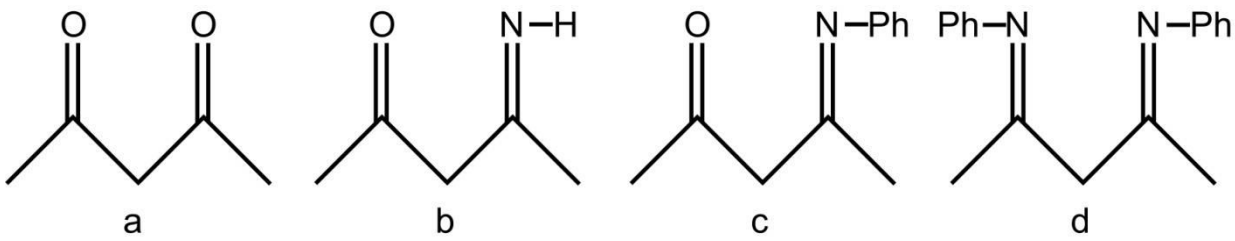

Figure 3.1: Structures of L,L'-BID ligand precursors utilized in this study: a) $CH_3COCH_2COCH_3$ (β-diketone) Hacac, b) $CH_3COCH_2CNHCH_3$ (imino-β-diketone) **1a**, c) $CH_3COCH_2CNPhCH_3$ (imino-β-diketone) **1b** and d) $CH_3CNPhCH_2CNPhCH_3$ (diimino-β-diketone) **1c**.

3.1.2 Synthesis

The synthesis of the ligands was followed as published in literature.[6,7] The synthesis of the ($CH_3COCH_2CNHCH_3$) **1a**, ligand was the first reaction performed. Addition of the ammonium hydroxide solution to the ($CH_3COCH_2COCH_3$), Hacac, ligand yielded a white solid, which after a few minutes dissolved to form a yellow solution. Leaving the mixture in a fume-hood overnight allowed for the final ligand, ($CH_3COCH_2CNHCH_3$) **1a**, to crystallize out. This procedure eliminated the use of organic solvents to extract the ligand from the water solution.

In this reaction between the ammonium hydroxide and the ($CH_3COCH_2COCH_3$) ligand, one of the O atoms on the ligand gets replaced by the NH group, with the remaining H atoms being consumed by the O atom to form water as byproduct. The use of an acid in the reaction facilitates the formation of the water byproduct. The general reaction sequence is seen in Scheme 3.1.

[6]S.G. McGeachin, *Can. J. Chem.*, 1968, **46**, 1904-1912

[7]M.J. Lacey, *Aust. J. Chem.*, 1970, **23**, 841-842

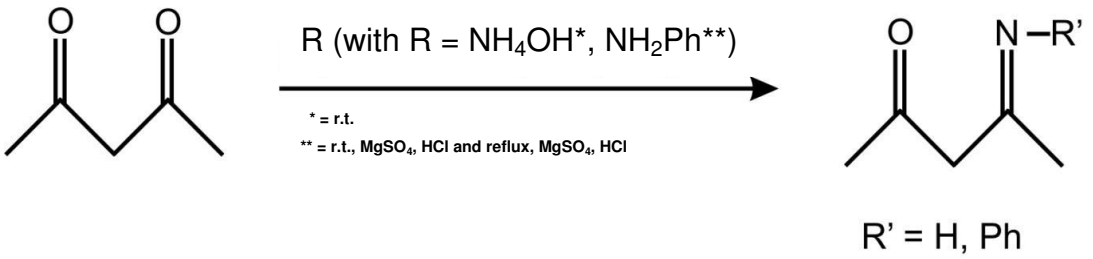

Scheme 3.1: Reaction pathway describing the formation of the desired N group containing ligands **1a** and **1b** from the ($CH_3COCH_2COCH_3$) starting material.

Synthesis of the ($CH_3COCH_2CNPhCH_3$) **1b** ligand was similar to the ($CH_3COCH_2CNHCH_3$) **1a** ligand's synthesis using NH_2Ph instead of NH_4OH. It was attempted to synthesize the ligand both by simple addition with low heat as well as through refluxing. The yield between the two methods (~90% for both methods) showed very little difference. The recrystallization of the ($CH_3COCH_2CNPhCH_3$) ligand was slow enough to yield large crystals that had a slight off-white colour.

The ($CH_3CNPhCH_2CNPhCH_3$) **1c** ligand synthesis was easy since the synthetic method for the ($CH_3COCH_2CNPhCH_3$) **1b** ligand synthesis was merely left to react at a low temperature with double the amount of acid. The recrystallization of the precipitate, which had a slight brown colour, yielded a yellow crystalline powder of high purity, as did all the synthesized ligands. The high purity was found to be evident in the NMR spectra. These spectra can be seen in Appendix A.

In Section 2.5.3, the possible tautomeric forms of the ligands have been discussed namely the keto and two enol forms.[8,9] However, since the ligands of interest in this study contain N atoms, the second possible enol form, with the H atom on the N atom, is referred to as an amine tautomer. There is only a single tautomeric form observed on the NMR as illustrated in Figure 3.2 for ($CH_3COCH_2CNPhCH_3$) **1b**. This tautomeric form is identified as the amine tautomer from the investigation done with the help of DFT calculations, for more information see Section 3.1.4.

---

[8]A. Kuhn, K.G. Von Eschwege, J. Conradie, *Electrochim. Acta*, 2011, **56**, 6211-6218

[9]T.E. Neal, R.W. Murray, *Anal. Chem.*, 1970, **42**, 1654-1656

RESULTS AND DISCUSSION

The NMR spectra of the ligands display no overlapping of the ^1H resonance peaks. The chemical shifts and the protons are summarized in Table 3.1 for **1a** – **1c**. NMR shifts for ($CH_3COCH_2COCH_3$) Hacac, is added for comparative purposes. The addition of an N atom to the ligand structure causes a slight difference ($\Delta\sigma$ = >0.1 ppm) in the values of the methyl group chemical shifts of the two methyl groups. The N atom is less electronegative than the O atom [χ_N = 3.04, χ_O = 3.44]. Therefore there is less electron density withdrawn from the general structure towards the N atom. Thus there is a shielding effect displayed. From Table 3.1 it can be seen that the effect of the more electron donating property of the substituted N atoms, relative to O, causes an upfield shift of the ^1H signals for the methine protons for the ($CH_3COCH_2CNPhCH_3$) **1b**, ($CH_3COCH_2CNHCH_3$) **1a**, and ($CH_3CNPhCH_2CNPhCH_3$) **1c**, ligands, and a downfield shift for the methyl protons relative to ($CH_3COCH_2COCH_3$) Hacac.

Table 3.1: Chemical shifts (σ) of the ^1H NMR signals, in ppm, for all L,L'-BID ligands in $CDCl_3$ solvent.

	Amine (N-H)	**Methine (C-H)**	**Methyls (CH_3)**	**Phenyl range**	**Enol (O-H)**
($CH_3COHCHCOCH_3$)	---	5.438 (s)	1.980 (s)	---	15.403 (s)
($CH_3COCHCNH_2CH_3$) **1a**	9.702 (s)	5.045 (s)	2.045 (s) ; 1.922 (s)	---	---
($CH_3COCHCNHPhCH_3$) **1b**	12.493 (s)	5.208 (s)	2.122 (s) ; 2.014 (s)	7.388 - 7.114 (m)	---
($CH_3CNHPhCHCNPhCH_3$) **1c**	12.720 (s)	4.906 (s)	2.032 (s)	7.346 - 6.971 (m)	---

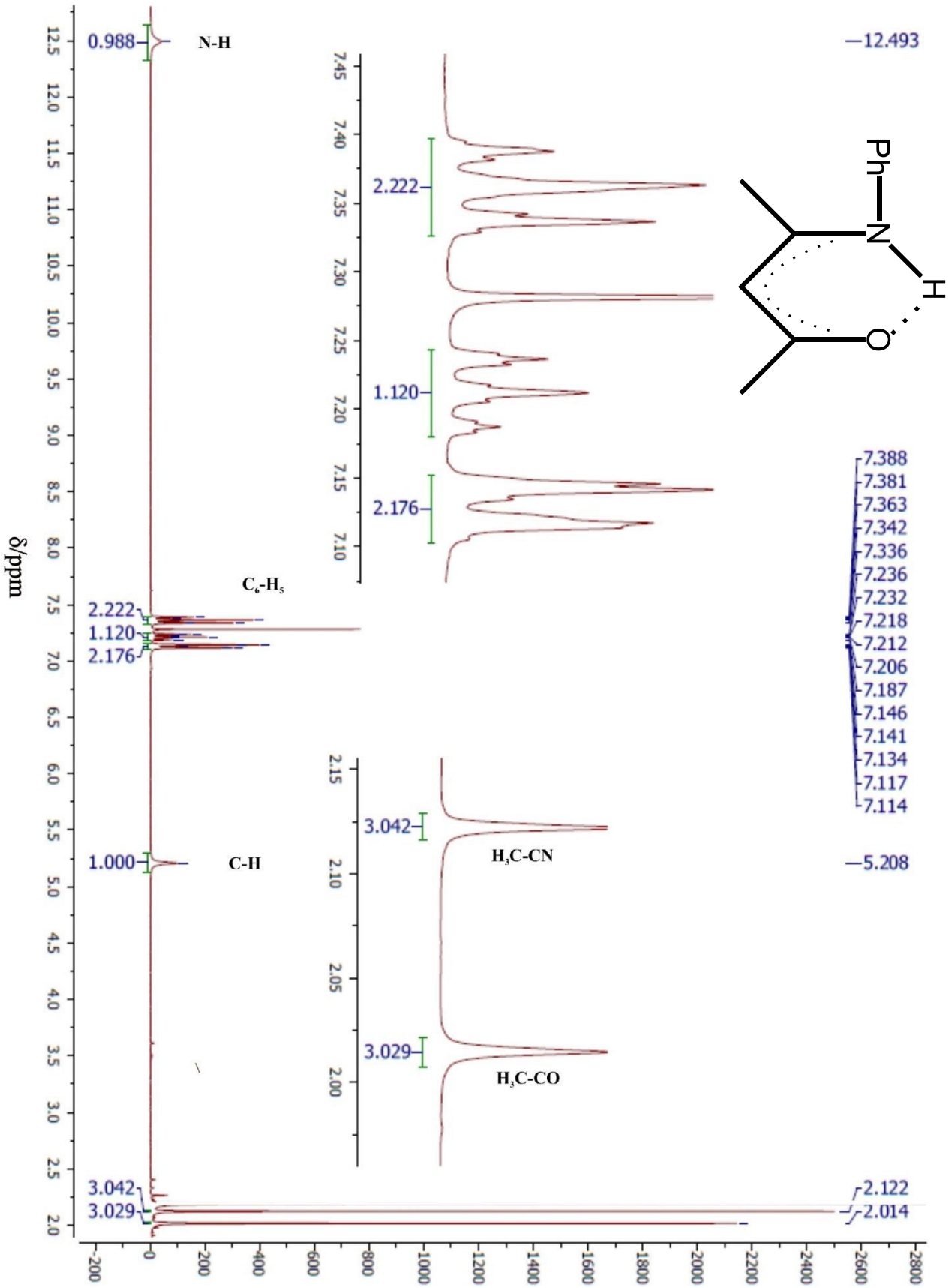

Figure 3.2: A ^{1}H NMR spectrum of the L,L'-BID ligand ($CH_3COCH_2CNPhCH_3$) **1b**.

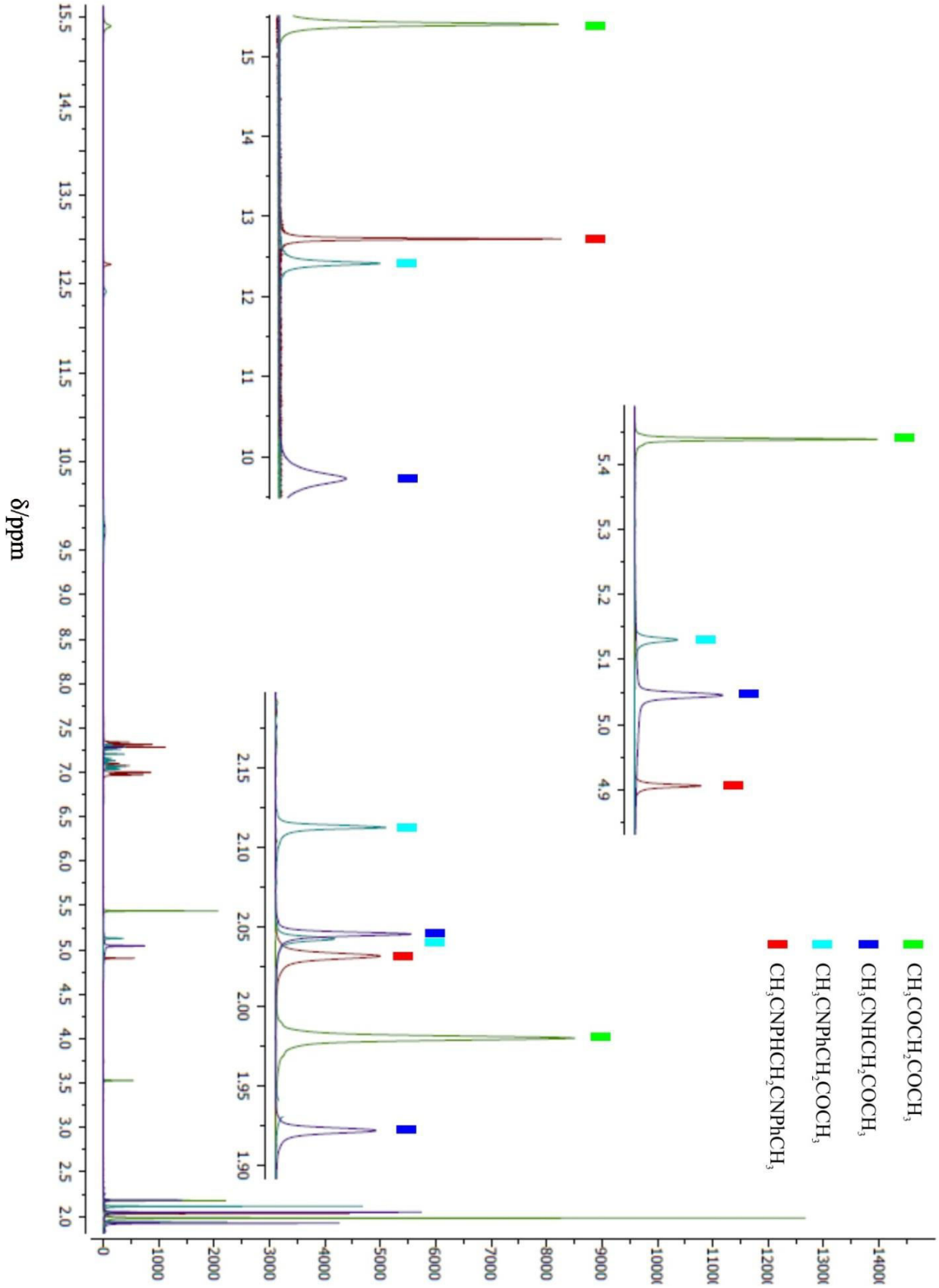

Figure 3.3: Superimposed ^{1}H NMR spectra of all indicated ligands.

3.1.3 Cyclic Voltammetry (CV)

In order to determine the electrochemical activity of the free ligands, cyclic voltammetry was utilized. The ligands ($CH_3COCH_2CNHCH_3$) **1a**, ($CH_3COCH_2CNPhCH_3$) **1b** and ($CH_3CNPhCH_2CNPhCH_3$) **1c** were analyzed and all showed similar electrochemical behaviour. The ($CH_3COCH_2CNPhCH_3$) **1b** ligand, as an example, shows a reduction peak at *ca* -2.7 V *vs* FcH/FcH^+ as seen in Figure 3.4. The reduced ligand (a radical with charge -1 and spin = ½, *i.e.* containing one unpaired electron) is unstable and decomposes before it can be re-oxidised. Therefore the reduction of ligands **1a** – **1c** can be described as electrochemically and chemically irreversible. However, as the scan rate increases, a small re-oxidation peak appears, as can be seen in Figure 3.4, for the CV at a scan rate of 5.0 V s^{-1}. The re-oxidation peak does not appear at slow scan rates, since the unstable reduced ligand decomposes and also migrates away from the electrode surface *via* diffusion at low scan rates. Once rate of diffusion is lower than the scan rate, *i.e.* at higher scan rates, the peak appears.[8,10]

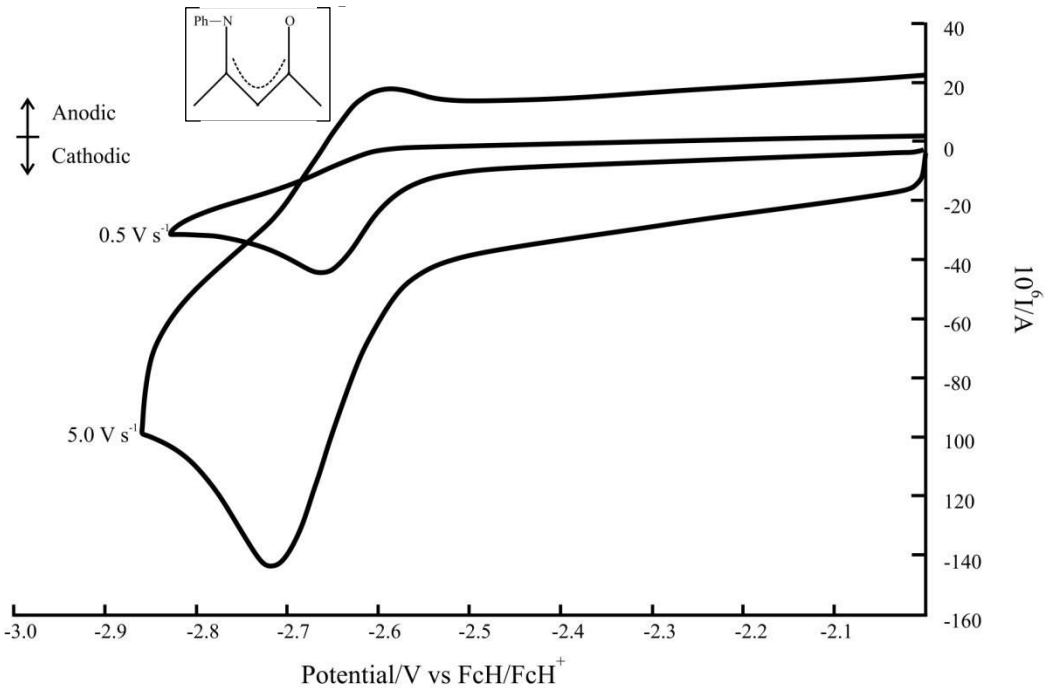

Figure 3.4: An overlay of the CV's at scan rates of 0.5 V s^{-1} and 5.0 V s^{-1} of a 0.001 M ($CH_3COCH_2CNPhCH_3$) **1b** in acetonitrile containing and 0.1 M TBAHFP as supporting electrolyte with a glassy carbon working electrode, a Pt wire auxiliary electrode and a $Ag/AgNO_3$ reference electrode. Scans were done at room temperature, 25°C.

---

[10]R.C. Buchta, D.H. Evans, *J. Org. Chem.*, 1970, **35**, 2844

The electrochemical behaviour of the ($CH_3COCH_2CNHCH_3$) **1a** ligand is shown in Figure 3.5. Table 3.2 gives the experimental parameters. It can be seen that the CV peak positions progressively move to more negative potentials as the scan rate increases, possibly due to slow electron transfer from the ligand to the electrode. The current involved in the reduction processes increases incrementally as well with increasing scan rate expected from the Randles-Sevcik equation $i_p = (2.69 \times 10^5) n^{1.5} AD^{0.5} C\nu^{0.5}$, where i_p = peak current (A), n = the number of exchanged electrons, A = the electrode area (cm^2), ν = the scan rate (Vs^{-1}), D = the diffusion constant ($cm^2\ s^{-1}$) and C = the bulk concentration (mol cm^{-3}) of the electroactive species. This behaviour was observed for all ligands. The linearity between the peak reduction current and the square root of the scan rate is shown in Figure 3.6 for **1a**.[8,10] All the complexes displayed the same linearity therefore only the one example is shown. The linear plot indicates that the reduction of **1a** – **1c** is diffusion controlled.[11]

Table 3.2: Reduction potentials (E_{pc}), scan rates (ν) and peak cathodic currents (i_{pc}) for the L,L'-BID ligand ($CH_3COCH_2CNHCH_3$) **1a**.

ν (V s^{-1})	E_{pc} (V)	$10^5 i_{pc}$ (A)
0.05	-2.951	-1.4
0.1	-2.966	-2.0
0.2	-2.974	-2.9
0.3	-2.985	-3.4
0.5	-3.006	-4.0
1.0	-3.016	-5.6
5.0	---	---

[11]D.H. Evans, K.M. O'Connell, R.A. Peterson, M.J. Kelly, *J. Chem. Ed.*, 1983, **60**, 290-293.

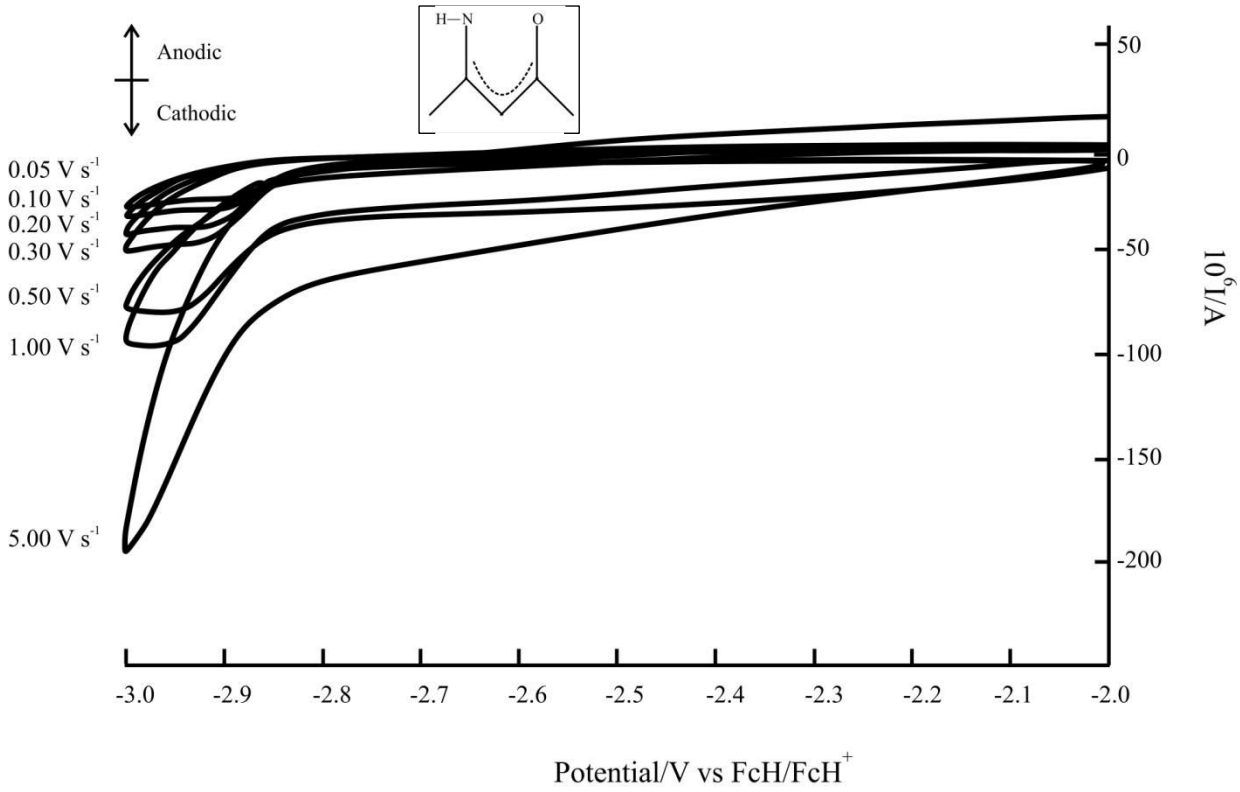

Figure 3.5: An overlay of the CV's at scan rates ranging from 0.5 V s^{-1} to 5.0 V s^{-1} of a 0.001 M acetonitrile solution containing the ($CH_3COCH_2CNHCH_3$) **1a** ligand and 0.1 M TBAHFP as supporting electrolyte with a glassy carbon working electrode, a Pt wire auxiliary electrode and a $Ag/AgNO_3$ reference electrode. Scans were done at room temperature, 25°C.

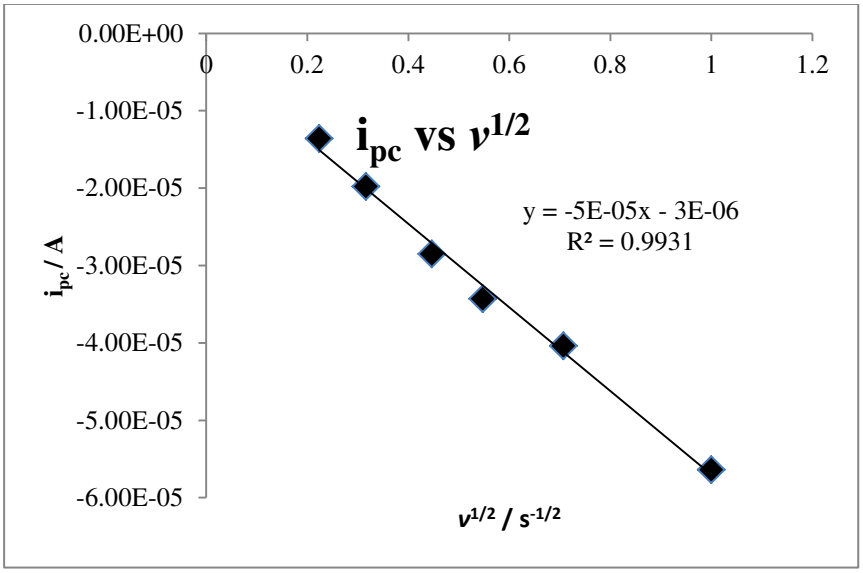

Figure 3.6: Peak current dependence on scan rate for the ($CH_3COCH_2CNHCH_3$) **1a** ligand.

Only the ($CH_3CNPhCH_2CNPhCH_3$) **1c** ligand displayed an oxidation at *ca* 0.7 V *vs* FcH/FcH^+, additional to the reduction peak at *ca* -2.7 V *vs* FcH/FcH^+, see Figure 3.7. Both the oxidation and the reduction processes are electrochemically and chemically irreversible.[8]

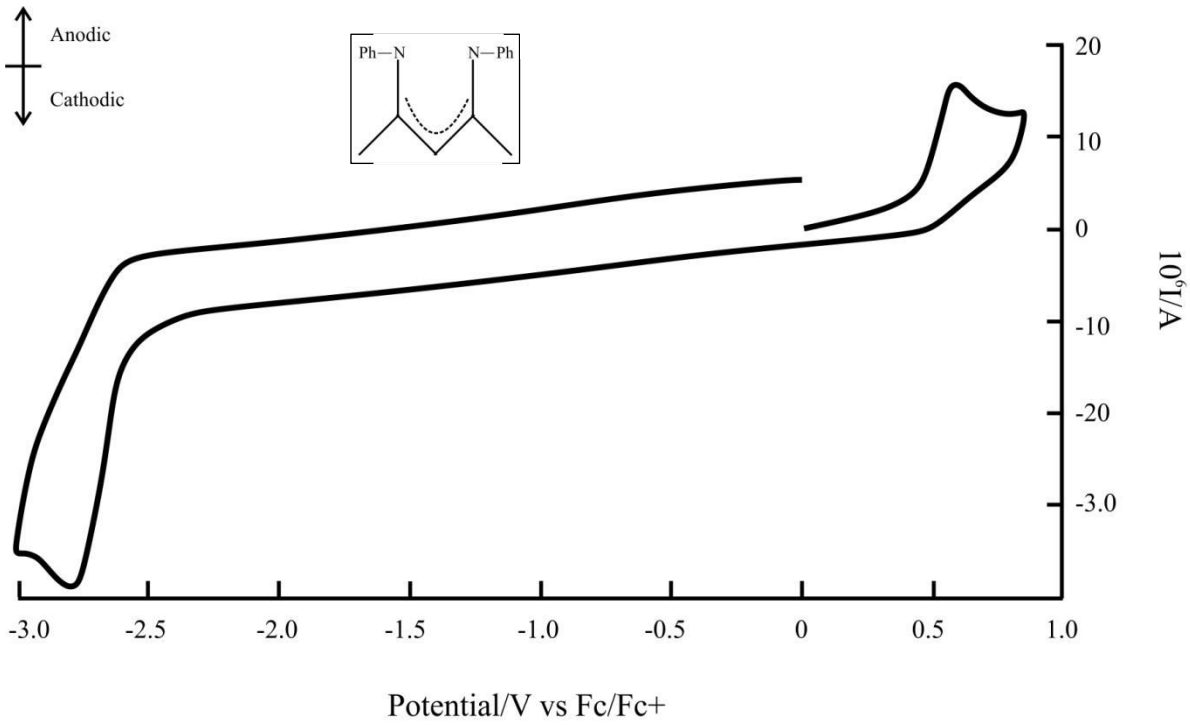

Figure 3.7: CV at a scan rate of 0.1 V s^{-1} of a 0.001 M acetonitrile solution containing the ($CH_3CNPhCH_2CNPhCH_3$) **1c** ligand and 0.1 M TBAHFP as supporting electrolyte with a glassy carbon working electrode, a Pt wire auxiliary electrode and a $Ag/AgNO_3$ reference electrode. Scans were done at room temperature, 25°C.

Figure 3.8 shows the CV's of ($CH_3COCH_2COCH_3$) with the three N containing ligands **1a** – **1c** of this study. Table 3.4 gives the electronegativities of selected atoms or groups that are present on the L,L'-BID ligands. The N atom is less electronegative than the O atom. Therefore the trend of lower cathodic reduction potential observed in Figure 3.8 between the various ligands are attributed to the differing electronegativities as will be explained next. Comparing the CV of ($CH_3COCH_2COCH_3$) with that of the three N containing ligands of this study it is seen that the N containing ligands show reduction at lower potentials. This is due to the N atom being less electronegative than the O atom. Less electron density is thus withdrawn from the ligand structure towards the N atom and more energy (more negative reduction potential) is needed to add an electron to the N containing ligands.

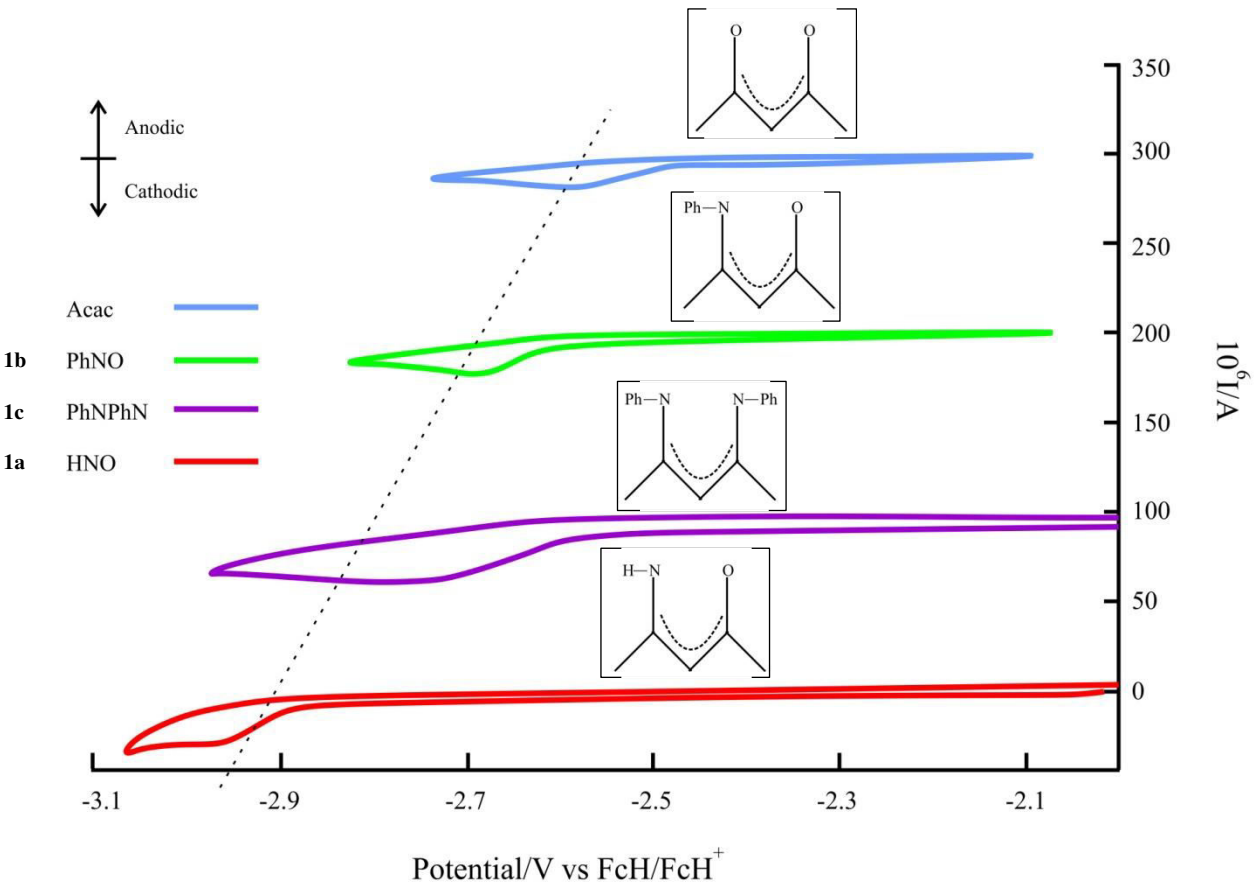

Figure 3.8: Overlay of the CVs of all the indicated ligands with concentrations of 0.001 M in acetonitrile as solvent with 0.1 M TBAHFP as supporting electrolyte and a glassy carbon working electrode, a Pt wire auxiliary electrode and a $Ag/AgNO_3$ reference electrode. The scan rate is 0.1 V s^{-1} at room temperature, 25°C.

Comparing the two N,O containing ligands **1a** and **1b** in Figure 3.8, with the peak cathodic potentials summarized in Table 3.3, it can be seen that the ligand containing an H atom bonded to the N atom reduces at a more negative potential than the ligand with one Ph group bonded to the N atom. This is due to the H atom having a much smaller electronegativity than the Ph group, see Table 3.4. Less electron density is thus withdrawn from the ligand structure therefore more energy (more negative reduction potential) is needed to add an electron to ($CH_3COCH_2CNHCH_3$) **1a**. Another reason for the more positive reduction potential of the Ph containing complex is due to the π electron density of the aromatic ring structure. It has an electron donating property through the conjugated electron density across the ligand's carbon backbone. This stabilises the electroactive centre of the ligand therefore causing the more positive reduction potential.

Comparing the two Ph containing ligands, ($CH_3COCH_2CNPhCH_3$) **1b** and ($CH_3CNPhCH_2CNPhCH_3$) **1c**, it can be seen that the ($CH_3CNPhCH_2CNPhCH_3$) **1c** ligand has a more negative reduction peak potential. The overall effect of the two N atoms on the ($CH_3CNPhCHCNPhCH_3$) **1c** ligand *vs* the one N atom and one O atom on the ($CH_3COCHCNPhCH_3$) **1b** ligand on the electron density of the ligands, can be compared by considering the sum of the electronegativities between the ($CH_3CNPhCH_2CNPhCH_3$) **1c** ($\chi_N + \chi_N = 6$) and ($CH_3COCH_2CNPhCH_3$) **1b** ($\chi_N + \chi_O = 6.5$). The ligand with smaller electronegativity, ($CH_3CNPhCH_2CNPhCH_3$) **1c** will thus be reduced at a lower, more negative, reduction potential due to the less electron density being removed from the electroactive centre of the ligand by the less electronegative atoms in **1c**, thus increasing the amount of energy required in order to add electron density to the centre.

Table 3.3: Electrochemical data at a scan rate of 0.1 V $s^{-1}$of the indicated L,L'-BID ligands.

Ligands	**E_{pc} *vs* FcH/FcH$^+$/V**
($CH_3COCH_2COCH_3$)	-2.575
($CH_3COCH_2CNHCH_3$) **1a**	-2.966
($CH_3COCH_2CNPhCH_3$) **1b**	-2.681
($CH_3CNPhCH_2CNPhCH_3$) **1c**	-2.741

Table 3.4: Electronegativities of atoms or groups on the L,L'-BID ligands.

Atom	**Electronegativity***
O	3.5
N	3
H	2.1
Ph	2.49

*Values obtained from published literature.[12]

3.1.4 DFT computational study

In this DFT computational section the optimized geometries and theoretical bond angles and lengths of the L,L'-BID ligands were investigated and compared to experimental observation.

[12]J.W. Huheey, *J. Phys. Chem.,* 1965, **69**, 3284-3291

As discussed in Section 2.5.3, there are three possible tautomeric forms possible for the L,L'-BID ligands namely the keto and two enol tautomers.[13] DFT calculations were used to determine the optimized geometries of these possible tautomers. The energies of the optimized isomer geometries are compared with each other to predict the preferential appearance of one isomer over another. Table 3.5 and Table 3.6 give the relative gas phase electronic energies and the calculated Boltzmann distribution, namely the probability of an isomer to exist of Hacac and **1a – 1c**. The results show that the ($CH_3COCH_2COCH_3$) ligand prefers the formation of an enol tautomer and all the N containing ligands prefer the formation of an amine type tautomer. This is in agreement with the NMR spectra where a single tautomer is observed. The NMR spectra display peaks above 10 ppm, which are typically attributed to OH or NH chemical shifts. The difference in the peak values between the OH shift of the Hacac ligand and the N containing L,L'-BID ligands is relatively large (> 2 ppm). There is a good correlation between the DFT calculated probabilities and the observed NMR experimental results.

[13]W.C. Du Plessis, T.G. Vosloo, J.C. Swarts, *J. Chem. Soc. Dalton Trans.*, 1998, 2507-2514

Table 3.5: PW91/TZP DFT calculated energies, structures and distribution probability of the ($CH_3COCH_2COCH_3$) and ($CH_3COCH_2CNHCH_3$) **1a**.

Ligands	**Tautomers**	**Structures**	**Energy (eV)**	**Relative energy (eV)**	**Boltzmann distribution**
($CH_3COCH_2COCH_3$)	enol	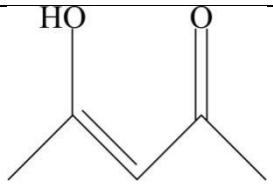	-88.34	0.00	100.0
	keto	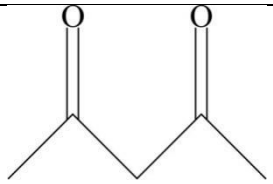	-87.93	0.40	0.0
($CH_3COCH_2CNHCH_3$) **1a**	amine	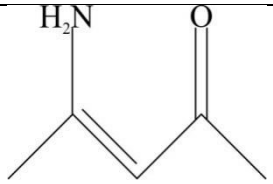	-93.58	0.00	100.0
	enol	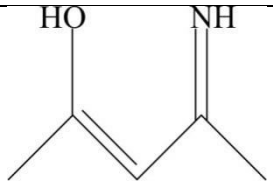	-92.49	1.09	0.0
	keto	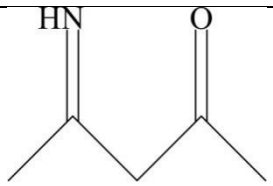	-92.97	0.62	0.0

Table 3.6: PW91/TZP DFT calculated energies, structures and distribution probability of ($CH_3COCH_2CNPhCH_3$) **1b** and ($CH_3CNPhCH_2CNPhCH_3$) **1c**.

Ligands	Tautomers	Structures	Energy (eV)	Relative energy (eV)	Boltzmann distribution
($CH_3COCH_2CNPhCH_3$) **1b**	amine	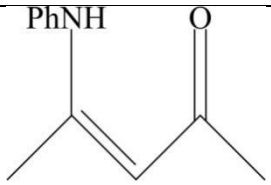	-161.98	0.00	100.0
	enol	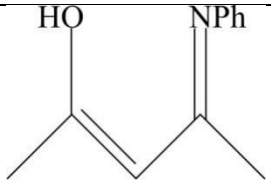	-161.00	0.97	0.0
	keto	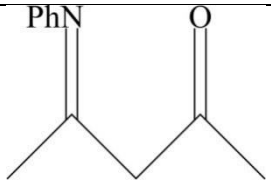	-161.44	0.54	0.0
($CH_3CNPhCH_2CNPhCH_3$) **1c**	amine	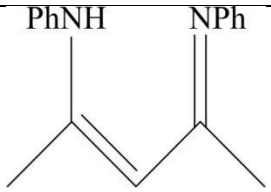	-235.42	0.00	100.0
	keto	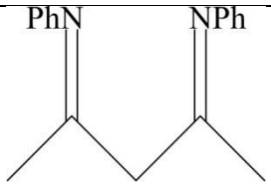	-234.94	0.48	0.0

In Figure 3.9 the structures of the DFT optimised geometries of the three [$CH_3COCH_2CNHCH_3$] **1a** tautomers are compared. It can be seen that there are slight differences between the amine and enol tautomers, however the keto tautomers have a twisted geometry. The twisted geometry for keto tautomers has been observed for related β-diketones such as ($C(CH_3)_3COCH(I)COC(CH_3)_3$) [14] and ($CPhCOCH(CH_2Ph)COCPh$). [15]

---

[14] S. Sans-Lenain, A. Reynes, A. Gleizes, *Acta Crystallogr. Sect.C: Cryst. Struct.Commun*. 1992, **48**, 1788 – 1791, CSD reference code KUGPUX

[15] N. Judas, B. Kaitner, *Acta Crystallogr. Sect.E: Struct. Rep. Online*. 2005, **61**, o4008-o4010, CSD reference code DAYLIZ

Selected bond lengths and selected angles of all the ligands in this study are summarized in Table 3.7, together with available experimental data from known solid state X-ray structures. All indicated ligands exhibit similar geometry structures, therefore only the ($CH_3COCH_2CNHCH_3$) **1a** ligand is illustrated as an example in Figure 3.9.

By comparing the published crystal structure of ($CH_3COCH_2COCH_3$)[16] and ($CH_3CNPhCH_2CNPhCH_3$) **1c**, with the theoretically determined DFT optimized geometry it can be seen that there is very little difference between the selected bond distances. For example for **1c** the difference in the N-C bond distance (Δa = 0.001) and the O-C bond distance (Δb = 0.017) is negligible. The selected bonding angles display more noticeable deviations ($\Delta\Theta = \sim 2^{o}$) between the experimental and DFT calculated values. These deviations are attributed to the fact that the calculations are performed for an ideal gas phase however the crystal data display the solid state structures.

The published crystal structure for ($CH_3COCH_2COCH_3$)[16] corresponds with the DFT lowest energy enol tautomer. The published crystal structure for ($CH_3CNPhCH_2CNPhCH_3$) **1c**[17] was found to be the amine tautomer, again in agreement with the DFT lowest energy geometry for **1c.**

Both the good agreement of DFT calculated geometries with published crystal structure data and the fact that the experimental published crystal structure agree with the lowest energy DFT calculated geometry, is a validation that the theoretical DFT method used is a good choice for the complexes and compounds of this study.

Table 3.7: Selected bond distances (Å) and bond angles (degrees) of the PW91/TZP DFT calculated geometries Hacac and **1a** – **1c** tautomeric forms.

Ligands	**Tautomers**	**Ref**	**a (Å)**	**b (Å)**	**c (Å)**	**Θ_1 (deg)**	**Θ_2 (deg)**
($CH_3COCH_2COCH_3$)	enol	calc	1.319	1.273	2.448	120.6	121.0
		exp[16]	1.331	1.238	2.535	120.5	122.8
	keto	calc	1.221	1.222	4.100	120.8	120.7
($CH_3COCH_2CNHCH_3$) **1a**	amine	calc	1.344	1.260	2.600	120.4	123.2
	enol	calc	1.291	1.363	2.828	122.1	121.6
	keto	calc	1.281	1.222	4.163	117.8	121.0
($CH_3COCH_2CNPhCH_3$) **1b**	amine	calc	1.353	1.264	2.593	118.3	123.0
	enol	calc	1.292	1.363	2.807	120.7	121.6
	keto	calc	1.283	1.222	4.169	117.0	121.1
($CH_3CNPhCH_2CNPhCH_3$) **1c**	amine	calc	1.315	1.359	2.639	119.1	119.8
		exp[17]	1.314	1.376	---*	121.1	118.8
	keto	calc	1.282	1.282	4.179	117.3	117.3

a is C-N bond, except ($CH_3COCH_2COCH_3$) where a is C-O bond

b is C-O bond

c is N-O separation distance

Θ_1 is N-C-CH bond angle

Θ_2 is O-C-CH bond angle

*Value is not supplied in literature.

[16] A. Camerman, D. Mastropaolo, N. Camerman, *J. Am. Chem. Soc*. 1983, **105**, 1583-1586, CSD refcode DPHEAD10. More structures see CSD refcode HADJUS, HADKAZ, KUPPAN, NUFREM, QASGAS, TITZEB, TUYREL

[17] S. Brownstein, E.J. Gabe, L. Prasad, *Can. J. Chem.,* 1983, **61**, 1410-1413

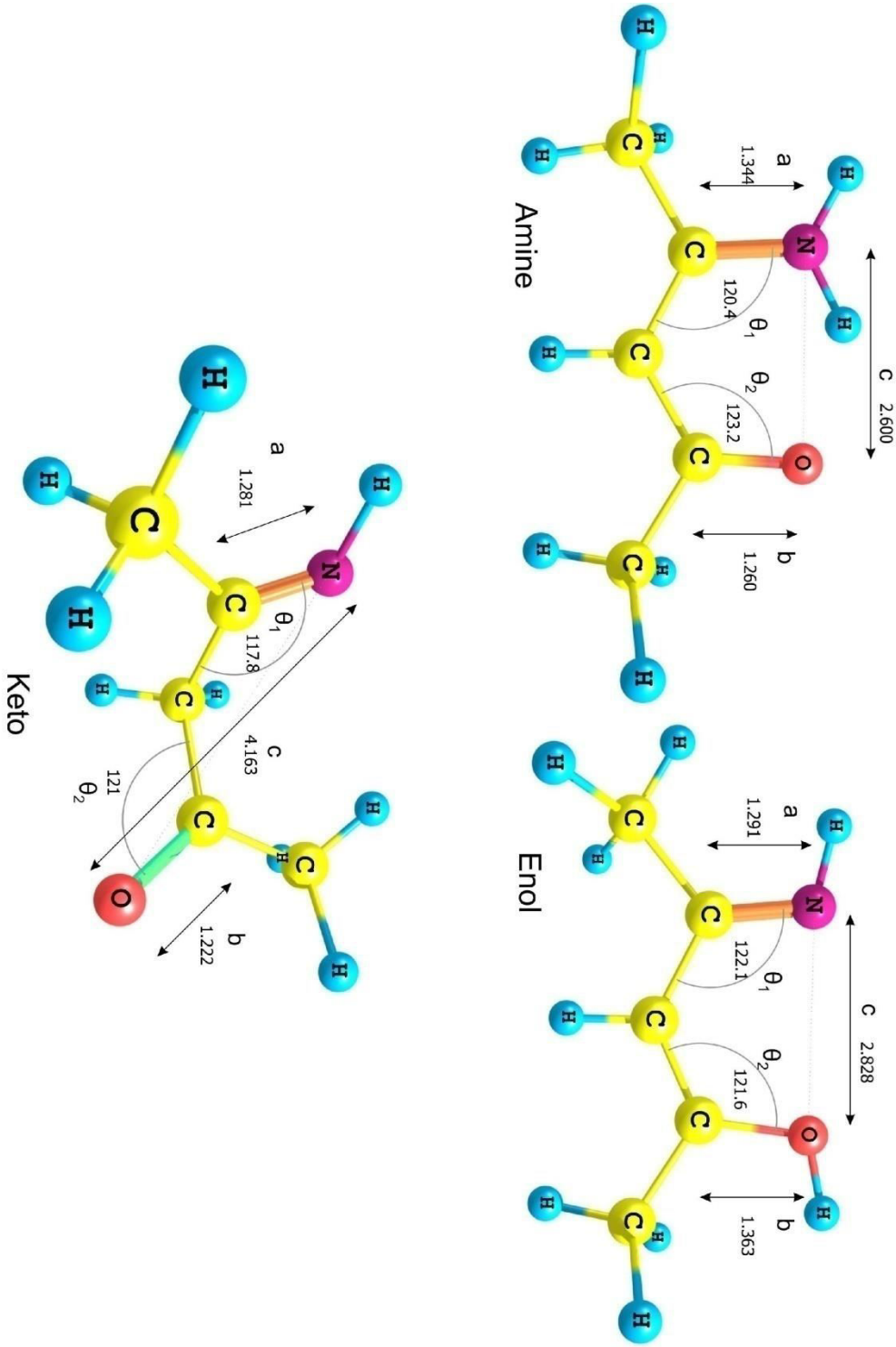

Figure 3.9: A comparison of the optimized geometries of the three tautomeric forms of ($CH_3COCH_2CNHCH_3$) **1a**, calculated with PW91/TZP DFT, illustrating various bond distances (Å) and bonding angles (degrees).

3.2 [Rh(L,L'-BID)(CO)$_2$] complexes with (L,L') = (O,N), (O,NPh), (NPh,NPh)

In this section the synthesis and characterisation of the Rh-dicarbonyl complexes [Rh($CH_3COCHCNHCH_3$)(CO)$_2$] **2a**, [Rh($CH_3COCHCNPhCH_3$)(CO)$_2$] **2b** and [Rh($CH_3CNPhCHCNPhCH_3$)(CO)$_2$] **2c** are presented.

3.2.1 Synthesis

Literature yielded two possible methods[18,19] to synthesize the dicarbonyl complexes of rhodium. The first is the heating of $RhCl_3.nH_2O$ in DMF, forming the salt $[NH_2(CH_3)_2]^+[Rh(CO)_2Cl_2]^-$. Addition of the appropriate L,L'-BID ligand to the reaction mixture, results in the precipitation of [Rh-L,L'-BID)(CO)$_2$], see Scheme 3.2.[18,19]

The second method is the direct reaction between μ-dichloro-tetracarbonyldirhodium and the ligand in methanol solution, see Scheme 3.3. The μ-dichloro-tetracarbonyldirhodium is available commercially and was used in this study.[20,21] The red methanol solution of the dirhodium complex turned to a yellow colour after the addition of the ligands. The extraction of the dicarbonyl complexes was done with *n*-hexane until the organic solvent used to extract was clear. The collected solvent containing the product was then concentrated by evaporation. After a fine powder crystallized, the solution was filtered again and the complex crystallized slowly from the *n*-hexane solution. The purity of the complexes was high as evident through the NMR analysis and the IR spectra as seen in Appendix A and Appendix B.

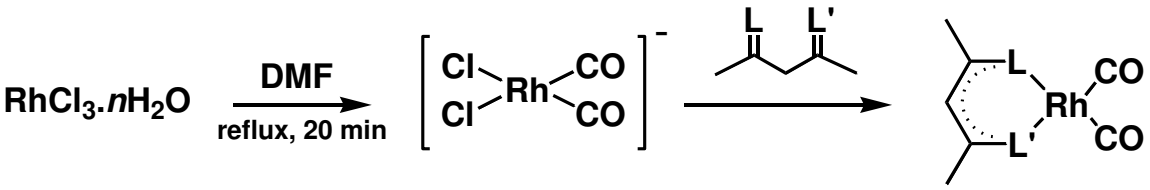

Scheme 3.2: General reaction scheme for the synthesis of [Rh(L,L'-BID)(CO)$_2$] complexes from $RhCl_3.nH_2O$.

---

[18]P. Serp, M. Hernandez, B. Richard, P. Kalck, *Eur. J. Inorg. Chem.* 2001, **9**, 2327-2336.

[19]Y.S. Varshavsky, M.R. Galding, T.G. Cherkasova, S.N. Smirnov, V.N. Khrustalev, *J. Organomet. Chem.,* 2007, **692**, 5788-5794

[20]J. Han, L.F. Zhang, W. Wan, *J. Organomet. Chem.*, 2003, **672**, 86-93

[21]C. Pretorius, A. Roodt, *Acta. Cryst*., 2012, **E68**, m1451-m1452

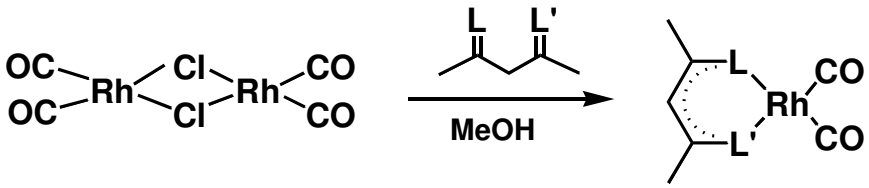

Scheme 3.3: General reaction scheme for the synthesis of [Rh(L,L'-BID)$(CO)_2$] complexes from μ-dichloro-tetracarbonyldirhodium.

The ^{1}H NMR spectra of the Rh-dicarbonyl complexes show ^{1}H resonance peaks similar to the free ligands, however at slightly different positions. As an example the focus will be placed on the [Rh(CH_3CNPhCHCNPhCH_3)$(CO)_2$] **2c** complex, with a ^{1}H NMR spectrum as seen in Figure 3.10. Selected ^{1}H resonance peak positions of the [Rh(CH_3CNPhCHCNPhCH_3)$(CO)_2$] **2c** and the (CH_3CNPhCHCNPhCH_3) **1c** free ligand are summarized in Table 3.8. All the dicarbonyl complexes and ligands displayed similar deviation between the peak resonance positions.

Table 3.8: ^{1}H NMR chemical shifts in ppm of the (CH_3CNPhCHCNPhCH_3) **1c** free ligand and the [Rh(CH_3CNPhCHCNPhCH_3)$(CO)_2$] **2c** complex.

Complex	**Methine (C-H)**	**Methyls (CH_3)**	**Phenyl range**
[CH_3CNPhCHCNPhCH_3] **1c**	4.906 (s)	2.032* (s)	7.346 - 6.971 (m)
[Rh(CH_3CNPhCHCNPhCH_3)$(CO)_2$] **2c**	5.101 (s)	1.871* (s)	7.372-7.166 (m)

* = A single peak of two overlapping peaks integrating for 3 each due to symmetry in complex.

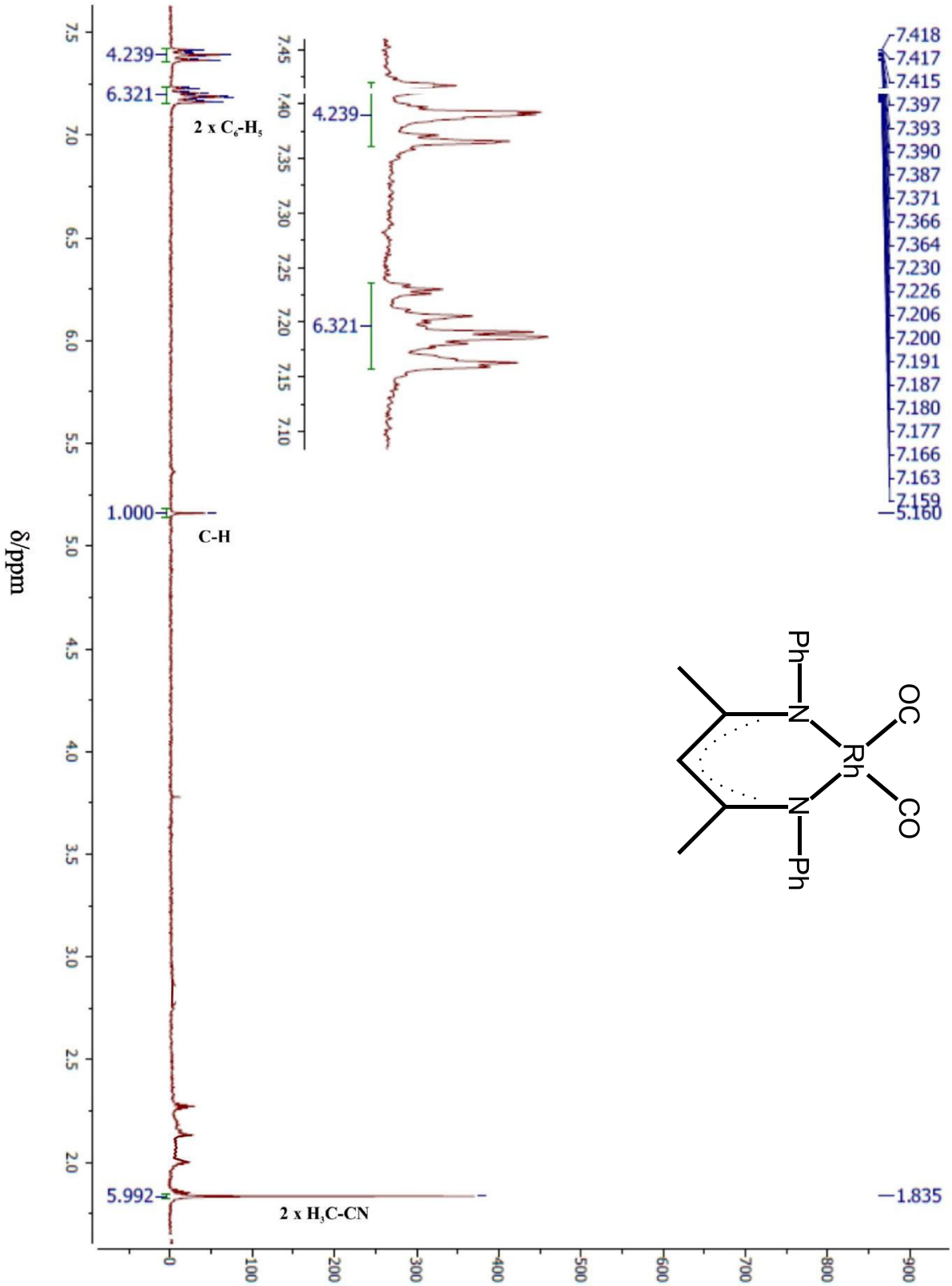

Figure 3.10: An ^{1}H NMR spectrum of the dicarbonyl rhodium complex $[Rh(CH_3CNPhCHCNPhCH_3)(CO)_2]$ **2c**.

From Table 3.8, which contains the ^{1}H chemical shifts of the free ($CH_3CNPhCHCNPhCH_3$) **1c** ligand and the accompanying dicarbonyl rhodium complex **2c**, it can be seen that the methine proton chemical shift (^{1}H) shifts to a more downfield position and the methyl proton chemical shifts are shifted to a more upfield position for **2c**. This was observed for all the complexes and ligands. The reason for the shifts is due to the pseudo aromatic six membered ring that is formed through the coordination to the Rh metal centre. The methine proton, which is directly bonded to the ring, experiences a shielding effect and the methyl protons are separated from the ring by one carbon atom and experience a deshielding effect. This causes the upfield and downfield appearance in the chemical shifts.

Table 3.9: ^{1}H NMR chemical shifts in ppm for all [Rh(L,L'-BID)$(CO)_2$] complexes.

	Methine (C-H)	**Methyls (CH_3)**	**Phenyl range**
[Rh($CH_3COCHCOCH_3$)$(CO)_2$]	5.63 (s)	2.08 (s)	---
[Rh($CH_3COCHCNHCH_3$)$(CO)_2$] **2a**	5.364/5.293 (d, J^4 = 2.311 Hz)	2.175/2.172 (d, J^4 = 0.74 Hz) 2.106 (s)	---
[Rh($CH_3COCHCNPhCH_3$)$(CO)_2$] **2b**	5.298 (s)	2.141 (s) 2.195 (s)	7.388 - 7.061 (m)
[Rh($CH_3CNPhCHCNPhCH_3$)$(CO)_2$] **2c**	5.101 (s) (5.160)*	1.871 (s) (1.835)*	7.372 - 7.166 (m) (7.366 - 7.159)*

*Chemical shifts in brackets are for acetone-D6 as solvent during analysis

The ^{1}H chemical shifts of the dicarbonyl complexes with the indicated L,L'-BID ligands are in Table 3.9. As can be seen from Table 3.9 it is clear that there is a definite upfield shift in the peak signal positions for the methyl groups as more O atoms are replaced by NH or NPh. Moving from a complex with no phenyl rings, [Rh($CH_3COCHCNHCH_3$)$(CO)_2$] **2a** with a chemical shift of 5.364 ppm for the methine proton, to a complex with 1 phenyl ring, [Rh($CH_3COCHCNPhCH_3$)$(CO)_2$] **2b** with a chemical shift of 5.298 ppm for the methine proton, to a complex with 2 phenyl rings, [Rh($CH_3CNPhCHCNPhCH_3$)$(CO)_2$] **2c** with a chemical shift of 5.101 ppm for the methine proton, it is evident that the phenyl ring attached to the N atom and the amount of N atoms that chelate to the Rh metal centre have an effect on the chemical shift of the methine proton. The reason for the shift of the resonances between the ligands and the dicarbonyl complexes is due to the available electron density across the dicarbonyl complexes as a whole. The electronegativity of the atoms affect the electron density available across the ligand structure. The less electronegative atoms (O > N >Ph> H) or groups increase the density

across the ligand's carbon backbone, which therefore causes a shielding effect resulting in an upfield shift in the peak position of the methine proton. The chemical shift for the proton bound to the N atom is not observed.

An example of the IR analysis of **2a** as representative example of the synthesized [Rh(L,L'-BID)$(CO)_2$] complexes is shown in Figure 3.11. The two dicarbonyl stretching frequencies can be seen at 2044.13 cm^{-1} and at 1971.02 cm^{-1}. The appearance of two stretching frequencies is due to the two types of stretching that occur for the two CO groups attached to the Rh metal centre. They are namely the symmetrical stretching, where both the CO groups contract and expand at the same time, and asymmetrical stretching, where the two CO groups are expanding and contracting oppositely. The stretching frequencies of the two CO groups attached to the Rh metal centre for all the [Rh(L,L'-BID)$(CO)_2$] complexes are in Table 3.10.

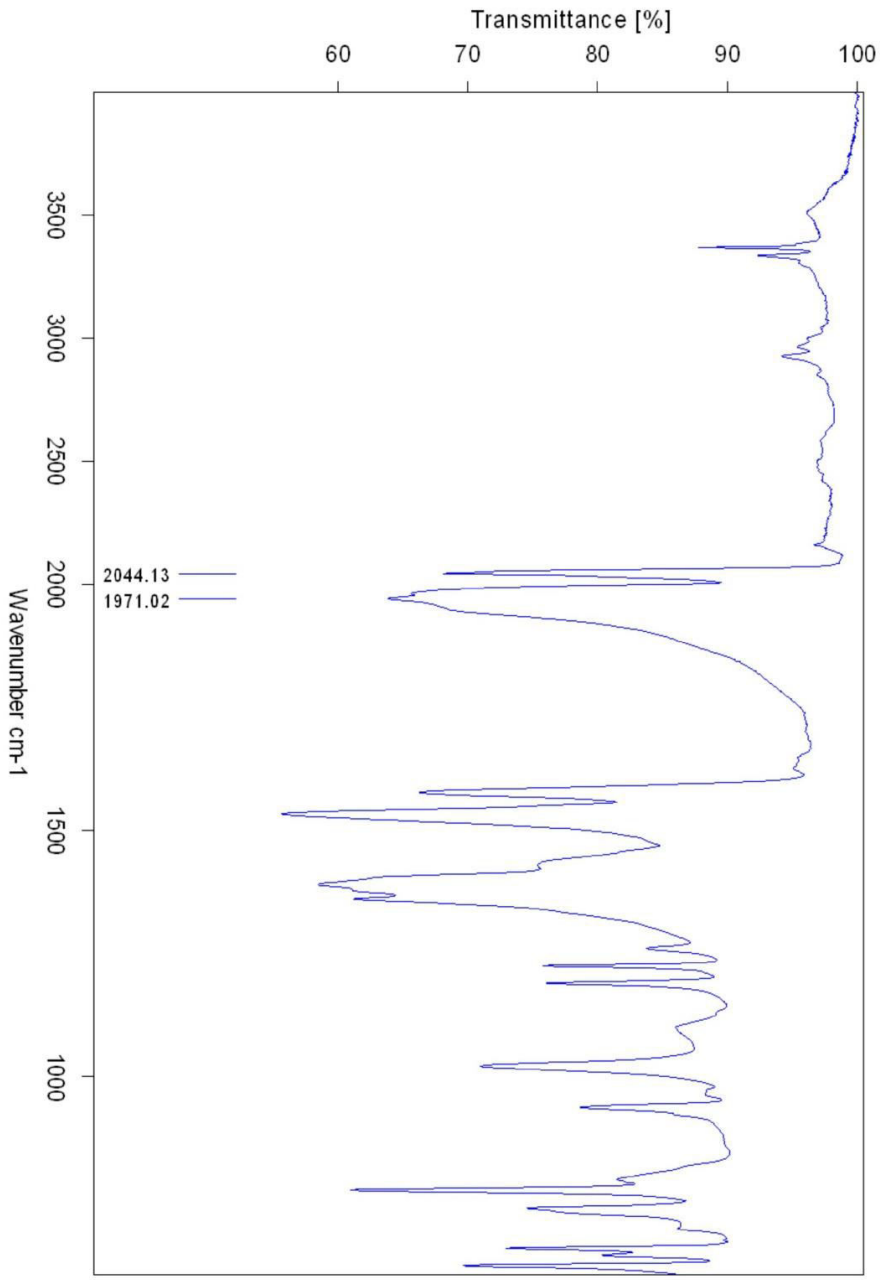

Figure 3.11: An IR spectrum of $[Rh(CH_3COCHCNHCH_3)(CO)_2]$ **2a** with carbonyl stretching frequencies at 1971.02 cm^{-1} and 2044.13 cm^{-1}.

Table 3.10: IR stretching frequencies ($\nu_{(CO)}$) of the carbonyl groups on the [Rh(L,L'-BID)$(CO)_2$] complexes.

	$\nu_{(CO)}$ **(cm^{-1})**
[Rh($CH_3COCHCNHCH_3$)$(CO)_2$] **2a**	2044.13 1971.02
[Rh($CH_3COCHCNPhCH_3$)$(CO)_2$] **2b**	2058.98 1997.69
[Rh($CH_3CNPhCHCNPhCH_3$)$(CO)_2$] **2c**	2055.60 2046.70 1992.10 1977.79

From Table 3.10 it can be seen that in comparing the [Rh($CH_3COCHCNHCH_3$)$(CO)_2$], which contains one O atom and one NH segment, and [Rh($CH_3COCHCNPhCH_3$)$(CO)_2$], which contains one O atom and one PhN segment, shifts the stretching frequency to a larger wavenumber. This is due to the electronegativity of the groups which affect the bond strengths. The more electronegative groups or atoms will attract electrons in a bond more towards themselves, therefore slightly shortening and thus strengthening the bonds which shifts the stretching frequency to smaller values. In the case of [Rh($CH_3CNPhCHCNPhCH_3$)$(CO)_2$] **2c**, theoretically there are only 2 stretching frequencies expected, see Section 3.2.2, however the experimental results display 4 frequencies. This is not yet explainable however it has been found previously.[41]

3.2.2 DFT computational study

Using DFT calculations the optimized geometries of the rhodium dicarbonyl complexes, after complexation with the indicated ligands, were determined. In Figure 3.12 the optimized geometries of the four complexes are illustrated with selected bond lengths and bond angles summarized in Table 3.11. All four complexes showed a square planar geometry formed by the two C atoms from the carbonyl groups and the two chelating atoms of the L,L'-BID ligands.

In the comparison of the published crystal structures of [Rh($CH_3COCHCOCH_3$)$(CO)_2$][22] and [Rh($CH_3COCHCNPhCH_3$)$(CO)_2$] **2b**[23] with the theoretically determined DFT optimized geometry, it can be seen that there is very little difference between the selected bond distances. All the differences are less than 0.02 Å, therefore the correlation between the two is considered

to be good. The Θ_1 bond angle shows a very small, negligible difference ($\Delta\Theta_1 = 0.1^o$) and the Θ_2 bond angle showed a more noticeable difference ($\Delta\Theta_2 = \sim 2^o$) between the experimental and DFT calculated values. These deviations are attributed to the fact that the calculations are performed for an ideal gas phase however the crystal data display the solid state structures.

Table 3.11: Selected PW91/TZP DFT calculated bond lengths (Å) and bond angles (deg) of the [Rh(L,L'-BID)(CO)$_2$] complexes. The symbols used for bond lengths and angles (deg) are shown in Figure 3.12.

Complex	**a**	**b**	**c**	**d**	**Θ_1**
[Rh($CH_3COCHCOCH_3$)(CO)$_2$]	1.289 (1.277)*	1.288 (1.285)*	2.051 (2.040)*	2.051 (2.044)*	90.8 (90.8)*
[Rh($CH_3COCHCNHCH_3$)(CO)$_2$] **2a**	1.326	1.293	2.038	2.052	89.0
[Rh($CH_3COCHCNPhCH_3$)(CO)$_2$] **2b**	1.336	1.293	2.078 (2.058)**	2.047 (2.032)**	90.5 (90.6)**
[Rh($CH_3CNPhCHCNPhCH_3$)(CO)$_2$] **2c**	1.341	1.340	2.076	2.079	89.9
	e	**f**	**g**	**h**	**Θ_2**
[Rh($CH_3COCHCOCH_3$)(CO)$_2$]	1.858 (1.831)*	1.858 (1.831)*	1.157 (1.144)*	1.157 (1.155)*	89.9 (88.9)*
[Rh($CH_3COCHCNHCH_3$)(CO)$_2$] **2a**	1.845	1.883	1.161	1.157	90.7
[Rh($CH_3COCHCNPhCH_3$)(CO)$_2$] **2b**	1.858 (1.841)*	1.874 (1.866)*	1.159 (1.143)*	1.157 (1.142)*	88.2 (86.5)*
[Rh($CH_3CNPhCHCNPhCH_3$)(CO)$_2$] **2c**	1.874	1.875	1.158	1.158	85.1

*Values obtained from published literature.[22]

** Values obtained from published literature.[23]

From Table 3.11, it can be seen that the C-N bond distance, **a**, and the Rh-N bond distance, **c**, increase as the electronegativity of the chelating atom decreases and the stabilizing effect of the group attached to the N atom increases. The [Rh($CH_3COCHCOCH_3$)(CO)$_2$] complex has an **a** value of 1.289 Å and a **c** value of 2.051 Å. When the chelating atom is changed to an N atom, the **a** and **c** values change to 1.326 Å and 2.038 Å respectively. With a phenyl ring attached to the N atom, as with complex [Rh($CH_3COCHCNPhCH_3$)(CO)$_2$], the bond lengths **a** and **c** increase to 1.336 Å and 2.078 Å respectively. This is due to the increased stabilization afforded by the phenyl ring's delocalized electron density. When both the chelating atoms are N atoms with phenyl rings attached as in the [Rh($CH_3CNPhCHCNPhCH_3$)(CO)$_2$] complex, the bond

[22]F. Hug, A.C. Skapski, *J. Cryst. Mol. Struct.*, 1974, **4**, 411-418, CSD reference code ACABRH02.

[23]G.J.S. Venter, G. Steyl, A. Roodt, *J. Coord. Chem.,* 2014, **67**, 176-193

length **a** increases to 1.341 Å and the **c** bond length remains relatively unchanged at 2.076 Å for reasons similar to the [Rh($CH_3COCHCNPhCH_3$)$(CO)_2$] complex. The **b** lengths increase as the electron density across the L,L'-BID ligand increases due to the type of atoms involved. The less electronegative chelating atom, N, and the addition of phenyl rings to the system cause an increase in the electron density which in turn increases the bond lengths.

The two carbonyl group bond lengths shows deviations between symmetrical and asymmetrical L,L'-BID ligands coordinated to the Rh atom. The C-O bond lengths show very little difference between them however the most notable difference is in the Rh-C atoms referred to as **e** and **f** in Figure 3.12.

The Rh-dicarbonyl complexes containing symmetrical ligands $[CH_3COCHCOCH_3]^-$ and $[CH_3CNPhCHCNPhCH_3]^-$ have **e** and **f** values of 1.858 Å and ~1.874 Å respectively. The Rh-dicarbonyl complexes containing asymmetrical ligands $[CH_3COCHCNHCH_3]^-$ and $[CH_3COCHCNPhCH_3]^-$ have **e** values of 1.845 Å and 1.858 Å and **f** values of 1.883 Å and 1.874 Å respectively. These slight differences between the **e** and **f** values are due to the *trans* effect of the N atom and the group attached to the N atom. The increased electron density that arises from the N atom and it's group/atom cause an increase in the bond length of the group attached to the Rh centre *trans* with respect to the N atom, however the difference between the **e** and **f** values is negligible (~0.02 Å).

Table 3.12: PW91/TZP DFT calculated and experimentally determined CO stretching frequencies of the [Rh(L,L'-BID)$(CO)_2$] complexes.

Complex	**Calculated** (cm^{-1})		**Experimental** (cm^{-1})	
[Rh($CH_3COCHCNHCH_3$)$(CO)_2$] **2a**	1960.3	2024.6	1971.0	2044.1
[Rh($CH_3COCHCNPhCH_3$)$(CO)_2$] **2b**	1964.8	2026.5	1997.7	2056.0
[Rh($CH_3CNPhCHCNPhCH_3$)$(CO)_2$] **2c**	1943.5	2015.7	2055.6, 2046.7, 1992.1, 1977.79	

Table 3.12 contains both the calculated and experimental CO stretching frequencies of the dicarbonyl complexes. It can be seen that the values differ somewhat (10 cm^{-1} – 40 cm^{-1})

between the theoretically determined and the experimentally measured values, due to the calculated values being under ideal, gaseous, conditions.

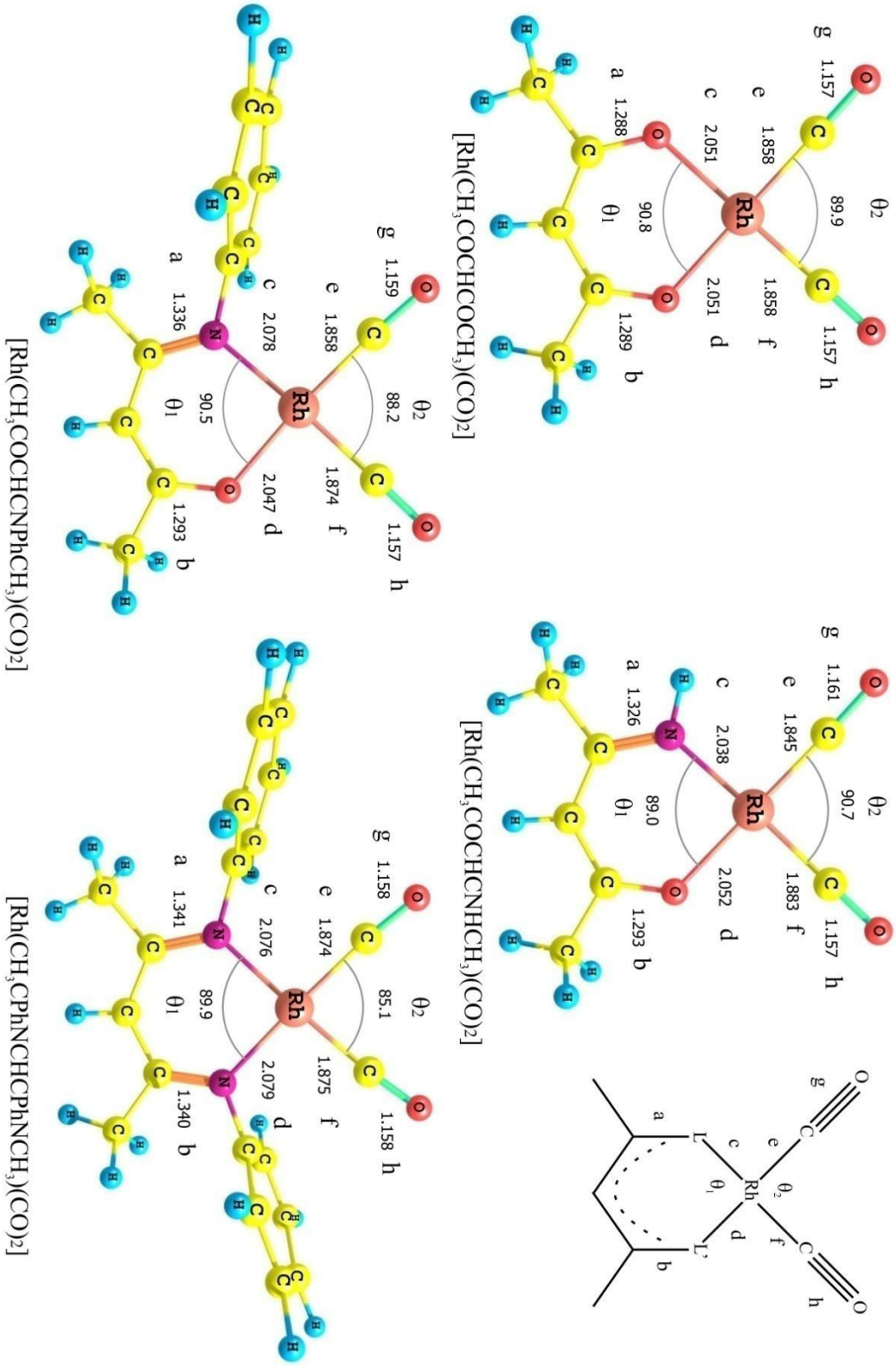

Figure 3.12: A comparison of the four [Rh(L,L'-BID)$(CO)_2$] complexes calculated *via* DFT illustrating various bond distances and bonding angles.

3.3 [Rh(L,L'-BID)(CO)(PPh_3)] complexes with (L,L') = (O,NH) or (O,NPh)

The synthesis and characterizations of the phosphine containing [Rh(L,L'-BID)(CO)(PPh_3)] complexes [Rh($CH_3COCHCNHCH_3$)(CO)(PPh_3)] **3a** and [Rh($CH_3COCHCNPhCH_3$)(CO)(PPh_3)] **3b** are presented in this section.

3.3.1 Synthesis

Synthesizing the triphenylphosphine containing Rh complexes were done similarly to the method of various researchers.[4,24,25] The slow addition of the triphenylphosphine hexane solution to the dicarbonyl Rh complex hexane solution yielded tiny bubbles of CO gas forming during the reaction. The reaction was left approximately 5 minutes, until no more bubbles were formed, and the flask then left at room temperature, with a slight draft in open air. The crystallization of the final products were similar to the dicarbonyl complexes. The general synthesis method is seen in Scheme 3.4. The purity of the complexes was high as can be seen from the NMR and IR spectra in Appendix A and Appendix B. It was not possible to synthesize the [Rh($CH_3CNPhCHCNPhCH_3$)(CO)(PPh_3)] **3c** complex, even when using PPh_3 in a large excess, only the starting [Rh($CH_3CNPhCHCNPhCH_3$)$(CO)_2$] **2c** complex was obtained.

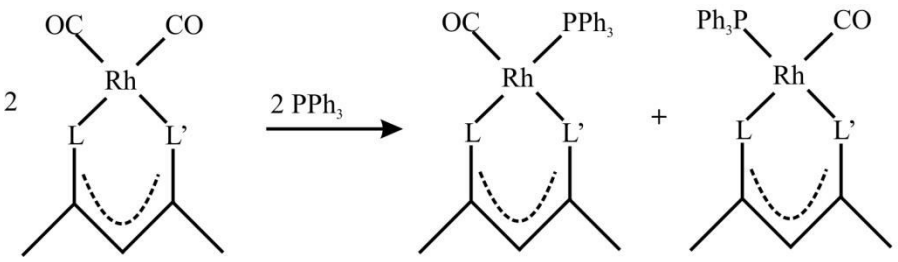

Scheme 3.4: General reaction scheme for the synthesis of [Rh(L,L'-BID)(CO)(PPh_3)] complexes.

[24]M.M. Conradie, J. Conradie, *Inorg. Chim.Acta*, 2008, **361**, 208-218

[25]G.J. Lamprecht, J.C. Swarts, J. Conradie, J.G. Leipoldt, *Acta Cryst.*, 1993, **C49**, 82-84

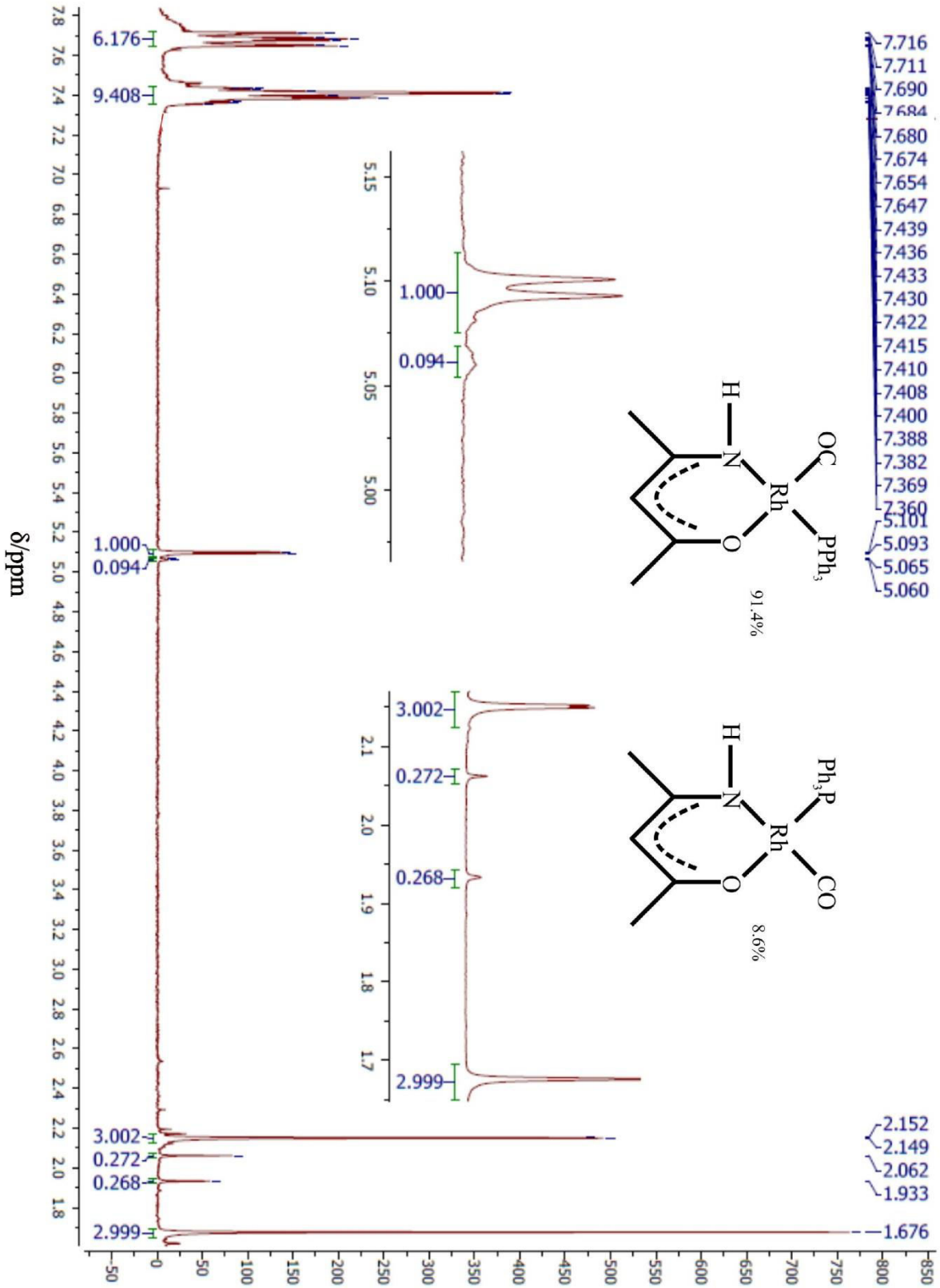

Figure 3.13: A ^{1}H NMR spectrum of [Rh($CH_3COCHCNHCH_3$)(CO)(PPh_3)] **3a**.

In order to determine whether one or both of the possible isomers of the [Rh(L,L'-BID)(CO)(PPh_3)] are present, NMR spectroscopy was utilized to characterise the complexes. As an example a ^{1}H NMR spectrum of [Rh($CH_3COCHCNHCH_3$)(CO)(PPh_3)] **3a** is seen in Figure 3.13 with the ^{1}H NMR chemical shifts of the protons summarized in Table 3.13.

From **Table 3.13**, which contains the ^{1}H chemical shift values for all the complexes that contain the [$CH_3COCHCNHCH_3$]$^-$ ligand, it can be seen that when the [$CH_3COCHCNHCH_3$]$^-$ ligand coordinates to the Rh metal centre, the chemical shifts (all shifts) are moved more downfield. This is evident in both the [Rh($CH_3COCHCNHCH_3$)$(CO)_2$] **2a** and [Rh($CH_3COCHCNHCH_3$)(CO)(PPh_3)] **3a** complexes. The chemical shifts of [Rh($CH_3COCHCNHCH_3$)$(CO)_2$] **2a** are more downfield than for the [Rh($CH_3COCHCNHCH_3$)(CO)(PPh_3)] **3a** complex. This is due to the PPh_3 group that is bonded to the Rh metal centre in the latter. The PPh_3 group adds additional electron density to the complex structure, which causes a shielding effect. The peak splitting of the methine and the methyl group closest to the N atom, which is observed for both the dicarbonyl Rh complex **2a** and the monocarbonyl-phosphine Rh complex **3a,** is due to the coupling that occurs between the H atom attached to the N atom and each of the respective protons. The chemical shift for the proton bound to the N atom is not observed.

Table 3.13: ^{1}H NMR chemical shifts (ppm) of the [$CH_3COCHCNHCH_3$] **1a** ligand, [Rh($CH_3COCHCNHCH_3$)$(CO)_2$] **2a** and [Rh($CH_3COCHCNHCH_3$)(CO)(PPh_3)] **3a** complexes.

Complex	**Isomer**	**Methine (C-H)**	**Methyls (CH_3)**	**Phenyl range**
[$CH_3COCH_2CNHCH_3$] **1a**	---	5.045 (s)	2.045 (s) 1.922 (s)	---
[Rh($CH_3COCHCNHCH_3$)$(CO)_2$] **2a**	---	5.364/5.293 (d, J_{HH} = 2.311 Hz)	2.175/2.172 (d, J_{HH} = 0.74 Hz) 2.106 (s)	---
[Rh($CH_3COCHCNHCH_3$)(CO)(PPh_3)] **3a**	Isomer A	5.101/5.093 (d, J_{HH} = 2.43 Hz)	2.152/2.149 (d, J_{HH} = 0.93 Hz) 1.676 (s)	7.7153-7.3524 (m)
	Isomer B	5.065/5.060 (d, J_{HH} = 2.11 Hz)	2.062 (s) 1.933 (s)	7.7153-7.3524 (m)

From Figure 3.13 it can be seen that the second isomer for the [Rh($CH_3COCHCNHCH_3$)(CO)(PPh_3)] **3a** complex is only present at 8.6% abundance. This agrees well with the theoretically calculated (PW91/TZP with chloroform as solvent taken into account) amount of the second isomer at 3.5%, see Section 3.3.3. For [Rh($CH_3COCHCNPhCH_3$)(CO)(PPh_3)] **3b** only one isomer was observed on NMR.

In Table 3.14, which contains the chemical shifts of both the phosphine complexes, it can be seen that there is a definite difference between the ^{1}H resonance peak positions for the protons attached to the ligand coordinated to the Rh metal centre. This effect can be seen in Figure 3.14 which contains the overlay of the ^{1}H NMR spectra. The chemical shift for the proton bound to the N atom is not observed.

Table 3.14: ^{1}H NMR chemical shifts (ppm) for the indicated [Rh(L,L'-BID)(CO)(PPh_3)] complexes.

	Methine (C-H)	**Methyls (CH_3)**	**Phenyl range**
[Rh($CH_3COCHCOHCH_3$)(CO)(PPh_3)]	5.43 (s)	2.20 (s), 1.62 (s)	7.35-7.80 (m)
[Rh($CH_3COCHCNHCH_3$)(CO)(PPh_3)] **3a** Isomer A	5.1005/5.0925 (d, J^4 = 2.43 Hz)	2.1520/2.1490 (d, J^4 = 0.93 Hz) 1.6758 (s)	7.7153-7.3524 (m)
[Rh($CH_3COCHCNHCH_3$)(CO)(PPh_3)] **3a** Isomer B	5.0635 (s)	2.0617 (s) 1.9335 (s)	7.7153-7.3524 (m)
[Rh($CH_3COCHCNPhCH_3$)(CO)(PPh_3)] **3b**	5.111 (s)	1.779 (s) 1.657 (s)	7.696-7.063 (m)

The IR analysis of the [Rh($CH_3COCHCNHCH_3$)(CO)(PPh_3)] **3a** complex shows only one major carbonyl stretching frequency at 1952.67cm^{-1} as can be seen in Figure 3.15. It was not possible to distinguish between the two isomers. The [Rh(L,L'-BID)(CO)(PPh_3)] complexes' carbonyl stretching frequencies display a similar trend as for the [Rh(L,L'-BID)$(CO)_2$] complexes namely that the addition of less electronegative atoms or groups (H = 2.1, Ph = 2.49) to the complex causes a decrease in the carbonyl stretching frequency as can be seen from Table 3.15. Comparing the [Rh(L,L'-BID)$(CO)_2$] stretching frequencies with those of the [Rh(L,L'-BID)(CO)(PPh_3)] complexes, it is seen that the triphenylphosphine containing complexes have carbonyl transmittance peaks ($\nu_{(CO)}$) at lower wavenumbers. This is indicative of a strengthening of the CO bonds due to the addition of the more electron rich triphenylphosphine ligand to the complex.

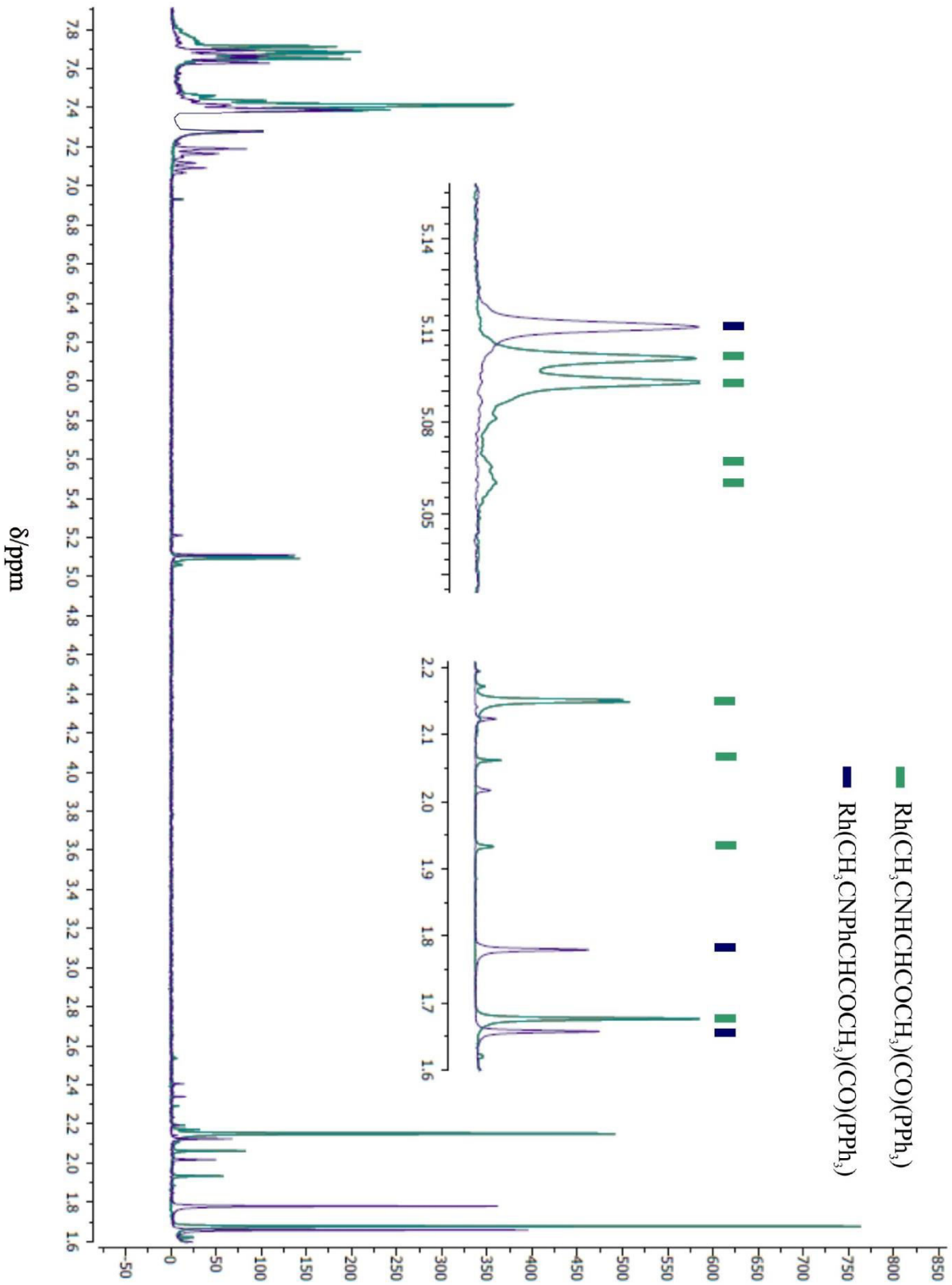

Figure 3.14: An overlay of the ^{1}H NMR spectra of the two [Rh(L,L'-BID)(CO)(PPh_3)] complexes.

Table 3.15: IR stretching frequencies ($\nu_{(CO)}$) of the carbonyl group on the [Rh(L,L'-BID)(CO)(PPh_3)] complexes.

Complex	$\nu_{(CO)}$ (cm^{-1})
[Rh($CH_3COCHCNHCH_3$)$(CO)_2$] **2a**	2044.13; 1971.02
[Rh($CH_3COCHCNHCH_3$)(CO)(PPh_3)] **3a**	1952.67
[Rh($CH_3COCHCNPhCH_3$)$(CO)_2$] **2b**	2058.98; 1997.69
[Rh($CH_3COCHCNPhCH_3$)(CO)(PPh_3)] **3b**	1966.60

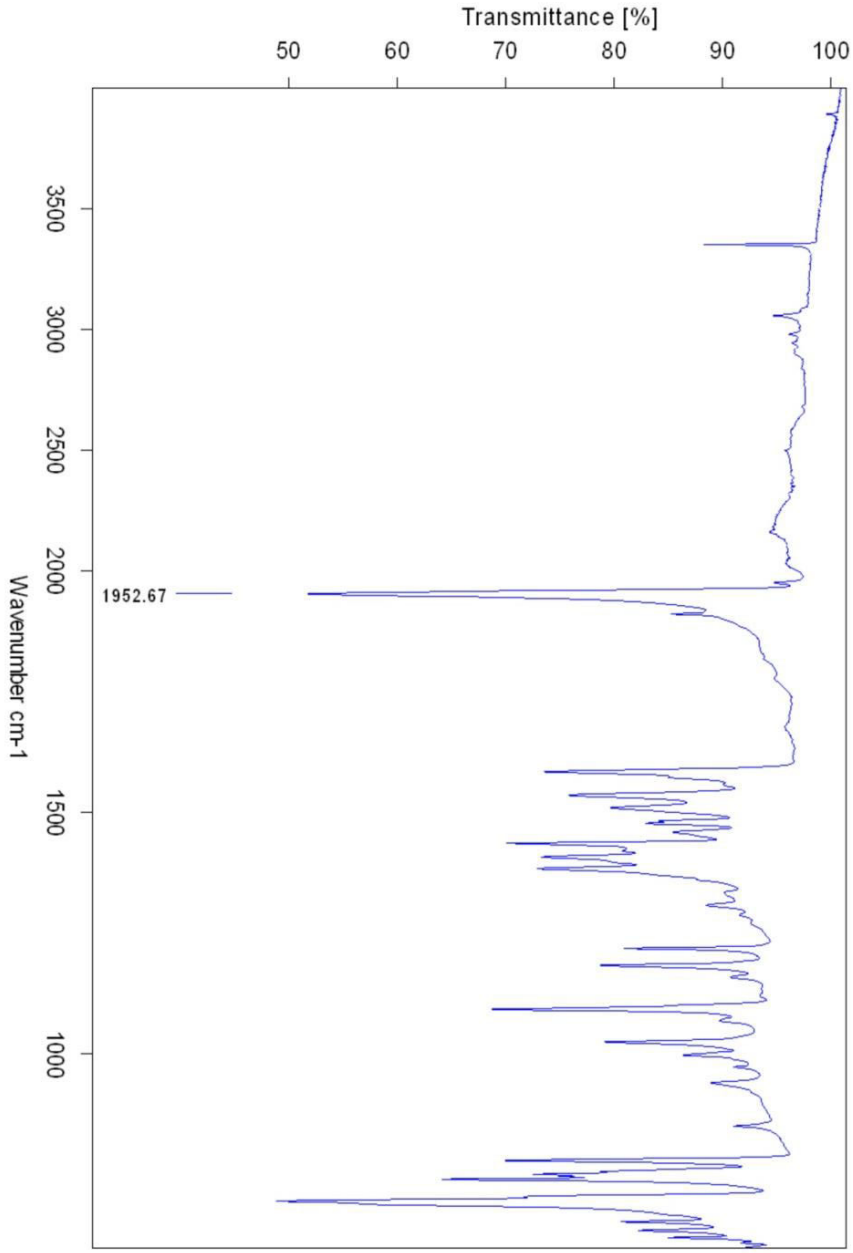

Figure 3.15: An IR spectrum of [Rh($CH_3COCHCNHCH_3$)(CO)(PPh_3)] **3a** with a carbonyl stretching frequency at 1952.67 cm^{-1}.

3.3.2 Cyclic Voltammetry (CV)

In the electrochemical analysis of [Rh(L,L'-BID)(CO)(PPh_3)] with L,L'-BID = $(CH_3CNHCHCOCH_3)^-$ and $(CH_3CNPhCHCOCH_3)^-$, an oxidation peak is observed at a potential > 0.2 V *vs* FcH/FcH^+, and a much smaller reduction peak more than 0.6 V away from the oxidation peak at a potential < -0.4 V *vs* FcH/FcH^+. A typical example is given in Figure 3.16. The rhodium(I) [Rh(L,L'-BID)(CO)(PPh_3)] complexes are d^8 complexes with electron occupation $d_{xy}^2 d_{xz}^2 d_{yz}^2 d_{z2}^2 d_{x2-y2}^0$, with the HOMO of the rhodium having mainly d_{z2} character, see the computational section 3.3.3.2 for the electronic structure of **3a**. Oxidation of a complex involves the removal of an electron from the HOMO of the complex, therefore the first oxidation observed for **3a** and **3b** is assigned to the oxidation of rhodium. The electrochemical oxidation of related [Rh(β-diketonato)(CO)(PPh_3)] complexes done under the same experimental conditions, indicated a two electron oxidation of the Rh(I) to an unstable Rh(III) radical and the small reduction peak to the reduction of the evolved Rh(III) radical to an as yet unidentified Rh(I) or Rh(II) complex.[26,27,28] Both the [Rh(L,L'-BID)(CO)(PPh_3)] complexes, with L,L'-BID = $(CH_3CNHCHCOCH_3)^-$ **3a** and $(CH_3CNPhCHCOCH_3)^-$ **3b**, showed similar electrochemical behaviour to the related [Rh(β-diketonato)(CO)(PPh_3)] complexes, [26,28] therefore the oxidation and reduction peaks observed for **3a** and **3b** is assigned accordingly.

The [Rh($CH_3CNHCHCOCH_3$)(CO)(PPh_3)] **3a** complex's results are used as a representative example to illustrate the observed behaviour. Figure 3.17 contains an overlay of the CVs of **3a** at various scan rates with the data summarized in Table 3.16. At slow scan rates, there is an oxidation peak present at *ca* 0.26 V *vs* FcH/FcH^+, however no reduction peak is observed in Figure 3.17. At higher scan rates the reduction peak appears at *ca* -0.6 V *vs* FcH/FcH^+. In order to determine the dependence of the reduction peak on the oxidation peak, the following electrochemical experiments were performed with the results illustrated in Figure 3.18. The CV scans were initiated in two directions namely one positive and one negative as seen in Figure 3.18. In the positive oriented scan the scans were initiated towards more positive potentials whereby the direction was reversed towards more negative potentials and the direction reversed again until the endpotential was reached. From this positive oriented scan it is seen that the CV shows the typical Figure 3.18 curve for these kind of complexes, that is an oxidation

---

[26] D. Lamprecht, G.J. Lamprecht, *Inorg. Chim. Acta*, 2000, **309**, 72-76.

[27] J.J.C. Erasmus, J. Conradie, *Dalton Trans.*, 2013, **42**, 8655-8666.

[28] J. Conradie, J.C. Swarts, *Eur. J. Inorg. Chem.*, 2011, **13**, 2439–2449

peak is seen where the Rh(I) metal centre is oxidized and a reduction peak where the Rh(III) species is reduced. In the negative oriented scan the scans were initiated towards more negative potentials first after which the direction is reversed towards more positive potentials until a predetermined limit has been reached and the direction is reversed again until the endpotential is reached. In the negative oriented scan it can be seen that as the potential is decreased, the reduction peak does not appear. After the direction is reversed and the potential is increased to a certain point, the oxidation peak occurs as per the norm. With the second direction reversal the reduction peak appears at a specific negative potential. This shows the dependence of the reduction peak on the oxidation peak. This is described as follows: In the first scan in the negative direction there is no Rh(III) species present thus there is no reduction peak. When the direction is shifted to the positive potentials the Rh(I) molecules are oxidized. Upon the second reversal there is still a sufficient amount of Rh(III) species present near the electrode surface that can be reduced and the reduction peak is observed.

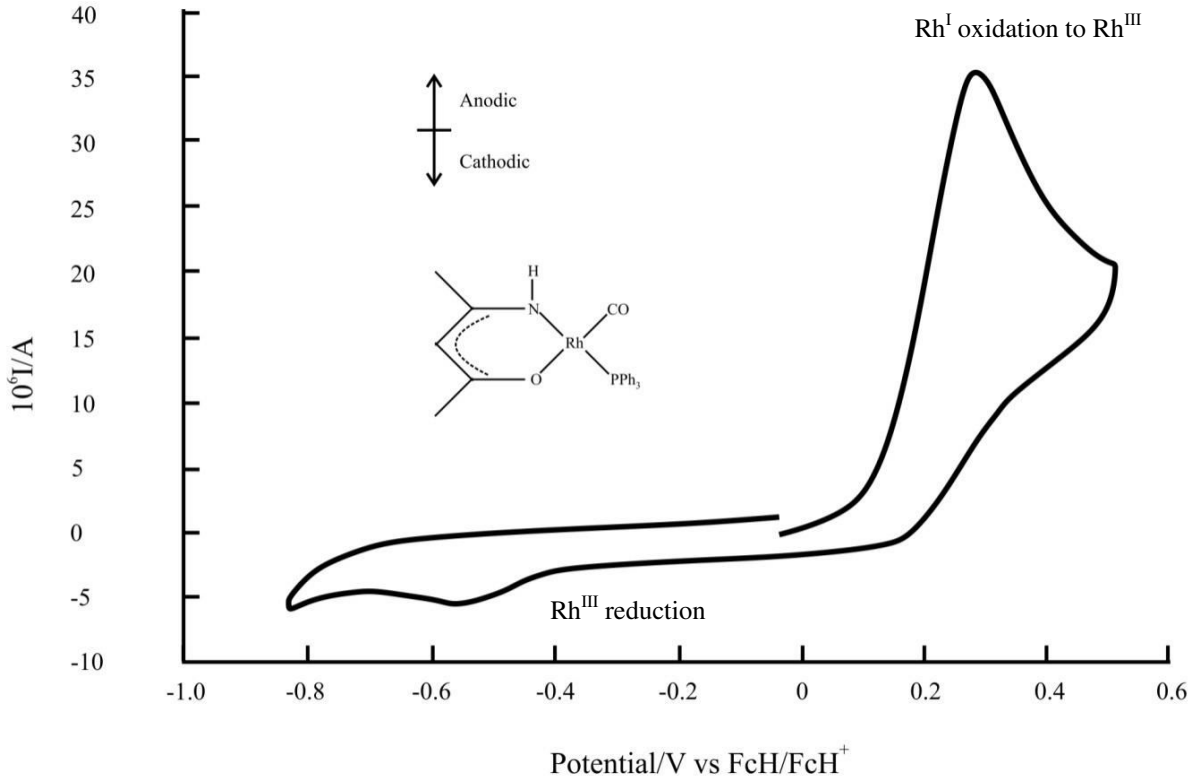

Figure 3.16: Cyclic Voltammogram of 0.002 M of [Rh($CH_3COCHCNHCH_3$)(CO)(PPh_3)] **3a** in dry acetonitrile with 0.1 M TBAHFP as supporting electrolyte, a glassy carbon working electrode, Pt auxiliary electrode and a Ag/$AgNO_3$ reference electrode. Scan rate of 0.2 V s^{-1} at 25°C.

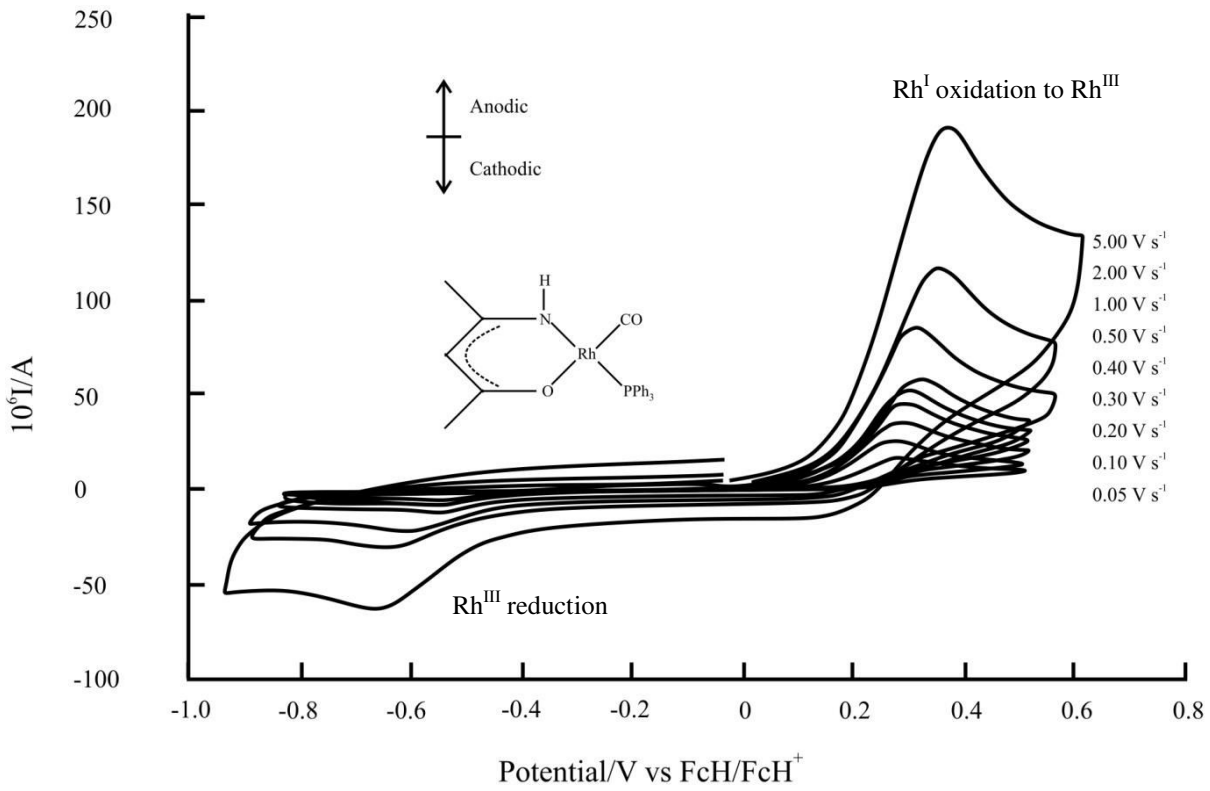

Figure 3.17: Cyclic voltammograms of 0.002 M [Rh($CH_3COCHCNHCH_3$)(CO)(PPh_3)] **3a** in dry acetonitrile with 0.1 M TBAHFP as supporting electrolyte, a glassy carbon working electrode, a Pt auxiliary electrode and a Ag/$AgNO_3$ reference electrode, with scan rates ranging from 0.05 V s^{-1} to 5.0 V s^{-1}. All measurements were done at 25°C.

The peak currents of the anodic and cathodic peaks of the [Rh($CH_3CNHCHCOCH_3$)(CO)(PPh_3)] **3a** complex are not the same, as seen in Table 3.16. This shows that the redox process is chemically irreversible, since the peak current ratio show large deviation from the ideal of unity. The peak oxidation and peak reduction currents are linear proportional to the square root of the scan rate as illustrated in Figure 3.20 a. This linearity according to the Randles-Sevcik equation indicates that the oxidation and reduction processes of the Rh complex are diffusion controlled.

The peak potential separation between the anodic and cathodic processes is in excess of 0.8 V. This deviates largely from the accepted peak separation of 0.08 V for an electrochemical reversible process. Therefore the oxidation and reduction processes are electrochemically irreversible.[27]

The oxidized Rh(III) radical generated is unstable in a square planar geometry. It has been proposed for related [Rh(β-diketonato)(CO)(PPh_3)] complexes that the Rh(III) complex relieves the instability by the possible coordination of solvent molecules to the apical positions of the

metal centre to create an octahedral geometry, thereby stabilizing it.[26,28] The observed reduction peak is therefore due to the Rh(III)-solvent adduct. Due to diffusion of the Rh(III)-solvent adduct that is formed during oxidation away from the electrode surface, the observed reduction is much smaller than the oxidation. The diffusion rate may be higher than the scan rate at low scan rates and only at higher scan rates some of the Rh(III)-solvent adduct is still available near the electrode surface to be reduced back to Rh(II) or Rh(I).[28]

Distinguishing between the oxidation potential of the two possible isomers of **3a** was not observed even at high scan rates. This could be due to a very fast equilibrium between the two isomers, or possibly the redox potentials of the two isomers are too close together to be distinguished at this time, or that one isomer dominates in the solution.

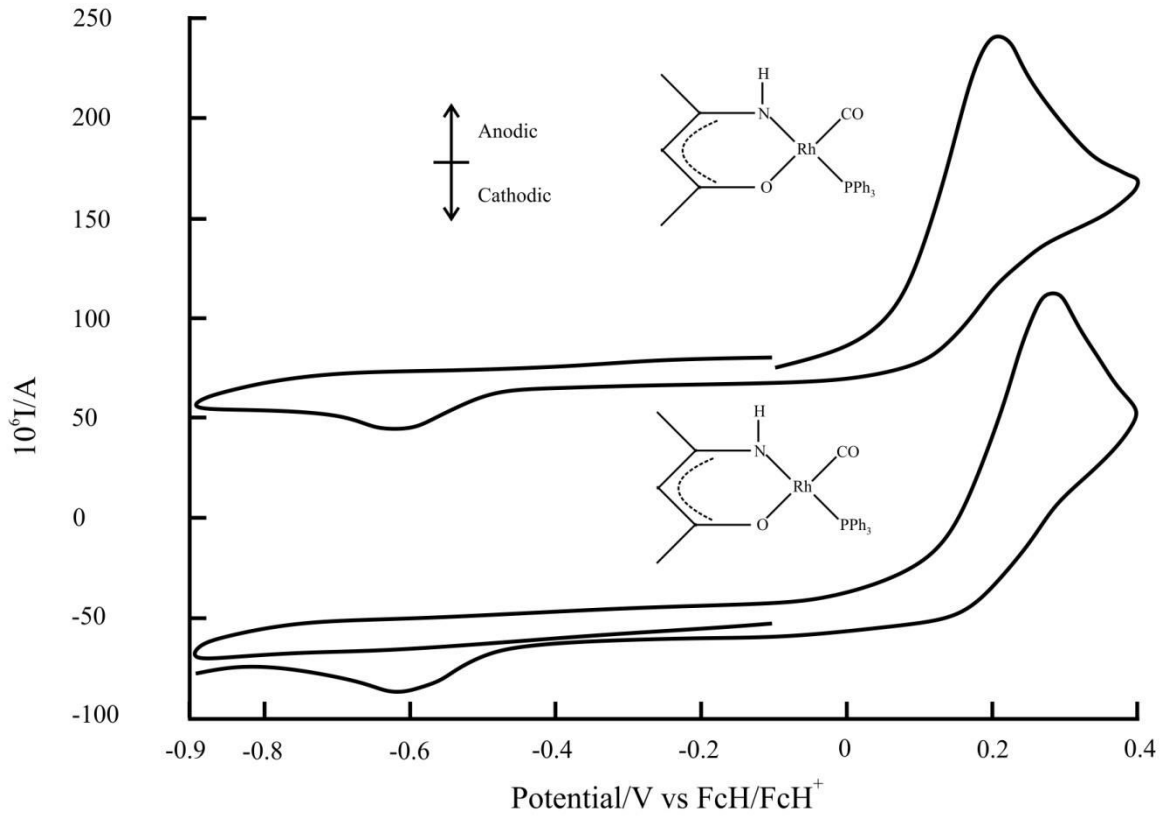

Figure 3.18: Scans initiated first in the positive (top) and then in the negative directions (bottom) of 0.002 M [Rh($CH_3COCHCNHCH_3$)(CO)(PPh_3)] **3a** in dry acetonitrile solution with 0.1 M TBAHFP as supporting electrolyte, utilizing a glassy carbon working electrode and a Ag/$AgNO_3$ reference electrode, at a scan rate of 0.1 V s^{-1}.

Table 3.16: Electrochemical parameters of the [Rh($CH_3CNHCHCOCH_3$)(CO)(PPh_3)] **3a** complex and the reduction potential (E_{pc}) of the free ligand ($CH_3CNHCHCOCH_3$) **1a** all referenced against FcH as internal standard in the acetonitrile mixture containing 0.1 M tetrabutylammonium hexafluorophosphate (TBAHFP) as supporting electrolyte.

v (V s^{-1})	E_{pa}(V)	E_{pc}(V)	i_{pa}(A)	i_{pc}(A)	ΔE (V)	i_{pc}/i_{pa}	LigandE_{pc}(V)
50	0.285	---	1.36E-05	0.00E+00	---	0.00	-2.951
100	0.261	---	2.22E-05	0.00E+00	---	0.00	-2.966
200	0.275	-0.544	3.02E-05	-2.30E-06	0.819	0.08	-2.974
300	0.278	-0.561	3.95E-05	-5.50E-06	0.839	0.14	-2.985
400	0.287	-0.568	5.80E-05	-5.50E-06	0.855	0.09	---
500	0.306	-0.584	4.90E-05	-4.50E-06	0.890	0.09	-3.006
1000	0.300	-0.593	7.20E-05	-1.35E-05	0.893	0.19	-3.016
2000	0.339	-0.635	9.90E-05	-1.40E-05	0.974	0.14	---
5000	0.356	-0.639	1.60E-04	-3.20E-05	0.995	0.20	---

In section 3.1.3 it was shown that the free ligands **1**a and **1b** are reduced at *ca* -2.7 V *vs* FcH/FcH^+. In an attempt to determine whether the coordinated ligand's electrochemical behaviour can be observable within the solvent window, scans were done with a significantly larger potential window with respect to the negative potential to accommodate both the Rh(I) complex and the ligand potentials as were determined earlier. Both complexes displayed similar results therefore only the [Rh($CH_3COCHCNPhCH_3$)(CO)(PPh_3)] **3b** complex's results are utilized as an example. In Figure 3.19 it can be seen that both the oxidation and reduction peaks of the [Rh($CH_3COCHCNPhCH_3$)(CO)(PPh_3)] **3b** are visible. The reduction peak of the ligand itself is also observed near the edge of the solvent potential window at *ca* -2.8 V *vs* FcH/FcH^+.

Table 3.17 gives a summary of the electrochemical data obtained at 0.100 V s^{-1}. The [Rh($CH_3COCHCOCH_3$)(CO)(PPh_3)] complex with two O atoms (more electronegative than N) has the higest reduction potential as expected. Comparing [Rh($CH_3COCHCNPhCH_3$)(CO)(PPh_3)] **3b** with [Rh($CH_3CNHCHCOCH_3$)(CO)(PPh_3)] **3a** we observe that **3b** with the more electronegative Ph group, has a higher reduction potential than **3a** with a H atom connected to N.

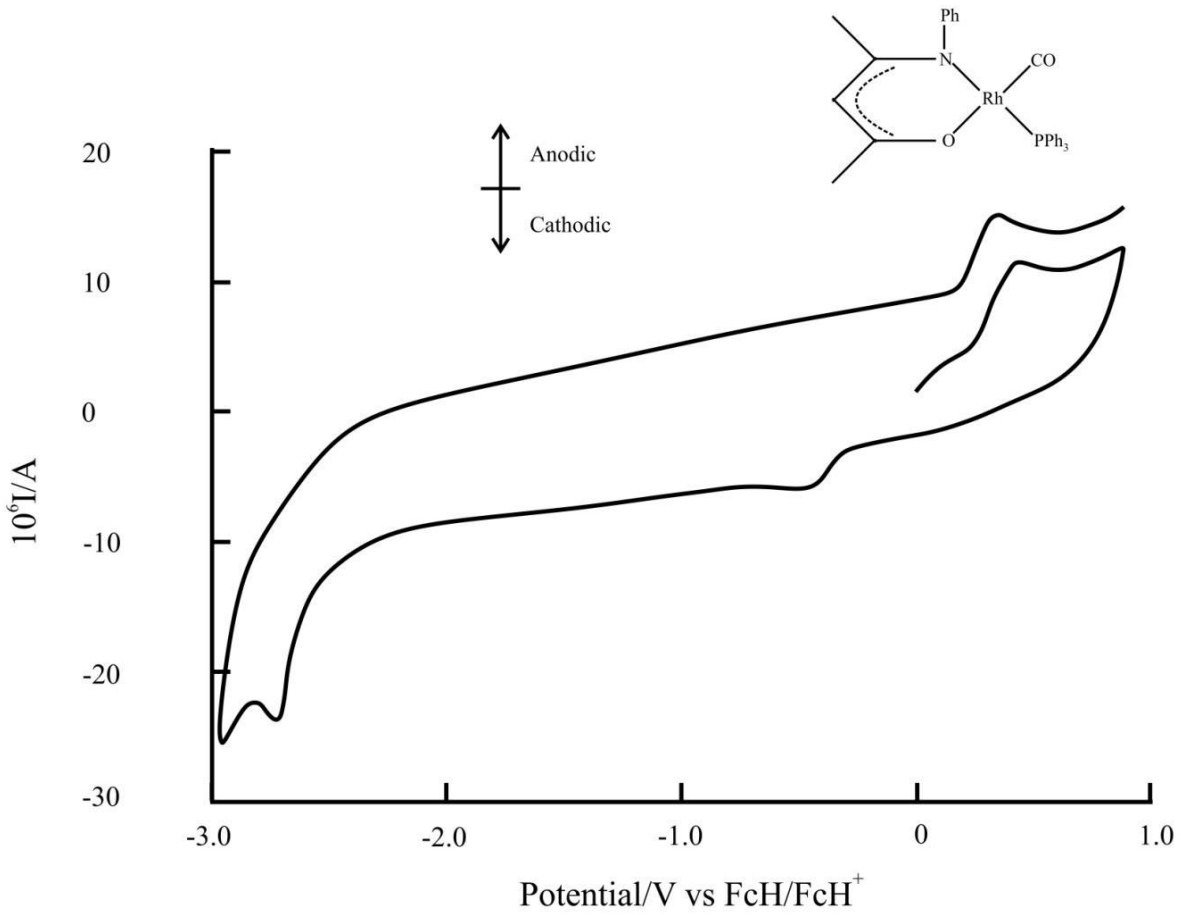

Figure 3.19: Cyclic Voltammogram of 0.002 M [Rh($CH_3COCHCNPhCH_3$)(CO)(PPh_3)] **3b** at a 5.0 V/s scan rate with a Ag/$AgNO_3$ reference electrode, glassy carbon working electrode and acetonitrile solvent with 0.1 M TBAHFP as supporting electrolyte.

Table 3.17: Electrochemical data at a scan rate of 0.1 V s^{-1} of [Rh($CH_3COCHCOCH_3$)(CO)(PPh_3)], [Rh($CH_3CNHCHCOCH_3$)(CO)(PPh_3)] **3a** and [Rh($CH_3COCHCNPhCH_3$)(CO)(PPh_3)] **3b**.

	E_{pa} (Rh) *vs* Fc/Fc^+/V
[Rh($CH_3COCHCOCH_3$)(CO)(PPh_3)]	0.357
[Rh($CH_3CNHCHCOCH_3$)(CO)(PPh_3)] **3a**	0.188
[Rh($CH_3COCHCNPhCH_3$)(CO)(PPh_3)] **3b**	0.247

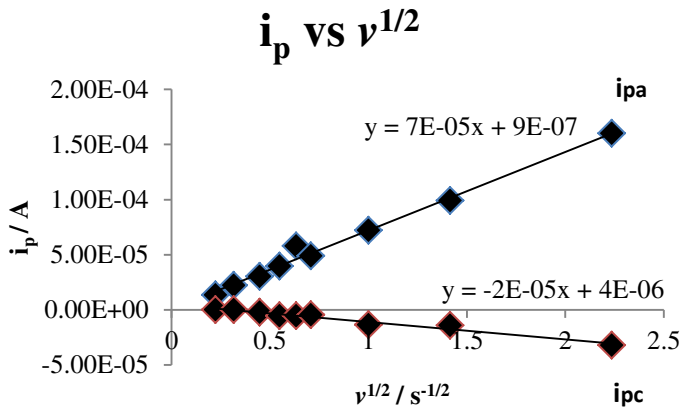

(a)

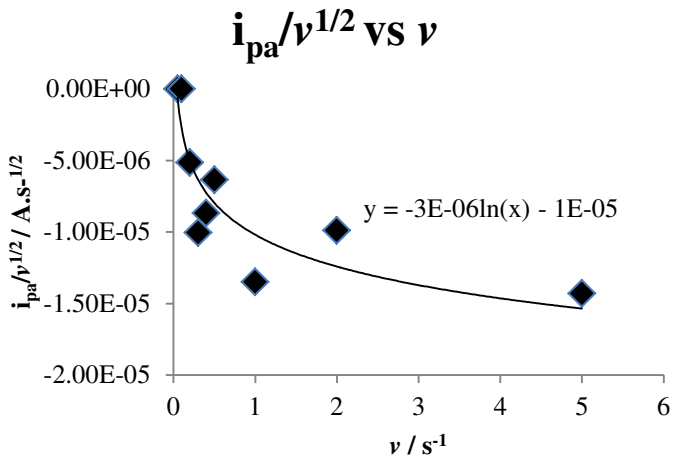

(b)

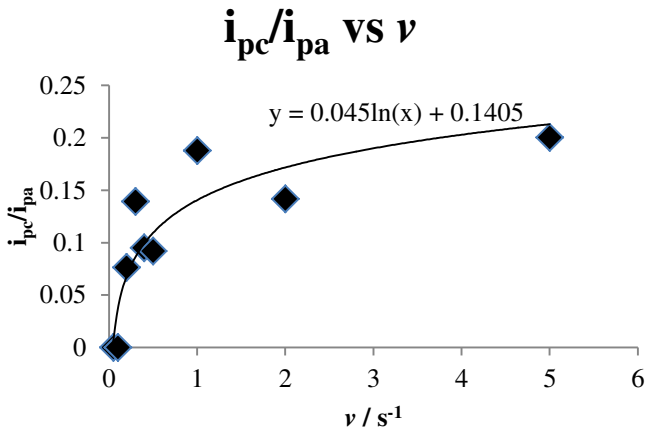

(c)

Figure 3.20: A collection of data comparisons for the electrochemical behaviour of [Rh($CH_3COCHCNHCH_3$)(CO)(PPh_3)] **3a** in acetonitrile with a glassy carbon working electrode, Ag/$AgNO_3$ reference electrode and a Pt auxiliary electrode. The analyte concentration was 0.002 M with a 0.1 M TBAHFP supporting electrolyte. Measurements were done at room temperature, 25°C. (a): current dependence on the $v^{1/2}$ (v = scan rate)(b): $i_{pa}/v^{1/2}$dependance on scan rate and(c): i_{pc}/i_{pa} dependence on scan rate.

Figure 3.20 shows different current and scan rate relationships for [Rh($CH_3COCHCNHCH_3$)(CO)(PPh_3)] **3a**. The following deductions can be made from the various parameters' dependence on scan rate for [Rh($CH_3COCHCNHCH_3$)(CO)(PPh_3)] **3a**.

Figure 3.20(a): The linearity of i_p, the peak current, *versus* $\nu^{1/2}$ for intercept at 0, within experimental error, indicates that the oxidation and reduction processes of the Rh complex is diffusion controlled, from the Randles-Sevcik equation.[31]

Figure 3.20(b): The decrease with scan rate of the $i_{pa}/\nu^{1/2}$ plots *versus* ν indicates that a reaction is coupled to the initial electron transfer are present.[29] It has previously been proposed that this coupled reaction is the coordination of two solvent molecules to the rhodium atom.[26]

Figure 3.20(c): This current ratio increases till 0.2, indicating that a maximum of *ca* 20% of the initially oxidized Rh(I) species may eventually be reduced, provided the coupled chemical reaction is extremely fast.

An attempt to determine whether the chemical instability of the solvated Rh(III) radical is the cause for the decreased reduction current by correlating the reduction current, i_{pc}, with parameters that estimate the electron density across the radical did not yield correlations. This is mainly due to the potential range between the complexes being too small and there are too few points from which to draw a conclusion.[30]

[29] R.S. Nicholson, I. Shain, *Anal. Chem.,* 1964, **36**, 706

[30] R. Freitag, J. Conradie, *Electrochim. Acta,* 2015, **158**, 418-426

3.3.3 DFT computational study: Rh(L,L'-BID)(CO)(PPh_3) with L,L'-BID = $(CH_3CNHCHCOCH_3)^-$, $(CH_3CNPhCHCOCH_3)^-$

In order to determine the optimized geometries and energies of all the possible [Rh(L,L'-BID)(CO)(PPh_3)] isomers, DFT calculations were utilized.

3.3.3.1 Geometry and isomer distribution

Table 3.18: PW91/TZP DFT calculated energies, structures and distribution probability of the [Rh(L,L'-BID)(CO)(PPh_3)] complexes.

Complex	Isomer	Structures	Energy (eV)	Relative Energy (eV)	Boltzmann Distribution (%)
[Rh($CH_3COCHCNHCH_3$)(CO)(PPh_3)] 3a	Isomer B	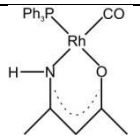	-334.48	0.09	3.5
	Isomer A	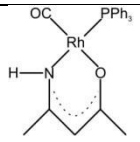	-334.57	0	96.5
[Rh($CH_3COCHCNPhCH_3$)(CO)(PPh_3)] 3b	NtransCO	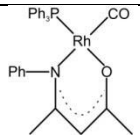	-402.31	0.4	0.0
	OtransCO	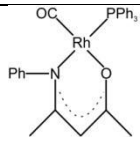	-402.71	0	100.0

From Table 3.18 the probability of the presence of an isomer with the N chelated atom being *trans* to the carbonyl group for both N containing Rh complexes is extremely low. This is in agreement with the ^1H NMR data in Section 3.3.1 where the second isomer for the [Rh($CH_3COCHCNHCH_3$)(CO)(PPh_3)] **3a** complex is present in 8.6% and only one isomer is observed for [Rh($CH_3COCHCNPhCH_3$)(CO)(PPh_3)] **3b**. The calculations indicate that the preferred orientation of the complexes is where the phenyl rings of the triphenylphosphine ligand and the groups or atoms attached to the N atom are far apart from each other as possible namely where the N atom is *trans* with respect to the P atom. From the calculations it is seen that there is a large distance (> 4.2 Å) between the phenyl rings of the phosphine group and the phenyl ring or H atom that is attached to the N atom, minimizing steric interactions between the

groups/atoms. This large separation between the groups allows for a lower overall energy of the complex.

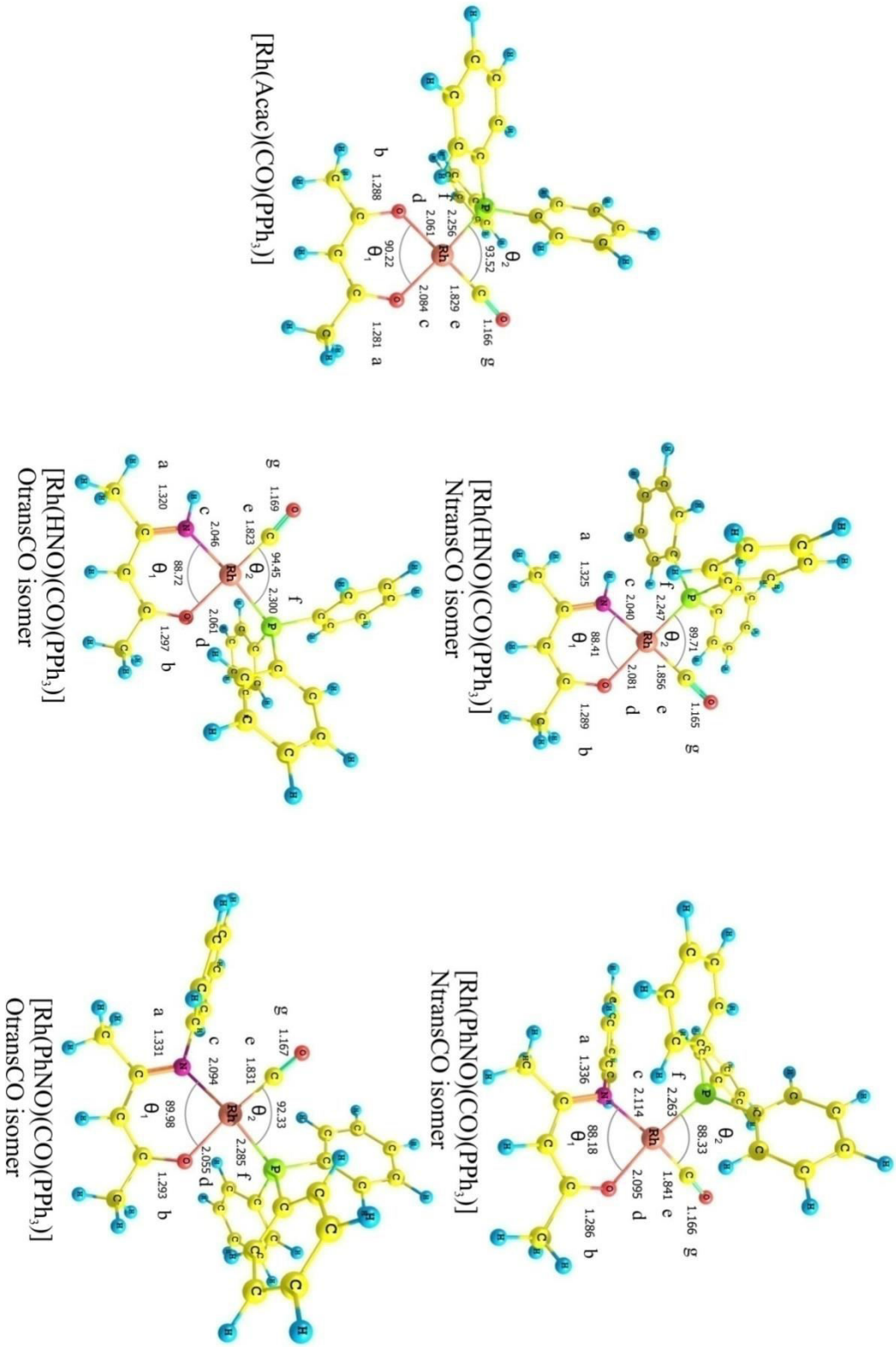

Figure 3.21: A comparison of the three indicated [Rh(L,L'-BID)(CO)(PPh_3)] complexes and the possible isomers calculated via PW91/TZP DFT illustrating various bond distances, in Angstrom, and bonding angles, in degrees.

Table 3.19: Selected PW91/TZP DFT calculated bond lengths and bond angles of the [Rh(L,L'-BID)(CO)(PPh_3)] complexes.

Complex	**Isomer**	**a**	**b**	**c**	**d**	**Θ_1**
[Rh($CH_3COCHCOCH_3$)(CO)(PPh_3)]	---	1.281	1.288	2.084	2.061	90.22
[Rh($CH_3COCHCNHCH_3$)(CO)(PPh_3)]	Isomer B	1.325	1.289	2.040	2.081	88.41
3a	Isomer A	1.320	1.297	2.046	2.061	88.72
[Rh($CH_3COCHCNPhCH_3$)(CO)(PPh_3)]	Isomer B	1.336	1.286	2.114	2.095	88.18
3b	Isomer A	1.331	1.293	2.094	2.055	89.98
	Isomer	**e**	**f**	**g**	**Θ_2**	
Rh($CH_3COCHCOCH_3$)(CO)(PPh_3)	---	1.829	2.256	1.166	93.52	
[Rh($CH_3COCHCNHCH_3$)(CO)(PPh_3)]	Isomer B	1.856	2.247	1.165	89.71	
3a	Isomer A	1.823	2.300	1.169	94.45	
[Rh($CH_3COCHCNPhCH_3$)(CO)(PPh_3)]	Isomer B	1.841	2.263	1.166	88.33	
3b	Isomer A	1.831	2.285	1.167	92.33	

Comparison between selected bond lengths and **Θ_1** and **Θ_2** bond angles are summarized in Table 3.19 shows that there are very small differences between the various complexes and their isomers (~0.04 Å).

The C-N distance referred to as **a**, shows that the distance increases through the effect of the less electronegative N atom and the group attached to it. In the B isomer of [Rh($CH_3COCHCNHCH_3$)(CO)(PPh_3)] **3a** the bond length is 1.325 Å; however in the A isomer the length is 1.320 Å. This is caused by the phosphine group in the A isomer. The three phenyl rings attached to the P atom cause a region of high stability for the delocalization and possible concentration of the electron density. This removes some of the density from the Rh metal centre and thus a slight decrease in the density available to the chelating atom of the L,L'-BID ligand trans to the phosphine group, causing a shortening in the bond lengths.

The second chelating atom, O, of the ligand with a C-O bond length referred to as **b**, also shows differences between the isomers again attributed to the groups trans to the O atom. In the A isomer the bond length **b** is 1.289 Å and in the A isomer the bond length is 1.297 Å. In the A isomer this is due to the C atom of the carbonyl group. The O atom is more electronegative than the C atom, which causes the electron density to accrue around the O atom and lengthening the bond distances.

The bond lengths of the chelating atoms to the Rh metal centre show the difference between the ligand effects. The Rh-N distance, **c**, shows that the phosphine group, which has greater electron density affects on the distance of the N atom, and its attached group, by increasing it slightly. The Rh-O distance, **d**, displays a more noticeable difference. The B isomer, with the phosphine group *trans* to the O atom of the ligand, has a much larger bond distance. This is due to the much larger contribution of electron density of the phosphine ligand, due to the *trans* influence it has, and the more electronegative O atom causes a concentration of the density from the Rh metal centre around the O atom, which increases the bond lengths.

The angle between the 2 chelating atoms and the Rh metal centre, $\mathbf{\Theta_1}$, shows that the steric influence of the phosphine atom's phenyl rings has an influence. In the B isomer, the group attached to the N atom is closer to the phenyl rings, which causes steric stress, pushing the N atom slightly inwards with respect to the L,L'-BID centre. Therefore the angle is slightly smaller. In the A isomer the N atom, and its group, and the phosphine group are *trans* to each other. Therefore there is very little steric stress and the angle is increased.

Considering the Rh-C, C-O carbonyl and Rh-P bond lengths referred to as **e**, **f** and **g** respectively as seen in Table 3.19. It can be seen that the *trans* influence of the atoms *trans* to the ligands do have a noticeable effect on the bond lengths. In the [Rh($CH_3COCHCNHCH_3$)(CO)(PPh_3)] **3a** complex the Rh-C bond distance is affected by the less electronegative N atom *trans* to it with an increased bond length in the B isomer due to the increased electron density. The same effect is seen in the [Rh($CH_3COCHCNPhCH_3$)(CO)(PPh_3)] **3b** complex. This effect is also seen in the C-O bond distance, **f**, for both the complexes as well. The Rh-P distance, **g**, shows very little difference though the isomers do have a slight change in the bond length as seen in the table.

The bond angle between the P, Rh and C atoms do differ between the isomers. This is due to the steric influence of the three phenyl rings and the chelated atom group that is *cis* to the P atom. Utilizing the [Rh($CH_3COCHCNHCH_3$)(CO)(PPh_3)] **3a** complex as an example it is seen that the B isomer has a bite angle of 89.71^o. This is a smaller angle than the A isomer with a bite angle of 94.45^o. This is due to the steric stress caused by the phenyl rings of the phosphine ligand interacting with the group attached to the N atom, which is *cis* with respect to the phosphine ligand. This pushes the N atom slightly inwards with respect to the L,L'-BID ligand centre.

Table 3.20: DFT calculated and experimentally determined CO stretching frequencies on an IR spectrum of the N containing [Rh(L,L'-BID)(CO)(PPh_3)] complexes.

Complex	**Isomer**	**Calculated (cm^{-1})**	**Experimental (cm^{-1})**
[Rh($CH_3COCHCNHCH_3$)(CO)(PPh_3)] **3a**	Isomer B	1967.00	1952.67
	Isomer A	1952.255	
[Rh($CH_3COCHCNPhCH_3$)(CO)(PPh_3)] **3b**	Isomer B	1962.487	1966.60
	Isomer A	1959.28	

Comparison between the calculated and experimental CO IR stretching frequencies shows that the [Rh($CH_3COCHCNHCH_3$)(CO)(PPh_3)] **3a** complex shows very good correlation with the DFT calculated preferred isomer, however the [Rh($CH_3COCHCNPhCH_3$)(CO)(PPh_3)] **3b** shows a slightly higher experimental frequency. There was no scaling factor used during the calculations.

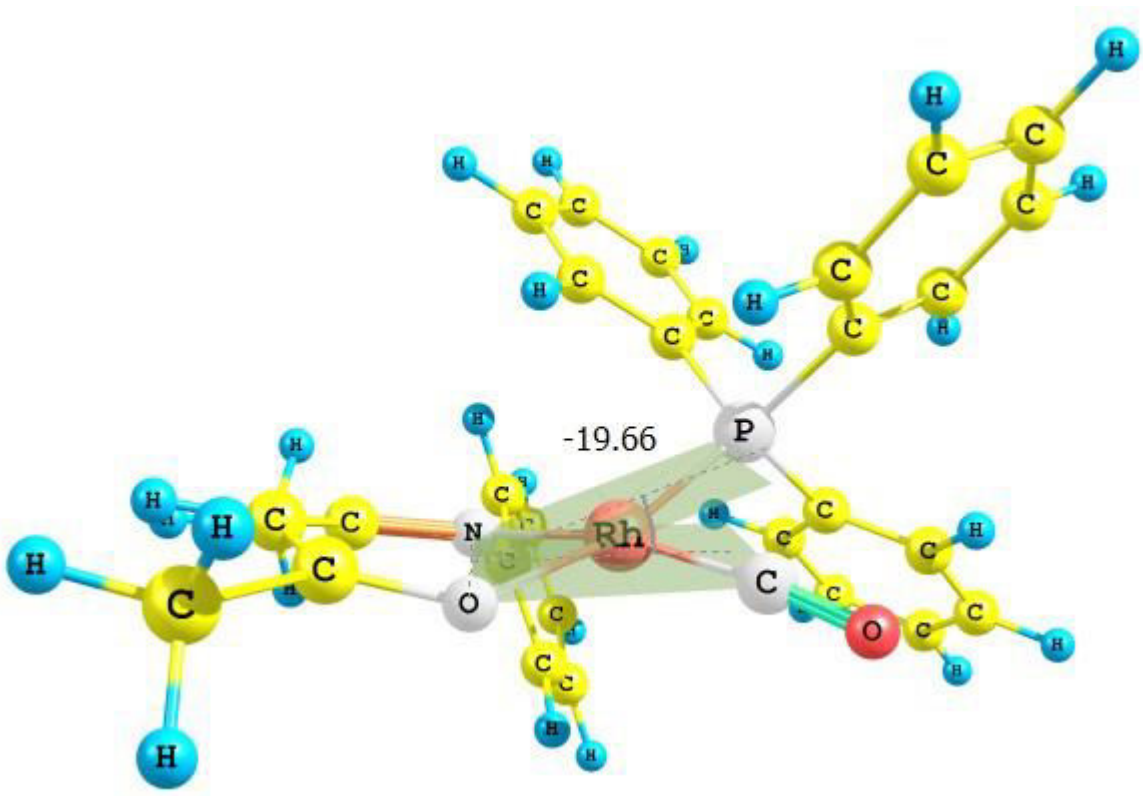

Figure 3.22: DFT calculated deviation of the PPh_3 group in the B isomer of the [Rh($CH_3COCHCNPhCH_3$)(CO)(PPh_3)] **3b** complex.

The [Rh($CH_3COCHCNPhCH_3$)(CO)(PPh_3)] **3b** B isomer's deviation from the typical square planar geometry is illustrated in Figure 3.22. There is a 19.66° displacement between the P atom and the plane created by the other N,O and C atoms. This is due to the steric stress created between the phenyl ring that is attached to the N atom and the phenyl rings attached to the P atom. This stress causes the P atom to be pushed out of the plane and therefore the geometry of the complex is changed to a distorted square planar geometry.

3.3.3.2 Electronic structure

Rhodium(I) [Rh(L,L'-BID)(CO)(PPh_3)] complexes are d^8 complexes with electron occupation $d_{xy}^2 d_{xz}^2 d_{yz}^2 d_{z2}^2 d_{x2-y2}^0$, as illustrated for [Rh($CH_3COCHCNHCH_3$)(CO)(PPh_3)] **3a** in Figure 3.23. The HOMOs of both **3a** and **3b** are mainly of rhodium d_{z2} character, see Figure 3.24 for **3b**.

HOMO-2 (d_{xy}^2) HOMO-1 (d_{xz}^2) HOMO (d_{z2}^2)

Figure 3.23: Selected Kohn-Sham frontier orbitals of the DFT PW91/TZP optimized geometry of the main isomer of [Rh($CH_3COCHCNHCH_3$)(CO)(PPh_3)] **3a**.

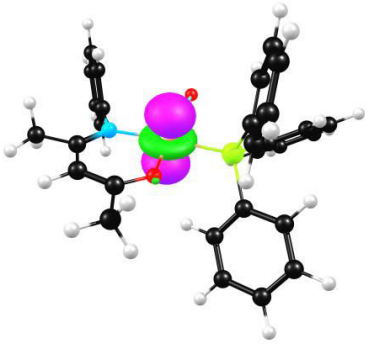

Figure 3.24: Kohn-Sham d_{z2}^2 HOMO of the DFT PW91/TZP optimized geometry of the main isomer of [Rh($CH_3COCHCNPhCH_3$)(CO)(PPh_3)] **3b**.

3.4 [Rh(L,L'-BID)(CO)(PPh_3)] complexes with (L,L') = (O,O).

The electrochemical analysis and a computational study of [Rh(L,L'-BID)(CO)(PPh_3)] with L,L'-BID = β-diketonato = $(C_4H_3SCOCHCOCPh)^-$ **M1**, $(C_4H_3SCOCHCOC_4H_3S)^-$ **M2** and $(C_4H_3SCOCHCOCF_3)^-$ **M3** is presented in this section.[31] These ligands will be abbreviated as bth, dtm and tta respectively.

3.4.1 Cyclic Voltammetry (CV)

The CVs of [Rh(β-diketonato)(CO(PPh_3) with β-diketonato = bth, dtm, tta are given in Figure 3.25. From Figure 3.25 it is seen that the different complexes, with different R,R' groups attached to the backbone of the β-diketone ligand, have different peak potentials, that are displayed in **Table 3.21**. It is also indicated that the anodic peak is the oxidation of the Rh(I) to a Rh(III) species and that the reduction peak is to a possible Rh(II) species.

In Figure 3.26 is an overlay the CVs of the multiple scan rates of [Rh(tta)(CO)(PPh_3)] **M3** showing that as the scan rates increase the peak oxidation potential shifts to a more positive value and the peak reduction potential shifts to a more negative value. The inequality of the peak currents indicate that the process is chemically irreversible and the large difference between the peak cathodic and peak anodic potentials (> 0.8 V) shows that the process is electrochemically irreversible. From Figure 3.26 it can also be seen that at very low scan rates there is an oxidation peak present, however almost no reduction peak whatsoever and at higher scan rates the size of the reduction peak increases. This is to be expected since the speed of diffusion of the radical or the proposed Rh(III)-solvent adduct formed during oxidation into the bulk solution, away from the electrode surface, is slowly overcome by the increased scan rate.

[31] H. Ferreira, M.M. Conradie, J. Conradie, *Electrochim. Acta*, 2013, **113**, 519-526

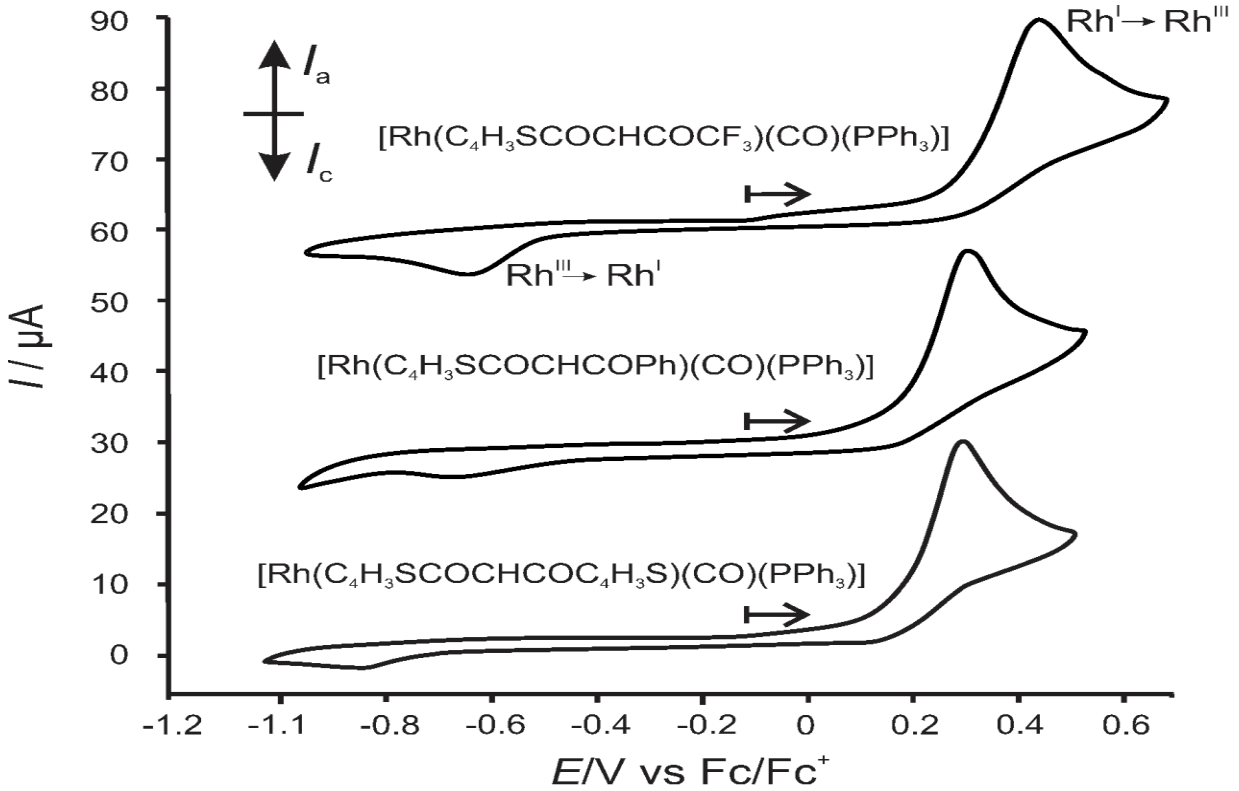

Figure 3.25: Overlay of the 0.002 M of [Rh(β-diketonato)(CO(PPh$_3$)] (with β-diketonato = bth **M1**, dtm **M2**, tta **M3**] complexes at scan rate 0.1 V s^{-1} in a solution of 0.1M TBAHFP in acetonitrile on a glassy carbon working electrode with a Ag/AgNO$_3$ reference electrode.

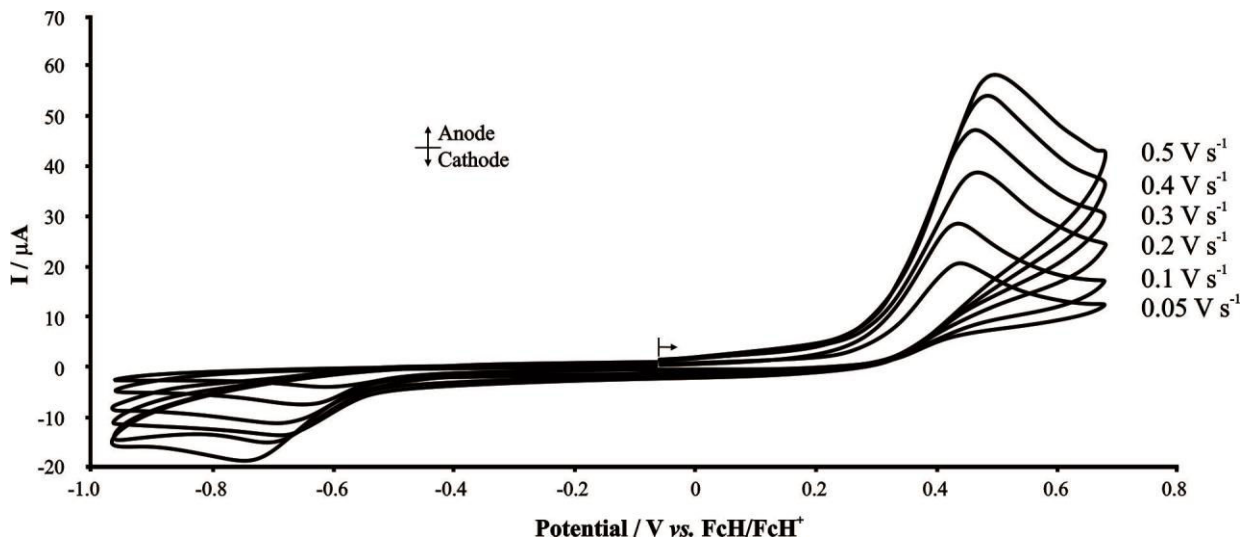

Figure 3.26: Cyclic voltammograms of 0.002 M [Rh(tta)(CO)(PPh$_3$)] **M3** in dry acetonitrile with 0.1 M TBAHFP as supporting electrolyte and a Ag/AgNO$_3$ reference electrode with scan rates ranging from 0.05 V s^{-1} to 0.5 V s^{-1}.

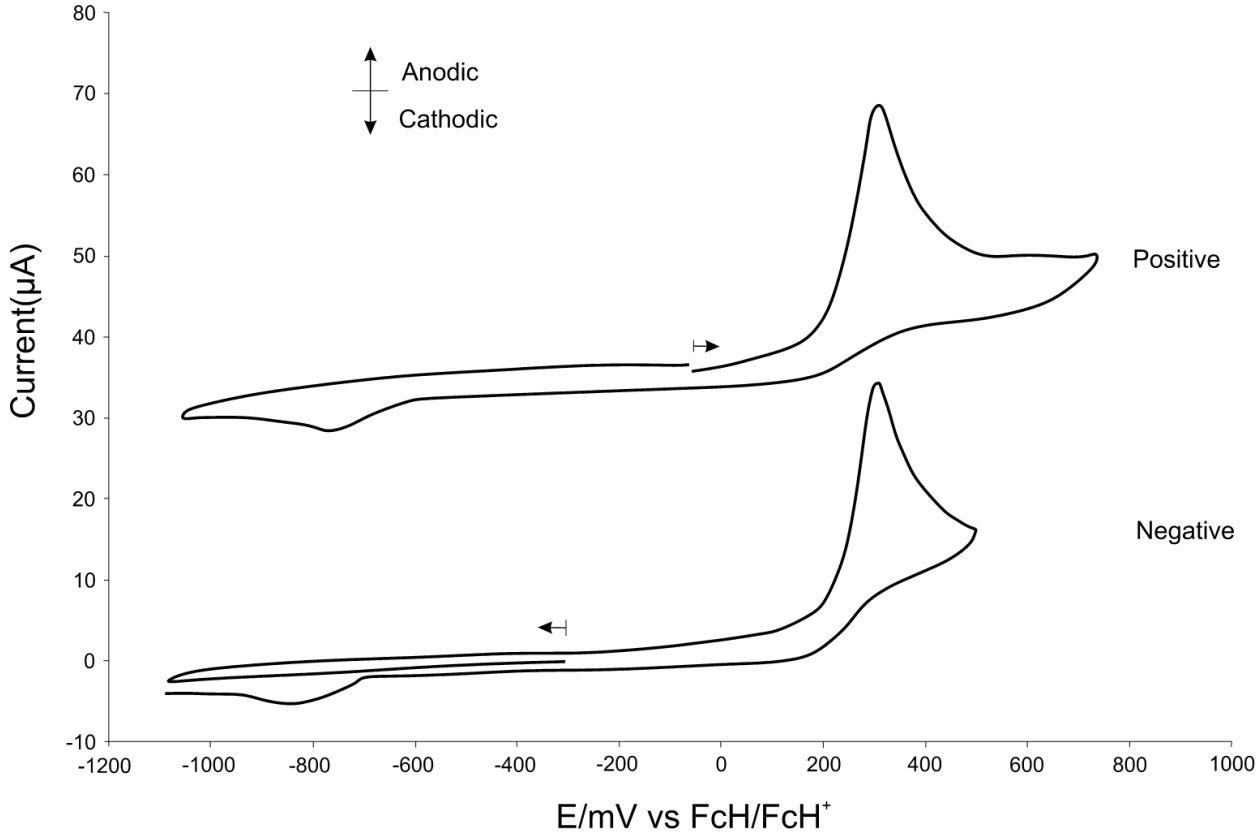

Figure 3.27: Scans initiated first in the positive and then in the negative directions of a 0.002 M [Rh(bth)(CO)(PPh_3)] **M1** in dry acetonitrile solution with 0.1 M TBAHFP as supporting electrolyte utilizing a glassy carbon working electrode and a Ag/$AgNO_3$ reference electrode at a scan rate of 0.1 V s^{-1}.

Figure 3.27 illustrates that the forward, or positive oriented, scan of a Rh complex shows no indication of the reliance of the reduction peak on the oxidation peak that is observed. However the reverse, or negative oriented, scan shows that with the first, reverse scan there is no peak, then with the second, forward scan there is the oxidation peak and then with the third and final reverse scan there is an anodic peak. Therefore it is concluded that the anodic peak is present only after the oxidation peak has been reached.

Figure 3.28 - Figure 3.30 shows different current and scan rate relationships for [Rh(tta)(CO)(PPh_3)] **M3**.

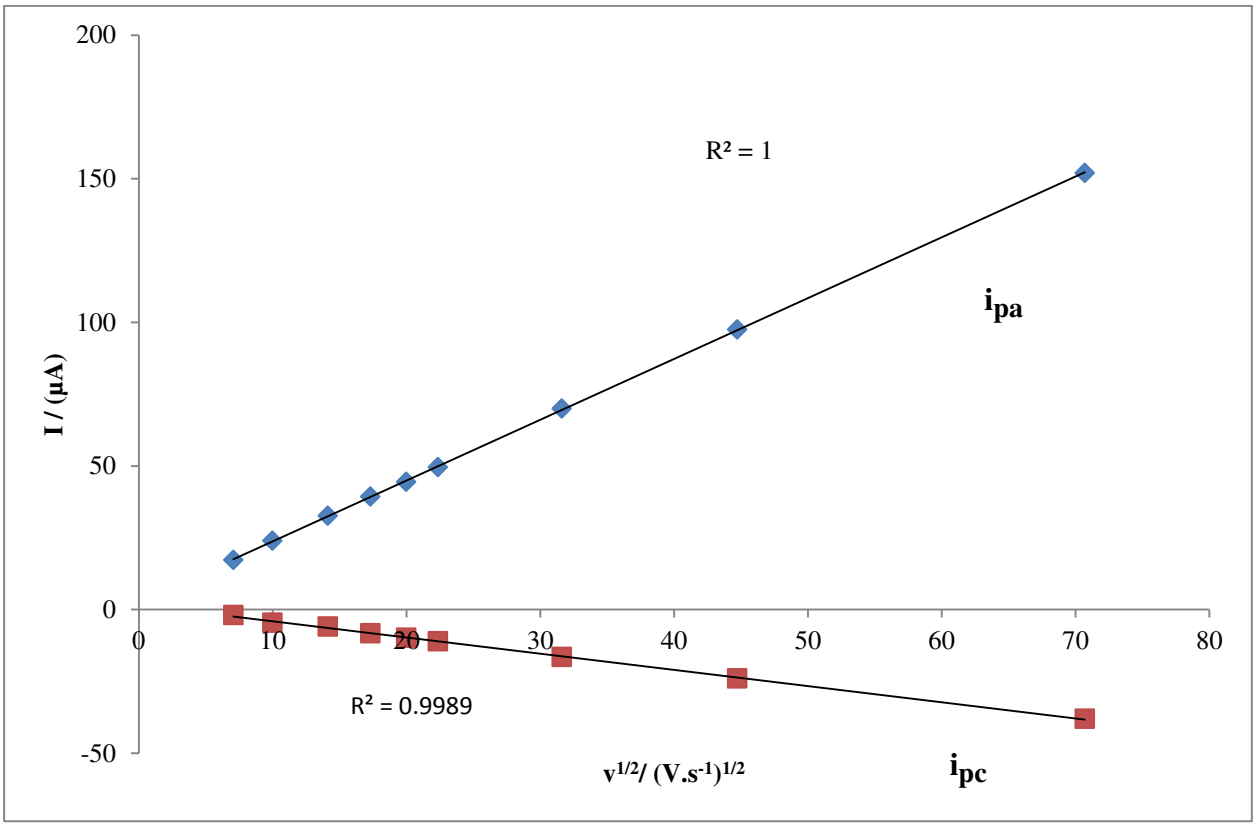

Figure 3.28: Peak current dependence on scan rate for [Rh(tta)(CO)(PPh_3)] **M3**. Blue points are i_{pa} and red points are i_{pc}.

The linearity with an intercept at 0, within experimental error, observed with Figure 3.28 for [Rh(tta)(CO)(PPh_3)] as representative example, indicates that the oxidation in the complexes from a Rh(I) species to a Rh(III) species is controlled by the diffusion of the complexes as seen in the Randles-Sevcik equation $i_p = (2.69X10^5)n^{1.5}AD^{0.5}C\nu^{0.5}$

where i_p = peak current (A), n being the number of exchanged electrons, A the electrode area (cm^2), ν scan rate ($V\ s^{-1}$), D the diffusion constant ($cm^2\ s^{-1}$) and C the bulk concentration (mol dm^{-3}) of the electroactive species.

The decreasing $i_{pa}/v^{1/2}$ as the scan rate increases, Figure 3.29, is a clear indication that there is a chemical reaction that is coupled with the initial electron transfer. Figure 3.26 shows that as the scan rates increase that the cathodic peak increases significantly and then gradually the increase starts to plateau. This shows that there is a possible maximum ratio between the two peak currents which arises from the chemical reaction evidenced in Figure 3.30.

Distinguishing between the two stereoisomers for [Rh(β-diketonato)(CO)(PPh_3)] (with β-diketonato = bth **M1**, tta **M3**] was not possible even at the very high scan rates possibly due to a very fast equilibrium between the two or perhaps the respective redox potentials are too close together to be distinguished at this time.

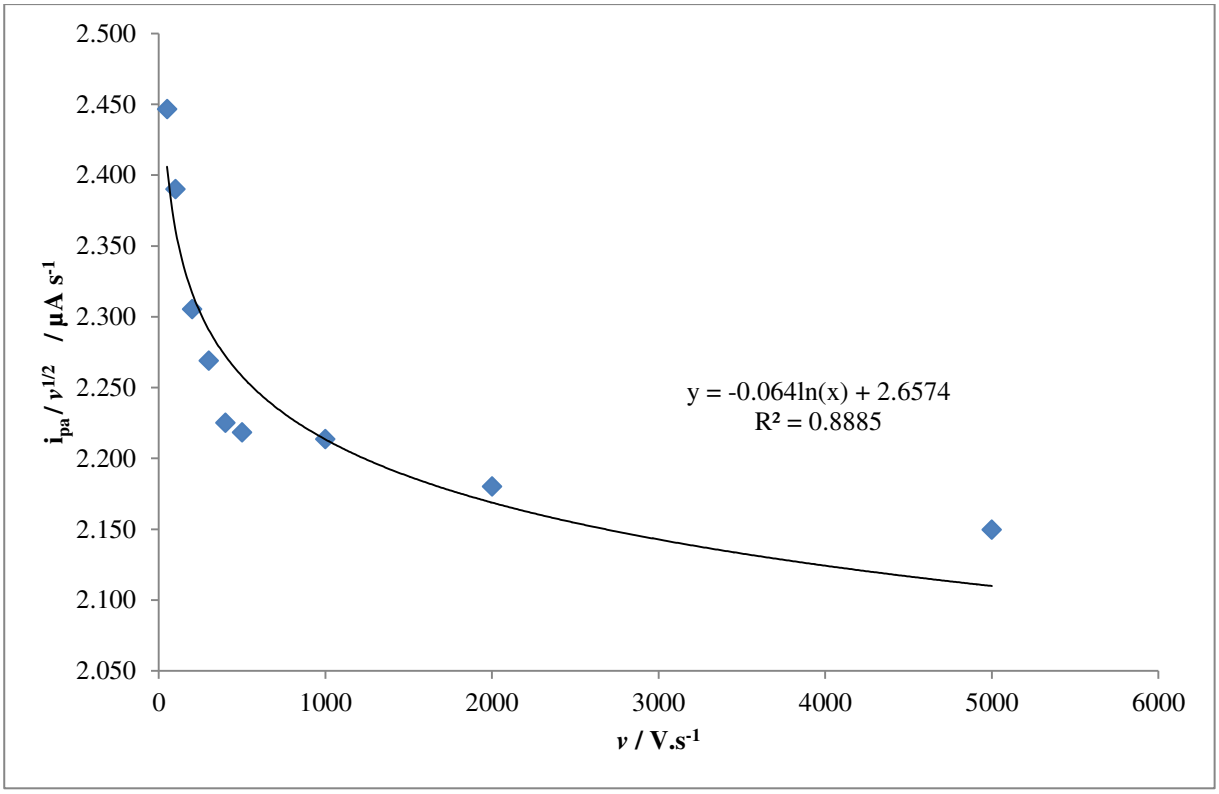

Figure 3.29: $i_{pa}/v^{1/2}$ dependance on the scan rate for [Rh(tta)(CO)(PPh_3)] **M3**.

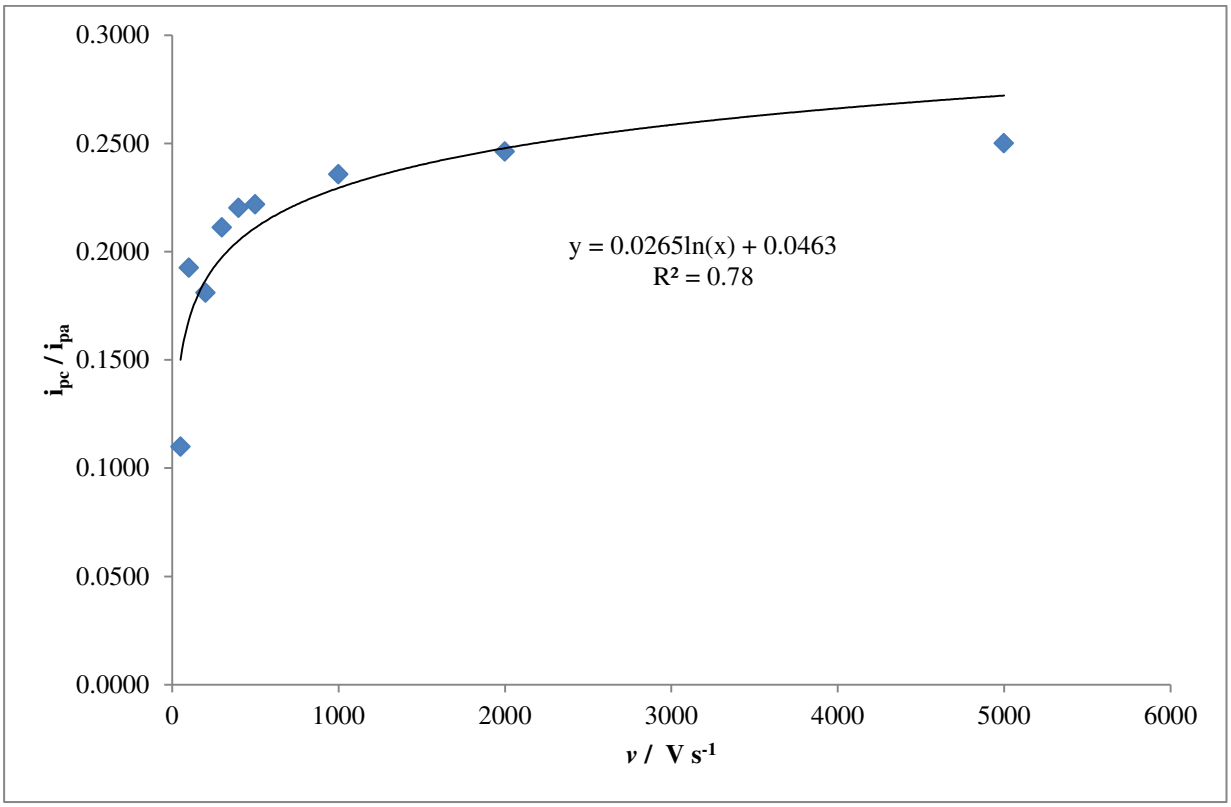

Figure 3.30: The cathodic to anodic peak current ratios versus the scan rate for [Rh(tta)(CO)(PPh_3)] **M3**.

An attempt to determine whether the chemical instability of the solvated Rh(III) radical is the cause for the decreased reduction current by correlating the reduction current, ipc, with parameters that estimate the electron density across the radical did not yield correlations. This is mainly due to the potential range between the complexes being too small and there are too few points from which to draw a conclusion. [30]

3.4.2 DFT computational study: [Rh(L,L'-BID)(CO)(PPh_3)] with L,L'-BID = $(C_4H_3SCOCHCOCPh)^-$ M1, $(C_4H_3SCOCHCOC_4H_3S)^-$ M2 and $(C_4H_3SCOCHCOCF_3)^-$ M3

In this section, the experimentally determined CV data of [Rh(β-diketonato)(CO(PPh_3) with β-diketonato = bth **M1**, dtm **M2**, tta **M3** will be compared and related to electronic descriptors, experimental kinetic rates and DFT calculated energies. Published CV data obtained for [Rh(β-diketonato)(CO(PPh_3)] with β-diketonato = $(CH_3COCHCOCH_3)^-$ (acac) and $(CF_3COCHCOCF_3)^-$ (tfaa) will be added to the relationships.[26,31] The experimentally determined peak oxidation potential(E_{pa}), second order rate constants (k_2) of the oxidative addition reaction

between the [Rh(β-diketonato)(CO)(PPh_3)] (with β-diketonato = $(RCOCHCOR')^-$ = bth **M1**, dtm **M2**, tta **M3**, acac or tfaa) complexes and CH_3I as well as the sum of Gordy scale group electronegativities ($\chi_R + \chi_{R'}$), sum of meta-substituent Hammet constants ($\sigma_R + \sigma_{R'}$), and the DFT calculated HOMO energy levels (energy of highest occupied molecular orbitals) of the complexes are listed in Table 3.21. The graphical representation of the data is in Figure 3.22.

Table 3.21: Data of the experimentally determined E_{pa}, PW91/TZP DFT calculated HOMO energies, sum of meta-group electronegativities, sum of meta-substituent Hammet constants and second order rate constants of [Rh(β-diketonato)(CO)(PPh_3)] (with β-diketonato = $(RCOCHCOR')^-$ = bth **M1**, dtm **M2**, tta **M3**, acac or tfaa)

β-diketonato	**E_{pa}(V)**	**E_{HOMO} (eV)[(a)]**	**$(\chi_R + \chi_{R'})$[(b)]**	**$(\sigma_R + \sigma_{R'})$[(c)]**	**ln(k_2)[(d)]**
$(CH_3COCHCOCH_3)^-$	0.357	-5.336	4.68	-0.14	-3.73
$(C_6H_5COCHCOC_4H_3S)^-$ **M1**	0.296	-5.416	4.31	0.15	-3.63
$(C_4H_3SCOCHCOC_4H_3S)^-$ **M2**	0.320	-5.415	4.2	0.18	-3.54
$(CF_3COCHCOC_4H_3S)^-$ **M3**	0.491	-5.622	5.11	0.52	-6.37
$(CF_3COCHCOCF_3)^-$	0.573	-5.908	6.02	0.86	-8.95

(a) Calculated via DFT with PW91/TZP basis set;(b) Sum of the group electronegativities ($\chi_R + \chi_{R'}$) calculated on Gordy scale, of the values χ_{CH3} = 2.34, χ_{C4H3S} = 2.10, χ_{CF3} = 3.01, χ_{Ph} = 2.21[13,32] ; (c) Sum of the Hammett meta substituent constants ($\sigma_R + \sigma_{R'}$) with values σ_{CH3} = -0.069, σ_{C4H3S} = 0.09, σ_{CF3} = 0.43, σ_{Ph} = 0.06.[33,34,35] ; (d) k_2 of values obtained from reference.[31]

[32]R.E. Kagarise, *J. Am. Chem. Soc.,* 1995, **77**, 1377

[33]L.P. Hammett, *Chem. Rev.,* 1935, **17**, 125

[34]L.P. Hammett, *J. Am. Chem. Soc.,* 1937, **59**, 96

[35]C. Hansch, A. Leo, R.W. Taft, *Chem. Rev.,* 1991, **91**, 165

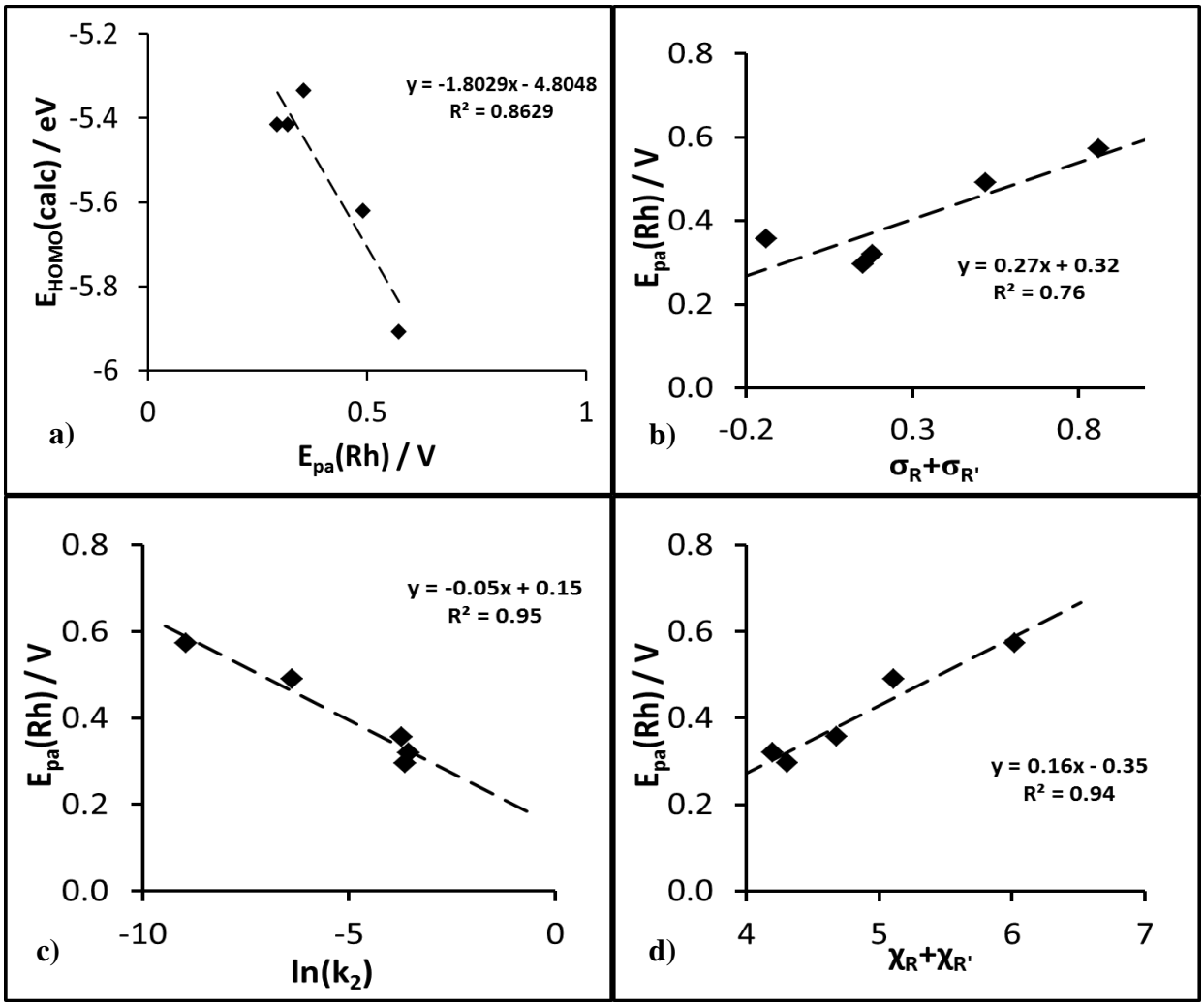

Figure 3.31: Graphical representation of values from Table 3.21: a) DFT calculated HOMO energies of the complexes versus E_{pa}, b) E_{pa} versus the sum of the *meta*-Hammet constants, c) E_{pa} versus the natural logarithm of the second order rate constants, d) E_{pa} versus the sum of the group electronegativities.

From the graphs in Figure 3.31 there is a linear trend observed between the peak oxidation potential and the various parameters.

With Figure 3.31 a) we see that the linear relationship allows the prediction of peak oxidation potentials with the help of the DFT calculated HOMO energy, which in turn can enable the design of β-diketonato ligands with particular redox potentials. The linear relationship indicates that the more positive the DFT calculated HOMO energy is, the less energy is required to overcome the energy barrier to facilitate the addition of electrons to the orbitals. The less positive the peak anodic potential is, the less energy is required to add electron density to the structure.

With Figure 3.31b) it can be seen that the Hammett constants sum of the groups at the *meta* position with respect to the rhodium metal centre have a profound effect on the oxidation potential of the complex. The Hammett constant sum indicates the activation energy required in order to permit electron density addition. The smaller the sum, the smaller the peak anodic potential.

In Figure 3.31c) the trend shows that the greater the oxidation potential of the complex is, the slower the kinetics in the oxidative addition reactions are. This is expected since the more energy that is required in order to add electron density to the complex structure, the slower a reaction will be.

Figure 3.31d) indicates that the group electronegativities have a similar effect on the redox properties as the Hammet constants in graph b). This is opposite to what is expected since a larger electronegativity sum decreases electron density across the complex, therefore lowering the energy required to add additional electron density to the structure.

From these graphs it can be seen that the oxidation potential of a complex increases as the electronegativies of the R and R' side groups or the sum of the Hammet constants increase. These affect the energy barrier of the Rh metal complex affecting the potential at which electron density addition occurs. [36,37]

Similar trends were obtained for other Rh(I)-β-diketonato complexes.[38]

---

[36]J. Conradie, J.J.C. Erasmus, *Electrochim. Acta*, 2011, **56**, 9287.

[37]M.M. Conradie, A.J. Muller, J. Conradie, *S. Afr. J. Chem*., 2008, **61**, 13.

[38]J. Conradie, *Dalton Trans.,*2015, **44**, 1503-1515

3.5 [Rh(L,L'-BID)(CO)(PPh_3)] + CH_3I kinetics

The oxidative addition reaction between the two [Rh(L,L'-BID)(CO)(PPh_3)] complexes (L,L'-BID = $(CH_3COCHCNHCH_3)^-$ and $(CH_3COCHCNPhCH_3)^-$) of this study and CH_3I will be presented. The reaction is followed by IR, UV/VIS and NMR. Additionally a DFT study of the reaction will be presented to compliment the experimental findings. The results of **3b** will be presented first and then the results for **3a** in each section, since it was found that **3b** exhibited a single reaction step while **3a** showed 2 steps.

3.5.1 IR in situ kinetic analysis

The oxidative addition reaction was first followed on IR, since this technique is ideal to distinguish between CO bonds in metal-CO complexes of Rh(I)-carbonyl and Rh(III)-complexes. CO groups in Rh(I)-carbonyl complexes vibrate at ~1980 – 2000 cm^{-1}, CO groups in Rh(III)-alkyl-carbonyl complexes vibrate at ~2050 – 2100 cm^{-1} and CO groups in Rh(III)-acyl complexes resonate at ~ 1700 – 1750 cm^{-1}.[3]

3.5.1.1 IR study of [Rh($CH_3COCHCNPhCH_3$)(CO)(PPh_3)] 3b and CH_3I

In Figure 3.32, which displays the IR spectrum of the CH_3I reaction with [Rh($CH_3COCHCNPhCH_3$)(CO)(PPh_3)] **3b**, it can be seen that there are two main peaks that vary during the reaction. The first peak, at 1972.62 cm^{-1} is assigned to the disappearance of the Rh(I) complex as the reaction progresses and a product is formed. The second peak at 2059.72 cm^{-1} is assigned to the formation of the Rh(III)-alkyl reaction product. There is a third increasing peak visible at *ca* 1600 cm^{-1}, which is lower than the area where a Rh(III)-acyl product could be observed. This peak is assigned to the CO of the $(CH_3COCHCNPhCH_3)^-$ **1b** ligand and not used in the kinetic study.

The rate constants determined from the IR kinetic experiments for different CH_3I concentrations is given in Table 3.22. From Table 3.22 it can be seen that the rate of disappearance of [Rh($CH_3COCHCNPhCH_3$)(CO)(PPh_3)] **3b** and the rate of the formation of the Rh(III)-alkyl product show very good correlation since the values are so close to each other. This trend is seen across all three concentrations. The increase in the observed kinetic rate constant with the increase in CH_3I concentration indicates that this reaction step is concentration dependent.

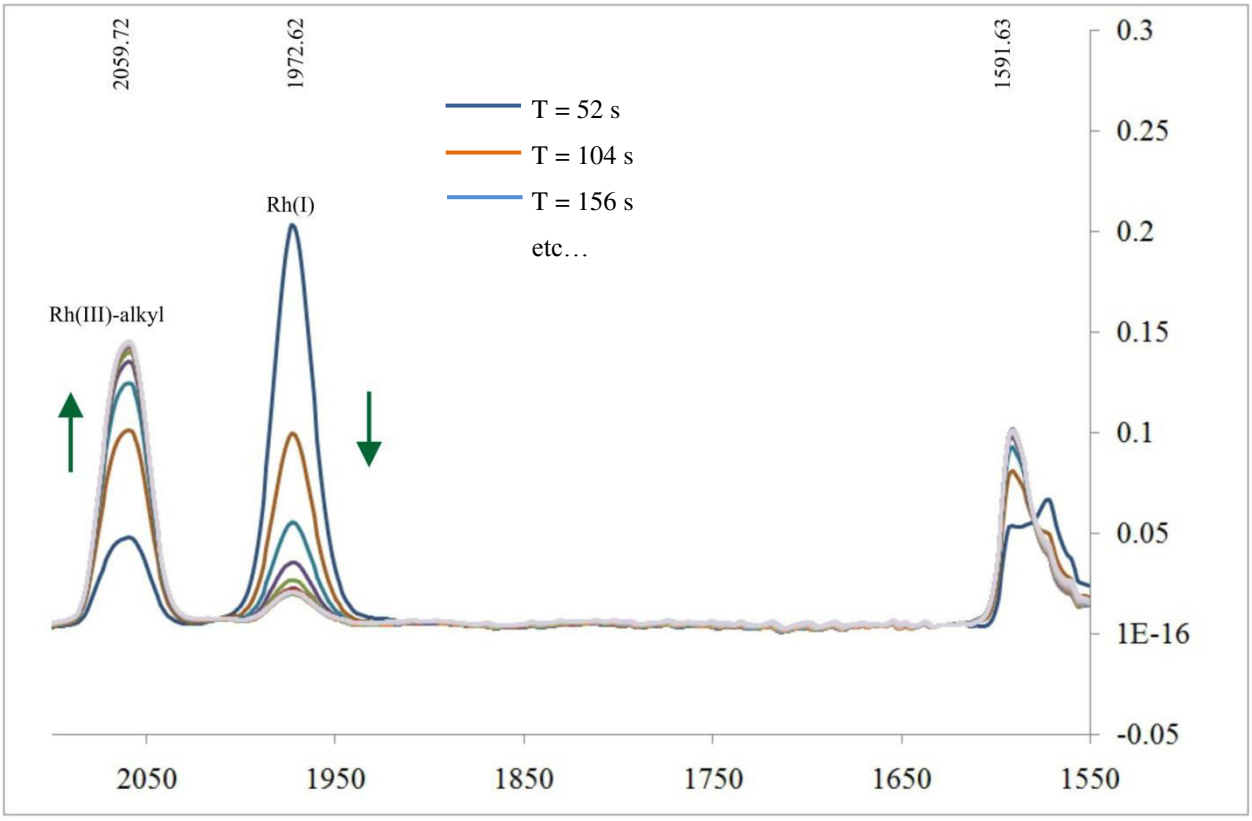

Figure 3.32: IR spectrum of the reaction between [Rh(CH_3COCHCNPhCH_3)(CO)(PPh_3)] **3b** and CH_3I at 25°C with the CH_3I concentration at 10x excess with respect to the [Rh(CH_3COCHCNPhCH_3)(CO)(PPh_3)] **3b** concentration. [CH_3I] = 0.0272 mol dm^{-3}. Time intervals are 52 s.

Table 3.22: Observed kinetic rate constants, wavelengths and concentrations utilized in the IR study of the oxidative addition reaction between [Rh(CH_3COCHCNPhCH_3)(CO)(PPh_3)] **3b** and CH_3I at 25°C. [CH_3I] = 0.0272 mol dm^{-3}.

Concentration CH_3I (mol dm^{-3})	**Reaction step**	**Wavelength (cm^{-1})**	**k_{obs} (s^{-1})**
0.02720	Rh(I) loss	1972.62	0.00720 (5)
	Rh(III)-alkyl gain	2059.72	0.007 (3)
0.05383	Rh(I) loss	1972.62	0.0132 (2)
	Rh(III)-alkyl gain	2059.72	0.0124 (1)
0.12780	Rh(I) loss	1972.62	0.02338 (4)
	Rh(III)-alkyl gain	2059.72	0.0242 (2)

From the results obtained from the IR study, the reaction step of the [Rh(CH_3COCHCNPhCH_3)(CO)(PPh_3)] **3b** + CH_3I reaction can thus be presented as given in Scheme 3.5:

$$\textbf{Rh(I)} + \textbf{CH}_3\textbf{I} \underset{k_{-1}}{\overset{k_1}{\rightleftharpoons}} \textbf{Rh(III)-alkyl}$$

Scheme 3.5: Reaction scheme for the [Rh(CH_3COCHCNPhCH_3)(CO)(PPh_3)] **3b** + CH_3I reaction.

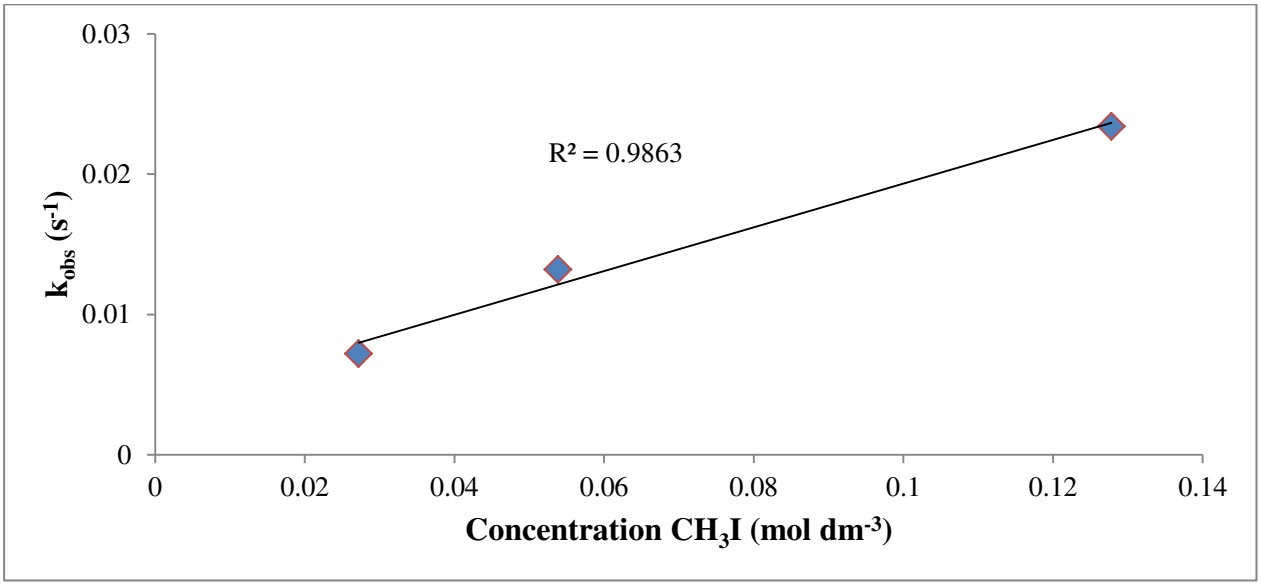

Figure 3.33: Graph of the observed kinetic rate constants against the concentrations of the reaction between [Rh(CH_3COCHCNPhCH_3)(CO)(PPh_3)] **3b** and CH_3I at 25° C. Data obtained from **Table 3.22**.

3.5.1.2 IR study of [Rh(CH_3COCHCNHCH_3)(CO)(PPh_3)] 3a and CH_3I

In Figure 3.34, which displays the IR spectrum of the CH_3I reaction with [Rh(CH_3COCHCNHCH_3)(CO)(PPh_3)] **3a**, it can be seen that there are three main peaks that vary during the reaction. The Rh(I) complex displays a CO stretching frequency peak at 1967.66 cm^{-1}. This absorbance peak decreases as the reaction progresses, which is explained by the disappearance of the Rh(I) complex as it reacts with CH_3I in order to form a Rh(III) complex.

The first product that forms is seen at the increase of the absorbance peak position at 2061.30 cm^{-1}. This is attributed to the formation of a Rh(III)-alkyl complex after the direct addition of the CH_3I to the Rh centre. This peak shows an increase at first, which shows the formation of the Rh(III)-alkyl product up to a maximum absorbance level, after which it starts to decrease in intensity. This is attributed to the formation of a second Rh(III) product. The

disappearance of the Rh(I) complex and the simultaneous formation of the Rh(III)-alkyl product is referred to as the first reaction step and showed seperately in Figure 3.35.

When the Rh(III)-alkyl product starts to decrease in intensity, the formation of a second Rh(III) product can be seen at an absorbance peak of 1713.74 cm^{-1}, see Figure 3.36. The peak at 1713.74 cm^{-1} is designated to the Rh(III)-acyl complex. The intensity of the peak at 1713.74 cm^{-1} increases up to a maximum amount. The formation of the Rh(III)-acyl is due to CO insertion of the Rh(III)-alkyl product and this step is called the second reaction step. Rh(III)-acyl is the final product observed for the $[Rh(CH_3COCHCNHCH_3)(CO)(PPh_3)]$ **3a** + CH_3I reaction.

The pseudo first order reaction constant calculated at the indicated wavelengths for each reaction step is given in Table 3.23.

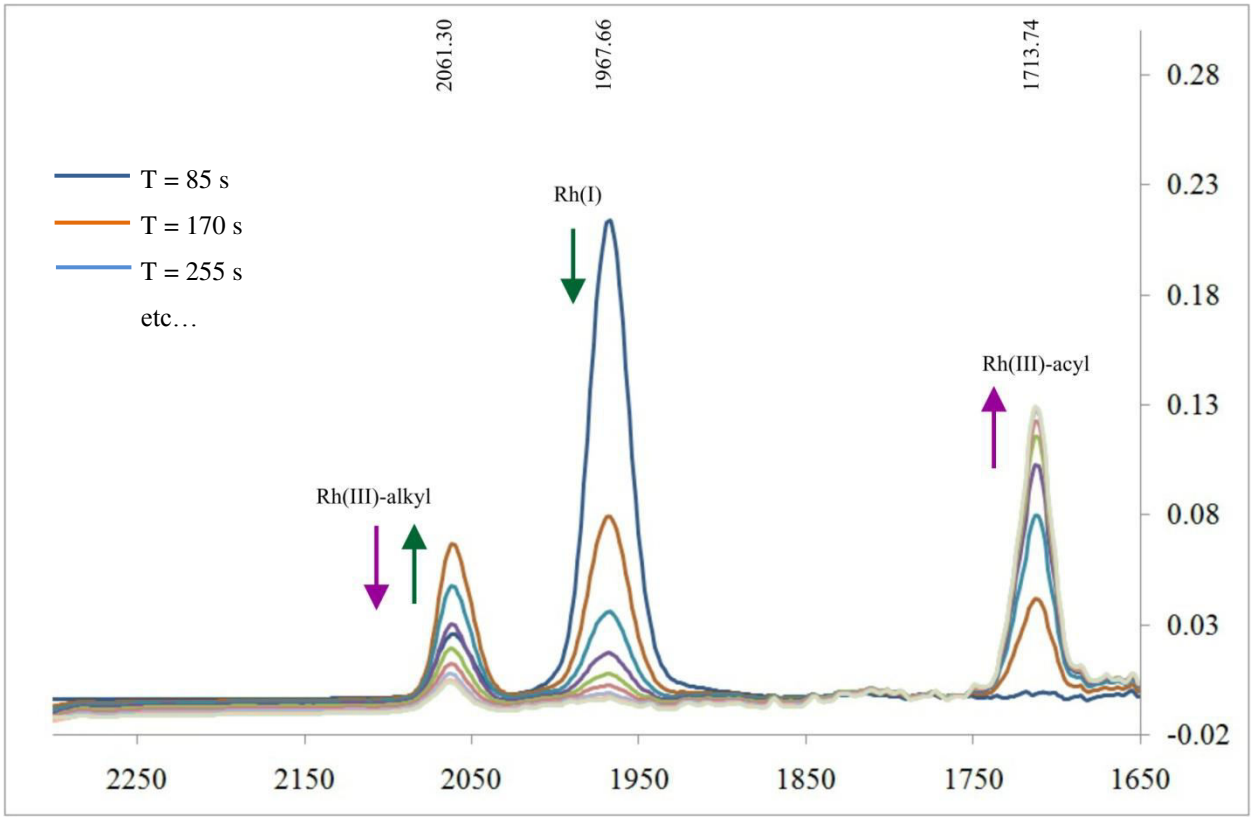

Figure 3.34: IR spectrum of the reaction between $[Rh(CH_3COCHCNHCH_3)(CO)(PPh_3)]$ **3a** and CH_3I at 25°C with the CH_3I concentration at 10x excess with respect to the $[Rh(CH_3COCHCNHCH_3)(CO)(PPh_3)]$ **3a** concentration. $[CH_3I]$ = 0.0537 mol dm^{-3}. Time intervals are 85 s.

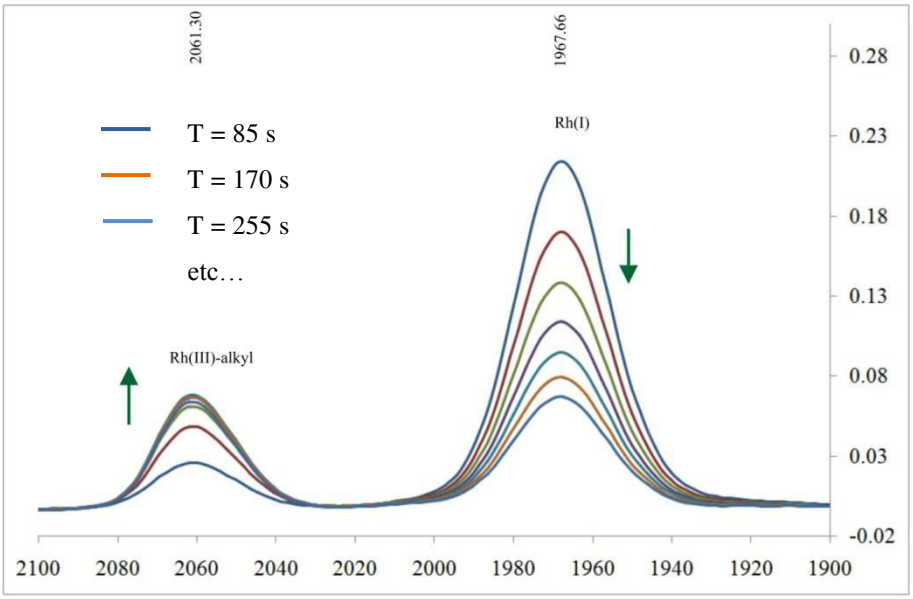

Figure 3.35: IR spectrum illustrating the formation of the [Rh($CH_3COCHCNHCH_3$)(CO)(PPh_3)(CH_3)(I)]-alkyl intermediate product of the reaction between [Rh($CH_3COCHCNHCH_3$)(CO)(PPh_3)] **3a** and CH_3I at 25°C with the CH_3I concentration at 10x excess with respect to the [Rh($CH_3COCHCNHCH_3$)(CO)(PPh_3)] **3a** concentration. [CH_3I] = 0.0537 mol dm^{-3}. Time intervals are 85 s.

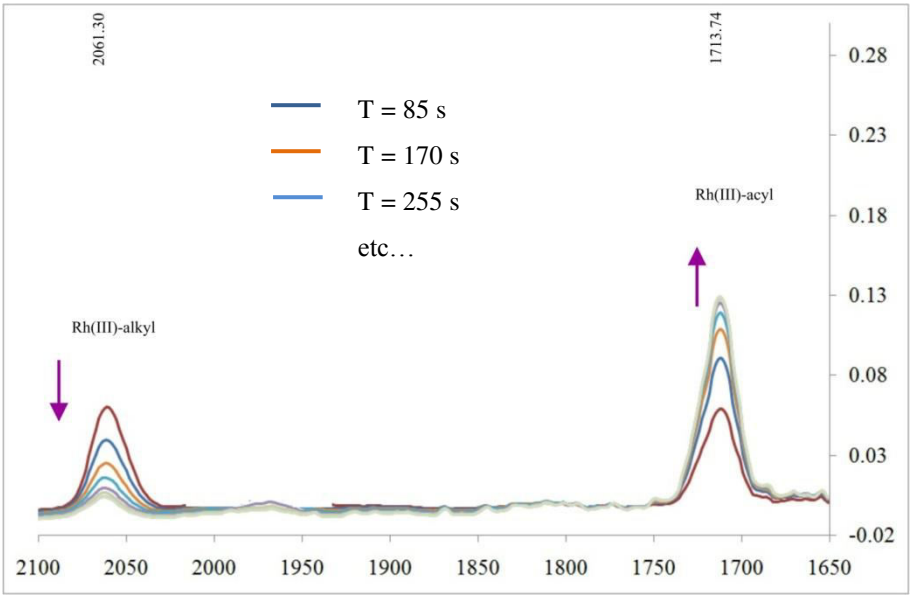

Figure 3.36: IR spectrum illustrating the formation of the [Rh($CH_3COCHCNHCH_3$)($COCH_3$)(PPh_3)(I)]-acyl final product of the reaction between [Rh($CH_3COCHCNHCH_3$)(CO)(PPh_3)] **3a** and CH_3I at 25°C with the CH_3I concentration at 10x excess with respect to the [Rh($CH_3COCHCNHCH_3$)(CO)(PPh_3)] **3a** concentration. [CH_3I] = 0.0537 mol dm^{-3}. Time intervals are 85 s.

Table 3.23: Observed kinetic rate constants, wavelengths and concentrations utilized in the IR study of the oxidative addition reaction between [Rh($CH_3COCHCNHCH_3$)(CO)(PPh_3)] **3a** and CH_3I at 25°C. [CH_3I] = 0.0537 M.

Concentration CH_3I (mol dm^{-3})	**Reaction step**	**Wavelength(cm^{-1})**	**k_{obs}(s^{-1})**
0.0236	Rh(I) loss	1967.66	0.00227(5)
	Rh(III)-alkyl gain	2061.30	0.0077(4)
	Rh(III)-alkyl loss	2061.30	0.00103(2)
	Rh(III)-acyl gain	1713.74	0.0014(5)
0.0537	Rh(I) loss	1967.66	0.0059(1)
	Rh(III)-alkyl gain	2061.30	0.015(1)
	Rh(III)-alkyl loss	2061.30	0.00174(3)
	Rh(III)-acyl gain	1713.74	0.00185(3)
0.1283	Rh(I) loss	1967.66	0.0158(2)
	Rh(III)-alkyl gain	2061.30	0.029(1)
	Rh(III)-alkyl loss	2061.30	0.00191(3)
	Rh(III)-acyl gain	1713.74	0.00181(2)

From the data presented in Table 3.23 it can be seen that the observed rate constants for the loss of the [Rh($CH_3COCHCNHCH_3$)(CO)(PPh_3)] **3a** complex and the formation of the Rh(III)-alkyl product, the first reaction step, indicate a CH_3I concentration dependent step. The small differences between the rate constants for the Rh(I) loss and the Rh(III)-alkyl gain, is due to the fact that the Rh(III)-alkyl is converted to Rh(III)-acyl already while the first reaction step proceeds. Thus the Rh(III)-alkyl increase during the first reaction step is virtually smaller.[39]

The observed rate constant for the loss of the Rh(III)-alkyl product and the formation of the Rh(III)-acyl product show good correlation with each other. There is barely any significant change in the rate values over the concentration range, which indicates that it is independent of the CH_3I concentration. It is expected since the conversion between the two products is not

[39]N.F. Stuurman, J. Conradie, *J. Organomet. Chem.,* 2009, **694**, 259-268

dependent on the concentration of CH_3I but on the individual properties of the complexes themselves *i.e.* the type of ligand system employed.

From the results obtained from the IR study, the reaction steps of the $[Rh(CH_3COCHCNHCH_3)(CO)(PPh_3)]$ **3a** + CH_3I reaction can thus be presented as given in Scheme 3.6:

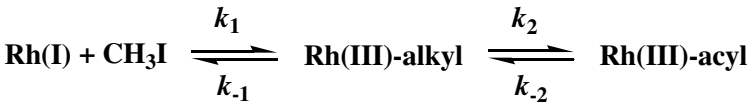

Scheme 3.6. Reaction scheme for the $[Rh(CH_3COCHCNHCH_3)(CO)(PPh_3)]$ **3a** + CH_3I reaction.

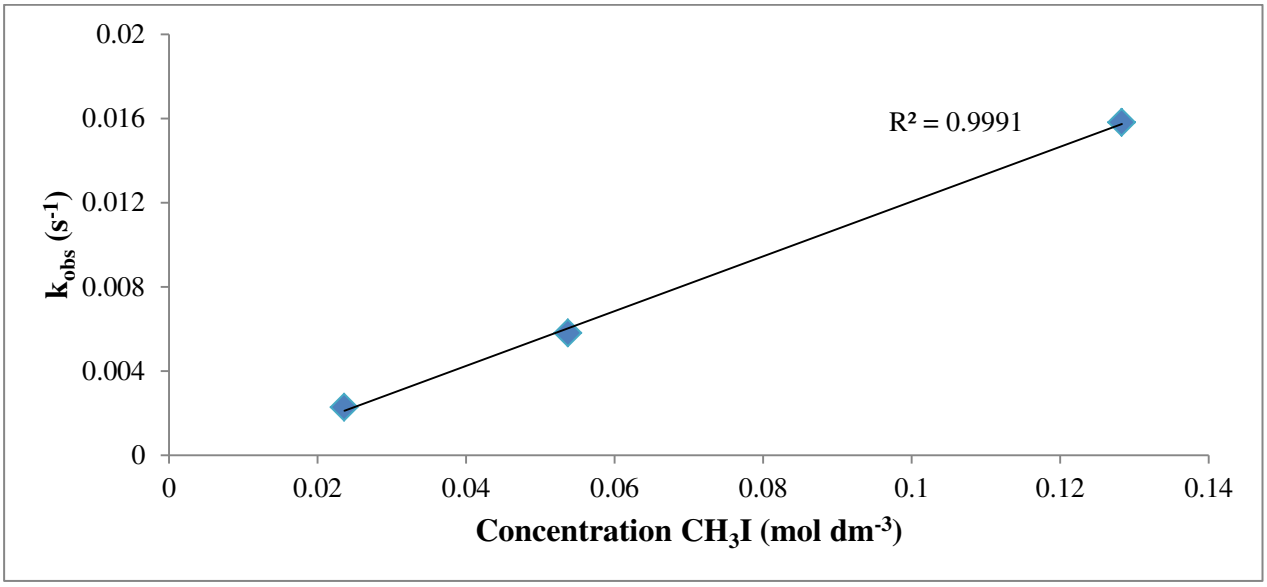

Figure 3.37:Graph of the observed kinetic rate constants against the concentrations of the reaction between $[Rh(CH_3COCHCNHCH_3)(CO)(PPh_3)]$ **3a** and CH_3I at 25° C. Data obtained from Table 3.23.

3.5.2 UV/VIS in situ kinetic analysis

The *in situ* analysis of the oxidative addition reaction between the $[Rh(L,L'\text{-BID})(CO)(PPh_3)]$, with L,L'-BID = $(CH_3COCHCNHCH_3)^-$ **1a** and $(CH_3COCHCNPhCH_3)^-$ **1b**, complexes and CH_3I are also measured by UV/VIS spectroscopy. Only the first step of both reactions, the $[CH_3I]$ dependent step, was followed on UV/VIS (Scheme 3.7).

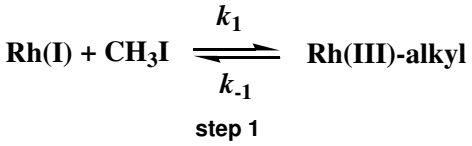

Scheme 3.7: Reaction scheme for the 1st step of the [Rh(L,L'-BID)(CO)(PPh_3)] + CH_3I reaction.

3.5.2.1 UV/VIS study of [Rh($CH_3COCHCNPhCH_3$)(CO)(PPh_3)] 3b and CH_3I

The reaction between the [Rh($CH_3COCHCNPhCH_3$)(CO)(PPh_3)] **3b** and CH_3I yields a UV/VIS spectrum as seen in Figure 3.38.

There is an increase in the absorbance at 335 nm, which is theorized to be the decrease in the concentration of the Rh(I) complex as it reacts with the CH_3I to form a Rh(III) product. The smooth increase in the absorbance at 404 nm is described as the increase in concentration of an unidentifiable, through UV/VIS methodology, Rh(III) product. A focus on the selected regions to illustrate the adherence to the half life of the reaction is given in Figure 3.39 and Figure 3.40. Rate constant determinations at different wavelengths (300 nm, 335 nm and 404 nm) yielded similar results with the data utilized from 404 nm considered to be most reliable since the absorbances at this wavelength are lower than 1, which is seen by the smoother lines obtained during analysis.[40,41]

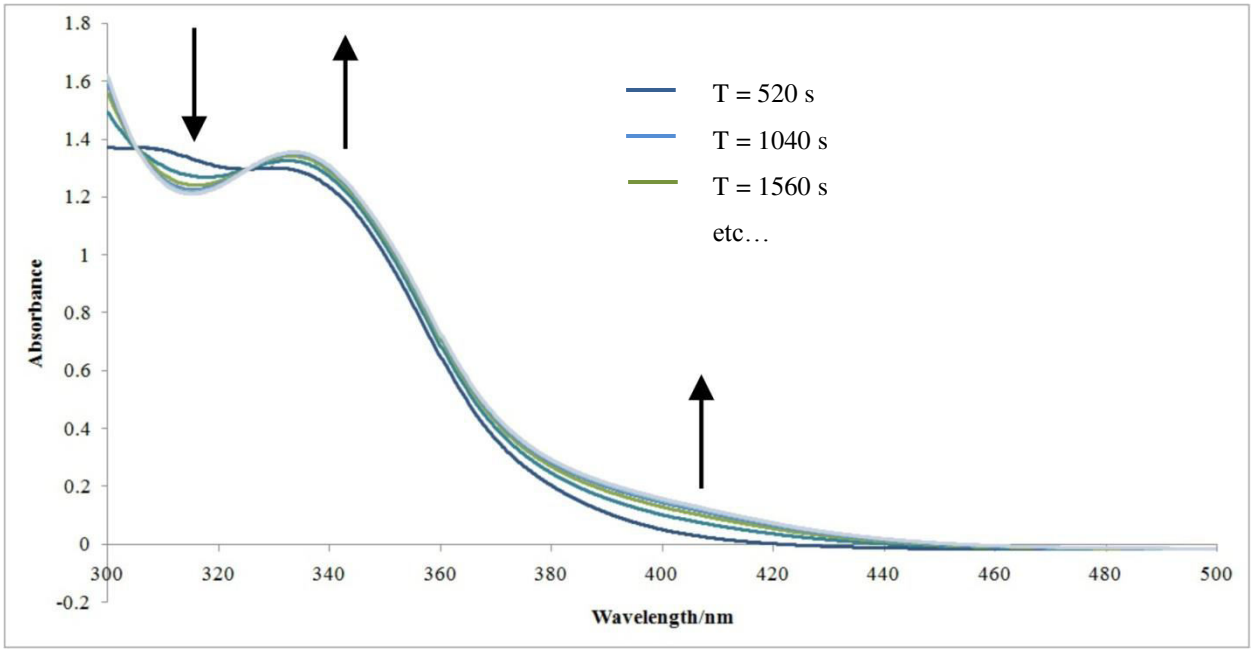

Figure 3.38: A UV/VIS spectrum of the reaction between [Rh($CH_3COCHCNPhCH_3$)(CO)(PPh_3)] **3b** and CH_3I at 15°C with the CH_3I concentration in 50x excess. [CH_3I] = 0.01642 mol dm^{-3}. The time intervals are 520 s.

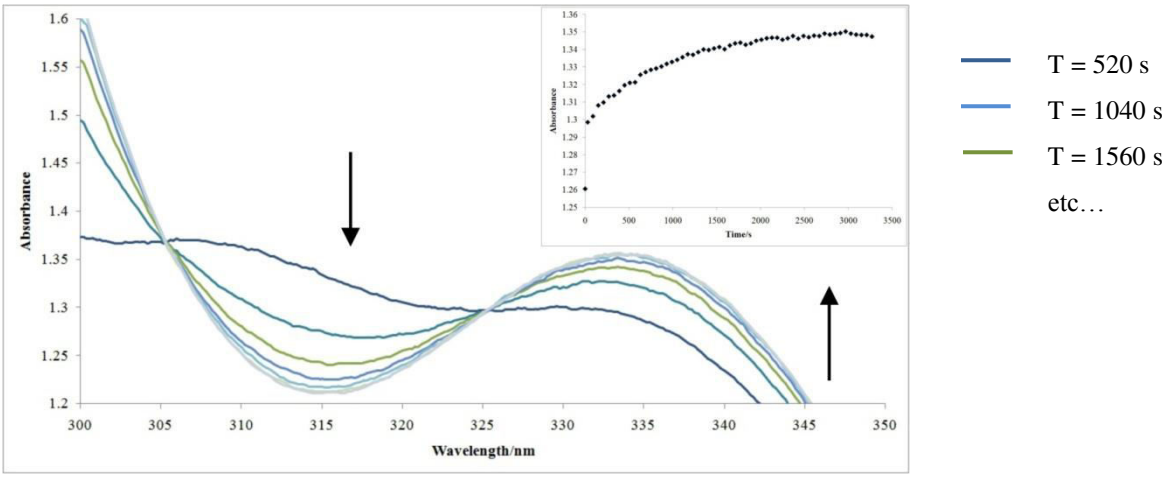

Figure 3.39: A UV/VIS spectrum of the reaction between [Rh($CH_3COCHCNPhCH_3$)(CO)(PPh_3)] **3b** and CH_3I at 15°C with the CH_3I concentration in 50x excess focussing on the 335 nm absorbance change. The time intervals are 520 s. The insert displays the change in absorbance over time. [CH_3I] = 0.01642 mol dm^{-3}.

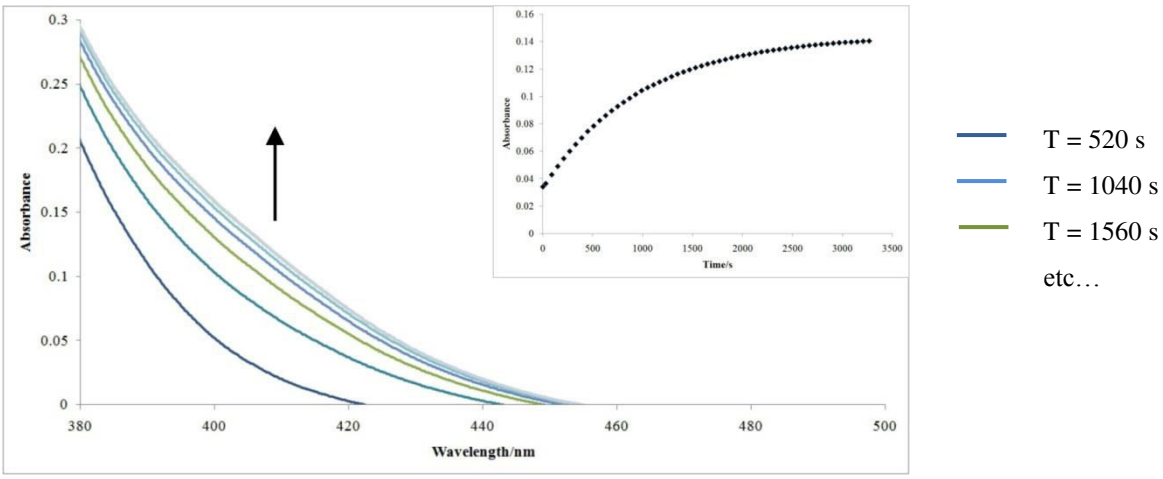

Figure 3.40: A UV/VIS spectrum of the reaction between [Rh($CH_3COCHCNPhCH_3$)(CO)(PPh_3)] **3b** and CH_3I at 15°C with the CH_3I concentration in 50x excess focussing on the 404 nm absorbance change. The time intervals are 520 s. The insert displays the change in absorbance over time. [CH_3I] = 0.01642 mol dm^{-3}.

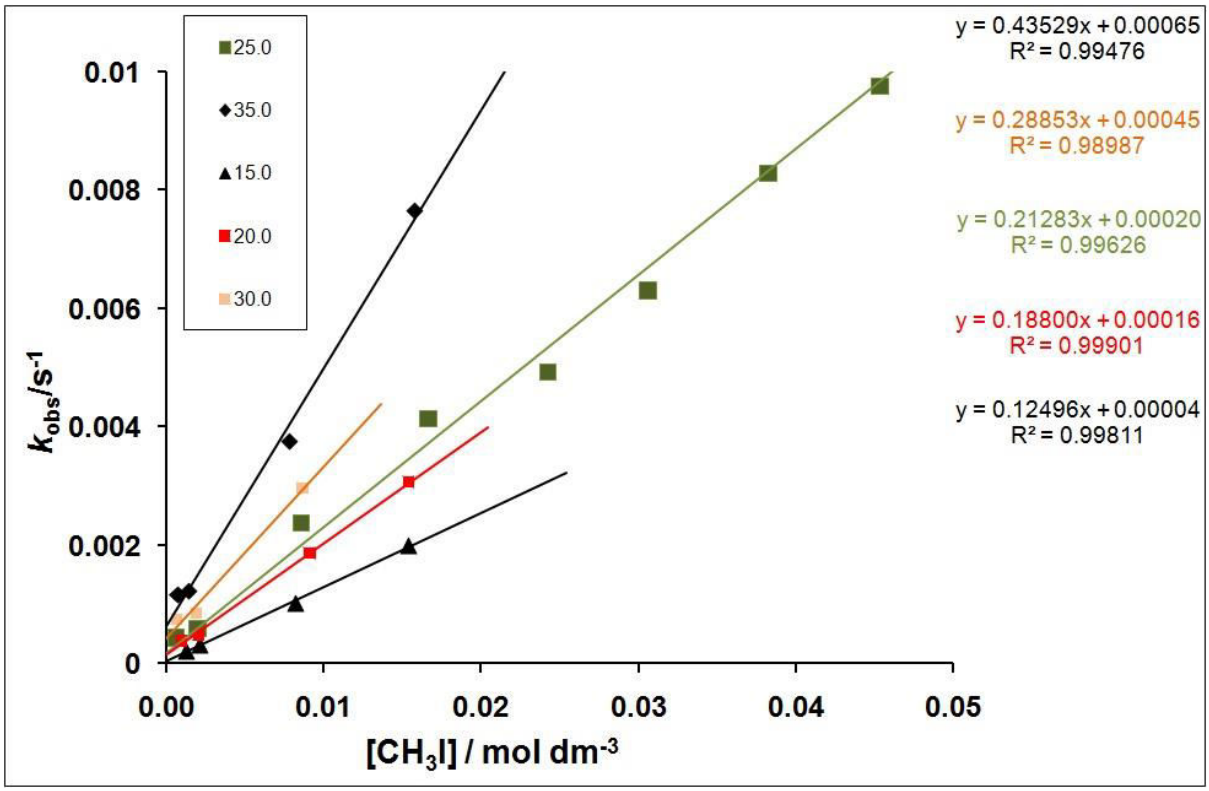

Figure 3.41: Graph of the observed kinetic rate constants against the concentrations of the reaction between [Rh($CH_3COCHCNPhCH_3$)(CO)(PPh_3)] **3b** and CH_3I at 15° C, 20° C, 25° C, 30° C and 35° C.

When the observed second order reaction rate constants of different temperatures are compared with the concentration of the CH_3I in the oxidative addition reaction with [Rh($CH_3COCHCNPhCH_3$)(CO)(PPh_3)] **3b** a graph is obtained as seen in Figure 3.41. The slope of the different lines give the second order rate constant for the oxidative addition reaction with [Rh($CH_3COCHCNPhCH_3$)(CO)(PPh_3)] **3b** + CH_3I at the indicated temperatures, see Table 3.25.

3.5.2.2 UV/VIS study of [Rh($CH_3COCHCNHCH_3$)(CO)(PPh_3)] 3a and CH_3I

The reaction between the [Rh($CH_3COCHCNHCH_3$)(CO(PPh_3)] **3a** complex and CH_3I yields a spectrum as seen in Figure 3.42. From Figure 3.42 it is seen that there is a decrease of the absorption around a wavelength of 330 nm and an increase of the absorption around 408 nm as the reaction progresses. The decrease in the absorption (330 nm) is theorized to be the decrease in the concentration of the Rh(I) complex as it reacts with CH_3I to form a Rh(III) complex. The increase in the absorption (408 nm) is identified as the Rh(III) product complex however the identification of the type of product is not possible. The Rh(III) products that are formed could either be the Rh(III)-alkyl, Rh(III)-acyl or a mixture of both.[40,41]

[40] J. Conradie, G.J. Lamprecht, A. Roodt, J.C. Swarts, *Polyhedron,* 2007, **26**, 5075-5087

[41] M.M. Conradie, J. Conradie, *Inorg. Chim. Acta,* 2008, **361**, 208-218

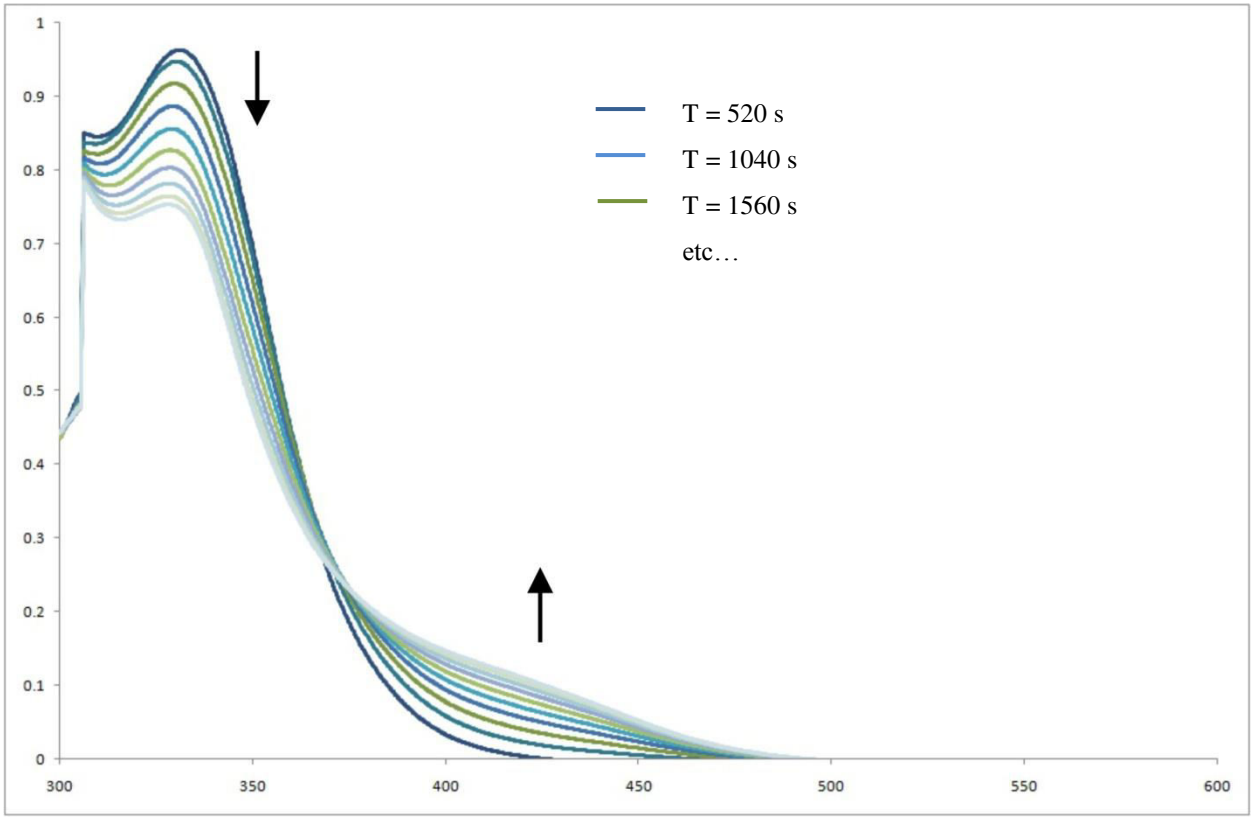

Figure 3.42: A UV/VIS spectrum of the reaction between[Rh($CH_3COCHCNHCH_3$)(CO)(PPh_3)] **3a** and CH_3I at 15°C with the CH_3I concentration in 50x excess. The time intervals are 520 s. [CH_3I] = 0.008384 mol dm^{-3}.

The results of the absorbance changes at both 330 nm and 408 nm show adherence to the half life of the reaction. Figure 3.43 and Figure 3.44 illustrate this half life adherence with the inserts illustrating the absorbance against time dependence for each selected wavelength.

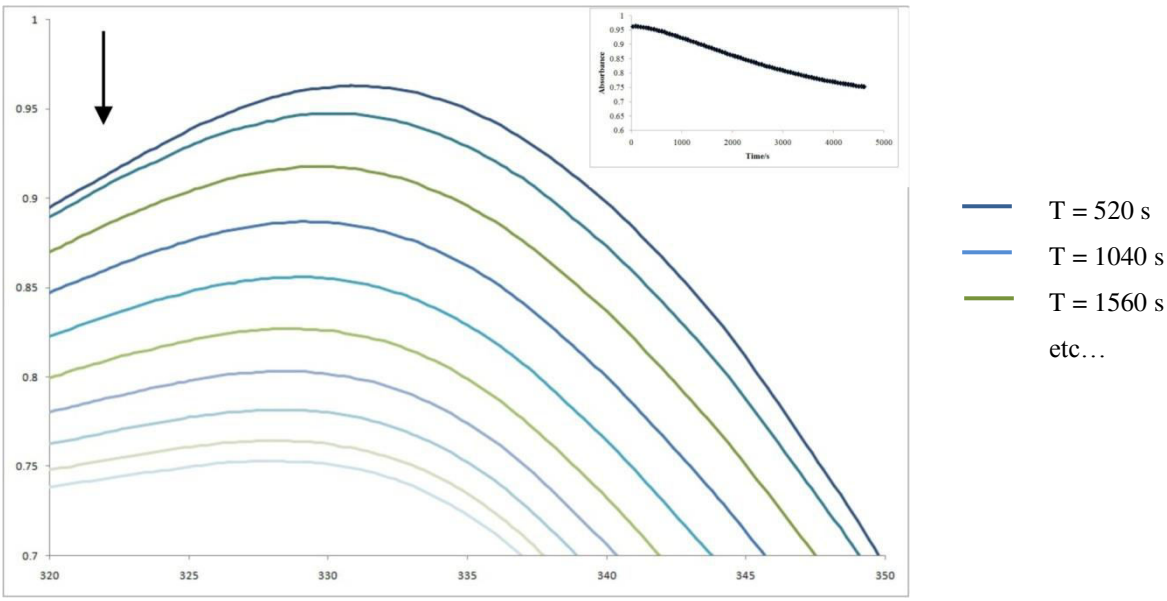

Figure 3.43: A UV/VIS spectrum of the reaction between [Rh($CH_3COCHCNHCH_3$)(CO)(PPh_3)] **3a** and CH_3I at 15°C with the CH_3I concentration in 50x excess focussing on the 330 nm absorbance change. The time intervals are 520 s. The insert displays the change in absorbance over time. [CH_3I] = 0.008384 mol dm^{-3}.

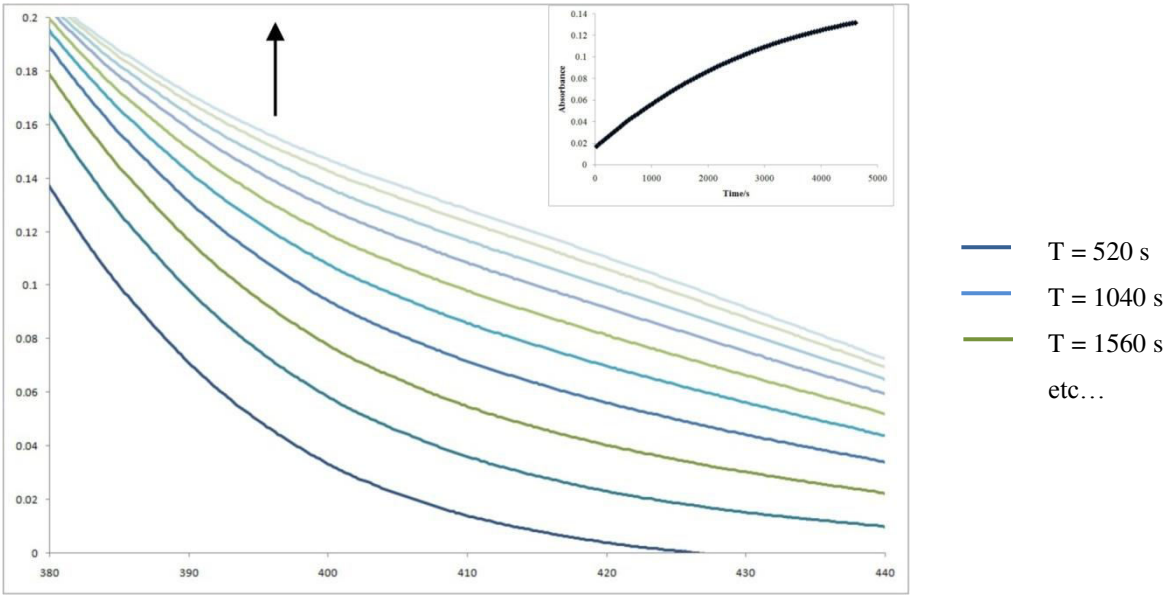

Figure 3.44: A UV/VIS spectrum of the reaction between [Rh($CH_3COCHCNHCH_3$)(CO)(PPh_3)] **3a** and CH_3I at 15°C with the CH_3I concentration in 50x excess focussing on the 408 nm absorbance change.The time intervals are 520 s. The insert displays the change in absorbance over time. [CH_3I] = 0.008384 mol dm^{-3}.

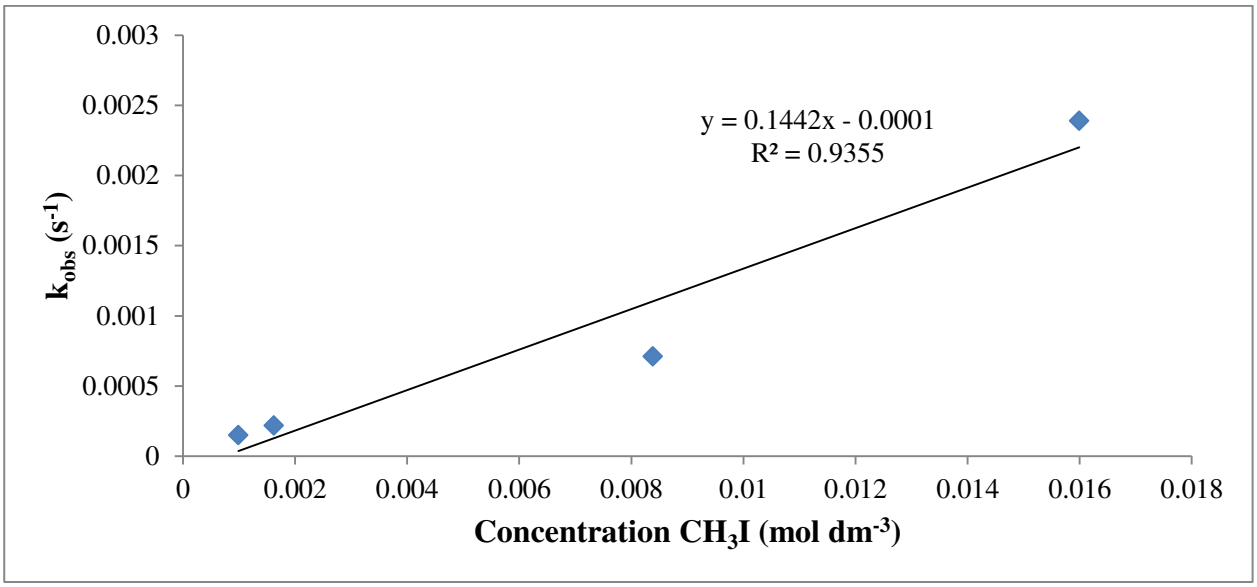

Figure 3.45: Graph of the observed kinetic rate constants against the concentrations of the reaction between [Rh($CH_3COCHCNHCH_3$)(CO)(PPh_3)] **3a** and CH_3I at 25°C.

Table 3.24: Pseudo first order reaction rate constant (k_{obs}) and concentration of CH_3I at 25°C for the oxidative addition of CH_3I to [Rh($CH_3COCHCNHCH_3$)(CO)(PPh_3)] **3a**.

Concentration CH_3I (mol dm^{-3})	**k_{obs} (s^{-1})**
0.0009865	0.000157(2)
0.0016205	0.000218(2)
0.0083840	0.00071(1)
0.0159925	0.002395(7)

Table 3.24 contains a summary of the experimentally determined pseudo-first order reaction rate constants (k_{obs}), the CH_3I concentration at the experimental temperature of 25°C with the results displayed in Figure 3.45. The slope of the graph represents the second order reaction rate constant (k_2 in s^{-1}) at the experimental temperature of 25°C.[40]

3.5.2.3 Comparison UV/VIS and IR results

Table 3.25: Second order reaction rate constants at different temperatures of the oxidative addition reaction between the [Rh(L,L'-BID)(CO)(PPh_3)] complexes and CH_3I.

Complex	**Temperature (K)**	**k_2 (mol^{-1} dm^3 s^{-1})**
[Rh($CH_3COCHCNHCH_3$)(CO)(PPh_3)] **3a**	298	0.144(1)
[Rh($CH_3COCHCNPhCH_3$)(CO)(PPh_3)] **3b**	288	0.125(3)
	293	0.188(4)
	298	0.213(5)
	303	0.29(2)
	308	0.44(2)

Comparison of all the second order reaction rate constants at 298 K, given in Table 3.25, show that for the two [Rh(L,L'-BID)(CO)(PPh_3)] complexes used in this study, the complex containing phenyl ring attached to the N atom, **3b**, has a higher second order reaction rate constant.

Taking the 25°C kinetic data obtained for the reaction between the [Rh($CH_3COCHCNPhCH_3$)(CO)(PPh_3)] **3b** and CH_3I that is monitored by UV/VIS spectroscopy and comparing it with the IR kinetic data as done in Figure 3.46, it can be seen that the same trend is followed with the observed kinetic rates.

Taking the 25°C kinetic data obtained for the reaction between the [Rh($CH_3COCHCNHCH_3$)(CO)(PPh_3)] **3a** and CH_3I that is monitored by UV/VIS spectroscopy and comparing it with the IR kinetic data as done in Figure 3.47, it can be seen that it there is a good correlation between the kinetic rate constants obtained by the two methods.

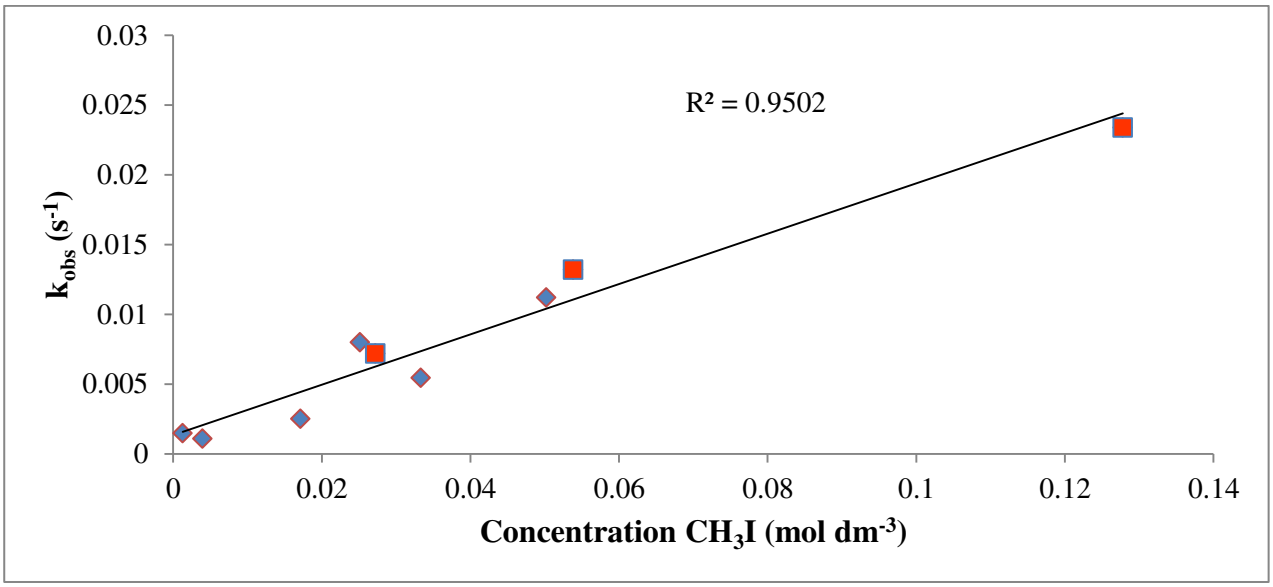

Figure 3.46: Comparison of the UV/VIS and IR spectroscopy observed reaction rates of the reaction between [Rh($CH_3COCHCNPhCH_3$)(CO)(PPh_3)] **3b** and CH_3I at 25°C. UV/VIS data in blue and IR data in red.

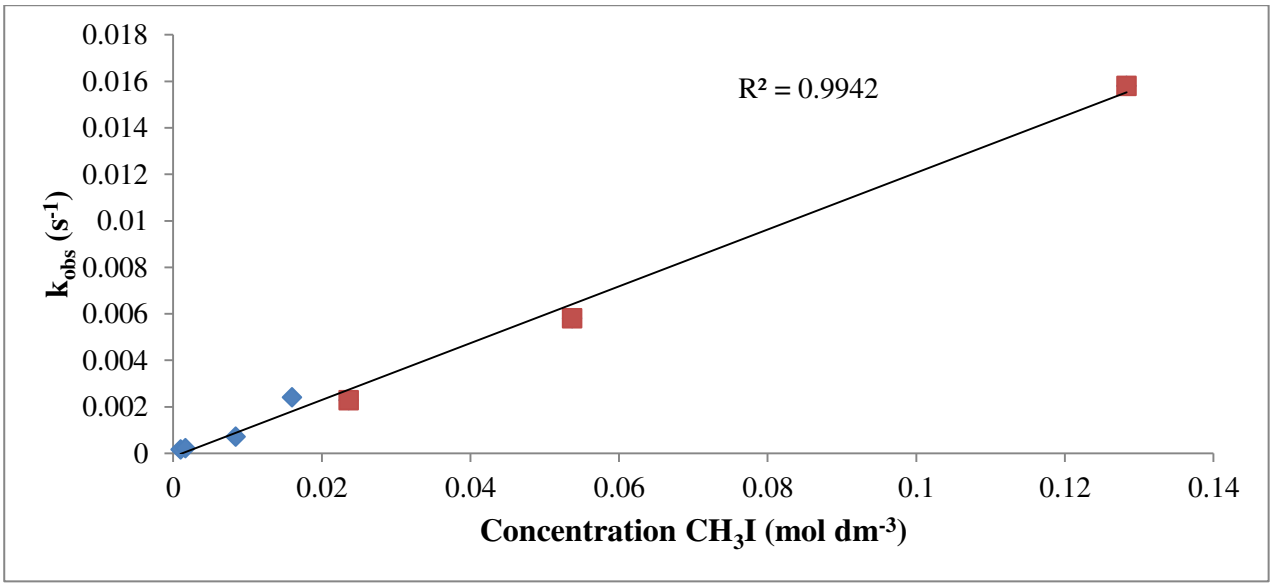

Figure 3.47: Comparison of the UV/VIS and IR spectroscopy observed reaction rates of the reaction between [Rh($CH_3COCHCNHCH_3$)(CO)(PPh_3)] **3a** and CH_3I at 25°C. UV/VIS data in blue and IR data in red.

3.5.3 NMR in situ analysis

The UV/VIS spectroscopic analysis yielded the observed second order rate constants for the two phosphine containing Rh complexes and the IR spectroscopic analysis yielded information regarding the types of products formed (alkyl and/or acyl) during the reaction between the Rh(I)

complexes and CH_3I. In order to determine whether more information regarding the types of products and possible isomers involved in the reaction, an *in situ* analysis of the reaction is done through the use of ^1H NMR spectroscopy. All possible product structures, of which there are multiples for each product type, will be presented and discussed in Section 3.5.5.

3.5.3.1 NMR study of [Rh($CH_3COCHCNPhCH_3$)(CO)(PPh_3)] 3b and CH_3I

The [Rh($CH_3COCHCNPhCH_3$)(CO)(PPh_3)] **3b** and CH_3I reaction yielded similar results as with the IR study in that there is only one product formed during the reaction, namely, the Rh(III)-alkyl product. Observations of the complexes in the reaction, as the concentrations change, can be seen in Figure 3.48 and Figure 3.49. Only one Rh(I) reactant **3b** and only one Rh(III)-alkyl product isomer is observed on NMR.

The methine proton signals are tabulated in Table 3.26 with the ^1H NMR region presented in Figure 3.48. From Figure 3.48 it can be seen that the resonance peak for the pure [Rh($CH_3COCHCNPhCH_3$)(CO)(PPh_3)] **3b** complex (5.018 ppm) decreases as the reaction progresses and that a resonance peak representing the methine proton signal for the Rh(III)-alkyl product (5.004 ppm) increases during the course of the reaction. [40,41,39]

Table 3.26: Methine proton signal positions of the [Rh($CH_3COCHCNPhCH_3$)(CO)(PPh_3)] **3b** and the Rh(III)-alkyl product.

Complex	**Methine signal (ppm)**
[Rh($CH_3COCHCNPhCH_3$)(CO)(PPh_3)] **3b**	5.018
Rh(III)-alkyl	5.004

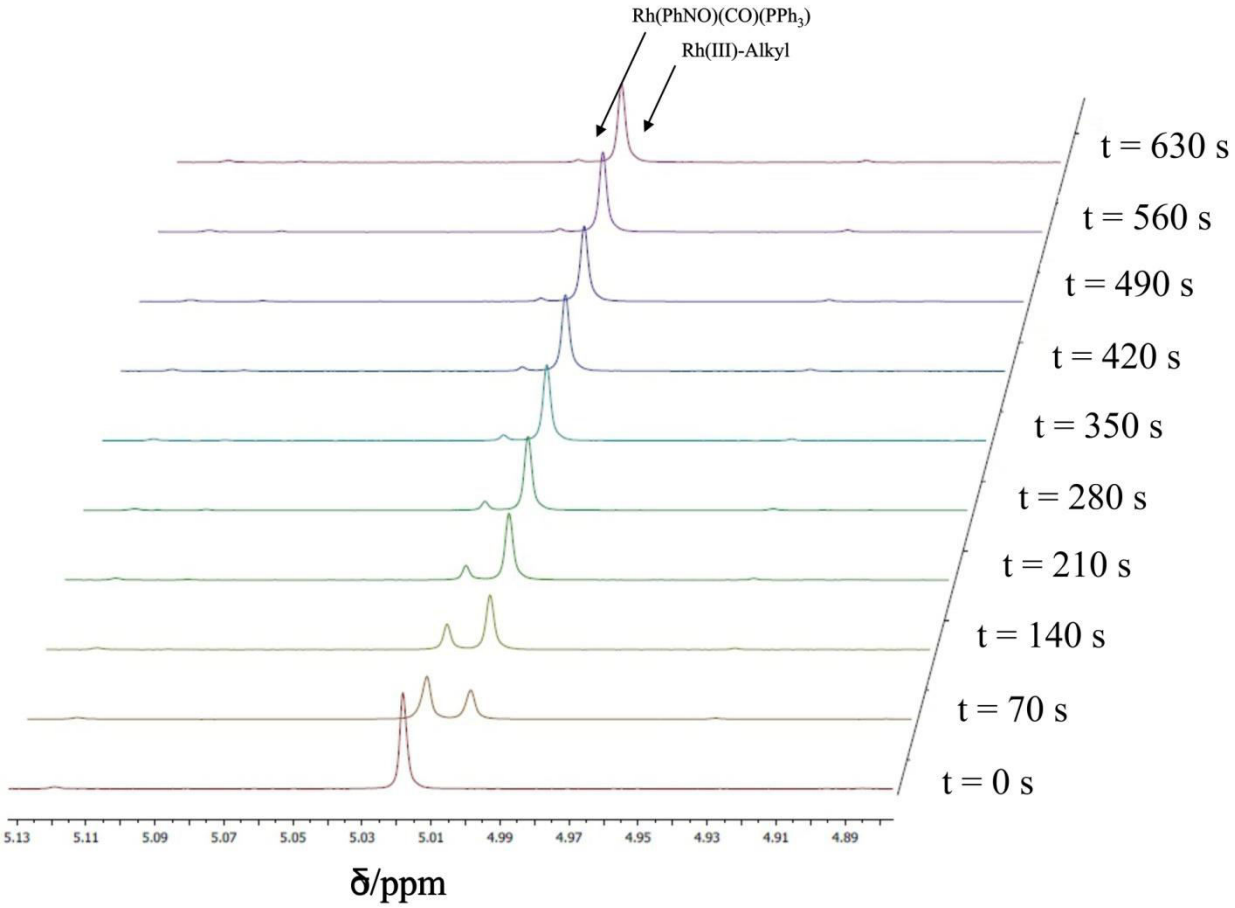

Figure 3.48: Stacked NMR spectra of the reaction between the [Rh(CH_3COCHCNPhCH_3)(CO)(PPh_3)] **3b** complex and CH_3I, focussing on the methine proton signals. The CH_3I concentration was in a 10x excess with the reaction taking place at 25°C. [CH_3I] = 0.0502 mol dm^{-3}.

Table 3.27: Methyl proton signal positions of the [Rh(CH_3COCHCNPhCH_3)(CO)(PPh_3)] **3b** and the Rh(III)-alkyl product.

Complex	**Methyl signals (ppm)**
[Rh(CH_3COCHCNPhCH_3)(CO)(PPh_3)] **3b**	1.688 1.567
Rh(III)-alkyl	1.869 1.655

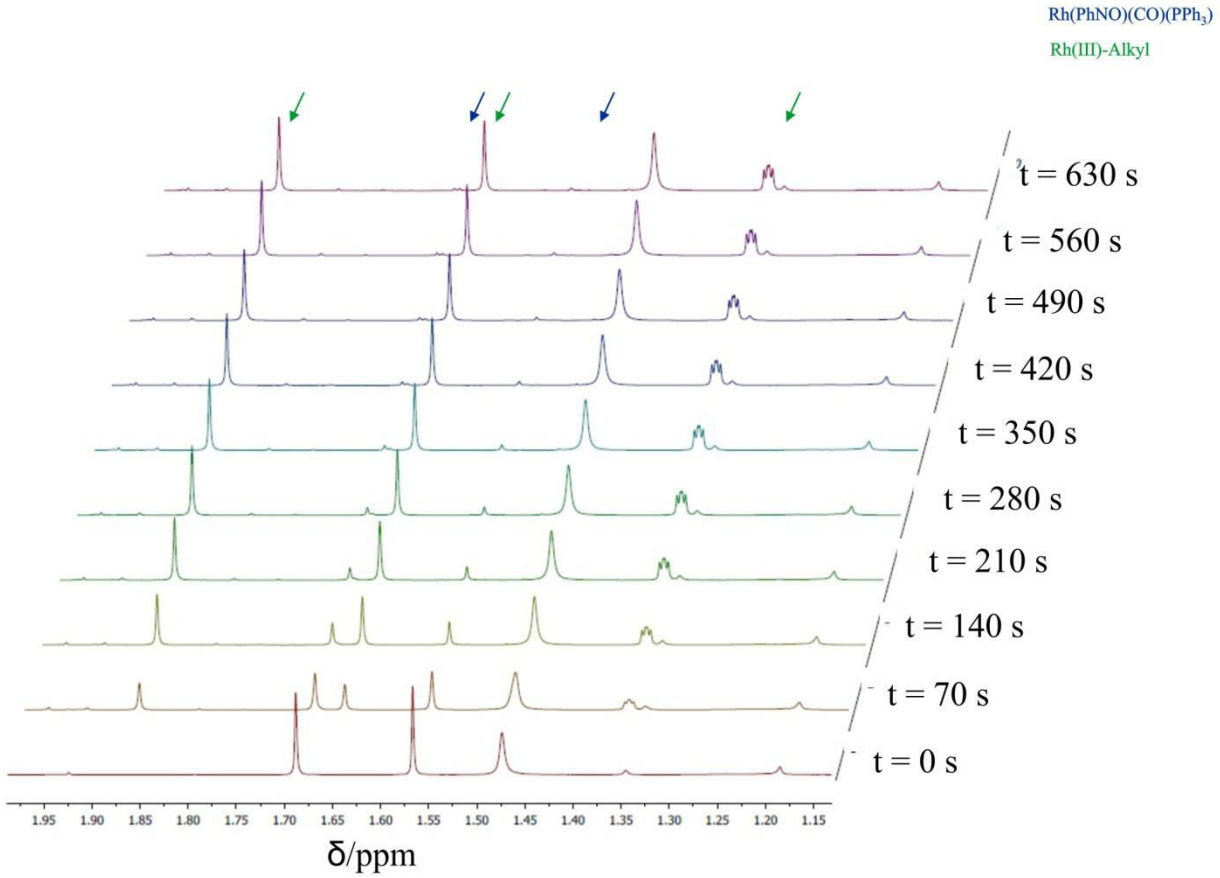

Figure 3.49: Stacked NMR spectra of the reaction between the [Rh(CH_3COCHCNPhCH_3)(CO)(PPh_3)] **3b** complex and CH_3I, focusing on the methyl proton signals. The CH_3I concentration was in a 10x excess with the reaction taking place at 25°C. [CH_3I] = 0.0502 mol dm^{-3}.

The methyl proton signals are tabulated in Table 3.27, with the methyl proton ^{1}H NMR region presented in Figure 3.49. Figure 3.49 illustrates the change in the resonance peak intensities as the reaction progresses with respect to the methyl proton signals. The [Rh(CH_3COCHCNPhCH_3)(CO)(PPh_3)] **3b** methyl resonances (blue arrows, 1.688 ppm and 1.567 ppm) decrease as the reaction proceeds and the Rh(III)-alkyl product that forms has methyl resonances (green arrows, 1.869 ppm and 1.655 ppm) that increase as the reaction proceeds. The triplet that forms (~1.370 ppm) is attributed to the CH_3 of the CH_3I attached to the Rh central atom (formation of an alkyl reaction product) and this signal also increases as the reaction proceeds.[40,39]

Both Figure 3.48 and Figure 3.49 show that only one isomer of the Rh(III)-alkyl product forms during the reaction from a single isomer of **1b**.

The observed kinetic rate constants when interpreting the integrated peak areas for the methine and methyl peaks, when compared with those obtained through UV/VIS and IR spectroscopy shows good correlation between the values as seen in Figure 3.50. Table 3.28 contains the pseudo first order reaction rate constants obtained from the change in concentration with time, of both the methine and methyl resonance signals.

Table 3.28: Pseudo first order reaction rate constant of the methine and methyl resonance signals of the oxidative addition reaction between CH_3I and [Rh($CH_3COCHCNPhCH_3$)(CO)(PPh_3)] **3b** at 25°C with [CH_3I] = 0.0502 M.

Reaction step	**Resonance signal**	**k_{obs} (s^{-1})**
Rh(I)-loss	Methine	0.0112(6)
	O-CH_3	0.0111(7)
	N-CH_3	0.0111(6)
Rh(III)-alkyl gain	Methine	0.014(1)
	O-CH_3	0.014(1)
	N-CH_3	0.014(1)

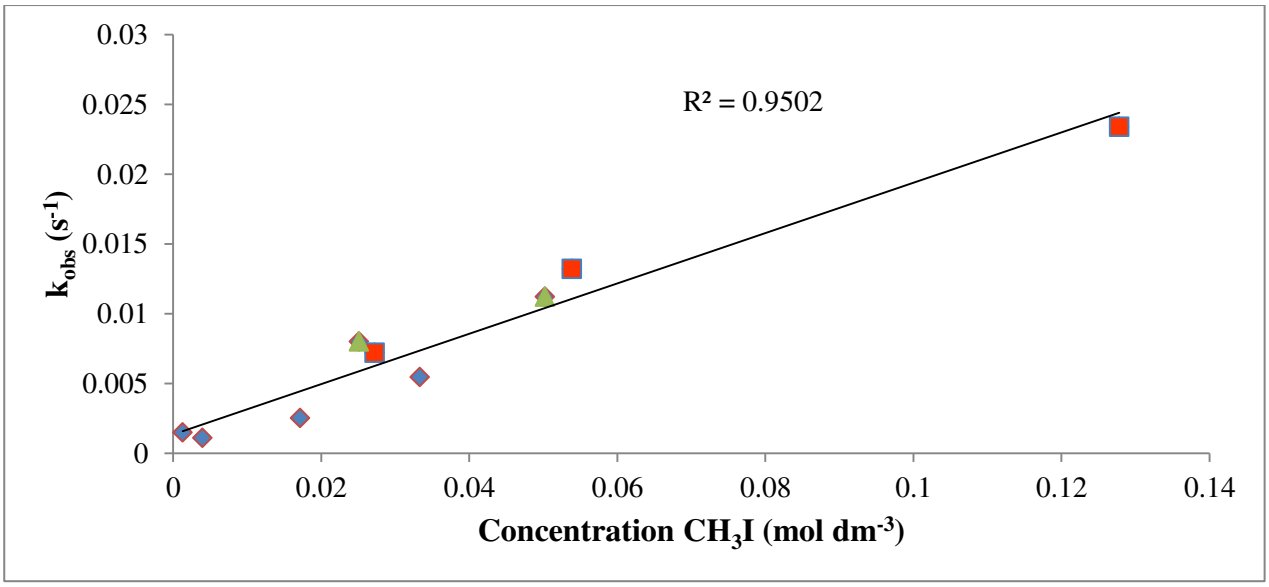

Figure 3.50: Observed kinetic rate constants for the reaction between [Rh($CH_3COCHCNPhCH_3$)(CO)(PPh_3)] **3b** and CH_3I obtained through UV/VIS spectroscopy, IR spectroscopy and NMR spectroscopy at 25°C.

3.5.3.2 NMR study of [Rh($CH_3COCHCNHCH_3$)(CO)(PPh_3)] and CH_3I

The [Rh($CH_3COCHCNHCH_3$)(CO)(PPh_3)] **3a** and CH_3I reaction yielded similar behaviour to those observed in the IR study in that there are two reaction steps observed during the reaction as shown in Scheme 3.6.

Table 3.29: Methine proton signal positions of the [Rh($CH_3COCHCNHCH_3$)(CO)(PPh_3)] **3a** isomers and the Rh(III)-alkyl and Rh(III)-acyl products isomers.

Complex	**Methine signal doublet(ppm)**	
[Rh($CH_3COCHCNHCH_3$)(CO)(PPh_3)] **3a** isomer A	5.002	(2 isomers)
[Rh($CH_3COCHCNHCH_3$)(CO)(PPh_3)] **3a** isomer B	4.990	
Rh(III)-alkyl	4.881	(only 1 isomer observed)
Rh(III)-acyl isomer A	4.976	(2 isomers)
Rh(III)-acyl isomer B	5.014	

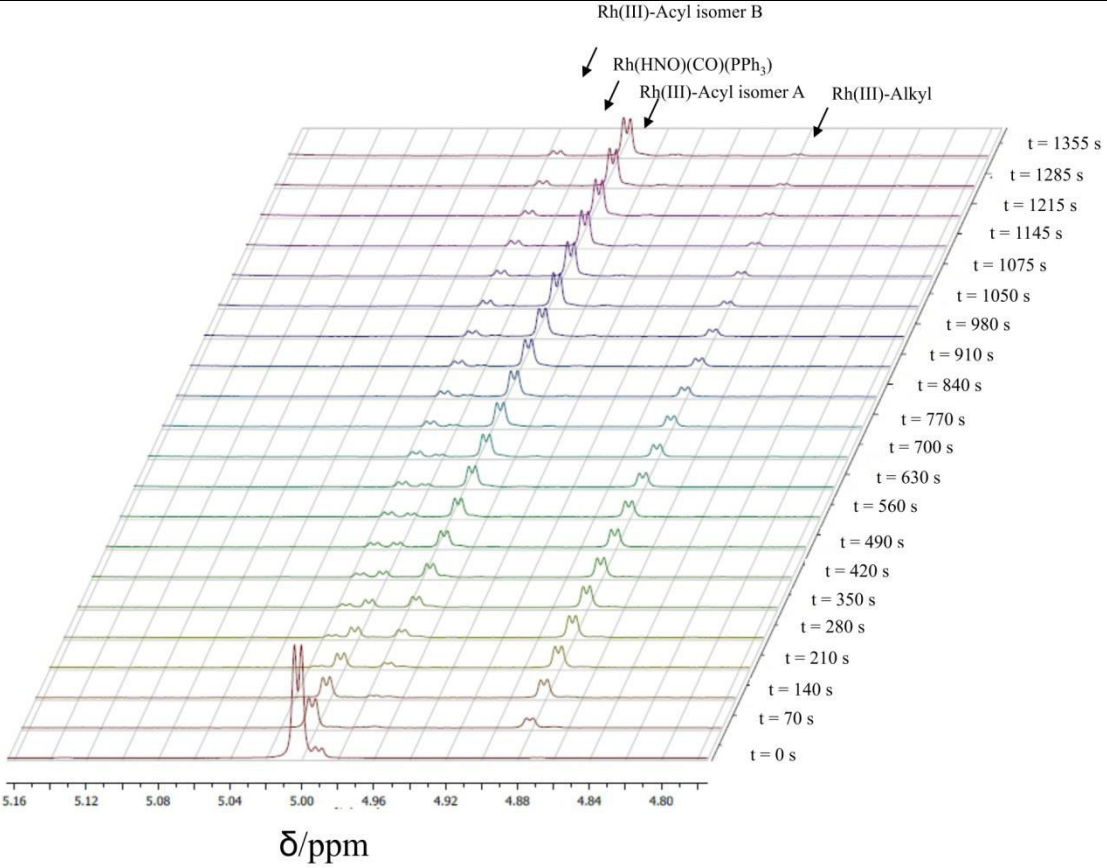

Figure 3.51: Stacked NMR spectra of the reaction between the [Rh($CH_3COCHCNHCH_3$)(CO)(PPh_3)] **3a** complex and CH_3I focusing on the methine proton signals. The CH_3I concentration was in a 6x excess with the reaction taking place at 25°C. [CH_3I] = 0.0502 mol dm^{-3}.

The methine proton signals are tabulated in Table 3.29 with the ^{1}H NMR region presented in Figure 3.51. Figure 3.51 illustrates the methine proton signals as the reaction progresses, with the peak positions given in Table 3.29. The pure [Rh($CH_3COCHCNHCH_3$)(CO)(PPh_3)] **3a** isomer A (5.002 ppm) and isomer B (4.990 ppm) show a decrease in the proton signal intensity as the reaction progresses with the formation of Rh(III)-alkyl appearing at 4.881 ppm. Only one Rh(III)-alkyl isomer is observed, but the exsistence of a second Rh(III) isomer cannot be excluded. The second Rh(I) isomer B is minute, therefore the alkyl that formed from the small Rh(I) isomer B could either not be observed since the peak is too small or possibly due to overlap with the Rh(III)-alkyl isomer observed.

The resonance peaks of the Rh(III)-alkyl isomers increase for a short time during the reaction up to a maximum intensity after which it starts to decrease. This is due to the formation of the Rh(III)-acyl product isomers (4.976 ppm and 5.014 ppm), which causes a decrease in the Rh(III)-alkyl isomers signal's intensity. Again it is observed that the intensity of the signals due to the second Rh(III)-acyl isomer B is very small and the formation of the second Rh(III)-acyl isomer B could not be followed kinetically.[3,42,43]

Table 3.30: Methyl proton signal positions of the [Rh($CH_3COCHCNHCH_3$)(CO)(PPh_3)] **3a** and the Rh(III)-alkyl and Rh(III)-acyl products.

Complex	**Methyl signals (ppm)**
[Rh($CH_3COCHCNHCH_3$)(CO)(PPh_3] **3a** isomer A	2.056; 1.583
[Rh($CH_3COCHCNHCH_3$)(CO)(PPh_3] **3a** isomer B	1.965; 1.838
Rh(III)-alkyl	2.017; 1.862
Rh(III)-acyl isomer A	2.861; 2.157
Rh(III)-acyl isomer B	2.555; 2.133

[42]M.M. Conradie, J. Conradie, *Dalton Trans.,* 2011, **40**, 8226-8237

[43]M.M. Conradie, J. Conradie, *Inorg. Chim.Acta.,* 2009, **362**, 519-530

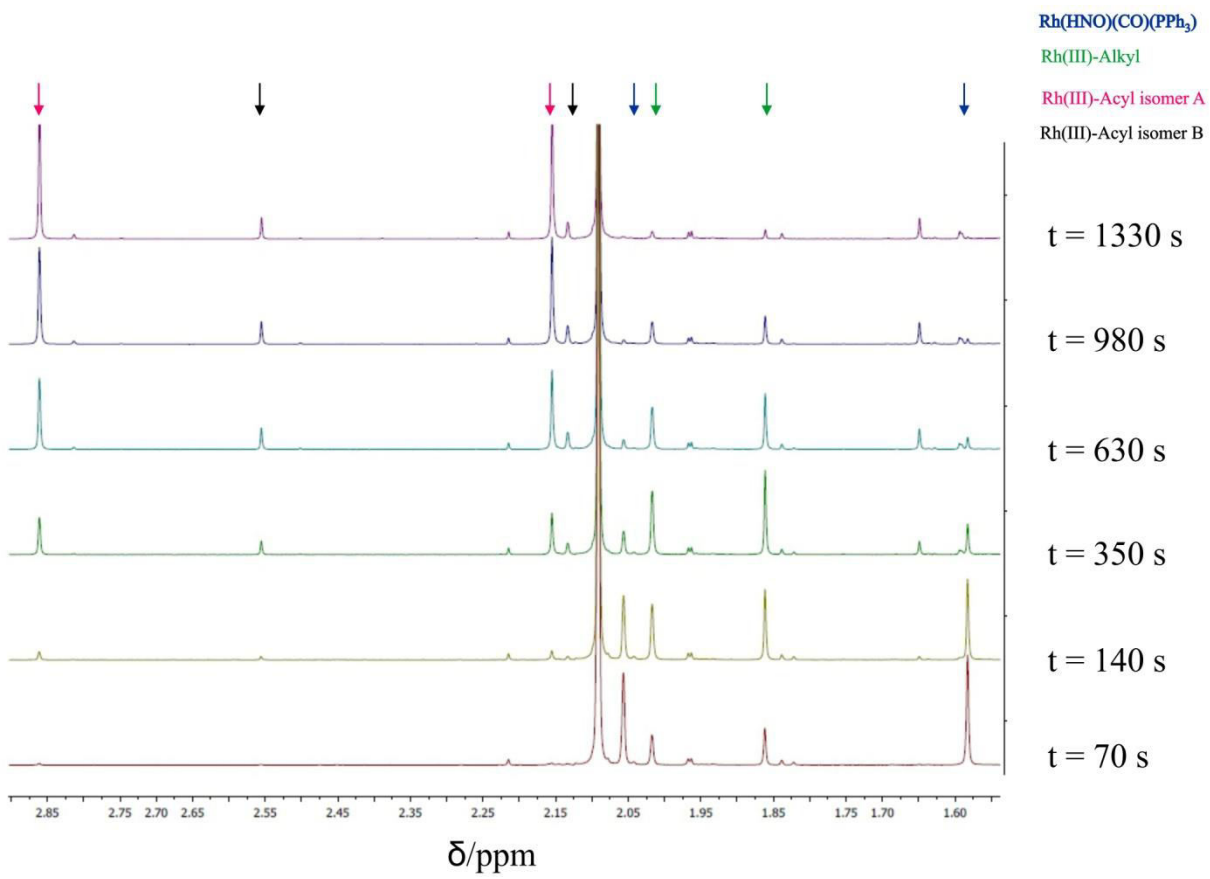

Figure 3.52: Stacked NMR spectra of the reaction between the [Rh($CH_3COCHCNHCH_3$)(CO)(PPh_3)] **3a** complex and CH_3I focussing on the methyl proton signals. The CH_3I concentration was in a 10x excess with the reaction taking place at 25°C. [CH_3I] = 0.0502 mol dm^{-3}.

The methine proton signals are tabulated in Table 3.30 with the ^1H NMR region presented in Figure 3.52. Figure 3.52 displays the change in the methyl proton signals between the two isomers of the starting material, [Rh($CH_3COCHCNHCH_3$)(CO)(PPh_3)] **3a** and the two isomers of the alkyl products that form as the reaction progresses. The Rh(I) starting material isomers (blue arrows, 2.056 ppm and 1.583 ppm and 1.965 ppm and 1.838 ppm) shows a decrease in the two methyl proton signals, the Rh(III)-alkyl product (green arrows, 2.017 ppm and 1.862 ppm) shows an increase in the signal strength at first. As the reaction progresses signals of the Rh(III)-alkyl product isomers decrease and the Rh(III)-acyl product isomers (main isomer A, pink arrows, 2.861 ppm and 2.157 ppm and minor isomer B, black arrows, 2.555 ppm and 2.133 ppm) show an increase in the signal strength as time goes on. The reason for the Rh(III)-alkyl methyl proton resonances showing an increase and then a decrease is the same as for the methine proton focussed analysis that is, the Rh(III)-alkyl product starts forming up to a maximum, after which it starts to convert to the Rh(III)-acyl product.[3,43]

The observed kinetic rate constants when interpreting the integrated peak area changes with time for the methine and methyl peaks, when compared with those obtained through UV/VIS and IR spectroscopy shows good correlation between the values as seen in Figure 3.53. Table 3.31 contains the pseudo first order reaction rate constants of both the methine and methyl resonance signals.

Table 3.31: Pseudo first order reaction rate constant of the methine and methyl resonance signals of the oxidative addition reaction between CH_3I and [Rh($CH_3COCHCNHCH_3$)(CO)(PPh_3)] **3a** at 25°C with [CH_3I] = 0.0502 M.

Reaction step	**Resonance signal**	**k_{obs} (s^{-1})**	**Average k_{obs} (s^{-1})**
Rh(I)-loss	Methine	0.0040(2)	0.0043(2)
	O-CH_3	0.0047(1)	
	N-CH_3	0.0042(2)	
Rh(III)-alkyl gain	Methine	---*	---*
	O-CH_3	---*	
	N-CH_3	---*	
Rh(III)-alkyl loss	Methine	0.00171(4)	0.00170(4)
	O-CH_3	0.00170(4)	
	N-CH_3	0.00168(4)	
Rh(III)-acyl gain	Methine	0.00157(2)	0.00152(1)
	O-CH_3	0.00150(1)	
	N-CH_3	0.00150(1)	

* Unable to obtain sufficient statistical data

The observed rate constants for the gain of Rh(III)-alkyl product was taken to be inaccurate since the reaction proceeded at too fast a pace. It was beyond the time scale of the ^{1}H NMR analysis, therefore there was insufficient amount of data points for statistical analysis. The loss of the Rh(III)-alkyl and the gain of the Rh(III)-acyl products showed good correlation between them.

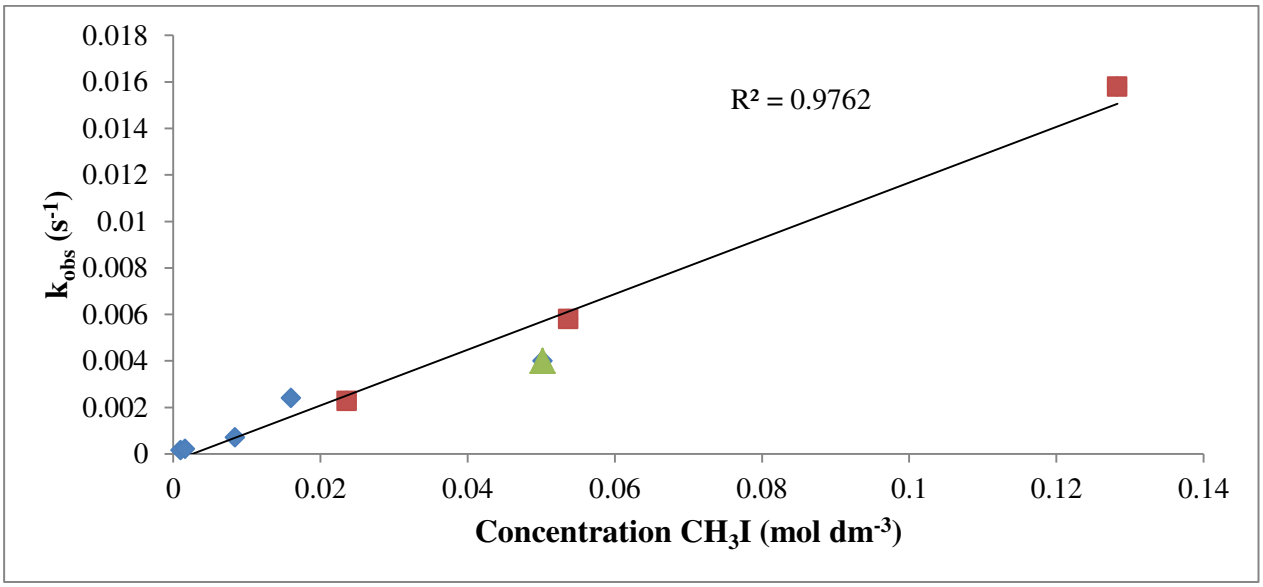

Figure 3.53: Observed kinetic rate constants for the reaction between [Rh($CH_3COCHCNPhCH_3$)(CO)(PPh_3)] **3a** and CH_3I obtained through UV/VIS spectroscopy, IR spectroscopy and NMR spectroscopy at 25°C. [CH_3I] = 0.1004 mol dm^{-3}.

3.5.4 Comparison of oxidative addition reaction rates for [Rh(L,L'-BID)(CO)(PPh_3)] + CH_3I reactions

Table 3.32 gives a summary of the second order reaction rate constants of the [Rh(L,L'-BID)(CO)(PPh_3)] + CH_3I oxidative addition reaction for various L,L'-BID ligands, as obtained from literature. From Table 3.32 it can be seen that the more electronegative the groups R and R' that are attached to the backbone of the ligand, the faster the reaction rate is. This is only applicable to the O,O-Bid ligands $(RCOCHCOR')^-$. The $(CF_3COCHCOCF_3)^-$ ligand complex has a reaction rate constant ~100 times smaller than the $(C_6H_5COCHCOC_6H_5)^-$ ligand complex. It has two CF_3 groups attached to the ligand, which are more electronegative than the two Ph groups, which are less electronegative than CF_3. When the complexes of the study are compared with the $(CH_3COCHCOCH_3)^-$ containing complex it can be seen that the substitution of one of the O atoms that coordinate to the metal centre with a less electronegative N atom causes a decrease in the reaction rate. As the atom or group that is attached to the N atom decreases in electronegativity the reaction rate also decreases ($(CH_3COCHCNHCH_3)^-$ = 0.1442 mol^{-1} dm^3 s^{-1}, $(CH_3COCHCNPhCH_3)^-$ = 0.21283 mol^{-1} dm^3 s^{-1}).

Table 3.32: Second order reaction rate constants of various complexes for the oxidative addition reaction between [Rh(L,L'-BID)(CO)(PPh_3)] and CH_3I obtained from literature including the complexes of this study at 25°C.

(L,L'-BID) of Rh(L,L'-BID)(CO)(PPh_3)	**k_2 (mol^{-1} dm^3 s^{-1})***	**Source**
$(C_4H_3SCOCHCOC_6H_5)^-$	0.0265	From ref [31]
$(C_6H_5COCHCOC_6H_5)^-$	0.00961	From ref [31]
$(C_4H_3SCOCHCOCF_3)^-$	0.00171	From ref [31]
$(CF_3COCHCOC_6H_5)^-$	0.00112	From ref [31]
$(C_4H_3SCOCHCOC_4H_3S)^-$	0.029	From ref [31]
$(CH_3COCHCOCH_3)^-$	0.024	From ref [31]
$(CH_3COCHCOC_6H_5)^-$	0.0093	From ref [31]
$(CH_3COCHCOCF_3)^-$	0.00146	From ref [31]
$(CF_3COCHCOCF_3)^-$	0.00013	From ref [31]
$(CH_3COCHCNHCH_3)^-$ **1a**	0.1442	From this study
$(CH_3COCHCNPhCH_3)^-$ **1b**	0.21283	From this study

3.5.5 Computational analysis of reaction mechanism

DFT calculations were utilized in order to determine the stereochemistry of the most likely products that could form during the oxidative addition reaction between [Rh(L,L'-BID)(CO)(PPh_3)] and CH_3I with L,L'-BID = $(CH_3COCHCNHCH_3)^-$ and $(CH_3COCHCNPhCH_3)^-$. The transition states involved in the reactions will also be presented, to shed light on the reaction mechanism of the oxidative addition and follow-up CO insertion reactions. DFT calculations of the reactants, transition states and products are also presented to support experimental observation. This was utilized in order to determine whether the linear oxidative addition of CH_3I to the [Rh(L,L'-BID)(CO)(PPh_3)] and the formation of the alkyl and acyl products is possible.

3.5.5.1 [Rh(CH_3COCHCNPhCH_3)(CO)(PPh_3)] 3b and CH_3I

Oxidative addition to the two possible [Rh(CH_3COCHCNPhCH_3)(CO)(PPh_3)] **3b** isomers can theoretically lead to 12 possible Rh(III)-alkyl products (indicated with 1a – 12a in Table 3.35, as well as their enantiomers 1b – 12b) and 6 possible Rh(III)-acyl products (indicated with 13a – 18a in Table 3.35, as well as their enantiomers 13b – 18b). The relative energies of the optimized geometries of all the possible Rh(III) isomers that could be optimized, are also given in Table 3.35. Some of the Rh(III)-acyl geometries could not be optimized and converted to the geometries of the lowest energy Rh(III)-acyl 13a and 13b. Since enantiomers have the same chemical properties and energies, we will only discuss the 12 possible Rh(III)-alkyl products (1a – 12a) and the 6 possible Rh(III)-acyl products (13a – 18a). In other words only 1a-18a will be discussed.

From the energies presented in Table 3.35, it is clear that Rh(III)-alkyl 2a and Rh(III)-acyl 13a have the lowest energy. It is also clear that Rh(III)-alkyl 1a and Rh(III)-acyl 13a are equi-energetic, in other words there is no driving force for the Rh(III)-alkyl 2a to convert to the Rh(III)-acyl 13a. This result is in agreement with the experimental observation that a Rh(III)-alkyl product is the final reaction product of the [Rh(CH_3COCHCNPhCH_3)(CO)(PPh_3)] **3b** + CH_3I reaction.

The lowest energy optimized geometry of the [Rh(CH_3COCHCNPhCH_3)(CO)(PPh_3)] **3b** alkyl product is with the N atom of the ligand trans to the PPh_3 ligand and the CH_3 and I atoms bonded at the apical positions (top and bottom with respect to the square planar geometry).

The [Rh(CH_3COCHCNPhCH_3)(CO)(PPh_3)] **3b** + CH_3I oxidative addition reaction is theoretically only possible if the activation barrier of the transition state is low enough to form the product, in this case the Rh(III)-alkyl 2a from Table 3.35. A DFT study of the transition state and the reaction steps is presented in Figure 3.54 - Figure 3.56, with the results summarized in Table 3.34.

Table 3.33: PW91/TZP DFT calculated energies and structures of the possible alkyl (1-12) and acyl (13-18) products of the oxidative addition reaction [Rh($CH_3COCHCNPhCH_3$)(CO)(PPh_3)] **3b** + CH_3I. Calculations are done with solvent effects (chloroform, $\varepsilon_0 = 4.8$) taken into account.

Product	Structures	Relative energy (eV)	Product	Structures	Relative energy (eV)	Product	Structures	Relative energy (eV)
1a	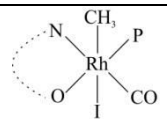	0.49	**7a**	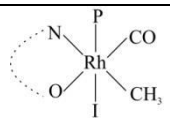	0.15	**13a**	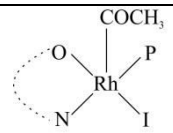	**0.00**
1b	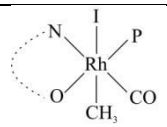	0.49	**7b**	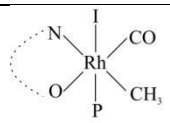	0.15	**13b**	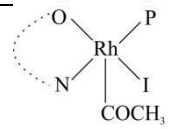	**0.03**
2a	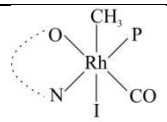	**0.01**	**8a**	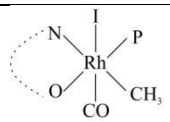	0.64	**14a**	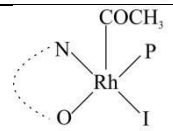	0.28
2b	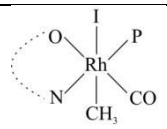	**0.02**	**8b**	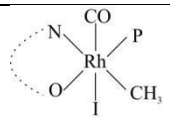	0.64	**14b**	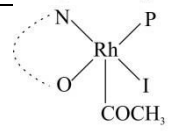	0.28
3a	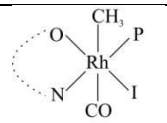	0.57	**9a**	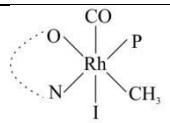	0.34	**15a**	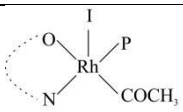	0.37
3b	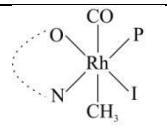	0.57	**9b**	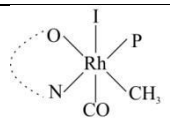	0.33	**15b**	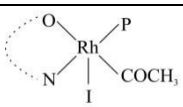	0.37
4a	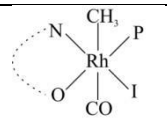	0.85	**10a**	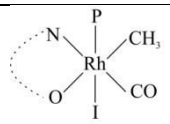	0.26	**16a**	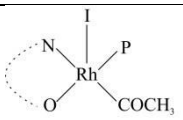	0.71
4b	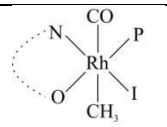	0.85	**10b**	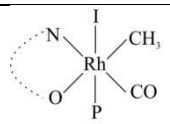	0.25	**16b**	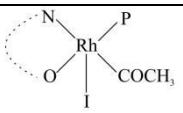	0.70
5a	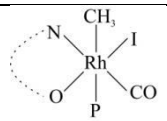	0.44	**11a**	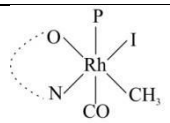	0.48	**17a**	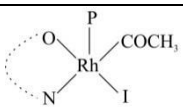	--
5b	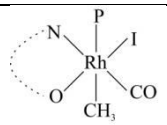	0.44	**11b**	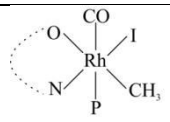	0.48	**17b**	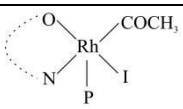	--
6a	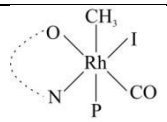	0.15	**12a**	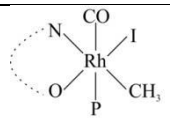	0.63	**18a**	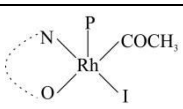	0.36
6b	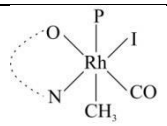	0.14	**12b**	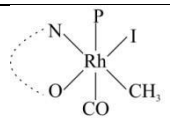	0.64	**18b**	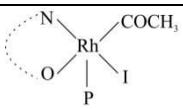	0.36

Figure 3.54 contains the optimized geometries of the reactant molecules, [Rh($CH_3COCHCNPhCH_3$)(CO)(PPh_3)] **3b** complex's reaction with CH_3I, before the reaction starts. There is a large separation between the reactant molecules (d = 32.731 Å) at the moment of the mixture. The reactant molecules then move through the bulk solution until the distance between them is short enough and the orientation of the molecules is sufficient to facilitate a reaction to occur.[42,43]

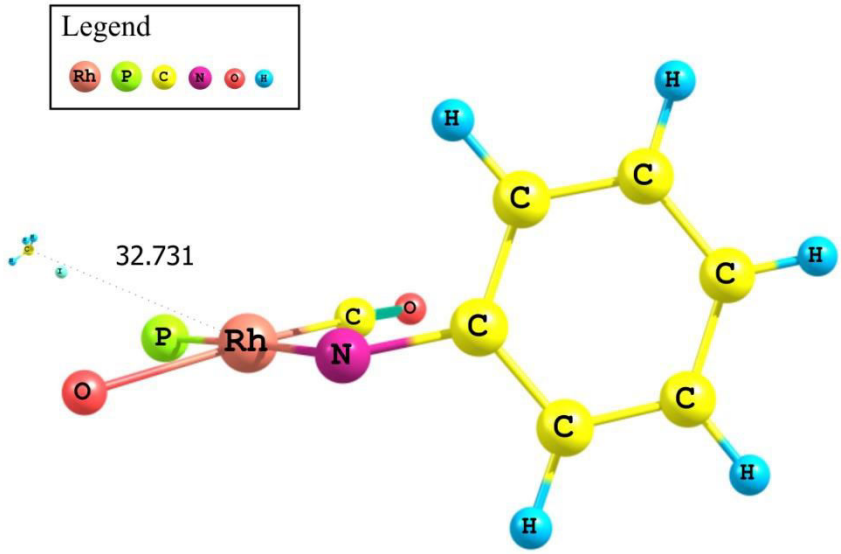

Figure 3.54: DFT calculated optimized geometries of the [Rh($CH_3COCHCNPhCH_3$)(CO)(PPh_3)] **3b** complex and CH_3I with a large separation between the reactant molecules. 3 x Ph of the PPh_3 ligand and C backbone and H atoms of [$CH_3COCHCNPhCH_3$] ligand excluded for clarity. Referred to as Reactants.

The oxidative addition reaction between CH_3I and square planar Rh(I) complexes can theoretically proceed *via* 3 different transition state structures.[44,45,46] The three methods of addition are a linear/back addition, where there is a near 180° angle formed between the approaching CH_3I and the Rh (*trans* addition), a bent addition, where the angle is between 90° and 180° (*trans* addition), and a front addition, where the angle is less than 90° (*cis* addition).

---

[44]T.R. Griffin, D.B. Cook, R. Haynes, J.M. Pearson, D. Monti, G.E. Morris, *J. Am. Chem. Soc.,* 1996, **118**, 3029-3030

[45]M. Feliz, Z. Freixa, P.W.N.M. Van Leeuwen, C. Bo, *Organometallics.,* 2005, **24**, 5718-5723

[46]M.M. Conradie, J. Conradie, *J. Organomet. Chem.,* 2010, **695**, 2126-2133

DFT computations showed that the most preferred addition method was a linear/back approach of the CH_3I to the Rh(I) metal centre. This method had an activation barrier that was ~7 times lower in energy than the other two methods.[42] Figure 3.55 contains the optimized geometry of the linear oxidative addition of the methyl group to the Rh(I) metal centre of the $[Rh(CH_3COCHCNPhCH_3)(CO)(PPh_3)]$ **3b** complex. The CH_3I molecule, when it is close enough to the Rh complex molecule, approaches linearly from the apical position (top as illustrated) with the methyl group closest to the Rh complex. This approach of the CH_3I molecule and the subsequent bond formation between the methyl group and the Rh metal centre cause an increase in the total system energy up to a maximum value, the activation energy.

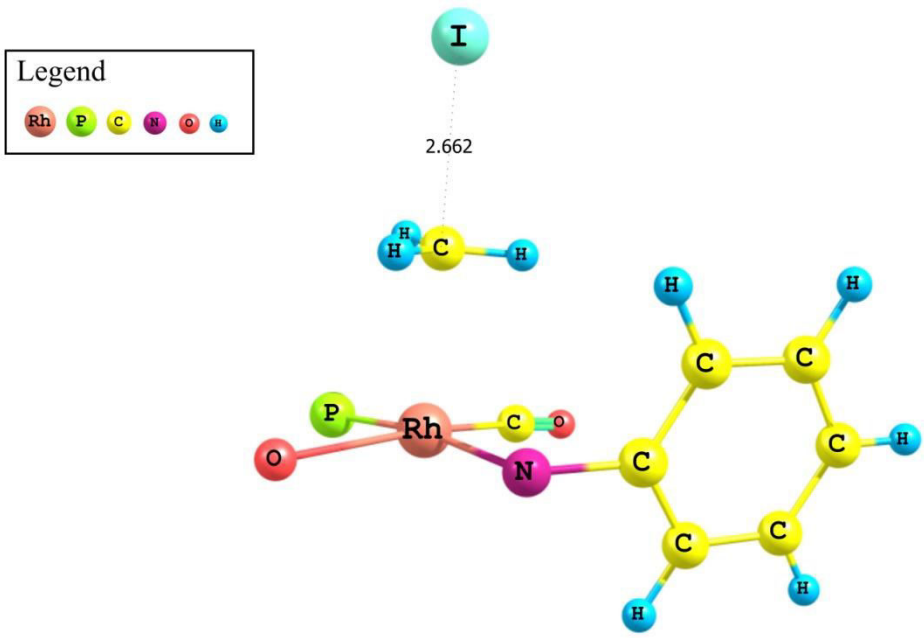

Figure 3.55: DFT calculated transition state of the linear oxidative addition reaction between the $[Rh(CH_3COCHCNPhCH_3)(CO)(PPh_3)]$ **3b** and CH_3I. 3 x Ph of the PPh_3 ligand and C backbone and H atoms of $[CH_3COCHCNPhCH_3]$ ligand excluded for clarity. Referred to as TS1.

After the Rh-$CH_{3(CH3I)}$ bond is formed the energy of the system decreases again as the bond formed stabilizes and the I^- ion diffuses away.[42,43] The I^- ion is then free to diffuse away into the bulk solution to react with another 5 coordinate Rh complex. The bond formation between the 5-coordinated cationic intermediate and a I^- ion is a barrierless process, with the formation of the Rh(III)-alkyl 2a product with the N atom of the ligand *trans* to the PPh_3 ligand and the CH_3 and I atoms bonded at the apical positions (top and bottom with respect to the square planar geometry), see Figure 3.56.

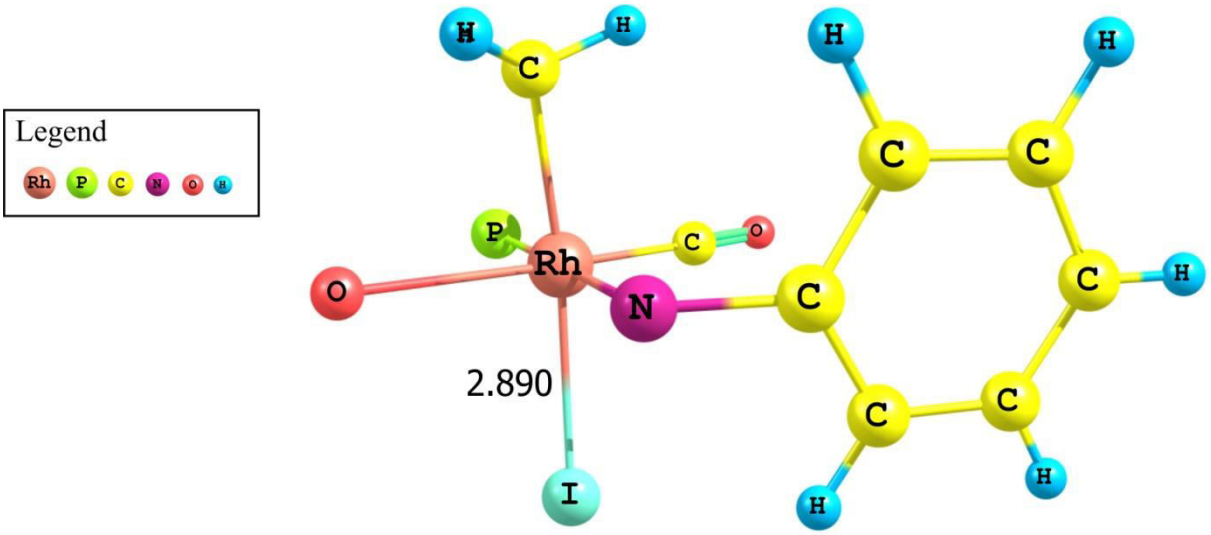

Figure 3.56: DFT calculated optimized geometry of the Rh(III)-alkyl 2a product. 3 x Ph of the PPh_3 ligand and C backbone and H atoms of [$CH_3COCHCNPhCH_3$] ligand excluded for clarity. Referred to as Alkyl 2a.

The energies of the reaction steps calculated by DFT are summarized in Table 3.34. The energies are given relative to the final product in the reaction mechanism. The energy barrier of the transition state (TS) is 0.29 eV and 0.83 eV higher than the reactants and [Rh($CH_3COCHCNPhCH_3$)(CO)(PPh_3)(CH_3)(I)]-alkyl 2a product respectively. The energy profile is thus favourable for the product formation.

Table 3.34: PW91/TZP DFT calculated energies (eV) for the reaction mechanism of the oxidative addition of CH_3I to [Rh($CH_3COCHCNPhCH_3$)(CO)(PPh_3)] **3b**.

Complex	**Energy (eV)**
Reactants: [Rh($CH_3COCHCNPhCH_3$)(CO)(PPh_3)] **3b** and CH_3I	0.54
TS1	0.83 (imaginary frequency -270.0 cm^{-1})
Alkyl: [Rh(III)-alkyl 2a]	0.00

All DFT attempts at determining a TS for formation of an acyl product through CO insertion at the Rh(III)-alkyl 2a failed. This fact, as well as the fact that Rh(III)-alkyl 2a and Rh(III)-acyl 13a are equi-energetic, compliment the experimental findings that a Rh(III)-alkyl is the final reaction product of the [Rh($CH_3COCHCNPhCH_3$)(CO)(PPh_3)] **3b** + CH_3I reaction.

3.5.5.2 [Rh($CH_3COCHCNHCH_3$)(CO)(PPh_3)] 3a and CH_3I

Table 3.35 contains the optimized geometry energies of the [Rh($CH_3COCHCNHCH_3$)(CO)(PPh_3)] **3a** + CH_3I reaction products, 12 possible Rh(III)-alkyl products (indicated with 1a – 12a Table 3.35, as well as their enantiomers 1b – 12b) and 6 possible Rh(III)-acyl products (indicated with 13a – 18a Table 3.35, as well as their enantiomers 13b – 18b). Some of the Rh(III)-acyl geometries could not be optimized and converted to the geometries of the lowest energy Rh(III)-acyl 13a and 14a. We will only discuss 12 possible Rh(III)-alkyl products (1a – 12a) and 6 possible Rh(III)-acyl products (13a – 18a), since enantiomers have the same chemical properties and energies. In other words only 1a-18a will be presented.

Evaluating the energies of the Rh(III)-alkyl isomers in Table 3.35, it can be seen that the most preferred orientation of the product geometry is N atom of the ligand *trans* to the PPh_3 ligand and the CH_3 and I atoms bonded at the apical positions (top and bottom with respect to the square planar geometry) since it has the lowest relative energy (2a and 2b). However, the Rh(III)-alkyl isomer with the N atom of the ligand *cis* to the PPh_3 ligand and the CH_3 and I atoms bonded at the apical positions (1a and 1b) is only slightly higher in energy (0.07 eV). This result is in agreement with the experimental result obtained on NMR that mainly one Rh(III)-alkyl product isomer is formed as the two Rh(I)-isomers react with CH_3I. The second Rh(III)-alkyl product isomer , 1a, is not observed, probably since it has a slightly higher energy than the main isomer and therefore will only form in very small amounts.

Evaluation of the energies of the Rh(III)-acyl isomers in Table 3.35, indicates that the two Rh(III)-acyl isomers 13a and 14a with the $COCH_3$ ligand in the apical position, have the lowest energy. Furthermore, the energy of Rh(III)-acyl isomers 13a and 14a are *ca* 0.3 eV lower than the energy of the lowest energy Rh(III)-alkyl isomers 1a and 2a. This is in agreement with the experimental result that the Rh(III)-alkyl product of oxidative addition converts *via* CO insertion to a lower more stable Rh(III)-acyl product as the final reaction product. Rh(III)-acyl 13a has slightly higher energy (0.04 eV) than 14a, therefore the amount of 13a will be less than 14a, in agreement with experimentally observed results.

Table 3.35: PW91/TZP DFT calculated energies and structures of the possible alkyl (1-12) and acyl (13-18) products of the oxidative addition reaction [Rh($CH_3COCHCNHCH_3$)(CO)(PPh_3)] **3a** + CH_3I. Calculations are done with solvent effects (chloroform, (ε_0 = 4.8) taken into account.

Product	Structures	Relative energy (eV)	Product	Structures	Relative energy (eV)	Product	Structures	Relative energy (eV)
1a	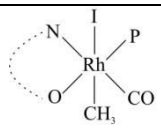	**0.34**	**7a**	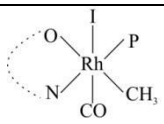	0.41	**13a**	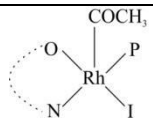	**0.04**
1b	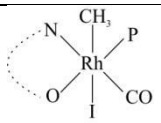	**0.33**	**7b**	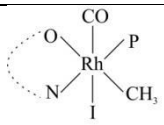	0.40	**13b**	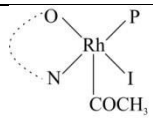	**0.04**
2a	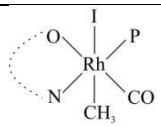	**0.25**	**8a**	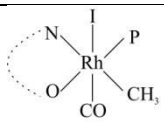	0.64	**14a**	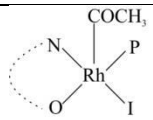	**0.00**
2b	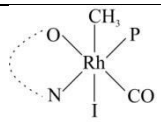	**0.26**	**8b**	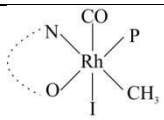	0.64	**14b**	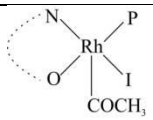	**0.00**
3a	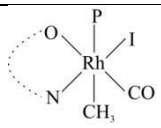	0.43	**9a**	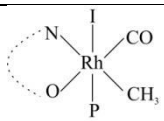	0.42	**15a**	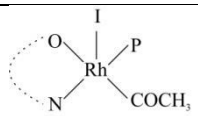	--
3b	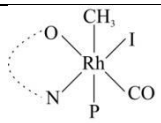	0.43	**9b**	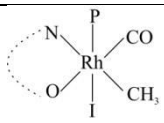	0.44	**15b**	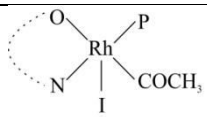	--
4a	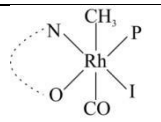	0.71	**10a**	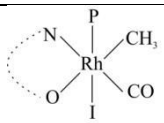	0.34	**16a**	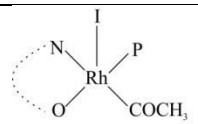	0.76
4b	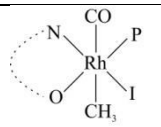	0.72	**10b**	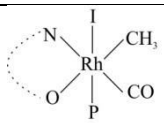	0.35	**16b**	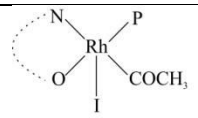	0.79
5a	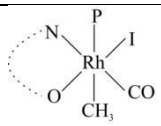	0.46	**11a**	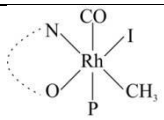	0.80	**17a**	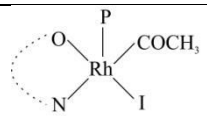	--
5b	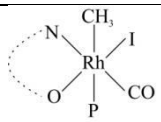	0.46	**11b**	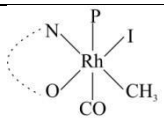	0.87	**17b**	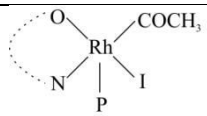	--
6a	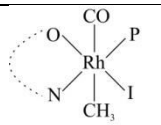	0.66	**12a**	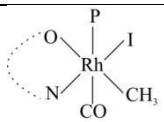	0.68	**18a**	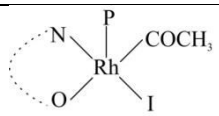	--
6b	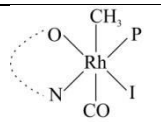	0.66	**12b**	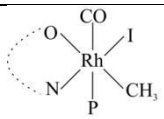	0.68	**18b**	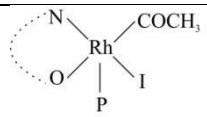	--

The DFT calculated results for the [Rh($CH_3COCHCNHCH_3$)(CO)(PPh_3)] **3a** +CH_3I oxidative addition reaction are presented in Figure 3.57 - Figure 3.61, with the results summarized in Table 3.36. The results related to the most stable reactant isomer, the isomer with the PPh_3 group *trans* to N, is presented.

The oxidative addition reaction between CH_3I and square planar Rh(I) complexes can theoretically proceed *via* 3 different transition state structures.[44,45,46] The three methods of addition are a linear/back addition, where there is a near 180° angle formed between the approaching CH_3I and the Rh (*trans* addition), a bent addition, where the angle is between 90° and 180° (*trans* addition), and a front addition, where the angle is less than 90° (*cis* addition). DFT computations showed that the most preferred addition method was a linear/back approach of the CH_3I to the Rh metal centre. This method had an activation barrier that was ~7 times lower in energy than the other two methods.[42] Figure 3.57 contains the optimized geometries of the the reactant molecules, [Rh($CH_3COCHCNHCH_3$)(CO)(PPh_3)] **3a** and CH_3I, before the oxidative addition reaction proceeds. It can be seen that there is a large separation between the two molecules. The molecules merely move through the bulk solution until both the distance between the two is short enough and the orientation of the molecules is correct in order to facilitate a reaction. There is a distance between the two molecules > 21.825 Å. As the molecules move through the bulk solution this distance decreases.

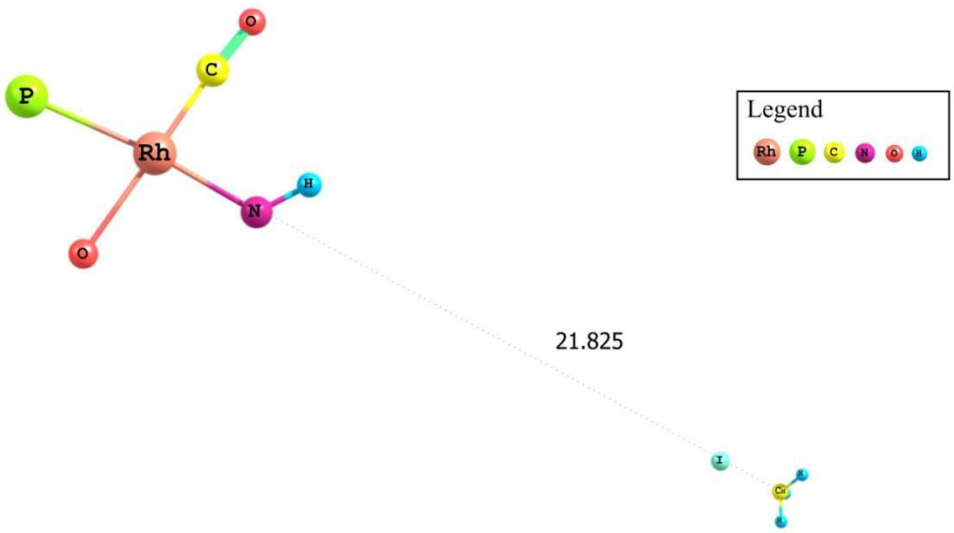

Figure 3.57: DFT calculated optimized geometries of the [Rh($CH_3COCHCNHCH_3$)(CO)(PPh_3)] **3a** complex and CH_3I with a large separation between the reactant molecules. 3 x Ph of the PPh_3 ligand and C backbone and H atoms of [$CH_3COCHCNHCH_3$] ligand excluded for clarity. Referred to as Reactants.

Figure 3.58 contains the optimized geometries of the first TS of the [Rh($CH_3COCHCNHCH_3$)(CO)(PPh_3)] **3a** + CH_3I reaction. The CH_3I approaches the [Rh($CH_3COCHCNHCH_3$)(CO)(PPh_3)] **3a** complex from the apical position linearly with the methyl group closest to the Rh metal centre. As the CH_3I molecule approaches, the distance between the methyl group and I increases from 2.1736 Å (DFT optimized geometry of CH_3I) to 2.610 Å and the distance between the methyl group and the Rh metal centre decreases until a bond is formed. When the distance between the methyl group and the I atom reaches a certain length the bond between the two breaks and the I^- ion is then free to diffuse back into the bulk solution in order to react with a 5 coordinate Rh intermediate that is formed. As the Rh-$CH_{3(CH3I)}$ distance decreases, the total energy of the system increases up to a maximum point. At this maximum the transition state occurs, where the CH_3I molecule breaks up into a methyl group and I^- ion and the methyl group then forms a bond with the Rh metal centre to form a 5 coordinate intermediate complex as seen in Figure 3.58. After the bond is formed the total system energy then starts to decrease.

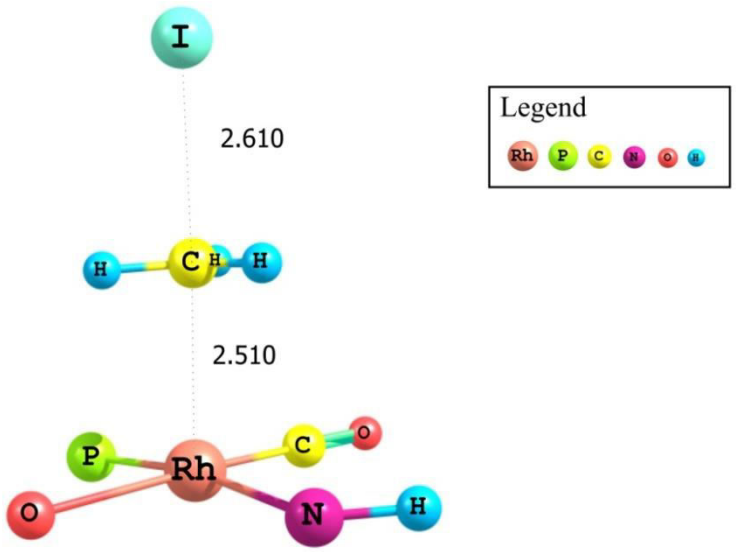

Figure 3.58: DFT calculated optimized geometry of the linear oxidative addition reaction between the [Rh($CH_3COCHCNHCH_3$)(CO)(PPh_3)] **3a** and CH_3I. The methyl group of the CH_3I moves towards the Rh metal centre in order to form a bond and the distance between the methyl group and the I atom increases. 3 x Ph of the PPh_3 ligand and C backbone and H atoms of [$CH_3COCHCNHCH_3$] ligand excluded for clarity. Referred to as TS1.

As the I^- ion approaches the Rh metal centre, the total energy of the system decreases up until the bond formation occurs, after which the system reaches a point of stability as shown in Figure 3.59 with the formation of the Rh(III)-alkyl complex.

The next reaction step is the CO insertion of the CH_3 migration step. The CH_3 group thus starts moving towards the C atom of the CO group. As the CH_3 migrates towards the CO group, the CO group gets lifted out of the plane formed between the N and O atoms of the ligand and the P atom of the PPh_3 ligand by 15.50° effectively decreasing the C_{methyl}-Rh-C_{co} bond angle even more. During the migration the Rh-C_{methyl}, the bond length increases and the C_{methyl}-C_{co} distance decreases. These changes continue up to a certain point (C_{methyl}-Rh-C_{co} = 56.92°) where the Rh-C_{methyl} bond breaks and the C_{methyl}-C_{co} bond forms. [42,43] As can be seen from Figure 3.60, when the moment of the transition state is reached, the ligand starts shifting, or flipping, in order to position the $COCH_3$ group in an apical position.

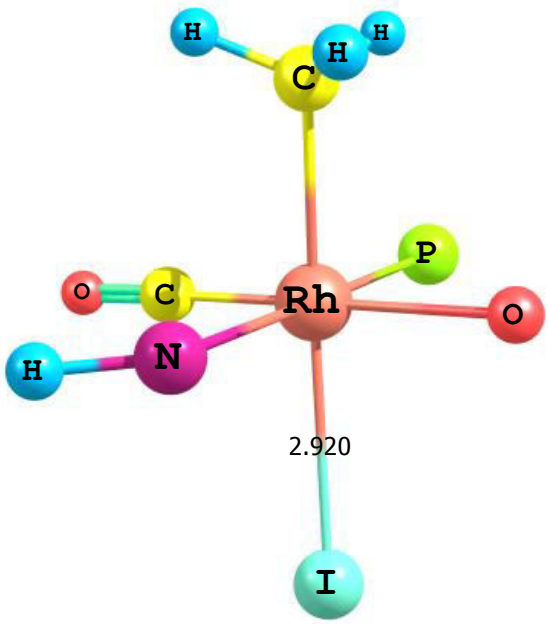

Figure 3.59: DFT calculated optimized geometry of the Rh(III)-alkyl 2a product formed during step 1. 3 x Ph of the PPh_3 ligand and C backbone and H atoms of [$CH_3COCHCNHCH_3$] ligand excluded for clarity. Referred to as Alkyl-2a.

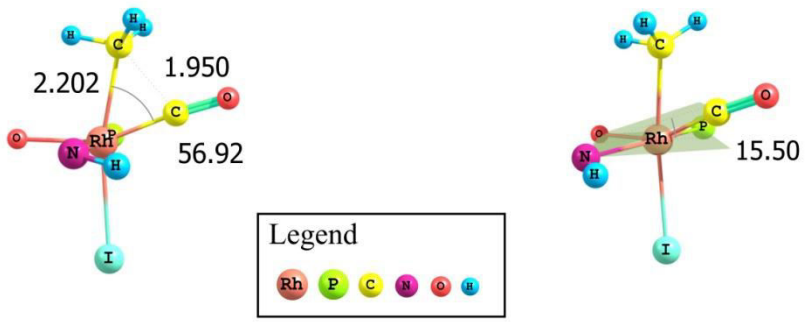

Figure 3.60: Left: Geometry of the DFT calculated transition state of the methyl migration towards the CO group in the formation of the [Rh($CH_3COCHCNHCH_3$)(CO)(PPh_3)] **3a** acyl 14a product. Right): Deviation of the CO group from the square planar geometry. 3 x Ph of the PPh_3 ligand and C backbone and H atoms of [$CH_3COCHCNHCH_3$] ligand excluded for clarity. Referred to as TS2.

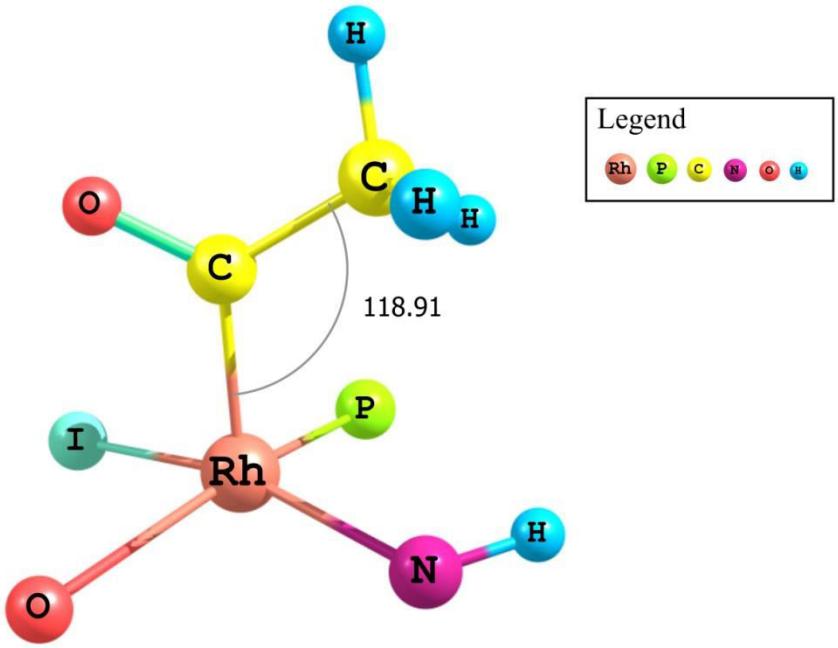

Figure 3.61: DFT calculated optimized geometry of the [Rh($CH_3COCHCNHCH_3$)(CO)(PPh_3)-acyl] product after the migration of the methyl group towards the CO group. 3 xPh of the PPh_3 ligand and C backbone and H atoms of [$CH_3COCHCNHCH_3$] ligand excluded for clarity. Referred to as Acyl.

Figure 3.61 illustrates the final product's geometry, optimized by DFT calculations, of the [Rh($CH_3COCHCNHCH_3$)(CO)(PPh_3)]-acyl product 14a. It can be seen that the acyl group is now in an apical position and that the I atom has taken the place of the PPh_3 group from the

[Rh($CH_3COCHCNHCH_3$)(CO)(PPh_3)]-alkyl product 2a with the PPh_3 group taking the place of the CO group of alkyl product 2a. This is due to this orientation having a smaller total system energy than any of the other orientations. After the bond is formed between the C_{methyl} and the C_{CO} atoms, the orientation starts to change. The 6 membered ring formed between the Rh metal centre and the L,L'-BID ligand 'flips'. The O atom moves in such a way as to allow for the I atom to be positioned *trans* to the N atom. During this shift the energy of the system decreases up to a minimum where the I atom is *trans* and no longer in an apical position until the final, stable geometry of the 5 coordinated Rh(III) complex is obtained.[42,43]

The energies of the two reaction steps calculated by DFT are summarized in Table 3.36. The energies are given relative to the final product in the reaction mechanism.

Table 3.36: PW91/TZP DFT calculated energies (kcal/mol) for the reaction mechanism of the oxidative addition of CH_3I to [Rh($CH_3COCHCNHCH_3$)(CO)(PPh_3)] **3a**.

Complex	**Energy (eV)**
Reactants: [Rh($CH_3COCHCNHCH_3$)(CO)(PPh_3)] **3a** and CH_3I	0.82
TS1	1.08 (imaginary frequency -266.0 cm^{-1})
Alkyl: [Rh(III)-alkyl product 2a]	0.26
TS2	1.17 (imaginary frequency -419.0 cm^{-1})
Acyl: [Rh(III)-acyl product 14a]	0.00

From Table 3.36 it can be seen that the first transition state, the linear addition of CH_3I, to the structure has an energy barrier of only 0.26 eV. This energy barrier calculated for the [Rh($CH_3COCHCNHCH_3$)(CO)(PPh_3)] **3a** + CH_3I reaction, is favourable for the reaction to occur and to proceed to the Rh(III)-alkyl reaction product that is 0.82 eV lower in energy than the TS1. The energy barrier of the second step is higher than the first step (0.91 eV *versus* 0.26 eV) indicating that the second reaction, is much slower than the first reaction step, in agreement with experimental results. The Rh(III)-acyl product has the lowest energy and thus most stable and constitutes the final reaction product. These computational results is thus corroborated by both the IR and NMR spectra illustrating the formation of an alkyl and acyl product with the acyl product being the final product.

3.5.6 Summary of oxidative addition reaction kinetics: CH_3I + [Rh(L,L'-BID)(CO)(PPh_3)]

3.5.6.1 [Rh($CH_3COCHCNPhCH_3$)(CO)(PPh_3)] 3b and CH_3I

In Table 3.37 the results for the second order reaction rate constants of the [Rh($CH_3COCHCNPhCH_3$)(CO)(PPh_3)] **3b** + CH_3I reaction as obtained by IR, UV/VIS and NMR are summarized. The second order reaction rate constants are comparable with each other within experimental error. These results, along with the DFT calculated results, suggest a one step reaction leading from [Rh($CH_3COCHCNPhCH_3$)(CO)(PPh_3)] **3b** and CH_3I as reactants, to a [Rh($CH_3COCHCNPhCH_3$)(CO)(PPh_3)(CH_3)(I)] alkyl product (2a) with no additional steps taking place in the reaction. The reaction scheme for this complex can be seen in Figure 3.62.

Table 3.37: Second order reaction rate constants (k_2) obtained *via* UV/VIS, IR and NMR spectrometry for the oxidative addition reaction between [Rh($CH_3COCHCNPhCH_3$)(CO)(PPh_3)] **3b** and CH_3I at 25°C.

Method used	**k_2 (s^{-1})**
UV/VIS	0.2128
IR	0.2383
NMR	0.2232

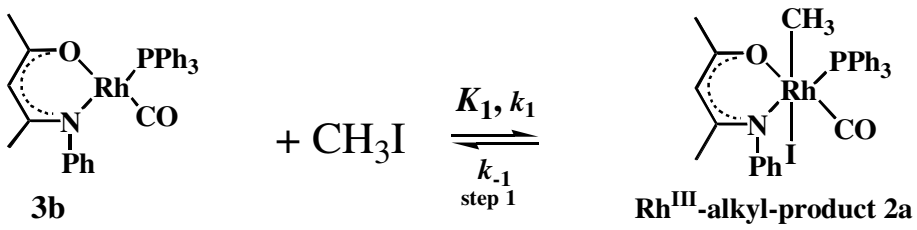

Figure 3.62: Reaction scheme for the oxidative addition reaction of [Rh($CH_3COCHCNPhCH_3$)(CO)(PPh_3)] **3b** and CH_3I.

3.5.6.2 [Rh($CH_3COCHCNHCH_3$)(CO)(PPh_3)] 3a and CH_3I

In Table 3.38 the results for the second order reaction rate constants of the [Rh($CH_3COCHCNHCH_3$)(CO)(PPh_3)] **3a** + CH_3I reaction as obtained by IR, UV/VIS and NMR are summarized. The results obtained for the second order reaction rate constants are comparable with each other within experimental error. The results obtained regarding the different reaction products from IR and NMR, along with the DFT calculated results, suggest a two step reaction leading from [Rh($CH_3COCHCNHCH_3$)(CO)(PPh_3)] **3a** (both isomers) and CH_3I as reactants, to two [Rh($CH_3COCHCNPhCH_3$)(CO)(PPh_3)(CH_3)(I)] alkyl products (2a and 1a, 1a currently unobserved experimentally), to the formation of two [Rh($CH_3COCHCNPhCH_3$)(PPh_3)($COCH_3$)(I)] acyl products (14a and 13a). The reaction scheme for this complex can be seen in Figure 3.63.

Table 3.38: Second order reaction rate constants (k_2) obtained *via* UV/VIS, IR and NMR spectrometry for the oxidative addition reaction between [Rh($CH_3COCHCNHCH_3$)(CO)(PPh_3)] **3a** and CH_3I at 25°C.

Method used	**k_2 (s^{-1})**
UV/VIS	0.1442
IR	0.1298
NMR	0.1328

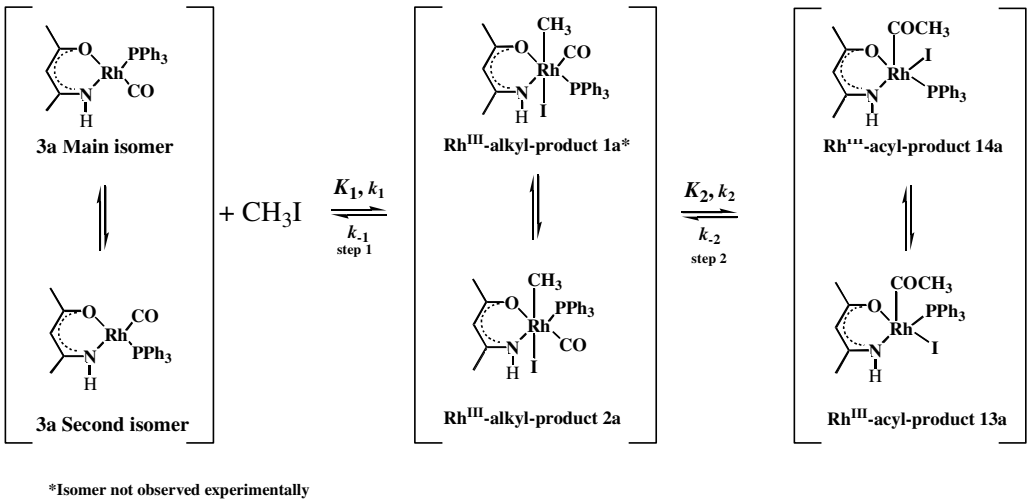

Figure 3.63:Reaction scheme for the oxidative addition reaction of [Rh($CH_3COCHCNHCH_3$)(CO)(PPh_3)] **3a** and CH_3I.

CHAPTER 3

4 Experimental

4.1 Experimental: Synthesis

4.1.1 [$CH_3COCHCNH_2CH_3$] 1a

1a

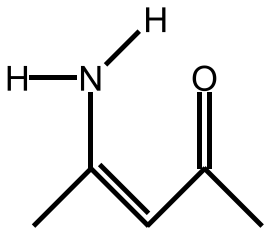

Acetylacetone (5 g, 5.2 ml) was placed in a round bottom flask. Ammonia (6.9763 g, 7 ml) was added to the acetylacetone whilst stirring. A white solid formed. After 30 minutes the white solid disappeared and a yellow solution was obtained. The flask was left in a fumehood overnight. A yellow precipitate was obtained. The solid was dried with filter paper and weighed.[1,2,3] Yield = 98%. ^{1}H NMR: 9.7226 ppm (s, N-H); 5.045 ppm (s, C-H); 2.0453 ppm (s, CH_3-CN); 1.9217 ppm (s, CH_3-CO)

4.1.2 [$CH_3COCHCNHPhCH_3$] 1b

1b

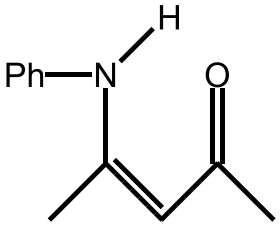

Acetylacetone (5 g, 5.2 ml) was placed in a round bottom flask outfitted with a condenser for refluxing. Aniline (6.9763 g, 7 ml) and concentrated hydrochloric acid (5 g, 4.3 ml) was added to the flask whilst stirring and the mixture was brought to reflux for 5hrs. Diethyl ether was

---

[1] A.F. Dove, V.C. Gibson, E.L. Marshall, A.J.P. White, D.J. Williams, *J. Chem. Soc. Dalton Trans.*, 2004, 570-578

[2] J.E. Parks, R.H. Holm, *Inorg. Chem.*, 1968, **7**, 1408-1416

[3] P.H.M. Budzelaar, N.N.P. Moonen, R. De Gelder, J.M.M. Smits, A.W. Gal, *Eur. J. Inorg. Chem.*, 2000, 753-769

added to the mixture and then placed in the fridge (-5 ^{o} C). The yellow crystalline precipitate was filtered and washed with cold diethyl ether and recrystallized.[1,2,3] Yield = 50%. ^{1}H NMR: 12.4912 ppm (s, O-H); 7.3875 ppm – 7.1168 ppm (m, C_6H_5-N); 5.2077 ppm (s, C-H); 2.1218 ppm (s, CH_3-CN); 2..0144 ppm (s, CH_3-CO)

4.1.3 [$CH_3CNHPhCHCNPhCH_3$] 1c

1c

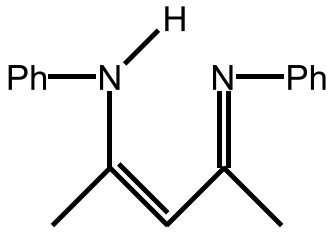

Acetylacetone (9.75 g, 10 ml) was placed in a round bottom flask within an ice bath. Aniline (18.36 g, 18 ml) was added to the acetylacetone whilst stirring. Hydrochloric acid (9.7857 g, 8.3 ml) was added dropwise over 5 mins to the mixture and the mixture was left to stir for 5hrs at low temperature. The mixture was then left stirring overnight. The precipitate was filtered and washed with petroleum ether, then dissolved in a mixture of dichloromethane (8 ml), water (50 ml) and triethylamine (20 ml). The solution was extracted with diethyl ether, evaporated under reduced pressure and the solid was recrystallized from ethanol.[1,2,3] Yield = 87%. ^{1}H NMR: 7.3400 ppm – 6.9707 ppm (m, 2 x C_6H_5-N); 4.9057 ppm (s, C-H); 2.0314 (s, 2 x CH_3-CN)

4.1.4 [Rh(L,L'-BID)$(CO)_2$] 2

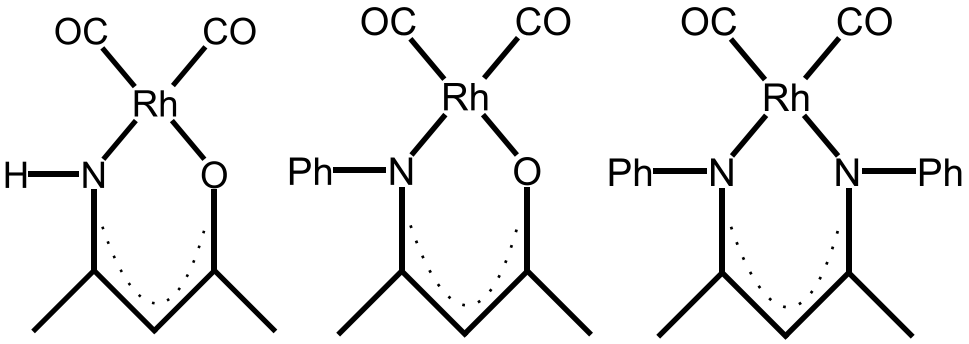

2a 2b 2c

Di-μ-chloro-tetracarbonyldirhodium(I) (0.05 g, 0.1286 mmole) was dissolved in methanol (5 ml) and the ligand (0.2572 mmole), also dissolved in methanol (2 ml) ,was added dropwise

over 10 minutes whilst stirring. The mixture was left to stir for 1 hour. The mixture was then extracted with N-hexane until the N-hexane was clear, the solvents combined and reduced under reduced pressure. The solid that precipitated out was then collected, recrystallized and weighed.[4,5,6]

2a: Yield = 69%. ^{1}H NMR: 5.3635 ppm - 5.2933 ppm (d, C-H, J^4 = 2.311 Hz); 2.1749 ppm – 2.1720 ppm (d, CH_3-CN, J^4 = 0.74 Hz); 2.1060 ppm (CH_3-CO). ν_{CO}: 2044.13 cm^{-1}; 1971.02 cm^{-1}.

2b: Yield = 78%. ^{1}H NMR: 7.3882 ppm – 7.0605 ppm (m, C_6H_5-N); 5.2977 ppm (s, C-H); 2.1949 ppm (s, CH_3-CN); 2.1414 ppm (s, CH_3-CO). ν_{CO}: 2058.98 cm^{-1}; 1997.69 cm^{-1}.

2c: Yield = 73%. ^{1}H NMR: 7.3720 ppm – 7.1656 ppm (m, 2 x C_6H_5-N); 5.1009 ppm (s, C-H); 1.8711 ppm (s, 2 x CH_3-CN). ν_{CO}: 2055.61 cm^{-1}; 2046.72 cm^{-1} 1992.07 cm^{-1}; 1977.79 cm^{-1}.

4.1.5 [Rh(L,L'-BID)(CO)(PPh$_3$)] 3

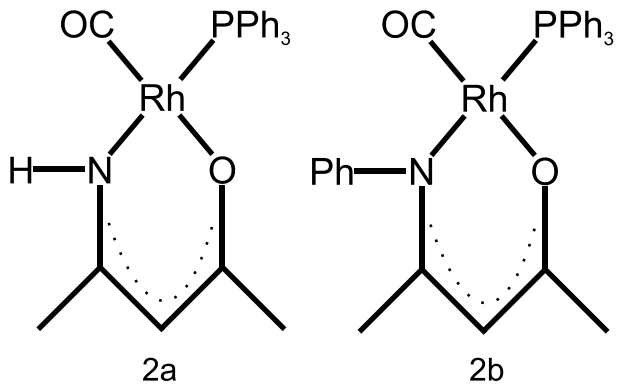

[Rh(Bid-L,L')(CO)$_2$] (0.2 mmol) was dissolved in N-hexane (3 ml). Triphenylphosphine (0.23 mmol) was dissolved in N-hexane (3 ml) and added dropwise over 10 minutes to the dicarbonyl complex solution whilst stirring. The mixture was then left to stir until no more bubbles were evolved. The precipitate that formed was filtered off, recrystallized and weighed.[7,8,9,10,11,12]

---

[4] J. Han, L.F. Zhang, W. Wan, *J. Organomet. Chem.*, 2003, **672**, 86-93

[5] F. Bonati, G. Wilkinson, *J. Chem. Soc.*, 1963, 3156-3160

[6] C. Pretorius, A. Roodt, *Acta. Cryst.*, 2012, **E68**, m1451-m1452

[7] K.H. Hopmann, N.F. Stuurman, A. Muller, J. Conradie, *Organometallics*, 2010, **29**, 2446-2458

[8] N.F. Stuurman, R. Meijboom, J. Conradie, *Polyhedron,* 2011, **30**, 660-665

3a: Yield = 77%. ^{1}H NMR: *Isomer A*: 7.7153 ppm – 7.3524 ppm (m, C_6H_5-P); 5.1005 ppm – 5.0925 ppm (d, C-H, , J^4 = 0.93 Hz); 2.1520 ppm – 2.1490 ppm (d, CH_3-CN, , J^4 = 2.43 Hz); 1.6758 ppm (s, CH_3-CO). *Isomer B*: 7.7153 ppm – 7.3524 ppm (m, 3 x C_6H_5-P); 5.0635 ppm (s, C-H); 2.0617 ppm (s, CH_3-CN); 1.9335 ppm (s, CH_3-CO). ν_{CO}: 1952.67 cm^{-1}.

3b: Yield = 65%. ^{1}H NMR: 7.3890 ppm – 7.0608 ppm (m, C_6H_5-N; 3 x C_6H_5-P); 5.2982 ppm (s, C-H); 2.1417 ppm (s, CH_3-CN); 1.7852 ppm (s, CH_3-CO). ν_{CO}: 1966.60 cm^{-1}.

4.2 Experimental: Instrumentation and characterization

4.2.1 Spectroscopic measurements: NMR

Characterization of the L,L'-BID ligands, the [Rh(L,L'-BID)(CO)$_2$] and the [Rh(L,L'-BID)(CO)(PPh$_3$)] complexes were done on a Bruker Avance DPX 300 NMR utilizing $CDCl_3$ and acetone-d^6 as solvent.

Kinetic measurements were done on a Bruker Avance 600 MHz NMR utilizing $CDCl_3$, passed through basic alumina, as solvent and the CH_3I at concentrations of 10 times in excess. All kinetic measurements were done at 25°C.

4.2.2 Spectroscopic measurements: IR

Characterization of the [Rh(L,L'-BID)(CO)$_2$] and [Rh(L,L'-BID)(CO)(PPh$_3$)] complexes were carried out with a Bruker Tensor 27 FTIR infrared spectrophotometer fitted with a Pike MIRacle single bounce and a diamond ATR.

Kinetic measurements of the [Rh(L,L'-BID)(CO)(PPh$_3$)] complexes were carried out on a Bruker Tensor 27 FTIR infrared spectrophotometer fitted for solution state analysis with a Rh complex concentration 0.005 mol.dm^{-3} and the CH_3I concentration varied between 10, 20 and 50

---

[9] N.F. Stuurman, J. Conradie, *J. Organomet. Chem.*, 2009, **694**, 259-268

[10] M.M. Conradie, J. Conradie, *Inorg. Chim. Acta*, 2008, **361**, 208-218

[11] J. Conradie, G.J. Lamprecht, S. Otto, J.C. Swarts, *Inorg. Chim. Acta*, 2002, **328**, 191-203

[12] G.J. Lamprecht, J.C. Swarts, J. Conradie, J.G. Leipoldt, *Acta Cryst.*, 1993, **C49**, 82-84

times in excess. Chloroform, passed through basic alumina, was utilized as solvent and all measurements were done at 25°C.

4.2.3 Spectroscopic measurements: UV/VIS

Kinetic measurements of the [Rh(L,L'-BID)(CO)(PPh_3)] complexes were carried out with a Shimadzu UV-1650PC UV/visible spectrophotometer fitted with a CPS-240A cell positioner and temperature controller. Chloroform, passed through basic alumina, was utilized as solvent and the Rh complex concentrations were 0.0003 mol.dm^{-3} with the concentration of the CH_3I at 5, 10, 50, 100 times in excess. Measurements were taken at 15°C, 20 °C, 25°C, 30°C and 35°C for complex **3b** and measurements were taken at 25°C for the **3a** complex.

4.2.4 Electrochemistry

Cyclic voltammetry experiments were carried out on a Princeton Applied Research Parstat 2273 advanced electrochemical system and a BAS100B electroanalytical system. The Parstat system was utilized in the electrochemical analysis of 0.002 mol.dm^{-3} [Rh(C_4H_3SCOCHCOR)(CO)(PPh_3)] (with R = CF_3, Ph, S) complexes and the BAS100B system was utilized in the electrochemical analysis of 0.001 mol.dm^{-3} of both the L,L'-BID ligands and the [Rh(L,L'-BID)(CO)(PPh_3)] complexes. A three electrode cell setup was employed with a glassy carbon working electrode (surface area 7.07 x 10-6 m^2), a Pt auxiliary electrode and a Ag/Ag$^+$ (0.01 mol.dm-3 $AgNO_3$ in acetonitrile)[13] reference electrode mounted on a Luggin capillary.[14] The solvent employed was anhydrous acetonitrile and the supporting electrolyte was tetra-n-butylammonium hexafluorophosphate ([N(Bu_4)][PF_6]) (0.1 mol.dm^{-3}). A purified Ar gas blanket was employed and all measurements were taken at room temperature, 25°C. Scan rates were varied between 0.05 V s^{-1} and 5 V s^{-1}. Repetitions with the same experimental conditions showed all reduction potentials were reproducible within 0.010 V. All cited potentials were referenced against the Fc/Fc$^+$ couple, as suggested by IUPAC.[15] Ferrocene exhibited a formal reduction potential of $E^{\circ\prime}$ = 0.072 V *vs.* Ag/Ag$^+$, a peak separation $\Delta E_p = E_{pa} - E_{pc}$ = 0.070 V and

---

[13] D.T. Sawyer, J.L. Roberts, *Experimental Electrochemistry for Chemists,* Wiley, New York, 1979, 54

[14] D.H. Evans, O'Connell, R.A. Peterson, M.J. Kelly, *J. Chem. Ed.,* 1983, **60**, 290; G.A. Mabbott, *J. Chem. Ed,* 1983, **60,** 697

[15] G. Gritzner, J. Kuta, *Pure Applied Chemistry*, 1984, **56,** 461.

i_{pc}/i_{pa} = 0.98, under the experimental conditions. E_{pa} = anodic peak potential, E_{pc} = cathodic peak potential and i_{pa} = anodic peak current, i_{pc} = cathodic peak current. $E^{\circ\prime}$ (Fc/Fc$^+$) = 0.66(5) V *vs.* SHE in $[NBu_4][BF_4]/CH_3CN$. [16,17]

4.3 DFT computational

4.3.1 ADF

The ADF[18] - program was utilized in the calculations of the L,L'-BID ligands, the [Rh(L,L'-BID)$(CO)_2$] and the [Rh(L,L'-BID)(CO)(PPh_3)] complexes. A TZP basis set with the PW91[19] functional was utilized in the optimization of the geometries. The theoretical IR frequencies were also calculated with the selected basis set and functional. For transition states, solvent effects were taken into account using chloroform as solvent, using the COSMO[20] model of solvation.

---

[16] M.F.C. Guedes da Silva, A.M. Trzeciak, J.J. Ziólkowski, A.J.L. Pombeiro, *J. Organomet. Chem.,*2001, **620**, 174.

[17] A.J.L. Pombeiro, *J. Organomet. Chem.,* 2005, **690**, 6021

[18] Selected examples: (a) ADF 2008.01, SCM, Theoretical Chemistry, Vrije Universiteit, Amsterdam, The Netherlands, 2008, http://www.scm.com; (b) G. Te Velde, F.M. Bickelhaupt, E.J. Baerends, C.F. Guerra, S.J.A. Van Gisbergen, J.G. Snijders, T. Ziegler, *J. Comput. Chem.,* 2001, **22**, 931-967; (c) C. Fonseca Guerra, J.G. Snijders, G. Te Velde, E.J. Baerends, *Theor. Chem. Acc.*, 1998, **99**, 391-403

[19] J.P. Perdew, J.A. Chevary, S.H. Vosko, K.A. Jackson, M.R. Pederson, D.J. Singh, C. Fiolhais, *Phys. Rev. B.,* 1992, **46**, 6671-6687; (Erratum: J.P. Perdew, J.A. Chevary, S.H. Vosko, K.A. Jackson, M.R. Perderson, D.J. Singh, C. Fiolhais, *Phys. Rev. B.,* 1993, **48**, 4978)

[20] COSMO (Conductor like Screening Model) is described in: (a) A. Klamt, G. Schuürmann, *J. Chem. Soc., Perkin Trans.,* 1993, **2**, 799; (b) A. Klamt, *J. Phys. Chem.*, 1995, **99**, 2224-2235 (c) A. Klamt, V. Jones, *J. Chem. Phys.*, 1996, **105**, 9972-9981

4.3.2 Gaussian

The Gaussian 09[21] program was utilized in the DFT calculations of the [Rh($C_4H_3SCOCHCOR$)(CO)(PPh_3)] (with R = CF_3, Ph, C_4H_3S) complexes. Geometries were optimized with the hybrid DFT functional B3LYP.[22] Optimizations were done in gas phase, with the triple-ζ basis set 6-311G(d,p)[23] on all atoms except rhodium. The LanL2DZ basis set,[24] corresponding to the Los Alamos ECP plus DZ, was used for rhodium.

---

[21] M.J. Frisch, G.W. Trucks, H.B. Schlegel, G.E. Scuseria, M.A. Robb, J.R. Cheeseman, J.A. Montgomery Jr., T. Vreven, K.N. Kudin, J.C. Burant, J.M. Millam, S.S. Iyengar, J. Tomasi, V. Barone, B. Mennucci, M. Cossi, G. Scalmani, N. Rega, G.A. Petersson, H. Nakatsuji, M. Hada, M. Ehara, K. Toyota, R. Fukuda, J. Hasegawa, M. Ishida, T. Nakajima, Y. Honda, O. Kitao, H. Nakai, M. Klene, X. Li, J.E. Knox, H.P. Hratchian, J.B. Cross, V. Bakken, C. Adamo, J. Jaramillo, R. Gomperts, R.E. Stratmann, O. Yazyev, A.J. Austin, R. Cammi, C. Pomelli, J.W. Ochterski, P.Y. Ayala, K. Morokuma, G.A. Voth, P. Salvador, J.J. Dannenberg, V.G. Zakrzewski, S. Dapprich, A.D. Daniels, M.C. Strain, O. Farkas, D.K. Malick, A.D. Rabuck, K. Raghavachari, J.B. Foresman, J.V. Ortiz, Q. Cui, A.G. Baboul, S. Clifford, J. Cioslowski, B.B. Stefanov, G. Liu, A. Liashenko, P. Piskorz, I. Komaromi, R.L. Martin, D.J. Fox, T. Keith, M.A. Al-Laham, C. Peng, A. Nanayakkara, M. Challacombe, P.M.W. Gill, B. Johnson, W. Chen, M.W. Wong, C. Gonzalez, J.A. Pople, *Gaussian 09, revision B.01*; Gaussian, Inc.: Wallingford, CT, 2010

[22] (a)A.D. Becke, *J. Chem. Phys.,* 1993, **98**, 5648;
(b) P.J. Stephens, F.J. Devlin, C.F. Chabalowski, M.J. Frisch, *.J Phys. Chem. B,* 1994, **98**, 11623

[23] (a)A.D. Mclean, G.S. Chandler, *J. Chem. Phys.,* 1980, **72**, 5639;
(b)K. Raghavachari, J.S. Binkley, R. Seeger, J.A. Pople, *J. Chem. Phys.,* 1980, **72**, 650;
(c)J.P. Blaudeau, M.P. McGrath, L.A. Curtiss, L. Radom, *J. Chem. Phys.,* 1997, **107**, 5016;
(d)A.J.H. Wachters, *J. Chem. Phys.,* 1970, **52**, 1033;
(e)P.J. Hay, *J. Chem. Phys.,* 1977, **66**, 4377;

[24] (a)T.H. Dunning, P.J. Hay, H.F. Schaefer, *Modern Theoretical Chemistry* Plenum, New York, 3rd edition, 1976, Vol. 3, 1;
(b)P.J. Hay, W.R. Wadt, *J. Chem. Phys.,* 1985, **82**, 270;
(c)P.J. Hay, W.R. Wadt, *J. Chem. Phys.*, 1985, **82**, 284;
(d)P.J. Hay, W.R. Wadt, *J. Chem. Phys.*, 1985, **82**, 299

5 Concluding remarks and future perspectives

5.1 Concluding remarks

In this study L,L'-BID ligands were synthesized where the L and L' coordinating atoms were varied between O, NH and NPh. The synthesized ligands were: ($CH_3COCHCOHCH_3$) (**Hacac**), ($CH_3COCHCNH_2CH_3$) (**1a**), ($CH_3COCHCNHPhCH_3$) (**1b**), ($CH_3CNHPhCHCNPhCH_3$) (**1c**). The dicarbonyl Rh complexes [$Rh(CH_3COCHCNHCH_3)(CO)_2$] (**2a**), [$Rh(CH_3COCHCNPhCH_3)(CO)_2$] (**2b**), [$Rh(CH_3CNPhCHCNPhCH_3)(CO)_2$] (**2c**)) as well as the phosphine Rh complexes ([$Rh(CH_3COCHCNHCH_3)(CO)(PPh_3)$] (**3a**), [$Rh(CH_3COCHCNPhCH_3)(CO)(PPh_3)$] (**3b**)) were also synthesized and studied.

All the ligands (**Hacac**, **1a** - **1d**) showed a single reduction peak at a potential < -2.5 V *vs* FcH/FcH^+ during the electrochemical analysis. From the cyclic voltammetry (CV) data it is found that the electronegativity of the L,L' atoms, and the atoms or groups attached to L or L', have a significant electronic effect on the reduction potential. The observed trend was with the largest, less negative reduction potential: **Hacac > 1b >1c > 1a**. This trend was the same as with the trend in the electronegativies of the individual atoms or groups namely: O > N > Ph > H.

Complexes **3a** and **3b**, including selected complexes containing O,O'-BID ligands ([$Rh(CH_3COCHCOHCH_3)(CO)(PPh_3)$], [$Rh(C_4H_3SCOCHCOCPh)(CO)(PPh_3)$] **M1**, [$Rh\ (C_4H_3SCOCHCOCC_4H_3S)(CO)(PPh_3)$] **M2** and [$Rh(C_4H_3SCOCHCOCF_3)(CO)(PPh_3)$] **M3**) all displayed a single oxidation $Rh^{I/III}$ peak and a single reduction peak, that is coupled to the oxidation peak. A trend was found for complexes **3a** and **3b** that was exactly the same as with the results obtained for the ligands namely: Largest, more positive oxidation potential: [$Rh(CH_3COCHCOHCH_3)(CO)(PPh_3)$] > **3b** > **3a**.

The kinetic results, followed *in situ* by UV/VIS, IR and NMR, for the oxidative addition reaction between CH_3I and complexes **3a** and **3b** was also studied. From the results obtained it was seen that complex **3b** displayed only a single step in the reaction. This step is the formation of a single alkyl product. Complex **3a**, of which there was 2 isomers, displayed 2 steps in the oxidative addition reaction. These 2 steps are the formation of an alkyl product during the first

step and the formation of an acyl product, of which there are 2 isomers, during the second step. The second order reaction rate constants (k_2) for complexes **3a** and **3b**, when compared with [Rh($CH_3COCHCOHCH_3$)(CO)(PPh_3)] complex's kinetic results, was found to be in agreement with the electrochemical results, that both **3a** and **3b** has a larger (k_2) than [Rh($CH_3COCHCOHCH_3$)(CO)(PPh_3)]. Previous reported data showed that the complex with the slowest oxidative addition reaction, with the smallest rate constant (k_2), will be oxidized more difficultly (at higher potentials). However this study showed that the trend between **3a** and **3b** was opposite to what was expected. The trend in the kinetics was: smallest rate constant **3b** > **3a** > [Rh($CH_3COCHCOHCH_3$)(CO)(PPh_3)].

The PW91/TZP density functional theory calculations of the the optimized geometries and energies of the reactants, possible products and transition states during the oxidative addition reaction between CH_3I and complexes **3a** and **3b** corroborated the experimentally observed results. For complex **3b** it was found that a single transition step is present in the reaction leading to the formation of Rh(III)-alkyl product. The calculated energies of the Rh(III)-alkyl reaction product and a theoretically possible Rh(III)-acyl product's optimized geometries showed that they are equi-energetic and therefore there is no driving force facilitating the formation of the Rh(III)-acyl product. For complex **3a** it was found that there are 2 transition states in the oxidative addition reaction. The first is the formation of a Rh(III)-alkyl product. The second is the formation of the Rh(III)-acyl product from the alkyl product through CO insertion. The acyl product has the lowest energy.

5.2 Future perspectives

Possible additional work that could compliment the results obtained in this study regarding L,L'-BID ligands and their respective organometallic complexes are:

1) Varying the substituents R and R' on the backbone of the L,L'-BID ligand $(RCLCHCL'CR')^-$ to determine the influence of the electronegativity of the R and R' groups on the electrochemical behaviour and kinetics.

2) Regarding the imino-β-diketone, varying the substituents attached to the N atom and determining the influence of the electronegativity and the steric repulsion on the electrochemical behaviour and kinetics.

3) Coordinating the L,L'-BID ligands of this study to metallic centres other than rhodium.

4) Studying the effect of other phosphorous groups bonded to the metallic centres, instead of PPh_3.

5) Affixing the complexes of this study to a silicate or aluminate framework and studying the behaviour as a heterogeneous catalyst.

6) Varying the length of the L,L'-BID ligand backbone to determine the effect of the pseudo aromatic ring structure formed with coordination to a metallic centre.

CONCLUDING REMARKS AND FUTURE PERSPECTIVES

A Appendix

A. NMR spectra:

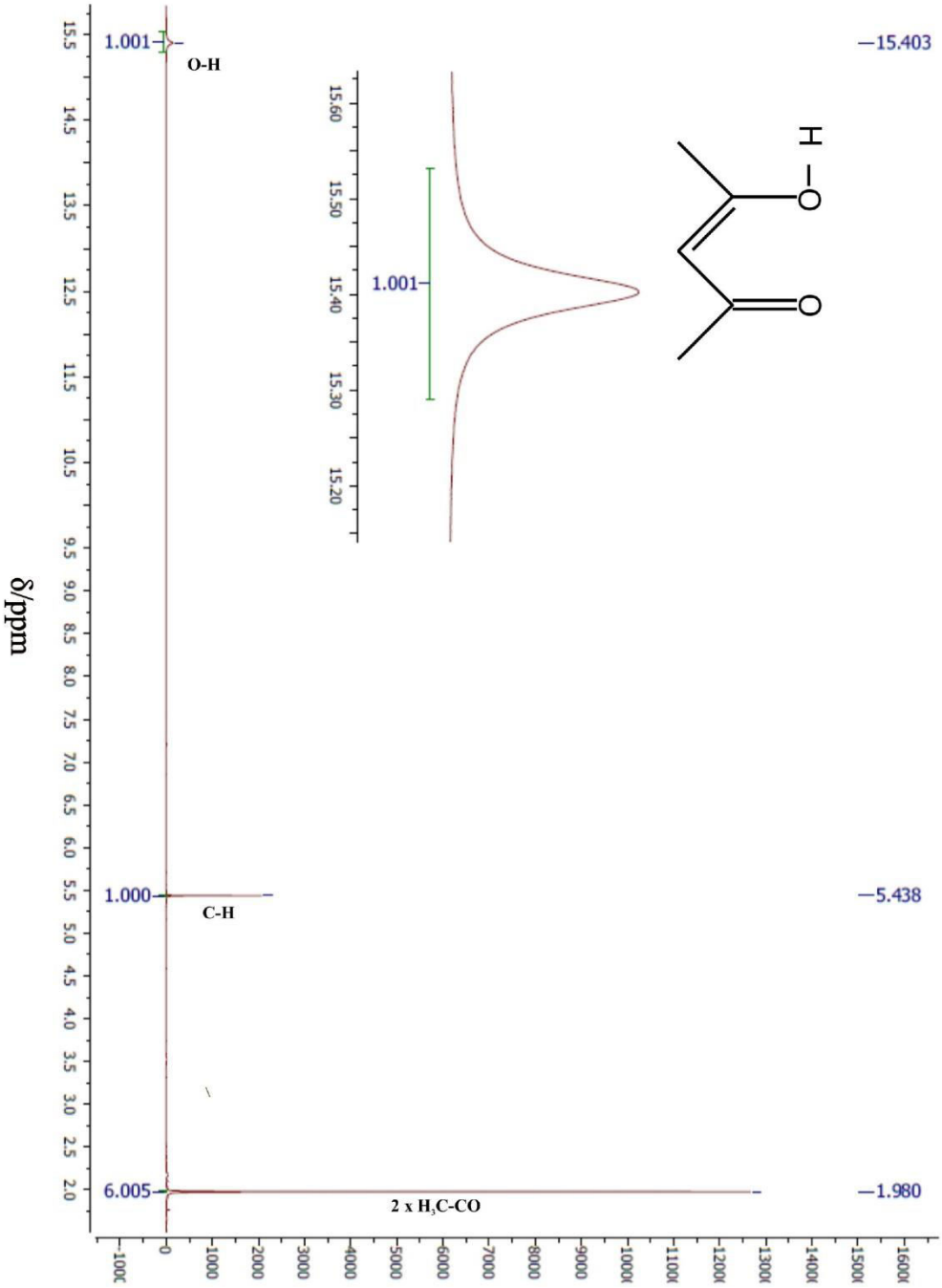

Figure A.1: A ^{1}H NMR spectrum of the L,L'-BID ligand ($CH_3COCH_2COCH_3$) (Hacac).

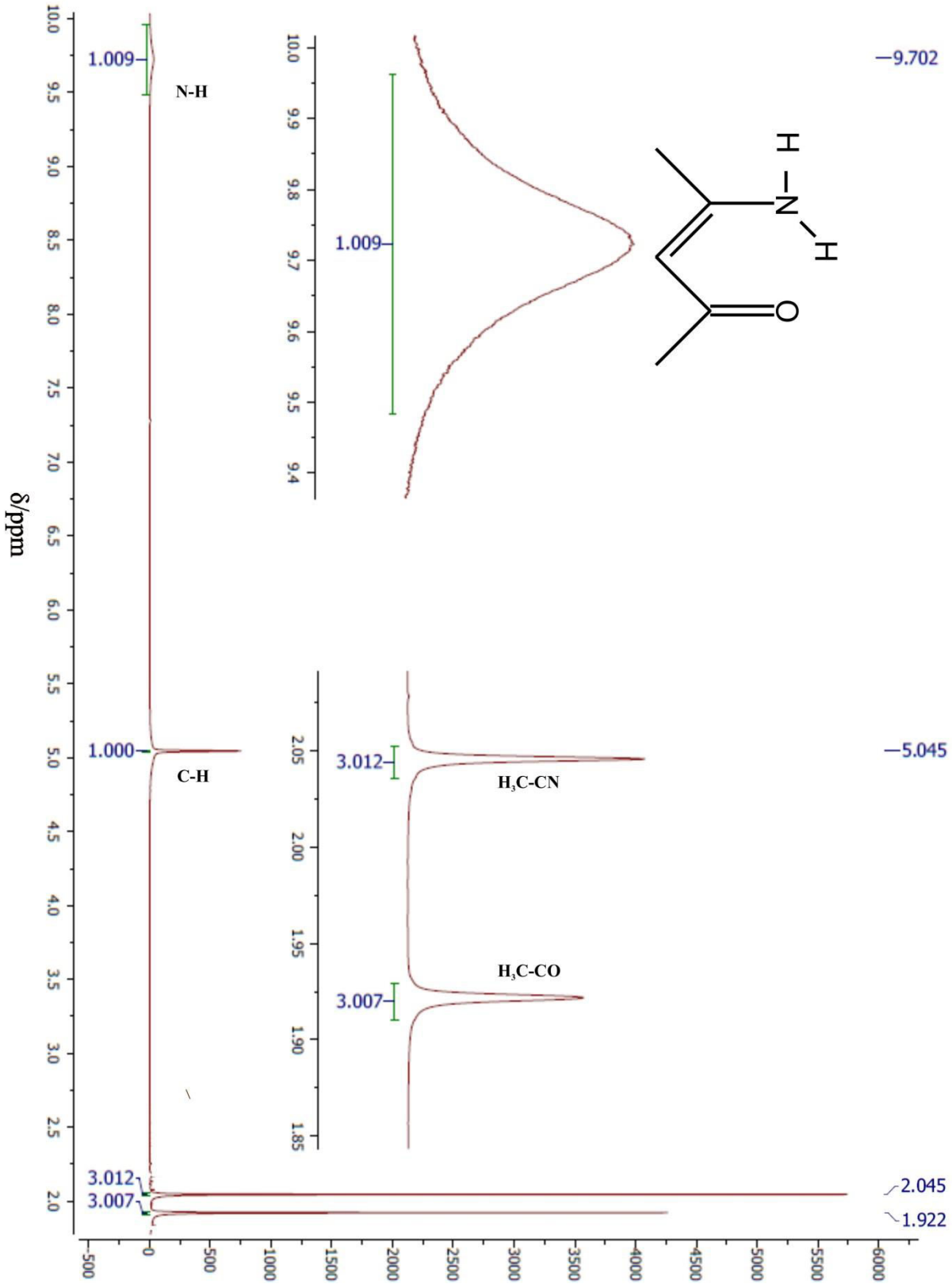

Figure A.2: A ^{1}H NMR spectrum of the L,L'-BID ligand ($CH_3COCH_2CNHCH_3$) **1a**.

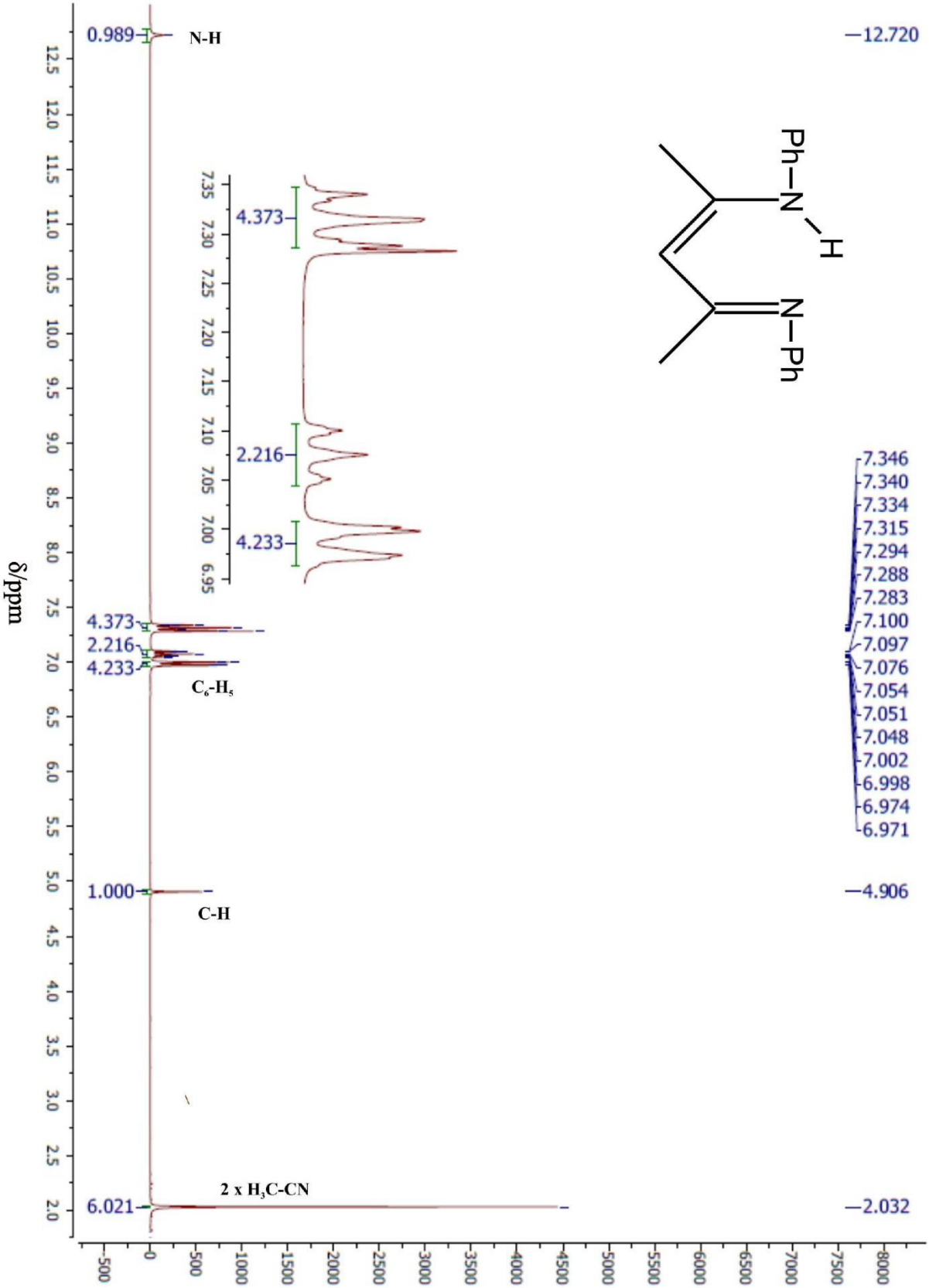

Figure A.3: A ^{1}H NMR spectrum of the L,L'-BID ligand ($CH_3CNPhCH_2CNHCH_3$) **1c**.

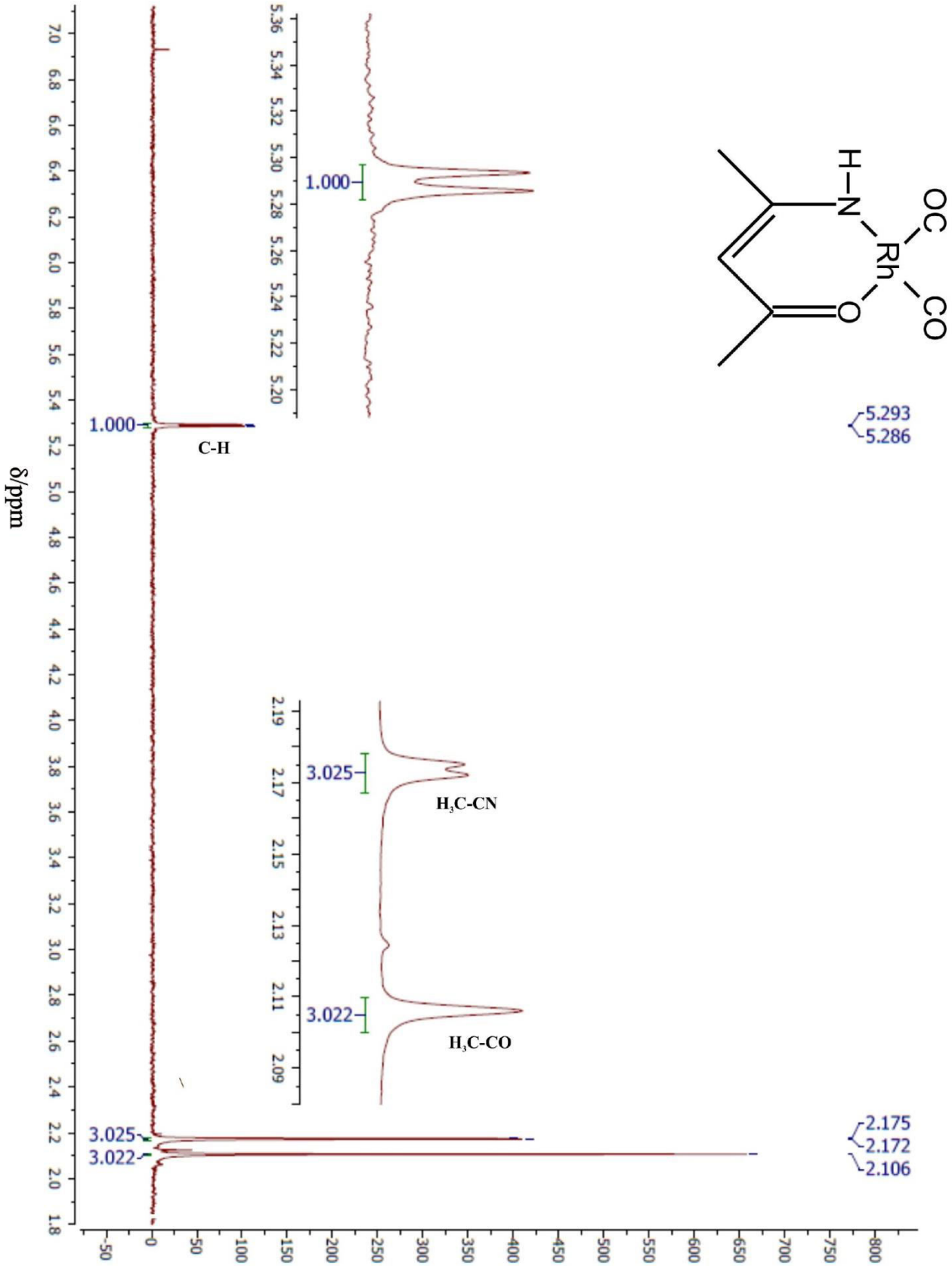

Figure A.4: An NMR spectrum of the dicarbonyl rhodium complex $[Rh(CH_3COCHCNHCH_3)(CO)_2]$ **2a**.

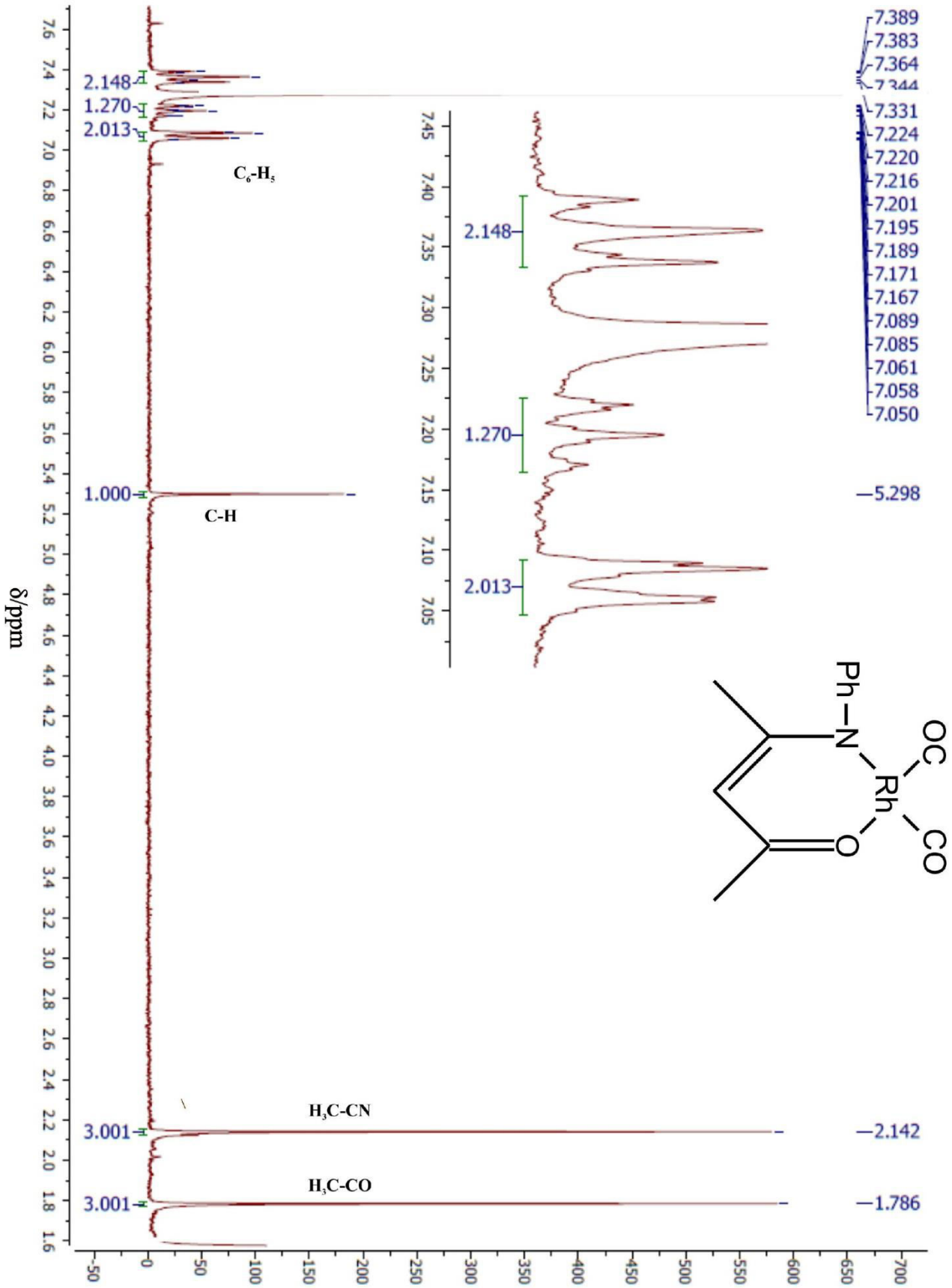

Figure A.5: An NMR spectrum of the dicarbonyl rhodium complex $[Rh(CH_3COCHCNPhCH_3)(CO)_2]$ **2b**.

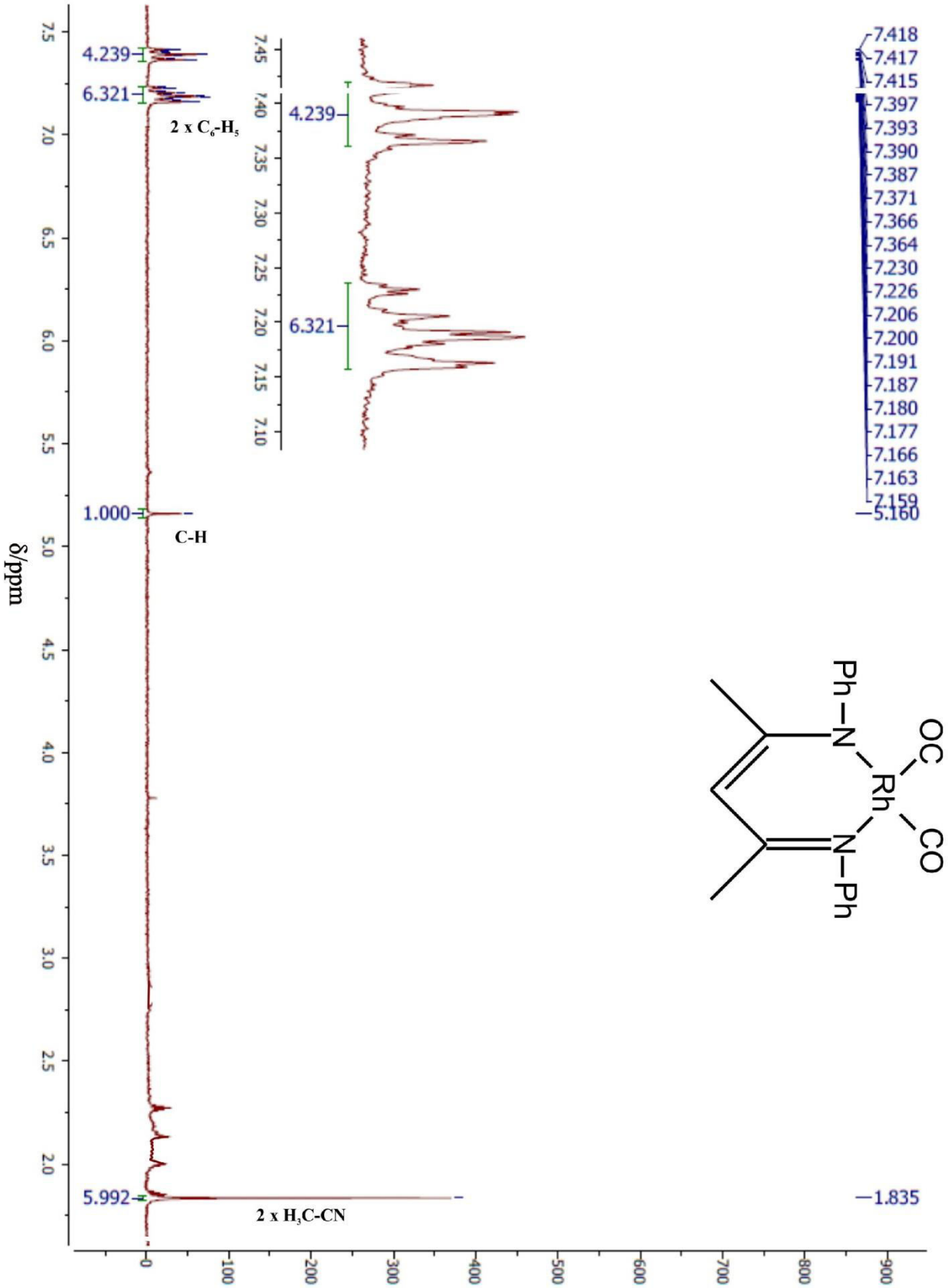

Figure A.6: An NMR spectrum of the dicarbonyl rhodium complex $[Rh(CH_3CNPhCHCNPhCH_3)(CO)_2]$ **2c**.

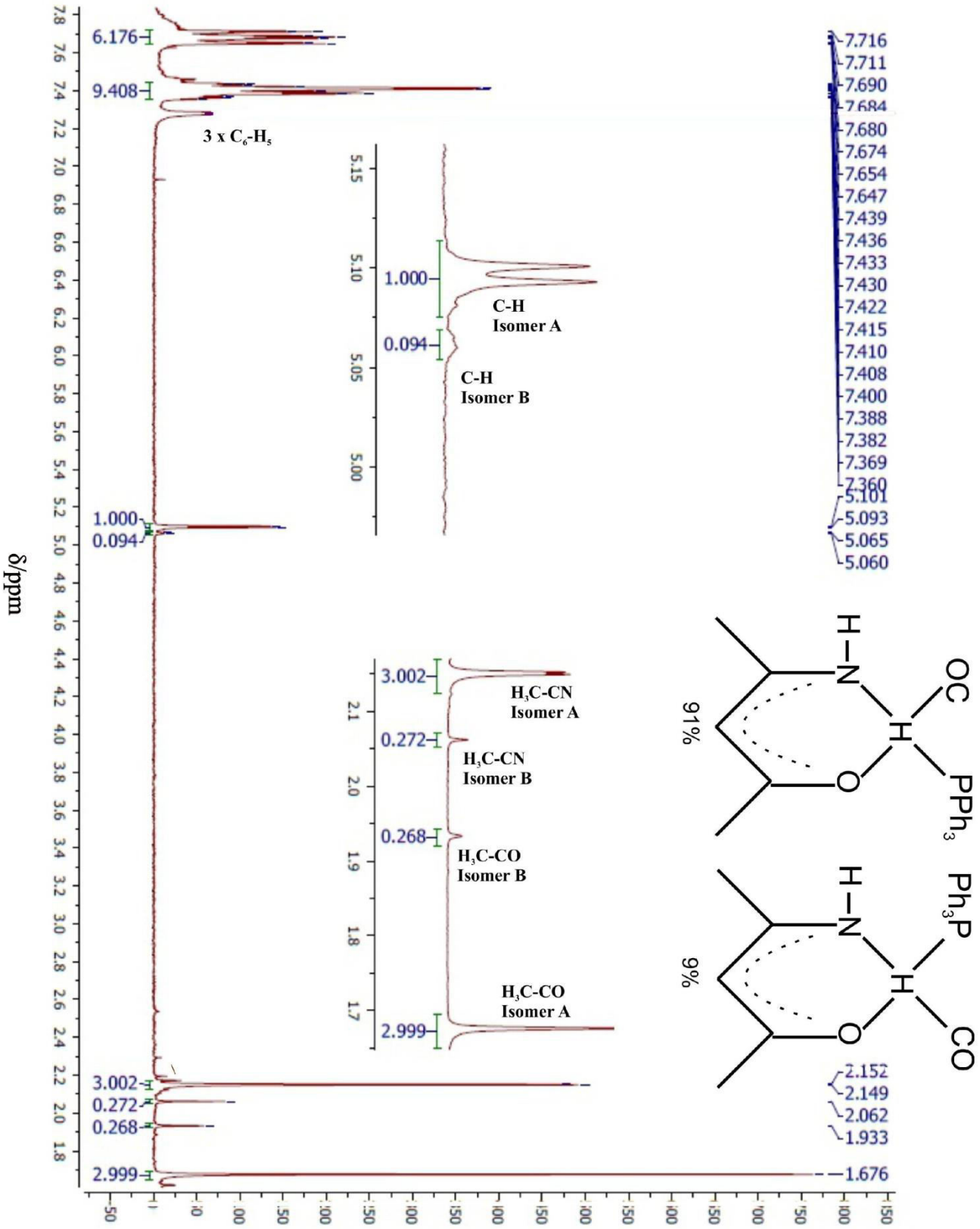

Figure A.7: A ^{1}H NMR spectrum of $[Rh(CH_3COCHCNHCH_3)(CO)(PPh_3)]$ **3a**.

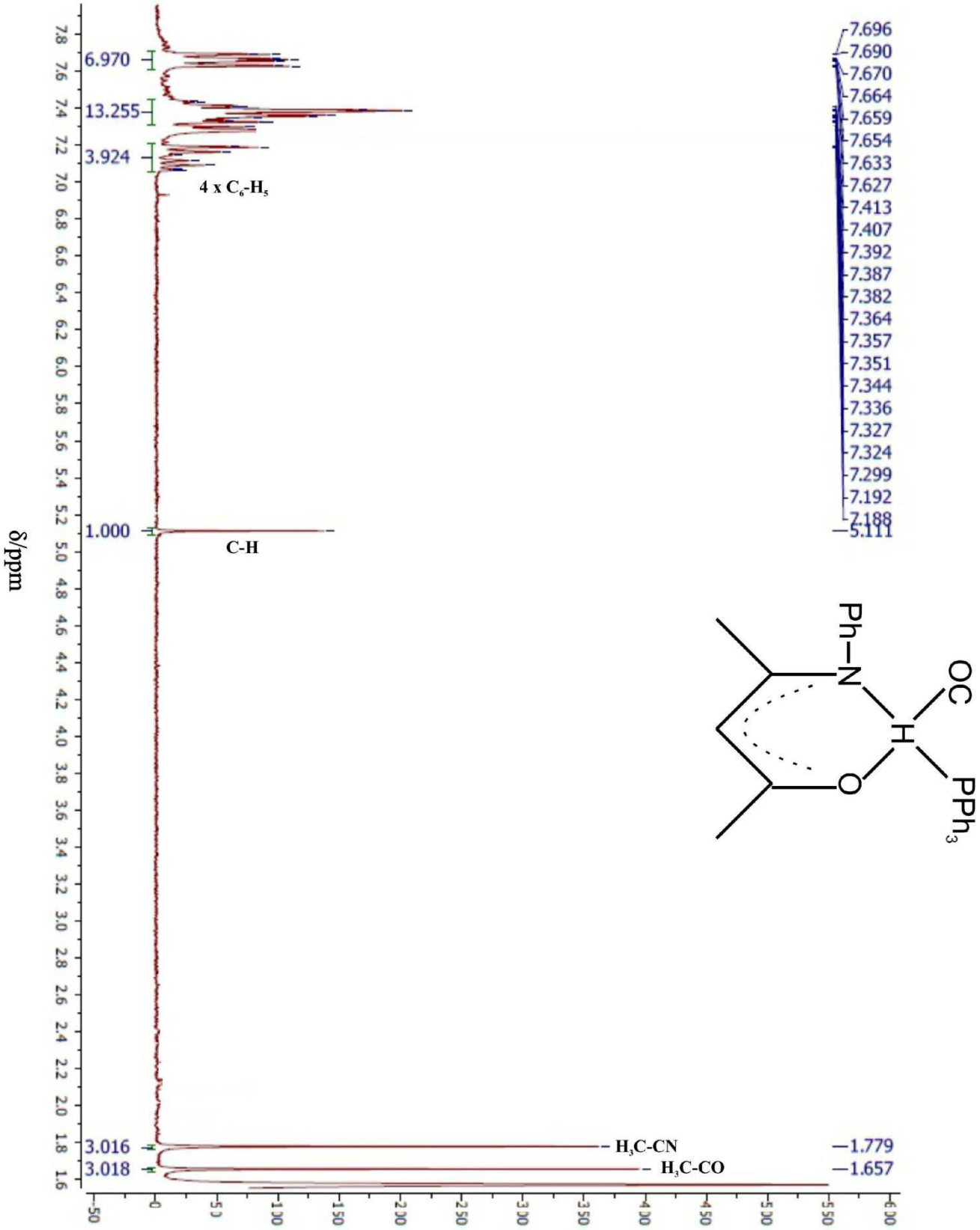

Figure A.8: A ^{1}H NMR spectrum of [Rh($CH_3COCHCNPhCH_3$)(CO)(PPh_3)] **3b**.

B. IR spectra

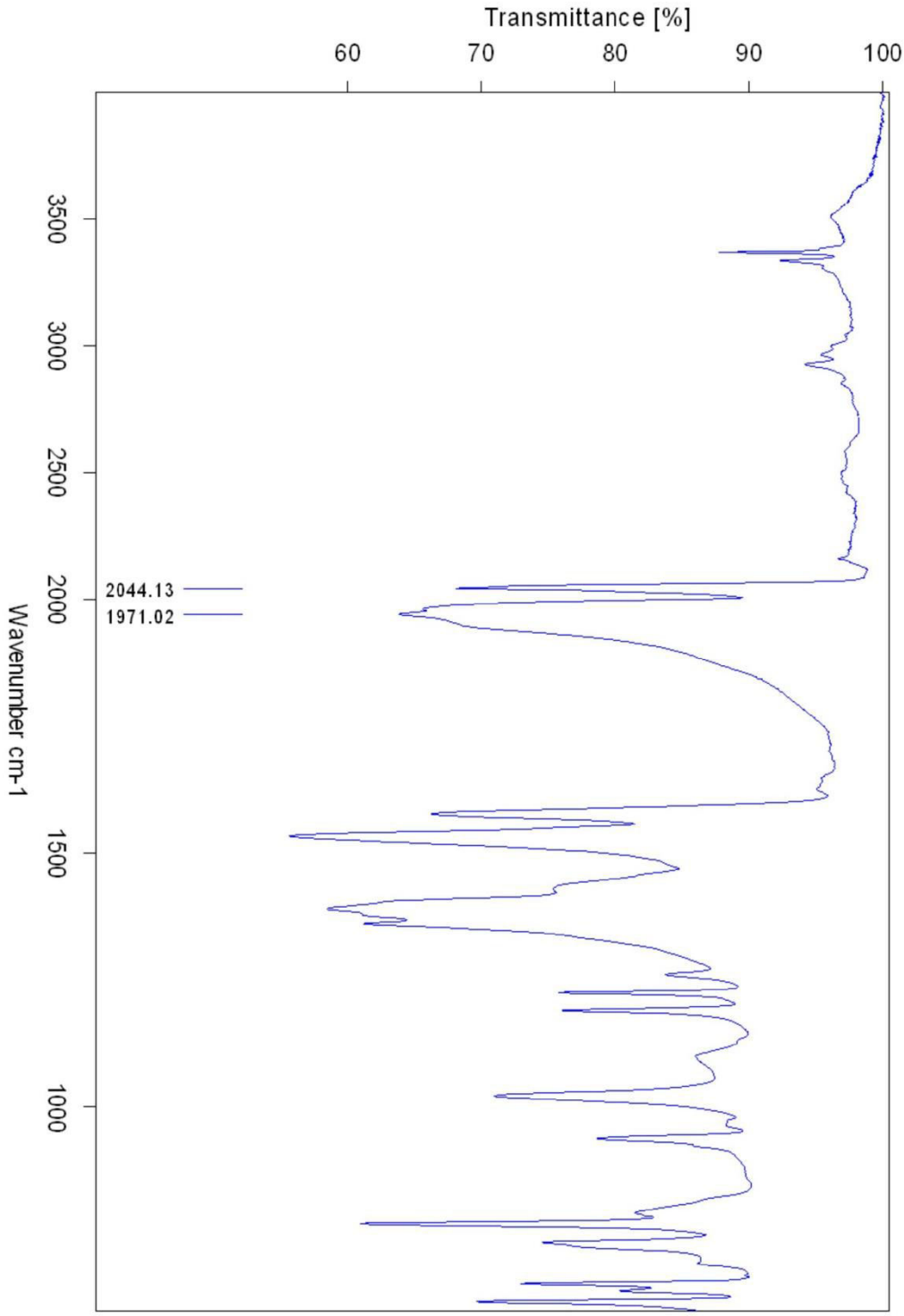

Figure B.1: An IR spectrum of $[Rh(CH_3COCHCNHCH_3)(CO)_2]$ **2a** with carbonyl stretching frequencies at 1971.02 cm^{-1} and 2044.13 cm^{-1}.

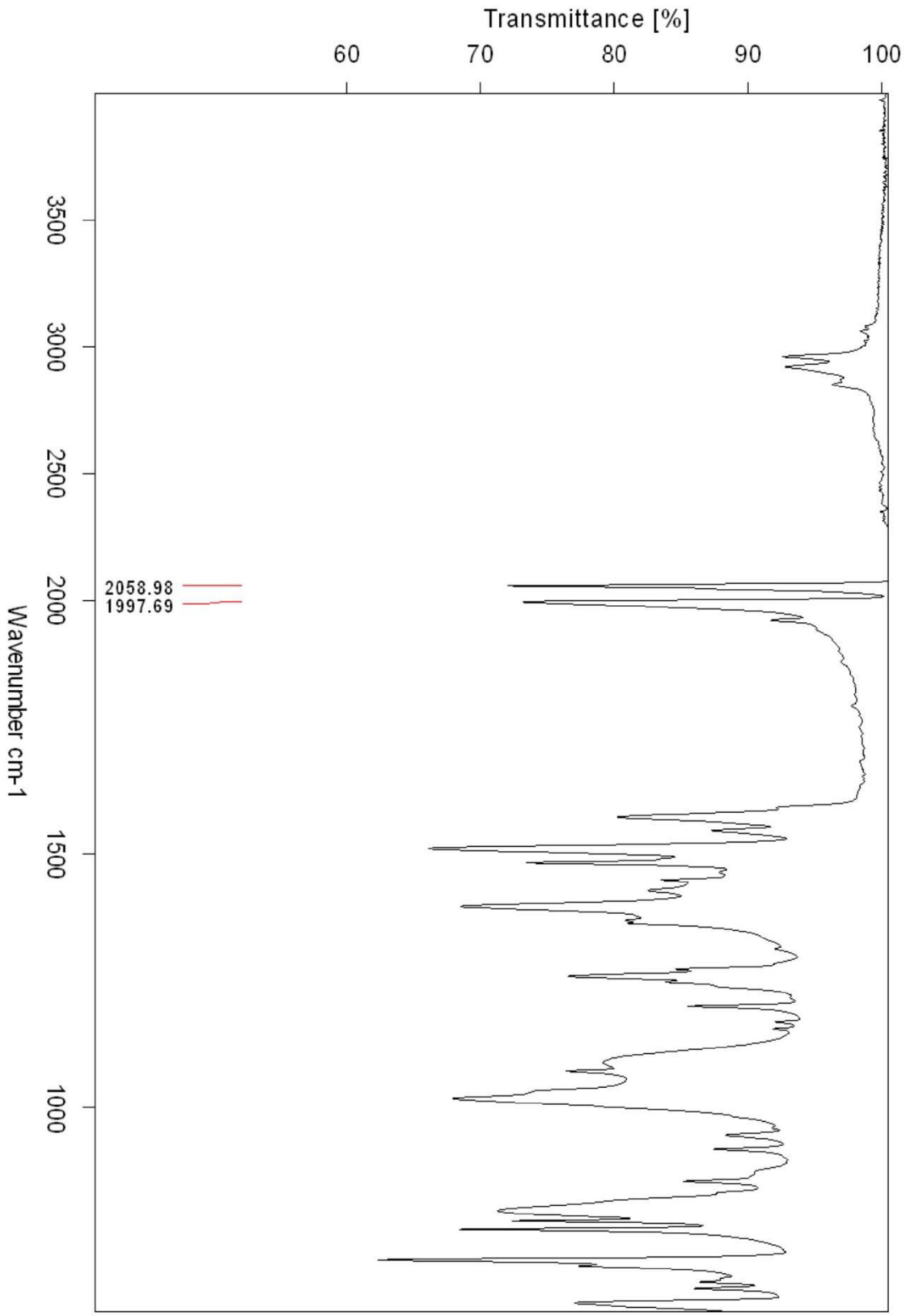

Figure B.2: An IR spectrum of $[Rh(CH_3COCHCNPhCH_3)(CO)_2]$ **2b** with carbonyl stretching frequencies at 1997.69 cm^{-1} and 2058.98 cm^{-1}.

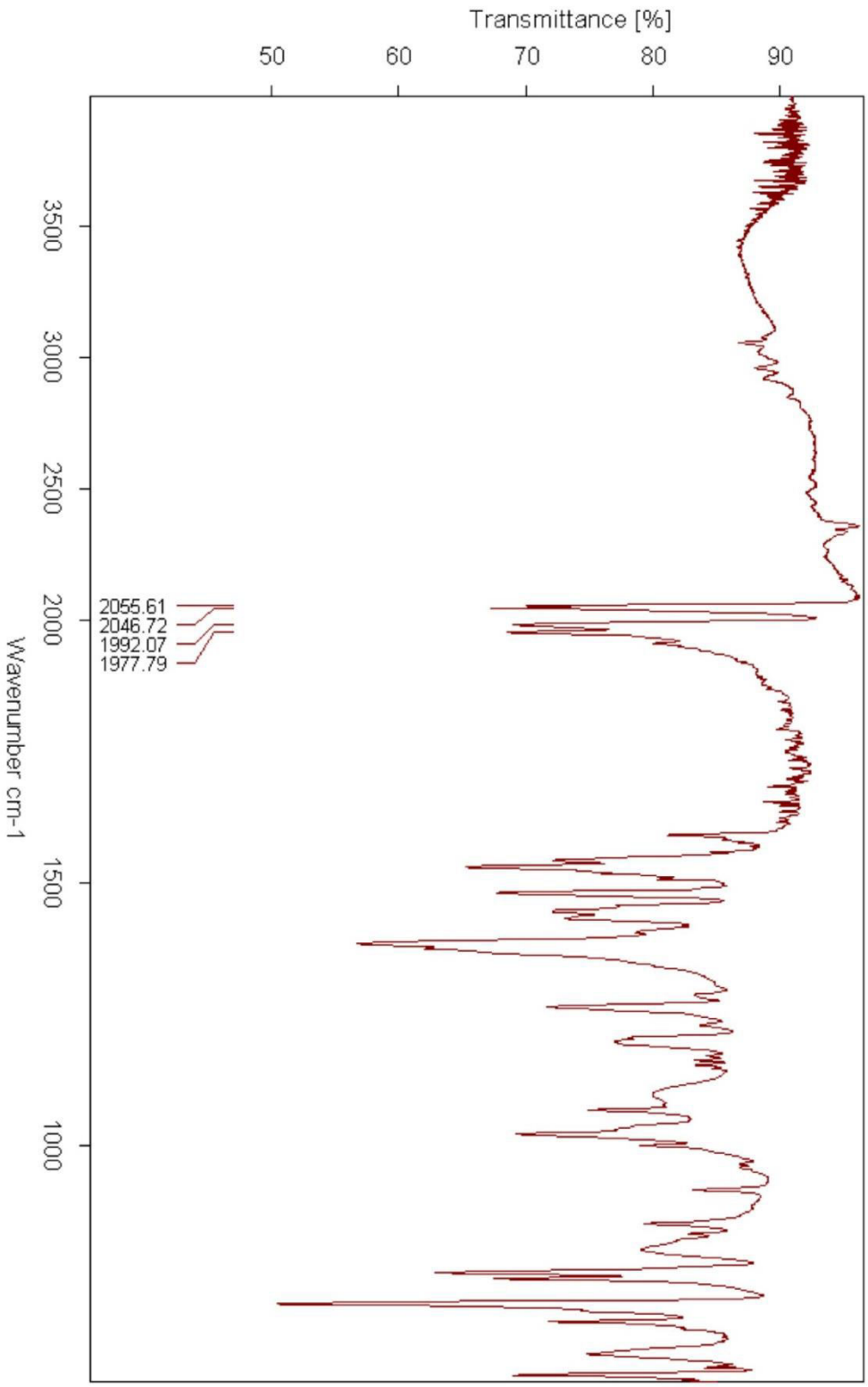

Figure B.3: An IR spectrum of $[Rh(CH_3CNPhCHCNPhCH_3)(CO)_2]$ **2c** with carbonyl stretching frequencies at 1977.79 cm^{-1}, 1992.07 cm^{-1}, 2046.72 cm^{-1} and 2055.61 cm^{-1}.

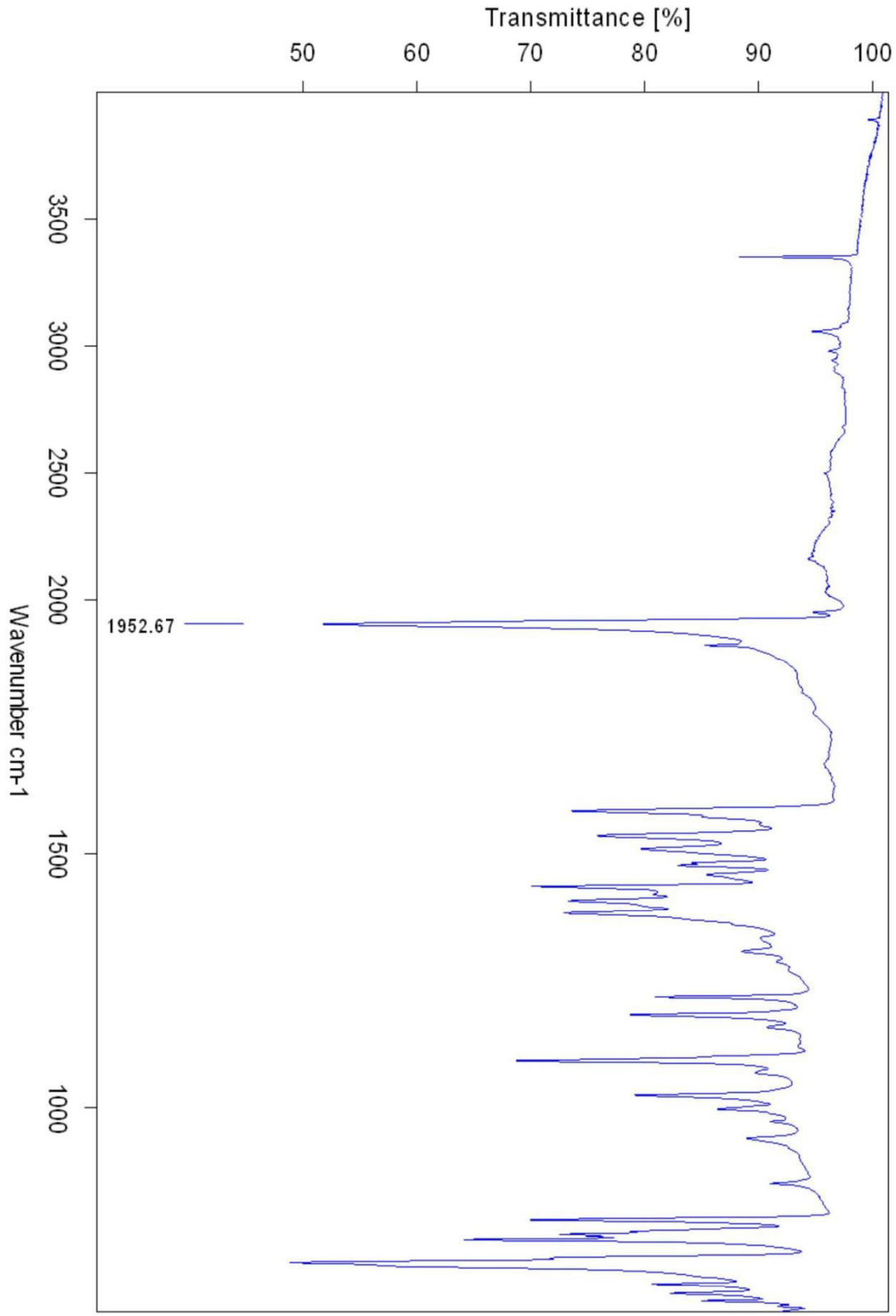

Figure B.4: An IR spectrum of $[Rh(CH_3COCHCNHCH_3)(CO)(PPh_3)]$ **3a** with a carbonyl stretching frequency at 1952.67 cm^{-1}.

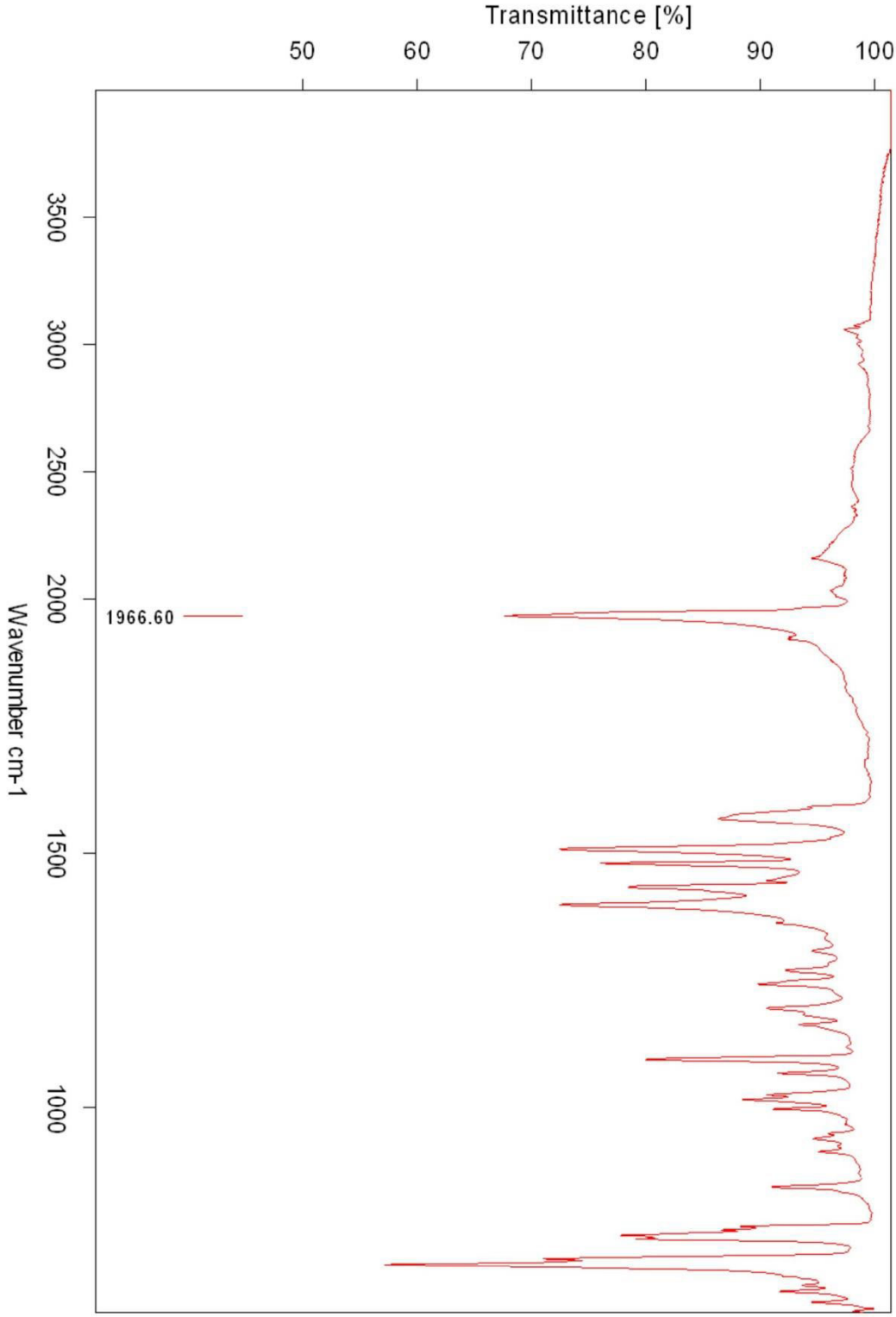

Figure B.5: An IR spectrum of $[Rh(CH_3COCHCNPhCH_3)(CO)(PPh_3)]$ **3b** with a carbonyl stretching frequency at 1966.60 cm^{-1}.

C. Electrochemistry

Table C.1: Reduction potentials (E_{pc}), scan rates (ν) and peak cathodic currents (i_{pc}) for the L,L'-BID ligand ($CH_3COCH_2COCH_3$) (Hacac).

Scan rate (V s^{-1})	E_{pc} (V)	i_{pc} (10^{-6} A)
0.05	-2.563	-9.00
0.1	-2.575	-11.00
0.2	-2.591	-14.00
0.3	-2.607	-14.00
0.5	-2.616	-18.00
1	-2.635	-24.00
5	-2.656	-63.00

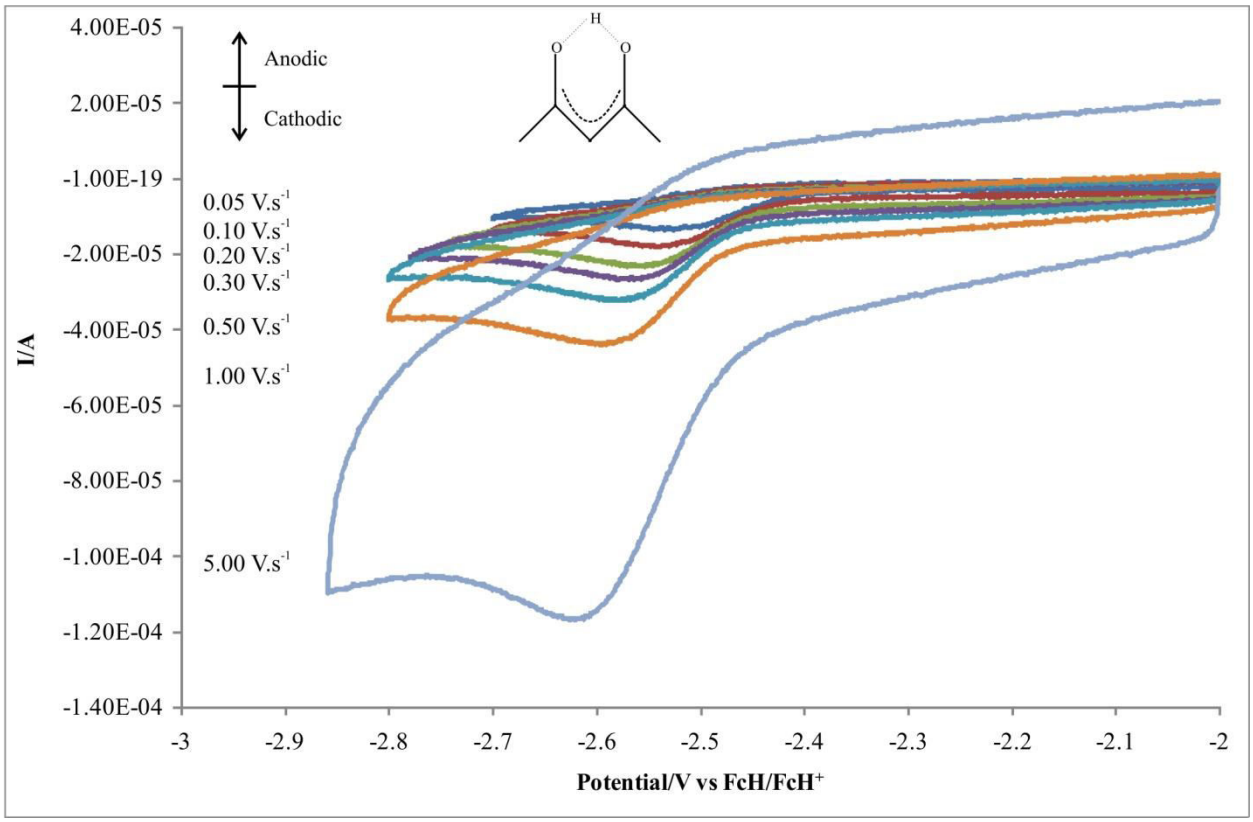

Figure C.1: Cyclic voltammograms of 0.002 moldm^{-3} ($CH_3COCHCOCH_3$) (Hacac) in dry acetonitrile with 0.1 M TBAHFP as supporting electrolyte, a glassy carbon working electrode, a Pt auxiliary electrode and a $Ag/AgNO_3$ reference electrode, with scan rates ranging from 0.05 V s^{-1} to 5.0 V s^{-1}. All measurements were done at 25°C.

Table C.2: Reduction potentials (E_{pc}), scan rates (ν) and peak cathodic currents (i_{pc}) for the L,L'-BID ligand ($CH_3COCH_2CNPhCH_3$) **1b**.

Scan rate (V s^{-1})	E_{pc} (V)	i_{pc} (10^{-6} A)
0.05	-2.673	-9.60
0.1	-2.681	-15.00
0.2	-2.691	-23.00
0.3	-2.699	-25.00
0.5	-2.71	-33.00
1	-2.721	-43.00
5	-2.758	-87.00

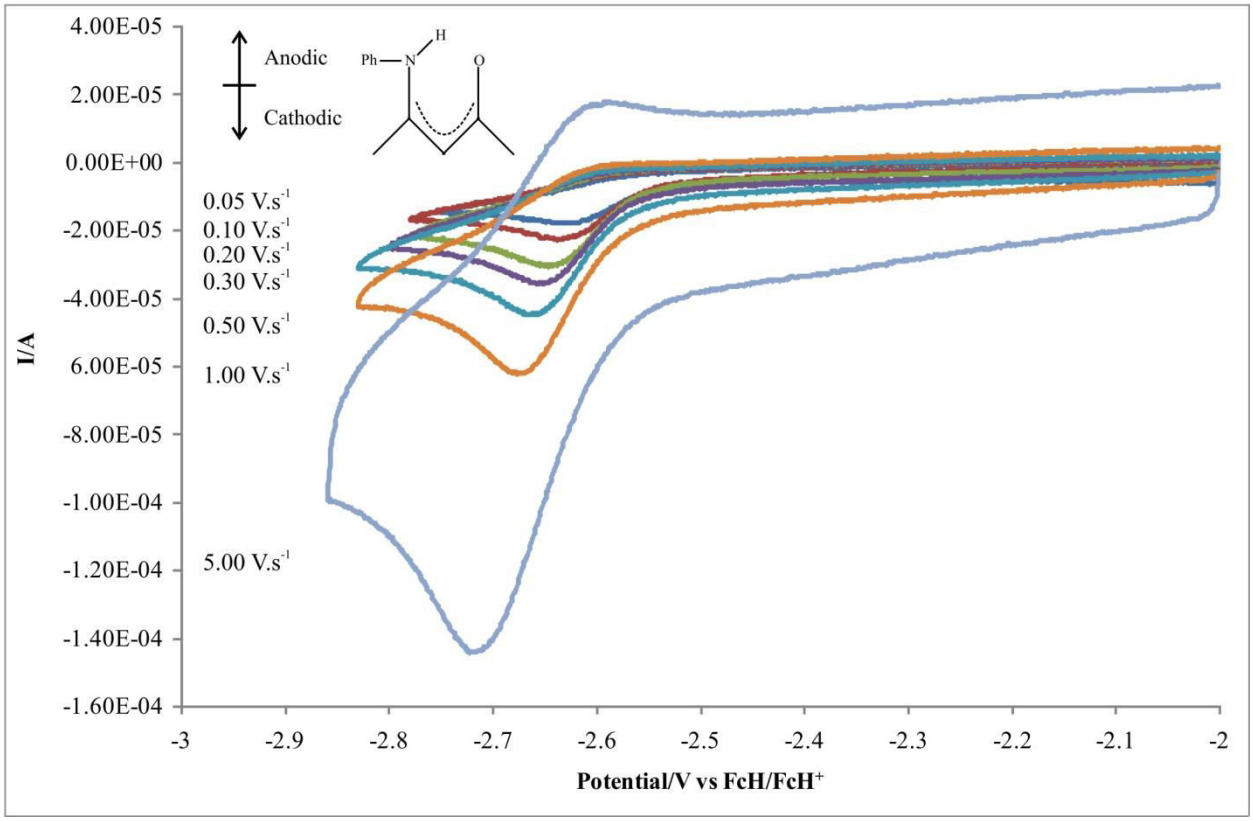

Figure C.2: Cyclic voltammograms of 0.002 moldm^{-3} ($CH_3COCHCNPhCH_3$) **1b** in dry acetonitrile with 0.1 M TBAHFP as supporting electrolyte, a glassy carbon working electrode, a Pt auxiliary electrode and a $Ag/AgNO_3$ reference electrode, with scan rates ranging from 0.05 V s^{-1} to 5.0 V s^{-1}. All measurements were done at 25°C.

Table C.3: Reduction potentials (E_{pc}), scan rates (ν) and peak cathodic currents (i_{pc}) for the L,L'-BID ligand ($CH_3CNPhCH_2CNPhCH_3$) **1c**.

Scan rate (V s^{-1})	E_{pc} (V)	i_{pc} (10^{-6} A)	E_{pa} (V)	i_{pa} (10^{-6} A)	ΔE (V)	i_{pa}/i_{pc}
0.05	-2.717	-1.91	0.563	8.04	3.28	0.24
0.1	-2.741	-25.20	0.583	11.00	3.32	0.44
0.2	-2.781	-34.20	0.605	14.40	3.39	0.42
0.3	-2.803	-38.70	0.611	17.70	3.41	0.46
0.5	-2.831	-49.50	0.635	29.60	3.47	0.60
1	-2.865	-67.20	0.665	49.90	3.53	0.74
5	---	---	0.837	12.90	0.84	---

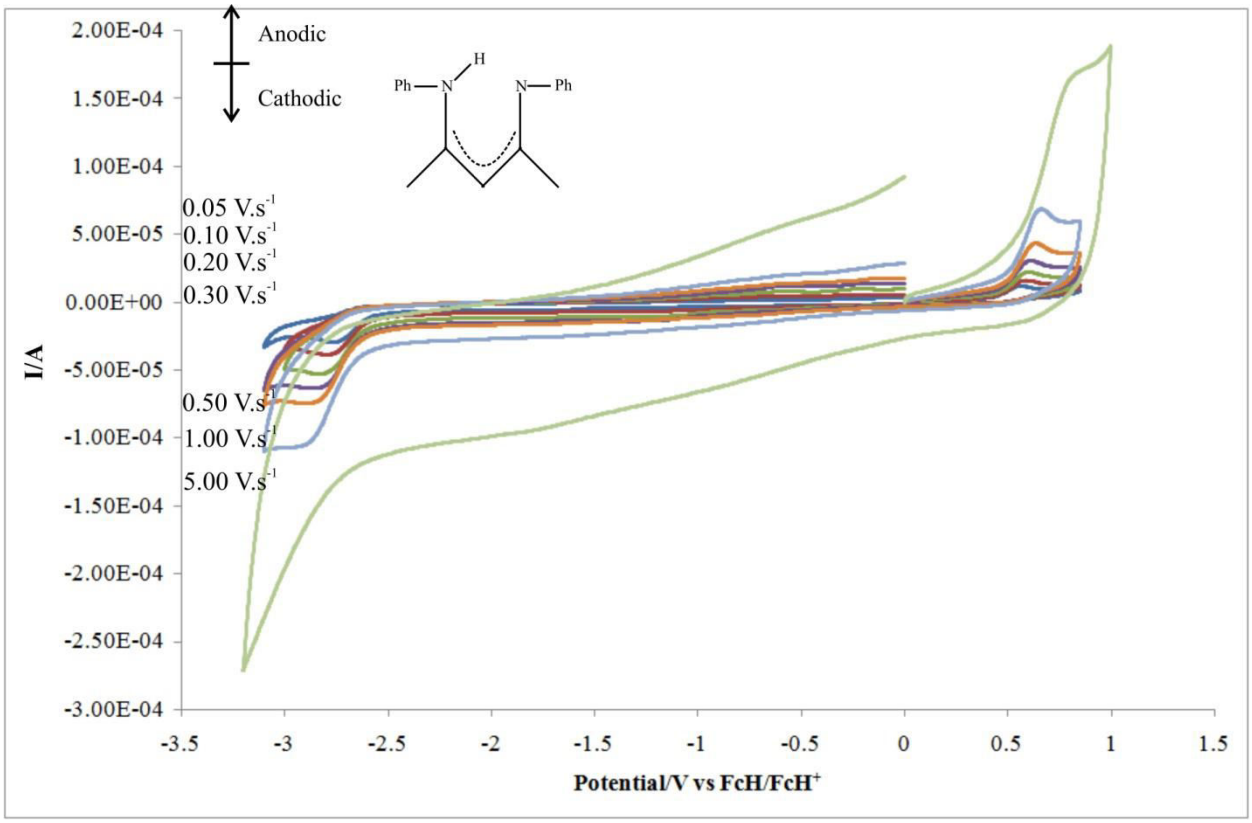

Figure C.3: Cyclic voltammograms of 0.002 moldm^{-3} ($CH_3CNPhCHCNPhCH_3$] **1c** in dry acetonitrile with 0.1 M TBAHFP as supporting electrolyte, a glassy carbon working electrode, a Pt auxiliary electrode and a $Ag/AgNO_3$ reference electrode, with scan rates ranging from 0.05 V s^{-1} to 5.0 V s^{-1}. All measurements were done at 25°C.

Table C.4: Electrochemical parameters (E_{pa}, E_{pc}, i_{pa}, i_{pc}) of the $[Rh(CH_3CNHCHCOCH_3)(CO)(PPh_3)]$ **3a** complex referenced against FcH as internal standard in the acetonitrile mixture containing 0.1 M TBAHFP as supporting electrolyte.

Scan rate (V s^{-1})	E_{pc} (mV)	i_{pc} (10^{-6} A)	E_{pa} (mV)	i_{pa} (10^{-6} A)	ΔE (mV)	i_{pa}/i_{pc}
0.05	---	0.00	285	13.60	285	---
0.1	---	0.00	261	22.20	261	---
0.2	-544	-2.30	275	30.20	819	0.08
0.3	-561	-5.50	278	39.50	839	0.14
0.4	-568	-5.50	287	58.00	855	0.09
0.5	-584	-4.50	306	49.00	890	0.09
1	-593	-14.00	300	72.00	893	0.19
2	-635	-14.00	339	99.00	974	0.14
5	-639	-32.00	356	160.00	995	0.20

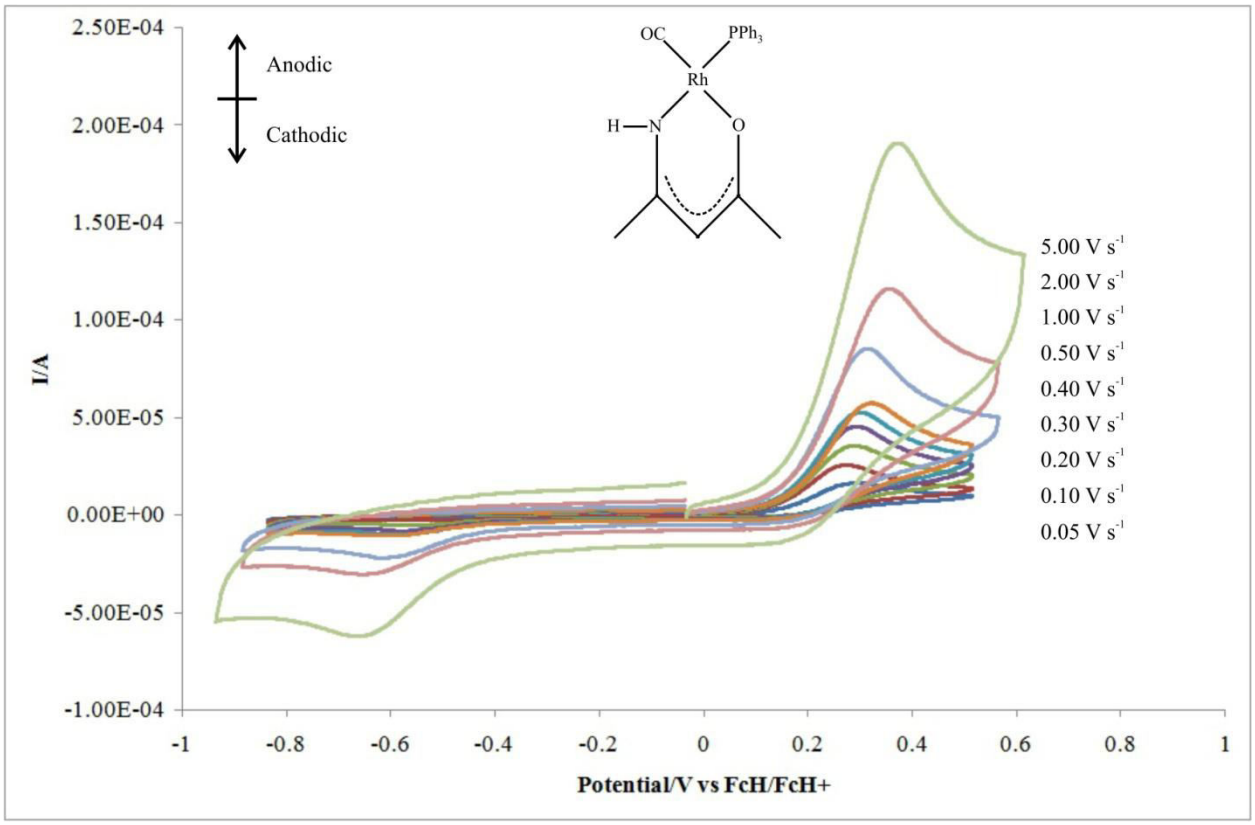

Figure C.4: Cyclic voltammograms of 0.002 moldm^{-3} $[Rh(CH_3COCHCNHCH_3)(CO)(PPh_3)]$ **3a** in dry acetonitrile with 0.1 M TBAHFP as supporting electrolyte, a glassy carbon working electrode, a Pt auxiliary electrode and a $Ag/AgNO_3$ reference electrode, with scan rates ranging from 0.05 V s^{-1} to 5.0 V s^{-1}. All measurements were done at 25°C.

Table C.5: Electrochemical parameters (E_{pa}, E_{pc}, i_{pa}, i_{pc}) of the $[Rh(CH_3CNPhCHCOCH_3)(CO)(PPh_3)]$ **3b** complex referenced against FcH as internal standard in the acetonitrile mixture containing 0.1 M TBAHFP as supporting electrolyte.

Scan rate (V s^{-1})	E_{pc} (mV)	i_{pc} (10^{-6} A)	E_{pa} (mV)	i_{pa} (10^{-6} A)	ΔE (mV)	i_{pa}/i_{pc}
0.05	-465	-1.60	377	9.60	842	0.17
0.1	-450	-1.50	338	10.20	788	0.14
0.2	-435	-3.10	353	14.70	788	0.21
0.3	-444	-6.50	355	18.70	799	0.35
0.4	-444	-5.10	355	22.40	799	0.23
0.5	-447	0.01	323	13.10	770	0.00
1	-444	-6.50	358	25.00	802	0.26
2	-485	-13.00	417	47.50	902	0.27
5	-500	-26.00	441	81.00	941	0.32

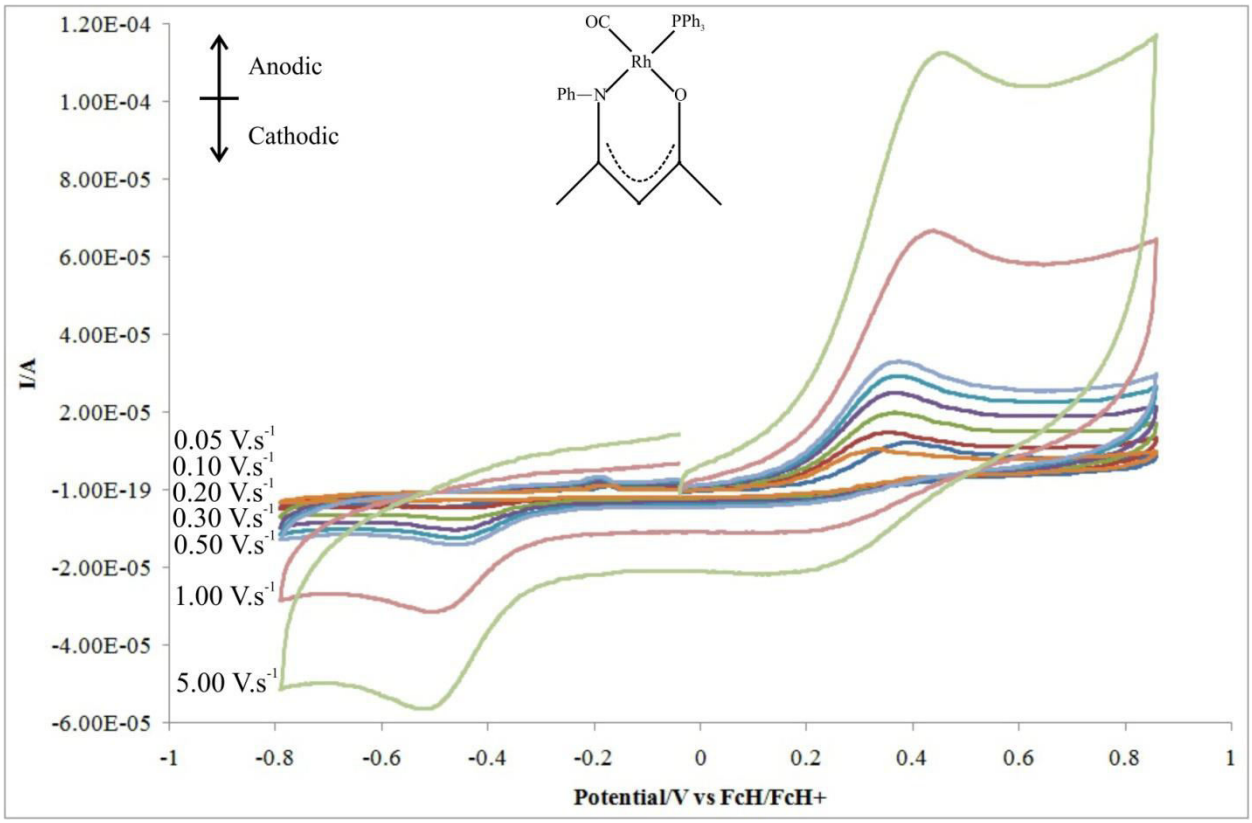

Figure C.5: Cyclic voltammograms of 0.002 moldm^{-3} $[Rh(CH_3COCHCNPhCH_3)(CO)(PPh_3)]$ **3b** in dry acetonitrile with 0.1 M TBAHFP as supporting electrolyte, a glassy carbon working electrode, a Pt auxiliary electrode and a $Ag/AgNO_3$ reference electrode, with scan rates ranging from 0.05 V s^{-1} to 5.0 V s^{-1}. All measurements were done at 25°C.

Table C.6: Electrochemical parameters (E_{pa}, E_{pc}, i_{pa}, i_{pc}) of the [Rh(bth)(CO)(PPh_3)] complex referenced against FcH as internal standard in the acetonitrile mixture containing 0.1 M TBAHFP as supporting electrolyte.

Scan rate (V s^{-1})	E_{pc} (mV)	i_{pc} (10^{-6} A)	E_{pa} (mV)	i_{pa} (10^{-6} A)	ΔE (mV)	i_{pa}/i_{pc}
0.05	----------	0.0	273.0	14.4	273	0
0.1	----------	0.0	286.0	19.9	286	0
0.2	-825.0	-1.2	308.0	28.0	1133	0.04
0.3	-821.0	-1.7	305.0	34.1	1126	0.05
0.4	-817.0	-2.1	310.0	39.2	1127	0.05
0.5	-813.0	-2.8	324.0	43.8	1137	0.06
1	-819.0	-4.6	342.0	61.7	1161	0.07
2	-843.0	-7.4	363.0	86.5	1206	0.09
5	-860.0	-14.3	389.0	137.0	1249	0.10

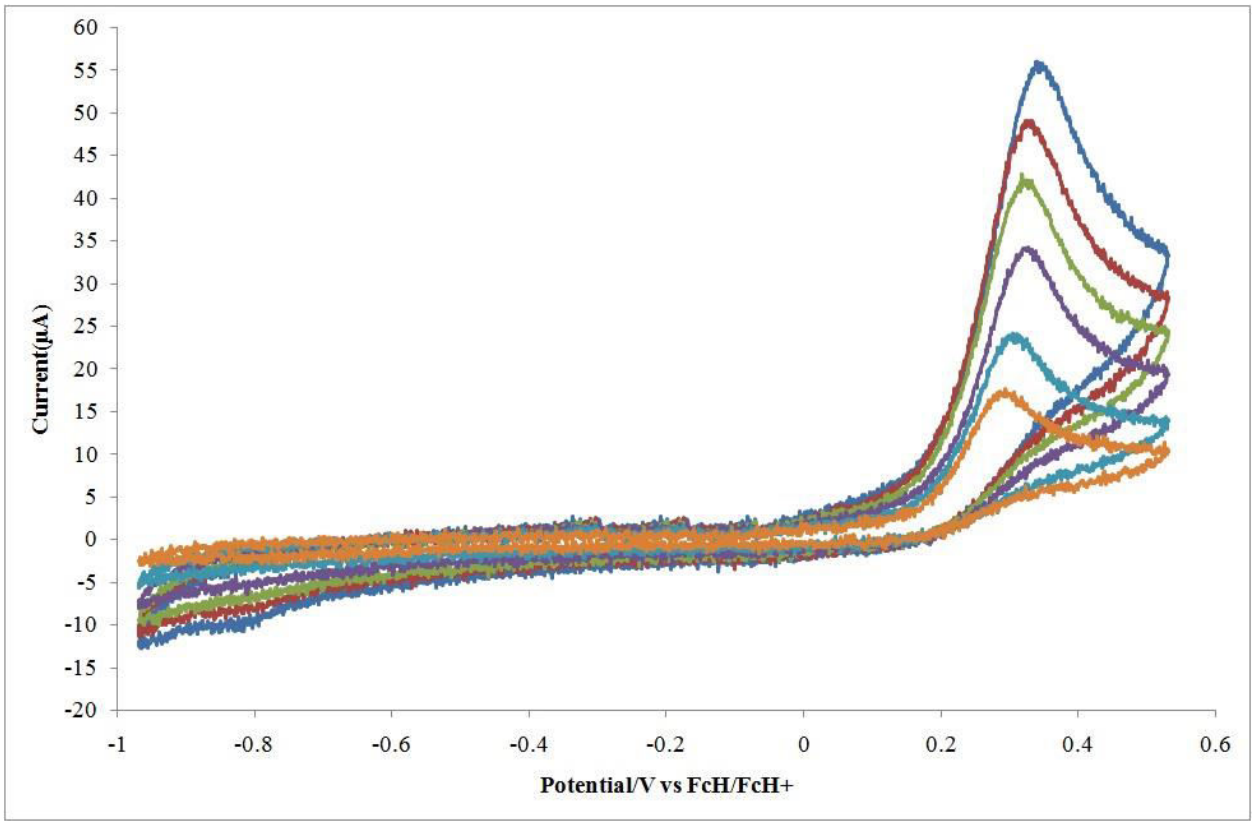

Figure C.6: Cyclic voltammograms of 0.002 M [Rh(bth)(CO)(PPh_3)] in dry acetonitrile with 0.1M TBAHFP as supporting electrolyte and a Ag/$AgNO_3$ reference electrode with scan rates ranging from 0.05 Vs^{-1} to 0.5 Vs^{-1}.

Table C.7: Electrochemical parameters (E_{pa}, E_{pc}, i_{pa}, i_{pc}) of the [Rh(dtm)(CO)(PPh_3)] complex referenced against FcH as internal standard in the acetonitrile mixture containing 0.1 M TBAHFP as supporting electrolyte.

Scan rate (V s^{-1})	E_{pc} (mV)	i_{pc} (10^{-6} A)	E_{pa} (mV)	i_{pa} (10^{-6} A)	ΔE (mV)	i_{pa}/i_{pc}
0.05	---	0.0	330.0	14.0	330	0
0.1	-757.0	-2.0	356.0	19.0	1113	0.11
0.2	-764.0	-4.0	364.0	24.5	1128	0.16
0.3	-749.0	-7.0	379.0	30.0	1128	0.23
0.4	-781.0	-7.5	366.0	36.5	1147	0.21
0.5	-841.0	-6.0	421.0	38.0	1262	0.16
1	-866.0	-12.0	381.0	58.0	1247	0.21
2	-836.0	-12.0	406.0	80.0	1242	0.15
5	-879.0	-29.0	429.0	116.0	1308	0.25

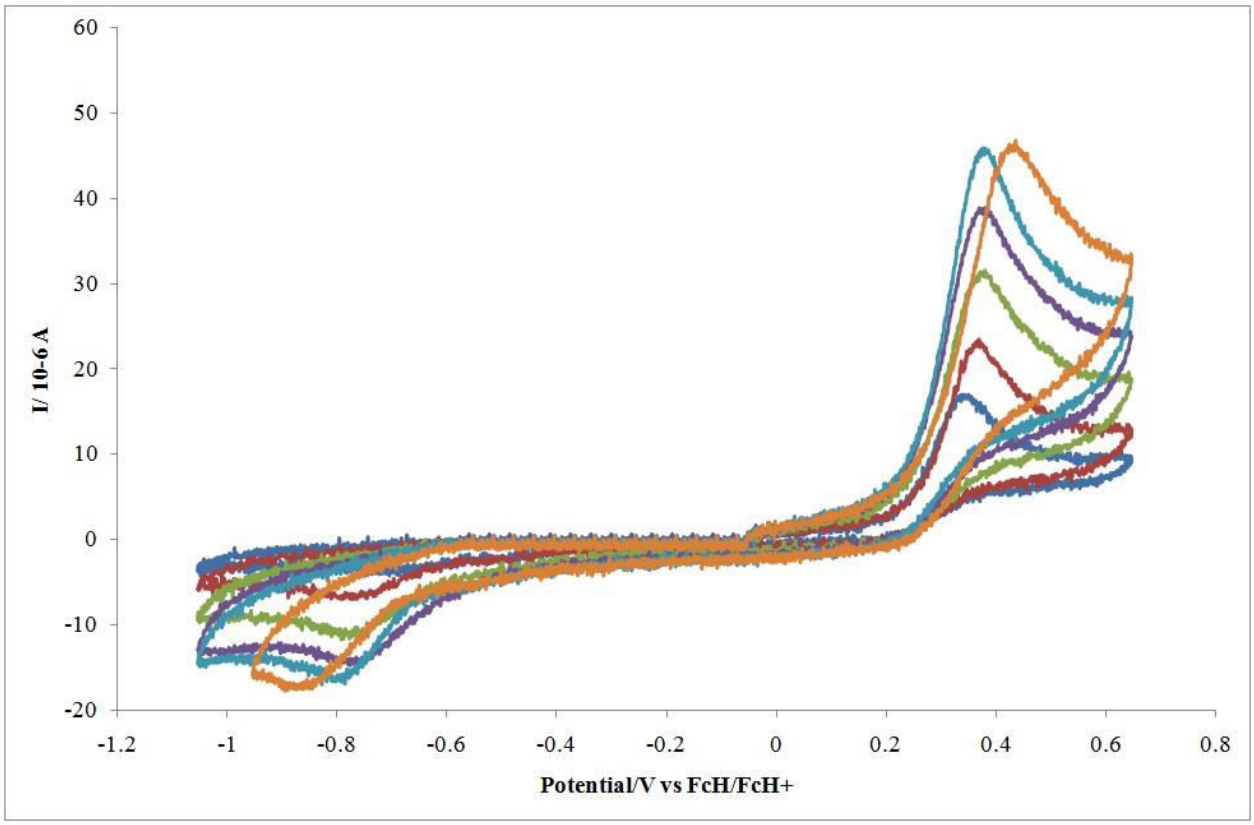

Figure C.7: Cyclic voltammograms of 0.002 M [Rh(dtm)(CO)(PPh_3)] in dry acetonitrile with 0.1M TBAHFP as supporting electrolyte and a Ag/$AgNO_3$ reference electrode with scan rates ranging from 0.05 Vs^{-1} to 0.5 Vs^{-1}.

Table C.8: Electrochemical parameters (E_{pa}, E_{pc}, i_{pa}, i_{pc}) of the [Rh(tta)(CO)(PPh_3)] complex referenced against FcH as internal standard in the acetonitrile mixture containing 0.1 M TBAHFP as supporting electrolyte.

Scan rate (V s^{-1})	E_{pc} (mV)	i_{pc} (10^{-6} A)	E_{pa} (mV)	i_{pa} (10^{-6} A)	ΔE (mV)	i_{pa}/i_{pc}
0.05	-586.0	-2.5	433.0	18.0	1019	0.14
0.1	-636.0	-3.2	426.0	20.7	1062	0.15
0.2	-671.0	-5.5	462.0	22.7	1133	0.24
0.3	-672.0	-8.3	456.0	27.5	1128	0.30
0.4	-694.0	-10.3	479.0	29.5	1173	0.35
0.5	-731.0	-13.0	492.0	31.7	1223	0.41
1	-727.0	-18.0	507.0	45.5	1234	0.40
2	-742.0	-27.0	532.0	51.5	1274	0.52
5	-789.0	-42.0	604.0	80.0	1393	0.53

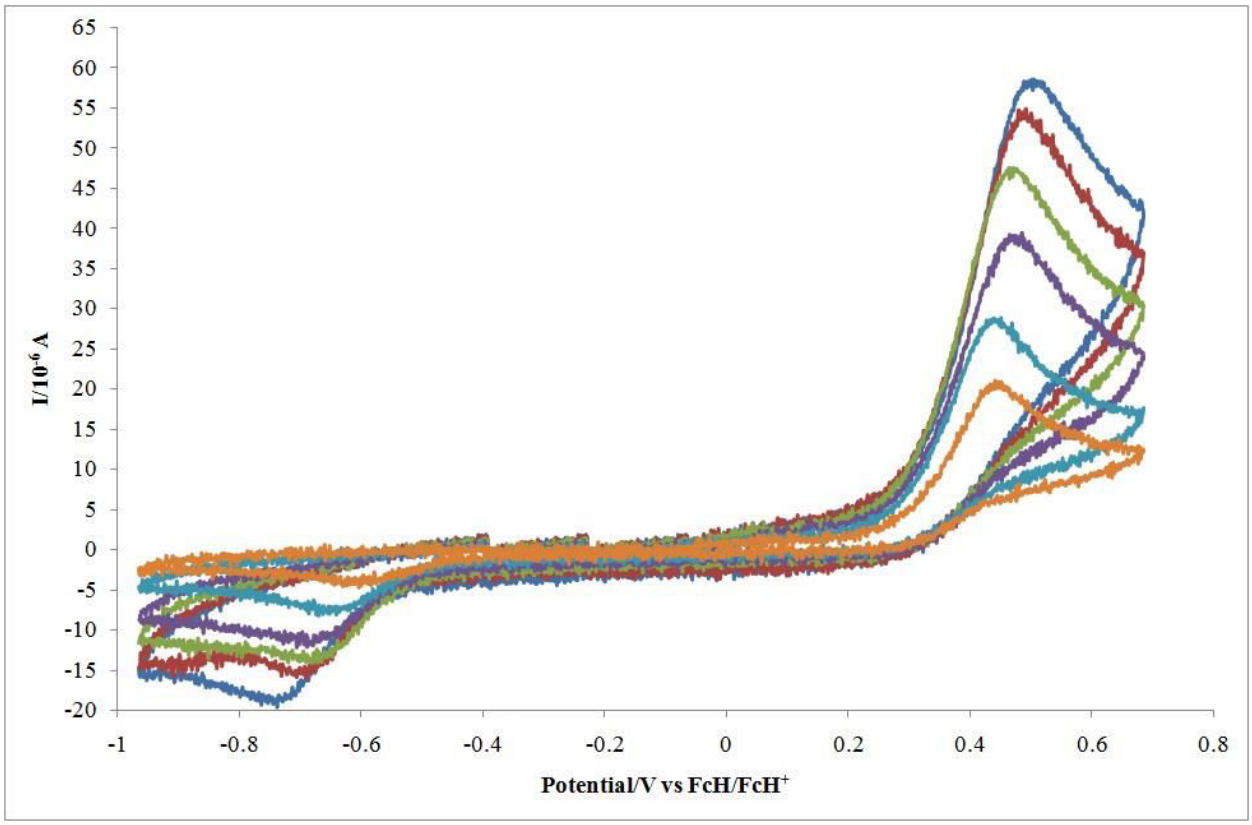

Figure C.8: Cyclic voltammograms of 0.002 M [Rh(tta)(CO)(PPh_3)] in dry acetonitrile with 0.1M TBAHFP as supporting electrolyte and a Ag/$AgNO_3$ reference electrode with scan rates ranging from 0.05 Vs^{-1} to 0.5 Vs^{-1}.

APPENDIX

Abstract

In this study L,L'-BID ligands were synthesized where the L and L' coordinating atoms were varied between O, NH and NPh. The ligands were ($CH_3COCHCOHCH_3$) (**Hacac**), ($CH_3COCHCNH_2CH_3$) (**1a**), ($CH_3COCHCNHPhCH_3$) (**1b**), ($CH_3CNHPhCHCNPhCH_3$) (**1c**). The dicarbonyl Rh complexes [Rh($CH_3COCHCNHCH_3$)$(CO)_2$] (**2a**), [Rh($CH_3COCHCNPhCH_3$)$(CO)_2$] (**2b**), [Rh($CH_3CNPhCHCNPhCH_3$)$(CO)_2$] (**2c**)) as well as the phosphine Rh complexes ([Rh($CH_3COCHCNHCH_3$)(CO)(PPh_3)] (**3a**), [Rh($CH_3COCHCNPhCH_3$)(CO)(PPh_3)] (**3b**)) were also synthesized and studied.

All ligands (**Hacac**, **1a** - **1d**) displayed a single reduction peak (<-2.5 V*vs*FcH/FcH^+) during electrochemical analysis. From the cyclic voltammetry (CV) data it is found that the electronegativity of the L,L' atoms, and their groups, have a significant electronic effect on the reduction potential. The observed trend was with the more positive reduction potential: Hacac>**1b>1c>1a**. This trend was the same as the trend in the electronegativies of atoms or groups. Complexes **3a** and **3b**, including selected complexes containing O.O'-BID ligands ([Rh($CH_3COCHCOHCH_3$)(CO)(PPh_3)], [Rh($C_4H_3SCOCHCOCPh$)(CO)(PPh_3)] **M1**, [Rh ($C_4H_3SCOCHCOCC_4H_3S$)(CO)(PPh_3)] **M2** and [Rh($C_4H_3SCOCHCOCF_3$)(CO)(PPh_3)] **M3**) all displayed a single $Rh^{I/III}$ oxidation peak and a single reduction peak, that is coupled to the oxidation peak. The [Rh(L,L'-BID)(CO)(PPh_3)] complexes displayed a similar trend to that observed for the free, unbound ligands, namely: [Rh($CH_3COCHCOHCH_3$)(CO)(PPh_3)]**>3b>3a**.

The kinetic results, followed *in situ* by UV/VIS, IR and NMR, for the oxidative reaction between CH_3I and complexes **3a** and **3b** indicated that complex **3b** displayed only one oxidative addition step in the reaction leading to an Rh(III)-alkyl, while complex **3a** displayed 2 steps: the first step is the formation of a Rh(III)-alkyl product and the second step the formation of a Rh(III)-acyl product.

Density functional theory calculations of the optimized geometries and energies of the reactants, possible products and transition states for the above mentioned reactions corroborated the experimentally observed results. For complex **3b** it was found that a single transition step is present in the reaction leading to the formation of a Rh(III)-alkyl product. For complex **3a** it was found that there are 2 transition states in the oxidative addition reaction. The first is the formation of the Rh(III)-alkyl product. The second is the formation of the Rh(III)-acyl product from the alkyl product through CO insertion. The Rh(III)-acyl product has the lowest energy.

Opsomming

In hierdie studie is L,L'-BID ligand gesintetiseer waar die L en L' koordinerende atome gevarieer is tussen O, NH en NPh. The ligande was: ($CH_3COCHCOHCH_3$) (**Hacac**), ($CH_3COCHCNH_2CH_3$) (**1a**), ($CH_3COCHCNHPhCH_3$) (**1b**), ($CH_3CNHPhCH_2CNPhCH_3$) (**1c**). Die dikarboniel Rh komplekse [Rh($CH_3COCHCNHCH_3$)$(CO)_2$] (**2a**), [Rh($CH_3COCHCNPhCH_3$)$(CO)_2$] (**2b**), [Rh($CH_3CNPhCHCNPhCH_3$)$(CO)_2$] (**2c**)) en die fosfien Rh komplekse ([Rh($CH_3COCHCNHCH_3$)(CO)(PPh_3)] (**3a**), [Rh($CH_3COCHCNPhCH_3$)(CO)(PPh_3)] (**3b**)) is ook gesintetiseer en bestudeer.

Alle ligande (**Hacac**, **1a** - **1d**) het 'n enkele reduksiepiek (<-2.5 V *vs* FcH/FcH^+) getoon gedurende elektrochemiese analise. Vanaf die sikliese voltammetrie (CV) data is bevind dat die elektronegatiwiteit van die L,L'atome, asook hulle groepe, 'n noemenswaardige elektroniese invloed het op die reduksie potensiaal. Die tendens, met die mees positiewe reduksie potensiaal: Hacac>**1b>1c>1a**. Die tendens was dieselfde as die tendens in die atoom en groep elektronegatiwiteite. Komplekse **3a** en **3b**, ingesluit sekere komplekse met O,O'-BID ligande ([Rh($CH_3COCHCOHCH_3$)(CO)(PPh_3)], [Rh($C_4H_3SCOCHCOCPh$)(CO)(PPh_3)] **M1**, [Rh ($C_4H_3SCOCHCOCC_4H_3S$)(CO)(PPh_3)] **M2** and [Rh($C_4H_3SCOCHCOCF_3$)(CO)(PPh_3)] **M3**) het almal 'n enkele $Rh^{I/III}$oksidasie piek en 'n enkele reduksiepiek, wat gekoppel is aan die oksidasie piek, getoon. Die [Rh(L,L'-BID)(CO)(PPh_3) komplekse het 'n tendens getoon soortgelyk aan dié waargeneem vir die vrye ligande, naamlik: [Rh($CH_3COCHCOCH_3$)(CO)(PPh_3)]>**3b>3a**.

Die kinetiese resultate, gevolg *in situ* deur UV/VIS, IR en NMR, vir die oksidatiewe addisie reaksie tussen CH_3I en komplekse **3a** en **3b** toon dat kompleks **3b** net 'n enkele stap het in die reaksie wat lei tot 'n RH(III)-alkiel produk, terwyl kompleks **3a** 2 stappe toon: die eerste stap is die vorming van 'n Rh(III)-alkiel produk en die tweede stap is die vorming van 'n Rh(III)-asiel produk.

Digtheids funksionaal teorie berekenings van die geoptimiseerde geometrieë en energieë van die reaktante, moontlike produkte en oorgangstoestande gedurende die bogenoemde reaksies staaf die eksperimentele resultate. Vir kompleks **3b** is 'n enkele oorgangstoestand gevind wat lei tot die vorming van die Rh(III)-alkielproduk. Vir kompleks **3a** was 2 oorgangstoestande gevind. Die eerste is die vorming van die Rh(III)-alkiel produk en die tweede is die vorming van die Rh(III)-asiel produk, wat die laagste energie besit.

Declaration

I, Hendrik Ferreira, declare that the dissertation/thesis hereby handed in for the qualification Magister Scientiae in Chemistry at the University of the Free State is my own independent work and that I have not previously submitted the same work for a qualification at/in another university/faculty. I furthermore cede copyright of the thesis in favour of the University of the Free State.

Signed Date

_____ _____